

博士論文

# A Study on Effective Control Mechanisms for Dynamic Flowfields around a Pitching Airfoil Using a DBD Plasma Actuator

(ピッチング翼周り動的流れ場のDBDプラズマアクチュエータによる  
効果的な制御メカニズムに関する研究)

Department of Aeronautics and Astronautics, University of Tokyo

Hiroaki Fukumoto

福本 浩章

March, 2017





# Abstract

Many kinds of fluid machinery are often operated in the environment where velocities and directions of flow around them have frequency fluctuation, resulting in deterioration in aerodynamic performances due to flow separation and stall. The stall phenomenon in a dynamic flowfield is called as “dynamic stall” and is distinguished from the stall phenomenon in a stationary flowfield. Details of dynamic stall around airfoils have been extensively investigated in the past several decades. It has been revealed that dynamic stall process is characterized by formation of a laminar separation bubble near the leading edge, its breakdown, formation of a dynamic stall vortex, and full stall after the convection of dynamic stall vortex into the wake. The dynamic stall results in increase in structural fatigue loading and deterioration of efficiency of fluid machinery, even if the operational conditions are under the rated condition. Dynamic stall can be observed around various flowfields; the examples of the flowfields severely suffered from dynamic stall are the flowfields around rotating blades of wind turbines and helicopters. Or the flowfield even around non-rotating blades, dynamic stall can occur in case of severe wing-gust encounters and it can lead aviation accidents. Therefore, mitigating or preventing dynamic stall has large beneficial effects on efficiency of fluid machinery.

In the past several decades, a lot of control technologies for separated or dynamically stalled flow have been studied in order to improve efficiency of fluid machinery. Recently, a dielectric barrier discharge (DBD) plasma actuator is proposed as a prospective alternative device to current complex mechanical or pneumatic systems. A typical plasma actuator consists of two thin electrodes and a dielectric. Because of its simple structure and high responsivity, it have been received a lot of attention as a perspective control device, and many researches have proved the applicability of the DBD plasma actuator for controlling separated flows around various fluid machinery. Since stationary flowfields are main target of separation control in most of the previous studies, knowledge of effective control mechanisms of the DBD plasma actuator on dynamic flowfields is limited.

The objective of this thesis is to find the guidelines of the DBD plasma actuators

to effectively enhance aerodynamic performances of wind turbine. In order to address this goal, the focus is put on clarifying the control effects of the DBD plasma actuator on dynamic flowfields, their control mechanisms, and the corresponding effective DBD plasma actuator parameter for each control effect. In this thesis, high-fidelity flow computation using large eddy simulations are conducted so as to investigate the details of the unsteady flowfield controlled by the DBD plasma actuator. The flowfield is modeled from that around a whole wind turbine to that around a pitching airfoil in the current research so as to evaluate as many cases as possible in details. The target flowfields are set to the flowfields around a pitching NACA0012 airfoil and a NACA63<sub>3</sub>-618 airfoil, which is one of the practical airfoils, at Reynolds number of  $2.56 \times 10^5$ . These airfoils dynamically pitch around their quarter-chord location from the leading edge with the reduced frequency of  $0.02\pi$ . Under these flow conditions, the flowfields undergo the deep dynamic stall.

This thesis comprises seven chapters. Chapter 1 introduces backgrounds and previous studies. Chapter 2 describes problem settings. Chapter 3 then describes governing equations, numerical methods, and numerical modeling of a DBD plasma actuator.

In Chapter 4, validation and verification results are described. The validation and verification studies show the significance of the spanwise length of the computational domain on dynamic flowfields. Through the validation and verification study, the sufficient spanwise length to resolve the flowfield through the entire pitching cycle is clarified.

In Chapter 5, the control effects of the DBD plasma actuator on the dynamic flowfield around a pitching NACA0012 airfoil are investigated and then the control effects, these mechanisms, and the corresponding effective DBD plasma actuator parameters are investigated in details and arranged. Investigation on the flowfield controlled with the DBD plasma actuator revealed that the control effects can be divided into three major ones; delaying dynamic stall onset, enhancing aerodynamic forces during full-stall, and promoting reattachment. The detailed investigations clarified the control mechanisms of each control effect and revealed the effective DBD plasma actuator parameters for each control effect. In delaying dynamic stall onset, the actuation frequency that can effectively stimulate the instability of the leading edge shear layer is revealed to be effective. In enhancing aerodynamic forces during full-stall and promoting reattachment, it is revealed that the effective actuation frequency depends on the frequency of the vortex shedding from the leading edge shear layer and the frequency based on the characteristic length and velocity of the large vortex which emanates from the leading edge. The findings in this chapter are summarized into two; the first is the related understandings of the control effects, mechanisms and the corresponding effective DBD plasma actuator

and the second is that the dynamic stall process and the control effects can be divided into some discrete stages/effects and discussions on the control effects and thus on the effective DBD plasma actuator parameters can be conducted isolated to each other control effect.

In Chapter 6, the findings in Chapter 5 are utilized to the dynamic flowfield around a pitching NACA63<sub>3</sub>-618 airfoil in order to support the conclusions and to discuss the effective control mechanisms and effective DBD plasma actuator parameters for controlling the dynamic flowfield around a pitching laminar airfoil. The flowfield around a NACA63<sub>3</sub>-618 airfoil has a different stall type from that around a NACA0012 airfoil. The result is that, however, the flow control attempts based on the findings from NACA0012 airfoil show good enhancements in the aerodynamic performances. In addition to basic cases, an adaptive control strategy is proposed for further enhancements and its effect is investigated. The result is that the adaptive case show great enhancements in the aerodynamic performances. This result supports the validity of the findings in Chapter 5 about the procedure for determining the DBD plasma actuator parameters; the DBD plasma actuator parameters can be determined by the investigation only on the flowfield in the corresponding stage of dynamic stall process. The control results and additional considerations on the applicability of the findings suggest that the findings are applicable to dynamic flowfields around various airfoils at various Reynolds number regime as long as the dynamic stall is characterized by LSB, and with various reduced frequencies.

Chapter 7 concludes this thesis. The goal of this thesis is attained by successfully revealing the control effects, mechanisms and the corresponding DBD plasma actuator parameters, not only for a simple airfoil but also for a practical airfoil.



# Acknowledgements

I would like to convey my sincere gratitude to all people who have helped and encouraged me to carry out my research. This thesis would not have been possible without those supports.

First of all I would like to express my deepest gratitude and appreciation to my advisor, Prof. Akira Oyama for his useful guidance, incredible patience, and considerable encouragements throughout my research. I am deeply grateful to my former advisor, Prof. Kozo Fujii for his expert guidance, insightful comments, and constructive criticism to my research. I would like to thank Prof. Kenichi Rinoie, Prof. Katsuhiko Nishinari, and Prof. Taro Imamura for being the thesis committee and their insightful comments and valuable suggestions.

My utmost thanks also go to Prof. Taku Nonomura and Prof. Hikaru Aono, I deeply appreciate their endless and generous guidance throughout my research. Their expertise in fluid dynamics and science helped me a lot in many aspects of all my accomplishments. This thesis would not have been possible without their extraordinary support. I am also thankful to Dr. Kazunori Mitsuo at Japan Aerospace Exploration Agency for fruitful discussions on the project.

I would like to thank the members of the wind turbine team on K project, Prof. Tomoaki Tatsukawa, Dr. Makoto Sato, Dr. Kengo Asada for their valuable comments. I also owe my sincere thanks to all the members in the laboratory for making my research days enjoyable.

This work is partially supported by Graduate program for Mechanical Systems Innovation (GMSI).

Last but not least, my deepest gratitude goes to my family for their generous understanding and tremendous support my pursuit of ambition.

March 2017  
Hiroaki Fukumoto



# Contents

<b>Abstract</b>	<b>i</b>
<b>Acknowledgements</b>	<b>v</b>
<b>1 Introduction</b>	<b>5</b>
1.1 Background . . . . .	5
1.2 Dynamic stall and its control attempts . . . . .	6
1.3 Overview of control mechanisms for stationary flowfields . . . . .	6
1.4 Researches on control of dynamic stalled flowfield DBD plasma actuator	8
1.5 Considerations on DBD plasma actuator application to laminar airfoils .	9
1.6 Objectives and outline . . . . .	10
<b>2 Problem Settings</b>	<b>13</b>
2.1 Target flowfield . . . . .	13
2.1.1 Flow conditions . . . . .	13
2.1.2 Target Airfoils . . . . .	16
2.1.3 Target aerodynamic performances . . . . .	16
2.2 DBD Plasma Actuator Parameters . . . . .	17
2.2.1 Parameters of Burst Wave . . . . .	17
<b>3 Numerical Methods</b>	<b>19</b>
3.1 Methods of Fluid Analysis . . . . .	19
3.1.1 LANS3D . . . . .	19
3.1.2 Governing Equations . . . . .	20
3.1.3 Numerical Schemes . . . . .	31
3.1.4 Computational Domain, Grid System, and Time Step Size . . . .	57
3.1.5 Modeling of airfoil pitching motion . . . . .	57
3.1.6 Boundary Conditions . . . . .	59
3.2 DBD Plasma Actuator Modeling . . . . .	63

3.2.1	Suzne and Huang Model . . . . .	63
3.2.2	Coupling with Fluid Governing Equations . . . . .	64
3.3	Data Processing . . . . .	66
3.3.1	Data acquisition . . . . .	66
3.3.2	Phase-averaging . . . . .	67
<b>4</b>	<b>Verification and validation</b>	<b>69</b>
4.1	Outline . . . . .	69
4.2	Validation and verification of spanwise length . . . . .	69
4.2.1	Verification of spanwise length on stationary flowfield . . . . .	70
4.2.2	Validation and verification of spanwise length on dynamic flowfield	76
4.2.3	Discussions . . . . .	82
4.3	Verification of grid spacing . . . . .	84
4.4	Verification of time step size . . . . .	85
4.5	Summary . . . . .	89
<b>5</b>	<b>Arrangement of effective control mechanisms of DBD plasma actuator on dynamic flowfields</b>	<b>91</b>
5.1	Outline . . . . .	91
5.2	Investigation on flowfield without control . . . . .	91
5.2.1	Stationary flowfield . . . . .	91
5.2.2	Dynamic flowfield . . . . .	92
5.2.3	Classification of dynamic stall process . . . . .	103
5.2.4	Consideration on DBD plasma actuator parameters . . . . .	103
5.3	Control effects . . . . .	108
5.3.1	Case description . . . . .	108
5.3.2	Control effects on cycle-averaged aerodynamic performances . . .	110
5.3.3	Control effects on phase-averaged flowfield . . . . .	111
5.3.4	Control effects on phase-averaged aerodynamic performances . . .	112
5.3.5	Control effects on phase-averaged separation and reattachment point . . . . .	122
5.3.6	Summary on control effects . . . . .	123
5.4	Control mechanisms . . . . .	127
5.4.1	Mechanisms on delaying dynamic stall onset . . . . .	127
5.4.2	Mechanisms on enhancing aerodynamic forces during full-stall . .	137
5.4.3	Mechanisms on promoting reattachment . . . . .	150



---

5.5	Summary . . . . .	159
<b>6</b>	<b>Study on effective control of dynamic flowfield around laminar airfoil</b>	<b>167</b>
6.1	Outline . . . . .	167
6.2	Investigation on flowfield without control . . . . .	167
6.2.1	Stationary flowfield . . . . .	167
6.2.2	Dynamic flowfield . . . . .	168
6.2.3	Considerations on DBD plasma actuator parameters . . . . .	174
6.3	Control of dynamic flowfield . . . . .	181
6.3.1	Case description . . . . .	181
6.3.2	Control effects on cycle-averaged aerodynamic performances . . .	182
6.3.3	Control effects on phase-averaged aerodynamic performances and characteristic $AoA$ . . . . .	182
6.4	Discussions . . . . .	183
6.4.1	Dynamic stall regimes . . . . .	194
6.4.2	Applicability to light stall regime . . . . .	194
6.4.3	Applicability to deep stall regime . . . . .	195
<b>7</b>	<b>Concluding Remarks</b>	<b>203</b>
	<b>Reference</b>	<b>209</b>



# List of Figures

1.1	Schematic of DBD plasma actuator and an actual DBD plasma actuator installed on an airfoil. . . . .	7
1.2	Large-scaled wind turbine installed with DBD plasma actuators in proving ground. . . . .	7
1.3	Lift curve for NACA64 <sub>3</sub> -618 airfoil at Reynolds number of $1.34 \times 10^5$ . <sup>1</sup> .	10
2.1	Lift curve obtained by the experiment. <sup>2</sup> OFF is for the case without DBD plasma actuation, ON is for with. . . . .	15
2.2	Airfoil shape. . . . .	16
3.1	Components of viscous stress tensor. . . . .	22
3.2	Concept of LES. . . . .	56
3.3	Computational grids. Every forth line is visualized here. . . . .	58
3.4	Force vectors obtaind by the Suzen-Huang model. . . . .	65
3.5	Example of time history of aerodynamic performance from the start of the computation. . . . .	66
4.1	$C_p$ and $C_f$ distributions for the stationary flowfields at $AoA$ of $10^\circ$ . . . .	72
4.2	Time- and span-averaged chordwise velocity flowfields for the stationary cases at $AoA$ of $10^\circ$ . . . . .	72
4.3	Autocorrelation of chordwise velocity for the stationary cases at $AoA$ of $10^\circ$ . . . . .	72
4.4	Time- and span-averaged chordwise velocity flowfield for the stationary cases at $AoA$ of $25^\circ$ . . . . .	74
4.5	Temporal development of $C_L$ in the quasi-steady state for the stationary cases at $AoA$ of $25^\circ$ . Tics for horizontal axis is for $tu_\infty/c$ of 5. . . . .	74
4.6	Temporal development of $C_L$ in the early stage of the computation for the stationary cases at $AoA$ of $25^\circ$ . . . . .	74

4.7	Snapshots of instantaneous flowfield for stationary flowfield at $25^\circ$ . The iso-surfaces indicate the second invariant of the velocity gradient tensor colored by total pressure coefficient. . . . .	75
4.8	Snapshots of instantaneous flowfields for the stationary cases at $AoA$ of $25^\circ$ . Isosurface of total-pressure colored by wall-normal vorticity is depicted from the chordwise view direction. For the case of S0.2c and S1.0c, flowfield is duplicated periodically for the comparison with the case of S5.0c. Every 5 point of LES calculation grid is visualized here. From top to bottom: S0.2, S1.0c and S5.0c. . . . .	77
4.8	<i>Continued.</i> . . . . .	78
4.9	$C_L$ , $C_D$ , and $C_M$ against the pitching angle for the dynamic cases. The experimental result <sup>2</sup> is plotted in the $C_L$ plot. . . . .	80
4.10	Phase- and span-averaged chordwise velocity flowfield for the dynamic cases. . . . .	81
4.11	Snapshots of instantaneous flowfields for the dynamic cases. Isosurface of total-pressure colored by wall-normal vorticity is depicted from the chordwise view direction. For the case of D0.2c and D1.0c, flowfield is duplicated periodically for the comparison with the case of D2.0c. Every 5 point of LES calculation grid is visualized here. From top to bottom: D0.2, D1.0c and D2.0c. . . . .	83
4.12	Aerodynamic performances against $AoA$ . . . . .	86
4.13	Chordwise $C_p$ and $C_f$ distributions for pitching NACA0012 airfoil at $phase$ of $76^\circ$ ( $AoA$ of $12.5^\circ$ ). . . . .	86
4.14	Phase- and span-averaged distributions of chordwise velocity, TKE, and Reynolds stress near the leading edge at $phase$ of $76^\circ$ ( $AoA$ of $12.5^\circ$ ). . . . .	87
4.15	Aerodynamic performances against $AoA$ . . . . .	88
4.16	Chordwise $C_p$ and $C_f$ distribution for pitching NACA0012 airfoil at $phase$ of $76^\circ$ ( $AoA$ of $12.5^\circ$ ). . . . .	89
4.17	Phase- and span-averaged distributions of chordwise velocity, TKE, and Reynolds stress near the leading edge at $phase$ of $76^\circ$ ( $AoA$ of $12.5^\circ$ ). . . . .	90
5.1	Chordwise $C_p$ and $C_f$ distributions of stationary NACA0012 airfoil. . . . .	93
5.2	Time- and span-averaged streamwise velocity flowfield with streamline of stationary NACA0012 airfoil. . . . .	94
5.3	Aerodynamic performances of stationary NACA0012 airfoil. . . . .	95
5.4	Phase- and span-averaged flowfield for pitching NACA0012 airfoil without control. . . . .	97

5.4	<i>Continued.</i>	98
5.5	Snapshots of instantaneous flowfield for pitching NACA0012 airfoil without control. The iso-surfaces indicate the second invariant of the velocity gradient tensor colored by total pressure coefficient.	99
5.6	Aerodynamic performances for pitching NACA0012 airfoil without control. Solid lines denote increasing $AoA$ , dashed lines decreasing $AoA$ .	100
5.7	Separation, reattachment, and secondary separation points against pitching phase for stationary and pitching NACA0012 airfoil without control. Corresponding $AoA$ is plotted with right axis.	104
5.8	Characteristic flowfields in each classified dynamic stall process. Left column: Phase- and span-averaged chordwise velocity field. Right column: Instantaneous flowfield. The iso-surfaces indicate the second invariant of the velocity gradient tensor colored by spanwise vorticity.	105
5.9	PSD of chordwise velocity on shear layer for pitching NACA0012 airfoil without control.	109
5.10	Top three rows: Phase- and span-averaged chordwise velocity field for pitching NACA0012 airfoil. Bottom row : Phase-averaged $C_p$ and $C_f$ distributions.	113
5.10	<i>Continued.</i>	114
5.10	<i>Continued.</i>	115
5.10	<i>Continued.</i>	116
5.10	<i>Continued.</i>	117
5.10	<i>Continued.</i>	118
5.10	<i>Continued.</i>	119
5.10	<i>Continued.</i>	120
5.11	Aerodynamic performances against $AoA$ for pitching NACA0012 airfoil.	121
5.12	Separation, reattachment, and secondary separation points against pitching phase for NACA0012 airfoil. Corresponding $AoA$ is plotted with right axis. Background color depicts phase- and span-averaged $C_p$ distribution.	124
5.12	<i>Continued.</i>	125
5.12	<i>Continued.</i>	126
5.13	Phase- and span-averaged chordwise velocity field near the leading edge at the <i>phase</i> of $76^\circ$ ( $AoA = 12.5^\circ$ )	128
5.14	Phase- and span-averaged chordwise velocity distributions near the leading edge at the <i>phase</i> of $76^\circ$ ( $AoA = 12.5^\circ$ ). Separation and reattachment points are presented respectively with circles and triangles.	129

5.15	Phase- and span-averaged TKE field near the leading edge at the <i>phase</i> of $76^\circ$ ( $AoA = 12.5^\circ$ ) . . . . .	129
5.16	Phase- and span-averaged Reynolds stress field near the leading edge at the <i>phase</i> of $76^\circ$ ( $AoA = 12.5^\circ$ ) . . . . .	130
5.17	Phase- and span-averaged chordwise TKE and Reynolds stress distributions near the leading edge at the <i>phase</i> of $76^\circ$ ( $AoA = 12.5^\circ$ ). Separation and reattachment points are presented respectively with circles and triangles. . . . .	131
5.18	Snapshots of instantaneous flowfields around $AoA$ of $10^\circ$ in the <i>phase</i> of $65^\circ$ for pitching NACA0012 airfoil. The iso-surfaces indicate the second invariant of the velocity gradient tensor colored by spanwise vorticity. Time lapses from top to bottom with time increment of $tu_\infty/c = 0.05$ . . .	132
5.18	<i>Continued.</i> . . . .	133
5.19	Side-view for instantaneous flowfield around the leading edge shear layer in the <i>phase</i> of $65^\circ$ . The black line contour depicts the second invariant of the velocity gradient tensor, and color contour depicts the spanwise vorticity. Time lapses from top to bottom with time increment of $tu_\infty/c = 0.065$ . .	134
5.19	<i>Continued.</i> . . . .	135
5.20	Closed-up of separation and reattachment points and angle of shear layer around the breakdown of LSB against pitching phase for NACA0012 airfoil. The actuation timing is presented at the bottom. . . . .	138
5.21	PSD of chordwise velocity on shear layer for pitching NACA0012 airfoil around the <i>phase</i> of $68^\circ$ ( $AoA$ : $10.7 \sim 11.3^\circ$ during pitching up). . . . .	139
5.22	Top row: Phase- and span-averaged total-pressure coefficient fields. Bottom row : Phase-averaged $C_p$ and $C_f$ distributions. . . . .	141
5.23	Snapshots of instantaneous flowfields in the <i>phase</i> of $223 \sim 244^\circ$ . The iso-surfaces indicate the second invariant of the velocity gradient tensor colored by total-pressure coefficient. Time lapses from top to bottom with time increment of $tu_\infty/c = 0.2$ . . . . .	143
5.23	<i>Continued.</i> . . . .	144
5.23	<i>Continued.</i> . . . .	145
5.24	Behaviour of the shear layer during the <i>phase</i> of $205 \sim 250^\circ$ , $AoA$ corresponds to $24 \sim 18.5^\circ$ . The actuation timing is presented at the bottom. .	146
5.25	PSD of chordwise velocity on shear layer for pitching NACA0012 airfoil around the <i>phase</i> of $225^\circ$ ( $AoA$ : $22.3 \sim 21.9^\circ$ during pitching down). . .	148

5.26	Size index for maximum vortex size near the leading edge during the <i>phase</i> of $205 \sim 250^\circ$ , $AoA$ corresponds to $24 \sim 18.5^\circ$ . The actuation timing is presented at the bottom. . . . .	150
5.27	Interactions around the large vortices in the case of ON $F^+ = 0.5$ and ON $F^+ = 6$ . Instantaneous iso-surfaces for the second invariant of the velocity gradient tensor colored by total-pressure coefficient are depicted with the black contour line for the spanwise-averaged second invariant of the velocity gradient tensor. . . . .	151
5.28	Top three rows: Phase- and span-averaged chordwise velocity field for pitching NACA0012 airfoil. Bottom row : Phase-averaged $C_p$ and $C_f$ distributions. . . . .	153
5.28	<i>Continued.</i> . . . . .	154
5.29	Left column: Phase- and span-averaged TKE field. Left column: Phase- and span-averaged Reynolds stress field. . . . .	155
5.29	<i>Continued.</i> . . . . .	156
5.30	Wall-normal distributions of phase- and span-averaged chordwise TKE (left) and Reynolds stress (right) near the leading edge. Separation and reattachment points are presented respectively with circles and triangles. $AoA$ are of in pitching down. . . . .	157
5.30	<i>Continued.</i> . . . . .	158
5.31	PSD of chordwise velocity on shear layer for pitching NACA0012 airfoil around the <i>phase</i> of $256^\circ$ ( $AoA$ : $18.1 \sim 17.5^\circ$ during pitching down). . .	160
5.32	Closed-up of the properties of the shear layer and the shed vortices around the reattachment phase. The actuation timing is presented at the bottom.	161
6.1	Chordwise $C_p$ and $C_f$ distributions for stationary NACA63 <sub>3</sub> -618airfoil. .	169
6.2	Time- and span-averaged streamwise velocity flowfield with streamline for stationary NACA63 <sub>3</sub> -618 airfoil. . . . .	170
6.3	Aerodynamic performances for stationary NACA63 <sub>3</sub> -618 airfoil. . . . .	171
6.4	Aerodynamic performances against $AoA$ for pitching NACA63 <sub>3</sub> -618 airfoil without control. Solid lines denote increasing $AoA$ , dashed lines decreasing $AoA$ . . . . .	172
6.5	Phase- and span-averaged flowfield for pitching NACA63 <sub>3</sub> -618 airfoil without control. . . . .	175
6.5	<i>Continued.</i> . . . . .	176

6.6	Snapshots of instantaneous flowfield for pitching NACA63 <sub>3</sub> -618 airfoil without control. The iso-surfaces indicate the second invariant of the velocity gradient tensor colored by total pressure coefficient. . . . .	177
6.7	Separation, reattachment, and secondary separation points against pitching phase for stationary and pitching NACA63 <sub>3</sub> -618 airfoil without control. Corresponding $AoA$ is plotted with right axis. . . . .	178
6.8	PSD of chordwise velocity on shear layer for pitching NACA63 <sub>3</sub> -618 airfoil before the breakdown of LSB. . . . .	178
6.9	Phase history of phase- and span-averaged surface $C_p$ at various chordwise location. . . . .	180
6.10	PSD of chordwise velocity on shear layer for pitching NACA63 <sub>3</sub> -618 airfoil during the full-stall. . . . .	180
6.11	Aerodynamic performances against $AoA$ for pitching NACA63 <sub>3</sub> -618 airfoil.	184
6.12	Top left to right : Phase- and span-averaged flowfield for basic cases of pitching NACA63 <sub>3</sub> -618 airfoil. Left to right: OFF, ON $F^+ = 0.5$ , $ONF^+ = 6$ , and $F^+ = 50$ . Bottom: Phase-averaged $C_p$ and $C_f$ distribution.	185
6.12	<i>Continued.</i> . . . .	186
6.12	<i>Continued.</i> . . . .	187
6.12	<i>Continued.</i> . . . .	188
6.12	<i>Continued.</i> . . . .	189
6.12	<i>Continued.</i> . . . .	190
6.12	<i>Continued.</i> . . . .	191
6.12	<i>Continued.</i> . . . .	192
6.13	Dynamic stall regimes. <sup>3</sup> $C_L$ , $C_M$ , and $C_D$ curves against $AoA$ are depicted for the flowfield around a pitching NACA0012 airfoil at Reynolds number of $\mathcal{O}(10^6)$ with $k = 0.1$ . $\alpha = \alpha_0 + 10^\circ \sin \omega t$ , solid lines denote increasing $\alpha$ , dashed lines decreasing $\alpha$ . . . . .	194
6.14	Dependencies on airfoil geometry of flowfield in deep stall regime <sup>3</sup> $C_L$ , $C_M$ , and $C_D$ curves against $AoA$ are depicted for the flowfield around pitching various airfoils at Reynolds number of $\mathcal{O}(10^6)$ with $k = 0.1$ . $AoA = 15^\circ + 10^\circ \sin \omega t$ , solid lines denote increasing $\alpha$ , dashed lines decreasing $\alpha$ .	197
6.15	Classification of dynamic stall process at Reynolds number $= 2.56 \times 10^5$ with $k = 0.02\pi$ . . . . .	198
6.16	Classification of dynamic stall process at Reynolds number $= 2.56 \times 10^5$ with $k = 0.03\pi$ . . . . .	199



---

6.17 Classification of dynamic stall process at Reynolds number = $2.56 \times 10^5$ with $k = 0.05\pi$ . . . . .	200
6.18 Classification of dynamic stall process by Carr. <sup>4</sup> Reynolds number is $2.6 \times 10^6$ and the reduced frequency $k$ is 0.15. . . . .	201
6.19 Classification of dynamic stall process at Reynolds number = $6.30 \times 10^4$ with $k = 0.02\pi$ . . . . .	202



# List of Tables

2.1	Series of researches on controlling dynamic flowfield around wind turbine.	15
2.2	Baseline flow conditions. . . . .	15
3.1	Coefficients of compact difference scheme . . . . .	38
3.2	Coefficients $a_{f,n}$ in tenth order tri-diagonal filtering. . . . .	42
3.3	Coefficients $a_{f,k}^n$ in tenth order tri-diagonal filtering. . . . .	42
3.4	Grid points. . . . .	58
4.1	Grids used for verification of spanwise length . . . . .	71
4.2	$C_L$ for the stationary flowfield at $AoA$ of $10^\circ$ . . . . .	71
4.3	Grid points . . . . .	84
4.4	Cycle-averaged aerodynamic performances. . . . .	85
4.5	Cycle-averaged aerodynamic performances. . . . .	88
5.1	Cases for stationary NACA0012 airfoil without control. . . . .	92
5.2	Case for pitching NACA0012 airfoil without control. . . . .	92
5.3	Cases for pitching NACA0012 airfoil. . . . .	110
5.4	Cycle-averaged aerodynamic performances. . . . .	111
5.5	Control effects on $AoA_{BD}$ , $AoA_{DS}$ , $AoA_{LD}$ , and $AoA_{RA}$ for pitching NACA0012 airfoil. $AoA_{BD}$ for the case of ON $F^+ = 0.5$ is obtained by rough estimation. $AoA_{BD}$ , $AoA_{DS}$ , and $AoA_{LD}$ are in the pitching up and $AoA_{RA}$ is in the pitching down. . . . .	123
6.1	Cases for stationary NACA63 <sub>3</sub> -618 airfoil without control. . . . .	168
6.2	Case for pitching NACA63 <sub>3</sub> -618 airfoil without control. . . . .	169
6.3	Cases for pitching NACA63 <sub>3</sub> -618 airfoil. . . . .	181
6.4	Cycle-averaged aerodynamic performances. . . . .	182

---

6.5 Control effects on  $AoA_{BD}$ ,  $AoA_{DS}$ ,  $AoA_{LD}$ , and  $AoA_{RA}$  for pitching NACA63-618 airfoil. Values in brackets are of rough estimation.  $AoA_{BD}$ ,  $AoA_{DS}$ , and  $AoA_{LD}$  are in the pitching up and  $AoA_{RA}$  is in the pitching down. . 183

6.6 List of auxiliary cases. . . . . 193

# Nomenclature

## Roman Symbols

$a$	speed of sound
$A$	amplitude of oscillation
$a_{cmpt}, b_{cmpt}, c_{cmpt}$	coefficients for compact scheme
$AoA$	angle of attack, also denoted as $\alpha$
$AoA_{BD}$	angle of attack at which the laminar separation bubble breaks down
$AoA_{DS}$	angle of attack at which maximum leading edge suction peak in $C_p$ is observed
$AoA_{LD}$	angle of attack at which first drop in $C_L$ is observed
$AoA_{LDDS}$	angle of attack at which drop in $C_L$ associated to dynamic stall is observed
$AoA_{RA}$	angle of attack at which flow starts to reattach
BR	burst ratio, $BR = \frac{T_{on}}{T_{BST}}$
$c$	chord length
$C_D$	drag coefficient
$C_L$	lift coefficient
$C_\mu$	momentum coefficient
$C_M$	moment coefficient
$C_Q$	torque coefficient
$C_T$	total-pressure coefficient
$C_f$	friction coefficient
$C_p$	pressure coefficient
$D_c$	ratio between electrostatic energy added from plasma actuator and dynamical pressure
$e$	total energy per unit volume
$E, F, G$	fluxes in Navier-Stokes equations
$E_i, E_k$	electric field vector induced by plasma actuator, $i, k = 1, 2, 3$
$f$	frequency
$f_{base}$	input voltage sine wave frequency

---

$f^+$	burst frequency, $f^+ = \frac{f_{base} \text{ BR}}{n} = \frac{1}{T_{BST}}$
$F^+$	non-dimensional burst frequency, $F^+ = \frac{f^+ c}{u_\infty}$
$L/D$	lift-to-drag ratio
$k$	reduced frequency , $\pi f c / u_\infty$
$M$	Mach number
$M_\infty$	free stream Mach number
$n$	wavenumber for one burst wave cycle
$p$	pressure
$Pr$	Prandtl number
$phase$	phase, $\omega t$
$q_c$	electric charge
$q_i$	heat flux vector, $i = 1, 2, 3$
$Q$	conservative variables in Navier-Stokes equations
$R$	autocorrelation
$Re$	Reynolds number based on chord length
$S_i$	body force vector, $S_i = q_c E_i$ , $i = 1, 2, 3$
$S_{max,i}$	maximum magnitude body force vector , $i = 1, 2, 3$
$s_{shed}$	distance between separation point and tip of leading edge shear layer
$St$	Strouhal number
$t$	time
$\Delta t$	time step size
$T$	temperature
$T_{BST}$	burst wave period
$T_{on}$	period of sine wave switch on in a burst wave period
$u, v, w$	velocity components in Cartesian coordinate $(x, y, z)$ ; also $u_i, u_k$ , $i, k = 1, 2, 3$
$u', v', w'$	velocity fluctuations in Cartesian coordinate $(x, y, z)$
$U, V, W$	contravariant velocity components in curvilinear coordinate
$x, y, z$	Cartesian coordinates; also $x_k$ , $k = 1, 2, 3$

### Greek Symbols

$\alpha$	angle of attack
$\alpha_{amp}$	pitching amplitude
$\alpha_{min}$	minimum angle of attack
$\alpha_{cmpt}, \beta_{cmpt}$	coefficient of compact scheme
$\alpha_f$	coefficient of filter

---

$\gamma$	specific heat ratio
$\delta_{ik}$	Kronecker's delta, $i, k = 1, 2, 3$
$\Delta$	discretized step size
$\kappa$	coefficient of heat conductivity
$\mu$	coefficient of viscosity
$\omega$	circular frequency, $2\pi f$
$\rho$	density
$\tau_{i,j}$	viscous stress tensor, $i, j = 1, 2, 3$
$\xi, \eta, \zeta$	curvilinear coordinates
$\zeta_d$	net-cycle pitch damping

### Subscripts

eff	effective value
lv	characteristic value of large vortex
ref	reference value
$\infty$	ambient (free stream) condition

### Superscripts

'	filtered quantity
'	fluctuation quantity
*	dimensional quantity

### Symbols

$\langle Q \rangle$	mean or ensemble average of Q
$\langle Q \rangle_{\text{rms}}$	root mean square of Q
$[Q]$	the largest integer less than or equal to Q

### Abbreviations

CFD	computational fluid dynamics
CFL	Courant-Friedrichs-Lewy
DBD	dielectric barrier discharge
DNS	direct numerical simulation
DSV	dynamic stall vortex
ILES	implicit large-eddy simulation
LES	large-eddy simulation
LSB	laminar separation bubble

MILES	monotonically integrated large-eddy simulation
MUSCL	monotonic upstream scheme for conservation laws
PIV	particle image velocimetry
Predet	predeterminant
PSD	power spectrum density
RANS	reynolds-averaged Navier-Stokes
Reatt	reattachment
Sep	separation
TKE	turbulence kinetic energy
TVD	total-variation diminishing



# Chapter 1

## Introduction

### 1.1 Background

Wind energy has been gathered a lot of attention as a renewable energy over the past decades. Usually, the blades of modern wind turbines are designed to produce power with maximum efficiency under the rated speeds of the wind and the rotor. The flow condition that each spanwise part of the blade experiences, however, is not static but dynamic due to the wind shear, yaw misalignment, gusts, or a combination of these phenomena. In wind farms, the wind condition becomes more “dynamic” due to the wake of the wind turbines located in the upstream side. With such dynamic condition, the flow around the blade is no longer fully attached but is somewhat separated, or, often deeply stalled because the flow condition can be out of the range of the design condition. The stall phenomena in a dynamic flowfield is called as “dynamic stall”<sup>4</sup> and is distinguished from the stall phenomena in a stationary flowfield. Dynamic stall is characterized by a dynamic stall vortex (DSV). DSV emanates from near the leading edge and sheds toward the downstream producing a temporary increase in lift and drag and a subsequent large oscillation in aerodynamic forces. The dynamic stall results in the increase in structural fatigue loading and the deterioration of power efficiency of the wind turbine, even if the speeds of the wind and the rotor are under the rated condition. Therefore, mitigating or preventing dynamic stall have large beneficial effects on the cost of energy generation by wind turbines.

Here, not only around wind turbines, but dynamic stall can be observed also around various flowfields. The other major flowfield which is suffered from the dynamic stall would be the flowfield around helicopter blades. The dynamic stall around helicopter blades limits the aircraft’s maneuverability, agility as well as speed.<sup>5</sup> Or even around non-rotating blades, dynamic stall can occur in case of severe wing-gust encounters<sup>6</sup> and

it can lead aviation accidents. Thus, control of dynamic stall have large beneficial effects also on general aircrafts, not only on wind turbines.

## 1.2 Dynamic stall and its control attempts

To address these problems stated above, many researches to understand the dynamic stall phenomena and to control this have been conducted. Now the dynamic stall phenomena has been gradually clarified along with development in the technologies both of experiment and of computational fluid dynamics (CFD). The onset of dynamic stall can be described as follows from low to moderate Reynolds number regime;<sup>7</sup> a laminar separation bubble (LSB) develops prior to stall, and this LSB reduces its size with increasing angle of attack ( $AoA$ ). This LSB eventually bursts and breaks down into larger vortex structure in a continuous manner.

The control of dynamic stall have been tackled by a lot of kinds of control device. For example, the control device can be a leading edge slat,<sup>8</sup> periodic jet forcing,<sup>9</sup> steady blowing,<sup>10</sup> and pulsed jets.<sup>11,12</sup> Recently, a dielectric barrier discharge (DBD) plasma actuator<sup>13</sup> is considered to be a prospective alternative device to the current complex mechanical or pneumatic systems. A typical DBD plasma actuator consists of two thin electrodes and one dielectric as depicted in Figure 1.1. When an alternating-current AC high voltage with high modulation frequency is imposed between the two electrodes, an atmospheric-pressure nonequilibrium plasma is created and this induces a wall-jet-like flow above the dielectric.<sup>14</sup> Because of its simple structure and characteristics, it can be easily installed on the existing machines. Recently, the studies that apply a DBD plasma actuator on a wind turbine began to be reported<sup>15–18</sup> (Figure 1.2). These study have successfully proved the applicability of DBD plasma actuator on dynamic flowfields.

## 1.3 Overview of control mechanisms for stationary flowfields

Many experimental and computational studies have been conducted to prove the availability of the DBD plasma actuator and to understand its control mechanism under various flow conditions around the following various stationary objects; simple airfoils,<sup>19–25</sup> low-pressure turbine blades,<sup>26–28</sup> bluff-bodies,<sup>29,30</sup> and wind turbine blades.<sup>31,32</sup>

Thus far, the effective control mechanisms on the flowfield around stationary objects are being clarified;<sup>33–37</sup> with regard to the way of actuation, it has been clarified that use

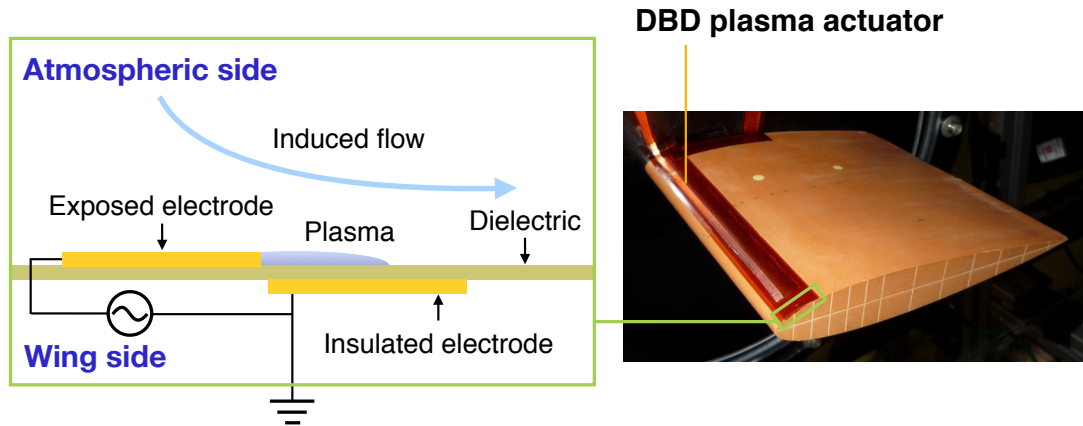


Figure 1.1: Schematic of DBD plasma actuator and an actual DBD plasma actuator installed on an airfoil.

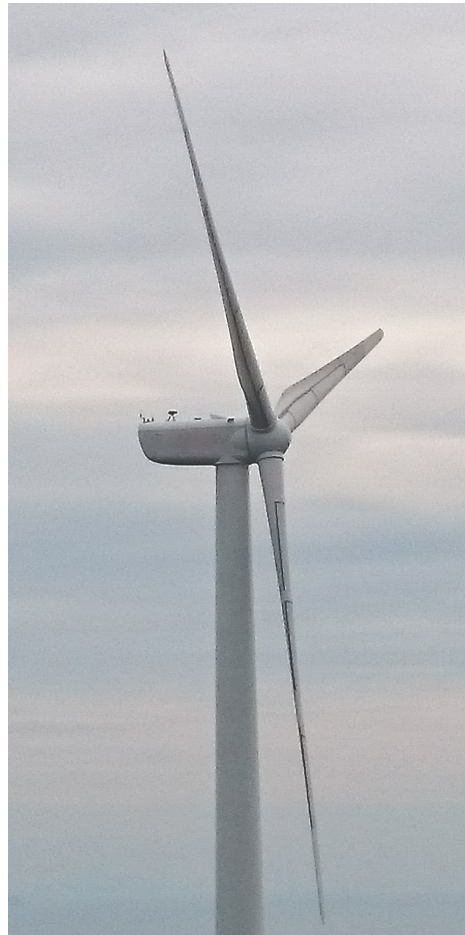


Figure 1.2: Large-scaled wind turbine installed with DBD plasma actuators in proving ground.

of the unsteady actuation provides better separation control capability than the steady actuation.<sup>38–41</sup> It has been reported that the most effective unsteady actuation parameter nondimensionalized by the freestream velocity and the chord length ( $F^+$ ) is the order of

unity,<sup>19,20,36</sup> or is near the subharmonic of the most unstable mode of the leading edge shear layer.<sup>6,42</sup> With regard to the installation position of the plasma actuator, Sato et al. investigated the effect of installation position and concluded that the effective installation position is just the upstream of the natural separation point.<sup>43</sup>

## 1.4 Researches on control of dynamic stalled flow-field DBD plasma actuator

Some studies have investigated the availability of the DBD plasma actuator for controlling dynamic flowfields. Post et al.<sup>20</sup> conducted experimental research to control the dynamic flowfield around a pitching NACA0015 airfoil using a DBD plasma actuator. They compared the effectiveness of  $F^+$  of 0.25 and unity, with the index of enhancing  $C_L$  and/or delaying momentum stall. Their conclusion is that the effective  $F^+$  for enhancing cycle-integrated  $C_L$  is 0.25, and that for delaying momentum stall is unity. Mitsuo et al.<sup>2</sup> conducted experiments to control the dynamic flowfield around a NACA0012 airfoil with a DBD plasma actuator. They explored the effectiveness of  $F^+$  from 0.25 to 1.0 with the aim of enhancing cycle-integrated  $C_L$ . Their result showed that  $F^+$  of 0.5 is the best. Frankhouser et al.<sup>44</sup> conducted experiments to control the dynamic flowfield around a NACA0015 airfoil with a nanosecond-DBD plasma actuator. They explored the effectiveness of  $F^+$  from 0.78 to 6.09 with the aim of delaying dynamic stall. Their result showed that  $F^+$  of 0.78 is the best for delaying dynamic stall. Visbal et al.,<sup>45</sup> Benton and Visbal et al.<sup>46</sup> conducted LES researches for controlling the flowfield around a pitching NACA0012 airfoil with zero-net mass flow device. They compared the effectiveness of  $F^+$  of 6.25 to 50 and explored the effective  $F^+$  within the range of 10 to 150 with the aim of delaying the stall, respectively. The results from these two references are the same, and  $F^+$  50 is found to be effective.

The objective differs between the references; some aim at delaying dynamic stall, and the other aim at enhancing  $C_L$ . With regard to the aim of delaying the stall, consecutive argument with these reference is not possible because the explored  $F^+$  range differs with each other. Or, a reference<sup>44</sup> says the lower frequency is better, while the other<sup>6</sup> says the higher frequency is better. With regard to the optimal  $F^+$  for enhancing  $C_L$  or  $L/D$ , the optimal  $F^+$  is reported as 0.25 or 0.5, and this seems to say the low frequency of the order of unity is better. However, these two references only explores under  $F^+$  of unity. If they explored above  $F^+ = 50$ , or if Visbal et al. aimed at enhancing  $C_L$  or  $L/D$ , the result might differ. Note that the group of Visbal is only the group which

conducts high-fidelity LES on the control of dynamic flowfield, however, their research does not mention about the cycle-integrated  $C_L$  or  $L/D$ . The number of references which address the effective  $F^+$  on controlling dynamic flowfields is not so large, but consistent conclusion cannot be deduced to the best of the author's reference research.

## 1.5 Considerations on DBD plasma actuator application to laminar airfoils

Generally speaking, actual sectional airfoils of wind turbine blades are asymmetric and relatively thick as seen in DU airfoils,<sup>47</sup> NACA 63-6XX, or NACA 64-6XX airfoils.<sup>48,49</sup> Here, NACA63<sub>3</sub>-618 airfoil, which is one of the objective airfoils of the current research and is a family of NACA 6 series airfoils, is used as a sectional airfoil of a certain large-scale wind turbine. NACA 6 series airfoils are developed for maximizing the region over which the flow remains laminar. Therefore, NACA 6 series airfoils, or DU airfoils,<sup>47</sup> are called as "laminar airfoil".

The references for the flowfield around a stationary laminar airfoil at moderate Reynolds numbers is a little limited. Mack et al. conducted experiments and CFDs for the flowfield around a stationary NACA64<sub>3</sub>-618 airfoil at Reynolds number of  $6.4 \times 10^4$  and  $1.37 \times 10^5$  with a DBD plasma actuator control. As they show the changes of the separation and reattachment points against  $AoA$ , the position of LSB drastically moves with change of  $AoA$ , while the secondary separation point, i.e., the trailing edge separation point come to observed as the increase of  $AoA$ . The area under the trailing edge separation is up to  $60\%c$ <sup>1</sup> of the chord length. Due to this characteristic of the trailing edge separation, the lift curve exhibits quite a large nonlinearity,<sup>1</sup> as shown in Figure 1.3. Moreover, they report that the LSB plays beneficial role on the aerodynamic performances, and the aerodynamic performance significantly worsened if the DBD plasma actuator at  $x/c = 2\%$  is actuated. Hipp et al.<sup>50</sup> conducted experiments for the flowfield around a stationary NACA64<sub>3</sub>-618 airfoil at Reynolds number of  $6.4 \times 10^4$  and  $1.28 \times 10^5$  with pulsed jet control. Their conclusion is, on the other hand, the aerodynamic performances can be enhanced with a jet installed at  $x/c = 2\%$  pulsed at  $F^+ = 1$ . The author's former research<sup>51</sup> supports the difficulty of the control of the dynamic flowfields around a laminar airfoil. This reference<sup>51</sup> presents the results of the numerical researches for the control of the flowfield around a pitching NACA63<sub>3</sub>-618 at Reynolds number of  $8.4 \times 10^4$  using a DBD plasma actuator. In the reference, the effective installation position is investigated with a constant  $F^+$  of 1.3. The result was that, the DBD plasma

actuator installed at the leading edge worsened the cycle-integrated  $L/D$ . Note that these results that the LSB is disrupted by the unsteady actuation is mentioned only at Reynolds number is  $\mathcal{O}(10^4)$ , whereas reference for Reynolds number in  $\mathcal{O}(10^5)$  which can help the understandings of the flow control is not available.

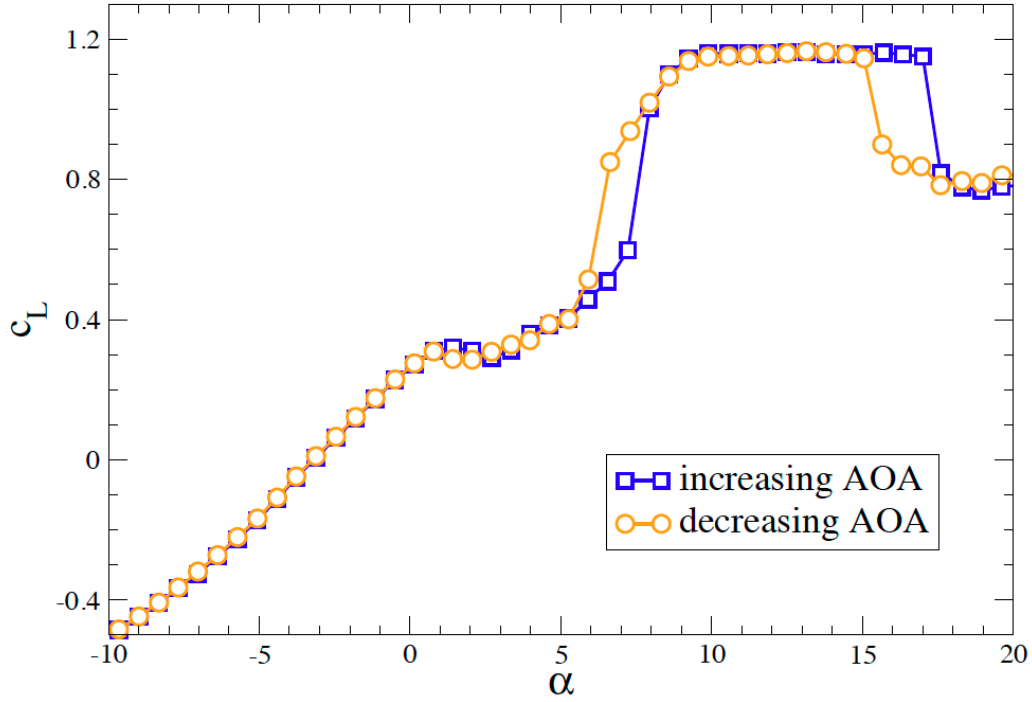


Figure 1.3: Lift curve for NACA64<sub>3</sub>-618 airfoil at Reynolds number of  $1.34 \times 10^5$ .<sup>1</sup>

## 1.6 Objectives and outline

The objective of this thesis is to find the guidelines of the DBD plasma actuators to effectively enhance aerodynamic performances of wind turbine. In order to address this goal, the focus is put on clarifying the control effects of the DBD plasma actuator on dynamic flowfields, their control mechanisms, and the corresponding effective DBD plasma actuator parameter for each control effect. In this thesis, high-fidelity flow computation using large eddy simulations are conducted so as to investigate the details of the unsteady flowfield controlled by the DBD plasma actuator. The flowfield is modeled from that around a whole wind turbine to that around a pitching airfoil in the current research so as to evaluate as many cases as possible in details. Considering that the complexity of the dynamic flowfields around a laminar airfoil and knowledge of controlling such flowfields is limited, control attempts not based on assured knowledge can result in fail. Then considering the limitation of the number of trials due to the limitation of the

computational resources, the current research takes safer step-by-step approach toward the goal.

The current research is divided into two steps. In the first step, so as to make use of the previous knowledge of effective control, the target airfoil is chosen to be a NACA0012 airfoil. The aim of this step is to build an arranged knowledge of controlling dynamic flowfields. The investigation results of the flowfield around a NACA0012 airfoil without control is integrated with the previous knowledge of effective control and the possible effective DBD plasma actuator parameters are studied. And then the computations for the flowfield with control is conducted. With the obtained control effects and mechanisms, the results are built into an arranged knowledge of controlling dynamic flowfields.

In the second step, which is the final step in this thesis, the objective airfoil step is set as an laminar airfoil. The investigation results of the flowfield around a laminar airfoil without control is first conducted, and then the investigation result is integrated with the arranged knowledge. Finally, the flowfield with control is calculated and investigated to discuss the effective control mechanisms to control the dynamic flowfield around a laminar airfoil.

By dividing into these stages, knowledge valid not only on the laminar airfoil but also on more general NACA0012 airfoil can be obtained.

Main part of this thesis includes Chapter 4. Considering that the comprehensive arrangement of the control effects on the entire pitching phase can be enabled only after the LES result is well validated, the validation study in this research is conducted with care.

The outline of this thesis is as follows. First, target flowfield is introduced in Chapter 2. The definition of the target aerodynamic performance index is defined here.

In the next chapter 3, numerical methods employed in this research are described. Then, the DBD plasma actuator model which is introduced to the fluid computation. The data processing procedure is briefly introduced.

In chapter 4 validation results of this research are described. First, the verification study of the spanwise length is introduced. Validation results by the comparison of the experimental results with the LES results are next presented. Then the verification results of the in-plane grid resolution are presented.

In Chapter 5, the control effects of the DBD plasma actuator on the dynamic flowfield around a pitching NACA0012 airfoil are investigated and then the control effects, these mechanisms, and the corresponding effective DBD plasma actuator parameters are investigated in details and arranged.

In Chapter 6, the findings in Chapter 5 are utilized to the dynamic flowfield around

a pitching laminar airfoil in order to support the conclusions and to discuss the effective control mechanisms and effective DBD plasma actuator parameters for controlling the dynamic flowfield around a pitching laminar airfoil. A discussion on the applicability of the findings in this thesis is briefly held here.

In chapter 7, the results of this thesis are summarized with the conclusions.



# Chapter 2

## Problem Settings

### 2.1 Target flowfield

#### 2.1.1 Flow conditions

A series of researches on controlling the dynamic flowfield around a wind turbine have been conducted both by wind tunnel experiments and LESs. The researches are not only on a whole wind turbine configuration but also on a pitching airfoil, which is a model of dynamic flowfield around a spanwise section of the blades. The current research is one of this series of researches on a pitching airfoil. The series of the researches is summarized in Table 2.1.

The wind turbine used in this series of researches<sup>2,52</sup> has three blades with uniform section shape of NACA0012 and uniform chord length of 0.2 meters. The blades have diameter of 2.376 meters and spanwise length of 1.0 meter, and are installed so as to have the angle of  $10^\circ$  between the rotating plane and the blade chord. The case mainly discussed in the references for the whole wind turbine configuration<sup>2,52</sup> has the inflow condition of the freestream velocity of 10 m/s and yaw misalignment of  $40^\circ$  from the rotating axis and the rotation speed of the blades of 174 rpm. The flow condition which experienced by each spanwise section of the blade (hereafter denoted “effective”) is the net velocity of the freestream and the rotational speed. If there is some yaw misalignment, wind shear, or any axial asymmetry, the effective flow condition fluctuates in synchronization with the azimuth angle.

The flow conditions in the “Modeled pitching airfoil” (the research by Mitsuo et al.<sup>2</sup> and the current research) roughly corresponds to the effective flow condition of a blade section whose rotation radius of 0.96 meters; at this section, the sectional airfoil experiences the flow with velocity of  $14.8 \sim 23.7$  m/s,  $AoA$  of  $7.7 \sim 24.2^\circ$ . The mean velocity

corresponds to 19.2 m/s, the mean  $AoA$  is  $14.8^\circ$ , and the frequency of the velocity and  $AoA$  fluctuation of 2.9 Hz. To consider the mean velocity as the characteristic velocity, the chord-based Reynolds number becomes  $2.56 \times 10^5$  and the frequency of the fluctuation is nondimensionalized to the reduced frequency of  $k = 0.03\pi$ . The exact flow conditions for the researches on the pitching airfoil (the research by Mitsuo et al.<sup>2</sup> and the current research) is Reynolds number of  $2.56 \times 10^5$ ,  $AoA$  range of  $5 \sim 25^\circ$ , and the reduced frequency  $k$  of  $0.02\pi$ , as listed up in Table 2.2. The airfoil dynamically rotates around its quarter-chord location from the leading edge. Note that with the reduced frequency  $k$  of  $0.02\pi$ , one pitching cycle corresponds to 50 flow-through time.

With regard to the validity of this modeling method from a three-dimensional rotating blade into a two-dimensional pitching airfoil, it is only recently that the detailed investigation on the three-dimensional effects are begin to be conducted by CFD.<sup>53</sup> Although the validity of this modeling method is not fully clarified yet, the effect of the three-dimensionality is characterized by the interaction of the tip vortex and DSV which results in the emergence of a omega-shaped vortex.<sup>53</sup> Considering that the omega-shaped-like vortex is observed also in the two-dimensional flowfield as presented in Chapter 4, the dynamic stall phenomena itself is not considerably affected by the three-dimensional effect. The same can be deduced from the reference.<sup>54</sup> Therefore, the modeling into the two-dimensional pitching airfoil can qualitatively resolve the dynamic stall phenomena although a certain level of quantitative discrepancies are observed.<sup>3</sup>

The curve for lift coefficient  $C_L$  are presented in Figure 2.1. Under the flow conditions, the flow experiences “dynamic stall” phenomena. Dynamic stall is characterized by formation and shedding of a large vortex which emanates from near the leading edge (DSV: dynamic stall vortex). In Figure 2.1, one of the characteristic effect of DSV that a sudden change in aerodynamic performances is observed between the angle of attack (hereafter denoted as  $AoA$ ) of  $15 \sim 20^\circ$ .

In the current study, all the conditions of the main case is set as the same as the experiment for the pitching airfoil.<sup>2</sup> One exception is the formulation of the pitching motion. In the current research, this pitching motion is formulated as follows;

$$\alpha = \alpha_{min} + \alpha_{amp}(1 - \cos(\omega t)) \quad (2.1)$$

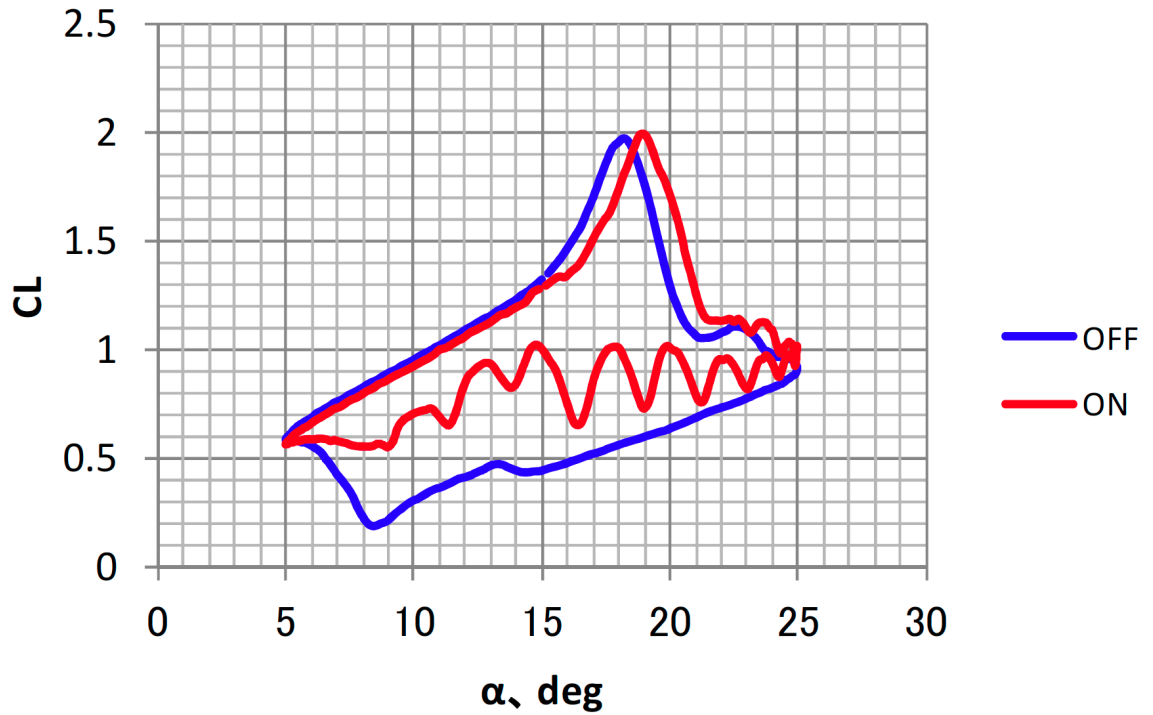
where minimum  $AoA$  of  $\alpha_{min}$  ( $= 5^\circ$ ), pitching amplitude of  $\alpha_{amp}$  ( $= 10^\circ$ ), and the reduced frequency of  $k$  ( $= \omega c / 2u_\infty$ , varied by case by case in this thesis). Note that the angle of  $\omega t$  denotes the phase of the pitching motion.

Table 2.1: Series of researches on controlling dynamic flowfield around wind turbine.

	Whole wind turbine configuration	Modeled pitching airfoil
Wind tunnel experiment	Mitsuo et al. <sup>55</sup>	Mitsuo et al. <sup>2</sup>
Numerical simulation	Aono et al. <sup>52</sup>	Current study

Table 2.2: Baseline flow conditions.

Reynolds number	Angle of attack	Reduced frequency	Rotation center
$2.56 \times 10^5$	$5 \sim 25^\circ$	$0.02\pi$	25% chord position

Figure 2.1: Lift curve obtained by the experiment.<sup>2</sup> OFF is for the case without DBD plasma actuation, ON is for with.

### 2.1.2 Target Airfoils



Figure 2.2: Airfoil shape.

The objective airfoils in the current research are NACA0012 and NACA63<sub>3</sub>-618 airfoil.

NACA0012 airfoil is a family of NACA 4 series airfoils and is a relatively simple airfoil. Owing to its relatively simple geometry, many researches on stationary or dynamic flowfields around this airfoil have been conducted over past several decades.

NACA63<sub>3</sub>-618 airfoil is a family of NACA 6 series airfoils, is used as a sectional airfoil of gliders<sup>56</sup> and wind turbines.<sup>48,49</sup> The airfoil shapes are depicted in Figure 2.2. NACA 6 series airfoils are developed so as to maximize the region over which the flow remains laminar, and are so-called as “laminar airfoil”. This airfoil has the maximum thickness of 18% of the chord length at the 36.7% chordwise position. This maximum thickness location indicates that the flow over this airfoil has long run to accelerate with adverse pressure gradient and thus can keep laminar over a large portion of the chord. However, unlike NACA0012 or other general airfoils, detailed knowledge on the flowfield around this airfoil which can be help to find the effective control is not widely published and is limited.

Toward the goal of the current research to find the effective control mechanisms on the dynamic flowfield around actual wind turbines, NACA63<sub>3</sub>-618 airfoils is employed as one of practical airfoil.

### 2.1.3 Target aerodynamic performances

Considering to investigate the control effect from the viewpoint both of the wind turbine specific performance and of the airfoil’s general aerodynamic performance, characteristic five cycle-averaged or cycle-integrated aerodynamic performances are used as the indicator of the control effect. First three ones are the cycle-averaged lift coefficient  $C_L$ , the cycle-averaged drag coefficient  $C_D$ , and the cycle-averaged lift-to-drag ratio  $L/D$ .

The forth one is the torque coefficient  $C_Q$ . Considering to enhance the generation torque of the wind turbine, the force whose direction corresponds to the rotation direction

of the section airfoil is the direct index for the torque generation. The torque coefficient  $C_Q$  is calculated as follows;<sup>57</sup>

$$C_Q = C_L \sin \phi - C_D \cos \phi \quad (2.2)$$

$$\phi = \alpha + \beta \quad (2.3)$$

where  $\phi$  is the angle between the direction of the effective flow and the rotation plane.  $\beta$  is the offset angle between the rotating plane and the blade chord, and  $\alpha$  is the angle of attack, which is the angle between the direction of the effective velocity and the blade chord. In this case, as aforementioned, the airfoil is installed with the offset angle  $\beta$  of  $10^\circ$ , and thus  $\phi$  corresponds to  $\alpha + 10^\circ$ .

The fifth one is the net damping  $\zeta_d$  and this value is calculated as follows;

$$\zeta_d = -\frac{1}{\alpha_{amp}} \int C_M d\alpha \quad (2.4)$$

where  $\alpha_{amp}$  is the pitching amplitude. This net damping presents the cycle-integrated moment damping. If this value is negative, the oscillation of airfoil becomes self-sustained due to the positive feedback of the pitching motion. With regard to the structural fatigue or the controllability of the aircrafts, higher  $\zeta_d$  is appreciated.

## 2.2 DBD Plasma Actuator Parameters

### 2.2.1 Parameters of Burst Wave

Burst waves consist of sinusoidal waves can be represented with four parameters ( $A^*$ ,  $f_{base}^*$ ,  $T_{BST}^*$ , and  $T_{on}^*$ ) as flow:

$$V(t)^* = \begin{cases} A^* \sin(2\pi f_{base}^* t^*) & mT_{BST}^* \leq t^* \leq T_{on}^* + mT_{BST}^* \\ 0 & T_{on}^* + mT_{BST}^* \leq t^* \leq (m+1)T_{BST}^* \end{cases} \quad (m = 0, 1, 2 \dots), \quad (2.5)$$

where  $m$  is an integer,  $A^*$  is an amplitude of the base sinusoidal wave,  $f_{base}^*$  is a frequency of the base sinusoidal wave,  $T_{BST}^*$  is a burst period,  $T_{on}^*$  is a period of sinusoidal wave switch on in a burst wave period. Superscripts  $*$  denote dimensional values.

We can represent the burst wave with other parameters depend on the objectives of studies. Especially, on the field of separated-flow control, burst ratio  $BR$  and burst

frequency  $F^*$  are used instead of  $T_{BST}^*$  and  $T_{on}^*$ . Relations between these parameters are as follow:

$$BR = \frac{T_{on}^*}{T_{BST}^*}, \quad (2.6)$$

$$F^* = \frac{1}{T_{BST}^*}. \quad (2.7)$$

As other representing parameters, we can consider  $n$  which is a wave number in  $T_{on}^*$ . A relation between the parameters in Equation 2.5 as flow:

$$n = f_{base}^* T_{on}^*. \quad (2.8)$$

When the  $BR$ ,  $n$ , and  $f_{base}^*$  are used  $F^*$  is written as follow:

$$F^* = \frac{BR}{n} f_{base}^*. \quad (2.9)$$

$$f_{base} = \frac{c^*}{u_\infty^*} f_{base}^*. \quad (2.10)$$

The magnitude of the actuation in the current study is determined so that the induced velocity by the DBD plasma actuator is almost same as the experiment by Mitsuo et al.<sup>2</sup> In the current study, the other unsteady parameters of  $BR$  and  $f_{base}$  are set as constant or dependent variable of  $F^+$ . These detailed considerations are presented in each chapter.

# Chapter 3

## Numerical Methods

In this chapter, numerical methods used in the current research are presented. First, methods of fluid analysis are described. The in-house code LANS3D which is utilized for the analysis of the current research, is introduced. Then governing equations of fluid are noted. The numerical schemes to solve the equations, the boundary conditions, and the grid systems are explained. Finally, the numerical model of the DBD plasma Actuator is presented.

### 3.1 Methods of Fluid Analysis

#### 3.1.1 LANS3D

In this research, in-house code LANS3D<sup>58–60</sup> (which stands for “LU-ADI<sup>61–64</sup> Navier-Stokes code for three-dimensional flows”) developed at ISAS/JAXA, is used. This code was developed by Prof. Kozo Fujii and Prof. Shigeru Obayashi (Currently Tohoku University), and modified by their colleagues. This code is based on an efficient and accurate method for complicated flow field by solving compressible Navier-Stokes equations. In recent years, Dr. Nobuyuki Iizuka implemented “ADI-SGS” method, Dr. Soshi Kawai implemented “LES/RANS hybrid methodology” and “compact difference scheme” and Dr. Taku Nonomura implemented “weighted compact nonlinear scheme” for this code. The latest version is written in Fortran 90 and parallelized by message passing interface (MPI) and autoparallelization. In addition, the scalar tuning of the code has been extremely done.<sup>65</sup> The algorithm used in this code and how it has been improved so far explain two important aspects of the computational fluid dynamics (CFD) codes: efficiency and accuracy. Some of the application examples show the capability of the code for engineering problems<sup>66</sup> as well as physical problems.<sup>67</sup> The computational meth-

ods, which are implemented in LANS3D and also used in this research, are described in following sections.

### 3.1.2 Governing Equations

The conservation form of the compressible Navier-Stokes equations in the three-dimensional, which are the governing equations of the fluid dynamics, is introduced.<sup>68-70</sup>

#### Navier-Stokes Equations in Cartesian Coordinate System

Three-dimensional Navier-Stokes equations in the Cartesian coordinate system are written as follows.

$$\frac{\partial Q^*}{\partial t^*} + \frac{\partial E^*}{\partial x^*} + \frac{\partial F^*}{\partial y^*} + \frac{\partial G^*}{\partial z^*} = \frac{\partial E_v^*}{\partial x^*} + \frac{\partial F_v^*}{\partial y^*} + \frac{\partial G_v^*}{\partial z^*}, \quad (3.1)$$

$$Q^* = \begin{bmatrix} \rho^* \\ \rho^* u^* \\ \rho^* v^* \\ \rho^* w^* \\ e^* \end{bmatrix}, \quad E^* = \begin{bmatrix} \rho^* u^{*2} \\ \rho^* u^* v^* \\ \rho^* u^* w^* \\ (e^* + p^*) u^* \end{bmatrix}, \quad F^* = \begin{bmatrix} \rho^* v^* \\ \rho^* v^* u^* \\ \rho^* v^{*2} + p^* \\ \rho^* v^* w^* \\ (e^* + p^*) v^* \end{bmatrix}, \quad G^* = \begin{bmatrix} \rho^* w^* \\ \rho^* w^* u^* \\ \rho^* w^* v^* \\ \rho^* w^{*2} + p^* \\ (e^* + p^*) w^* \end{bmatrix},$$

$$E_v^* = \begin{bmatrix} 0 \\ \tau_{xx}^* \\ \tau_{xy}^* \\ \tau_{xz}^* \\ \beta_x^* \end{bmatrix}, \quad F_v^* = \begin{bmatrix} 0 \\ \tau_{yx}^* \\ \tau_{yy}^* \\ \tau_{yz}^* \\ \beta_y^* \end{bmatrix}, \quad G_v^* = \begin{bmatrix} 0 \\ \tau_{zx}^* \\ \tau_{zy}^* \\ \tau_{zz}^* \\ \beta_z^* \end{bmatrix}, \quad (3.2)$$

$$\beta_x^* = \tau_{xx}^* u^* + \tau_{xy}^* v^* + \tau_{xz}^* w^* - q_x^*,$$

$$\beta_y^* = \tau_{yx}^* u^* + \tau_{yy}^* v^* + \tau_{yz}^* w^* - q_y^*,$$

$$\beta_z^* = \tau_{zx}^* u^* + \tau_{zy}^* v^* + \tau_{zz}^* w^* - q_z^*,$$

where  $\rho^*$  is the density,  $u^*$ ,  $v^*$ ,  $w^*$  are the  $x^*$ ,  $y^*$ ,  $z^*$  direction velocities, respectively.  $e^*$



is the total energy per unit volume,  $p^*$  is the pressure,  $\tau_{ij}^*$  is the viscous stress tensor. Moreover,  $q_i^*$  is the heat flux vector. First row corresponds to the conservation law of mass, second, third and forth rows correspond to the conservation laws of  $x^*$ ,  $y^*$  and  $z^*$  direction momentum, respectively, and fifth row corresponds to the conservation law of energy, where  $Q^*$  is the conservative variable vector,  $E^*$ ,  $F^*$  and  $G^*$  are the  $x^*$ ,  $y^*$  and  $z^*$  direction advection flux vectors,  $E_v^*$ ,  $F_v^*$  and  $G_v^*$  are the  $x^*$ ,  $y^*$  and  $z^*$  direction viscous flux vectors. Asterisks denote the dimensional numbers.

The static pressure  $p^*$  is related with the density  $\rho^*$ , the velocities  $u^*$ ,  $v^*$ ,  $w^*$  and the total energy  $e^*$  by the equation of state for the ideal gas written as

$$p^* = \rho^* R^* T^* = (\gamma - 1) \left\{ e^* - \frac{1}{2} \rho^* (u^{*2} + v^{*2} + w^{*2}) \right\}, \quad (3.3)$$

where  $R^*$ ,  $T^*$ ,  $\gamma$  represent the gas constant, static temperature and the ratio of specific heats, respectively. For air at standard conditions,  $R^* = 287 \text{ [ m}^2 / (\text{s}^2 \cdot \text{K})]$  and  $\gamma = 1.4$ .

$\tau_{ij}^*$  represent the viscous stress tensor as shown Fig. 3.1.  $\tau_{ij}^*$  is assumed to be a linear function of the rate of strain tensor. This assumption can be satisfied almost condition without flow past a strong shock wave.<sup>71</sup>  $\tau_{ij}^*$  for Newtonian fluid becomes

$$\tau_{ij}^* = \mu^* \left( \frac{\partial u_i^*}{\partial x_j^*} + \frac{\partial u_j^*}{\partial x_i^*} \right) + \lambda^* \delta_{ij} \frac{\partial u_k^*}{\partial x_k^*}, \quad (3.4)$$

where  $\mu^*$  is the dynamic viscosity coefficient,  $\lambda^*$  is the second viscosity coefficient. The tensor  $\delta_{ij}$  is the Kronecker delta, defined as  $\delta_{ij} = 1$  if  $i = j$  and  $\delta_{ij} = 0$  if  $i \neq j$ . Where the summation convention for repeated indices is used. Total surface stress tensor which consists of the static pressure  $p^*$  and the viscous stress tensor  $\tau_{ij}^*$  is given by

$$\sigma_{ij}^* = -p^* \delta_{ij} + \tau_{ij}^*. \quad (3.5)$$

Consider the averaged normal viscous stress  $\overline{P}^*$  (also called the mean pressure).

$$\overline{P}^* \equiv -\frac{\sigma_{ii}^*}{3} \quad (3.6)$$

$$= p^* - \left( \lambda^* + \frac{2}{3} \mu^* \right) \frac{\partial u_i^*}{\partial x_i^*} \quad (3.7)$$

$$= p^* - \mu_B^* \frac{\partial u_i^*}{\partial x_i^*}, \quad (3.8)$$

where the coefficient  $\mu_B^*$  is called bulk viscosity coefficient, and assumed to be zero in the

Stokes's hypothesis:  $\mu_B^* = 0$ .<sup>72</sup> Thus, the second viscosity coefficient  $\lambda^*$  can be written as

$$\lambda^* = -\frac{2}{3}\mu^*, \quad (3.9)$$

and  $\tau_{ij}^*$  becomes

$$\begin{aligned} \tau_{ij}^* &= \mu^* \left( \frac{\partial u_i^*}{\partial x_j^*} + \frac{\partial u_j^*}{\partial x_i^*} - \frac{2}{3} \delta_{ij} \frac{\partial u_k^*}{\partial x_k^*} \right) \\ &= \mu^* \begin{bmatrix} \frac{2}{3} \left( 2 \frac{\partial u^*}{\partial x^*} - \frac{\partial v^*}{\partial y^*} - \frac{\partial w^*}{\partial z^*} \right) & \frac{\partial u^*}{\partial y^*} + \frac{\partial v^*}{\partial x^*} & \frac{\partial w^*}{\partial x^*} + \frac{\partial u^*}{\partial z^*} \\ \frac{\partial u^*}{\partial y^*} + \frac{\partial v^*}{\partial x^*} & \frac{2}{3} \left( -\frac{\partial u^*}{\partial x^*} + 2 \frac{\partial v^*}{\partial y^*} - \frac{\partial w^*}{\partial z^*} \right) & \frac{\partial u^*}{\partial y^*} + \frac{\partial v^*}{\partial z^*} \\ \frac{\partial w^*}{\partial x^*} + \frac{\partial u^*}{\partial z^*} & \frac{\partial v^*}{\partial z^*} + \frac{\partial w^*}{\partial y^*} & \frac{2}{3} \left( -\frac{\partial u^*}{\partial x^*} - \frac{\partial v^*}{\partial y^*} + 2 \frac{\partial w^*}{\partial z^*} \right) \end{bmatrix}. \end{aligned} \quad (3.10)$$

The dynamic viscosity coefficient is given by Surtherland's law,

$$\mu^* = \mu_0^* \left( \frac{T^*}{T_0^*} \right)^{\frac{3}{2}} \frac{T_0^* + T_1^*}{T^* + T_1^*}, \quad T_1^* = 111 \text{ [K]}, \quad T_0^* = 273 \text{ [K]}, \quad \mu_0^* = 1.716 \times 10^{-5} \text{ [Pa} \cdot \text{s]}, \quad (3.11)$$

for air.<sup>73</sup>

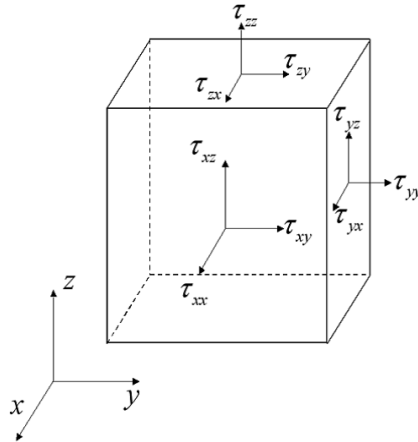


Figure 3.1: Components of viscous stress tensor.

Similar to the stress tensor, the heat flux vector  $q_i^*$  is assumed to be a linear function

of the gradient of the temperature by Fourier's law:

$$q_i^* = -\kappa^* \frac{\partial T^*}{\partial x_i^*}, \quad (3.12)$$

where  $\kappa^*$  is the thermal conductivity. Moreover Eq. 3.12 is modified with Prandtl number  $Pr = \frac{\mu^* c_p^*}{\kappa^*}$  ( $= 0.72$  for air) as follows.

$$q_i^* = -\kappa^* \frac{\partial T^*}{\partial x_i^*} = -\frac{\partial \left( \frac{\mu^* c_p^*}{Pr} T^* \right)}{\partial x_i^*} = -\frac{1}{\gamma - 1} \frac{\mu^*}{Pr} \frac{\partial a^{*2}}{\partial x_i^*}, \quad (3.13)$$

where  $c_p^*$  represents the specific heat at constant pressure,  $a^*$  is the speed of sound.

$$c_p^* = \frac{\gamma R^*}{\gamma - 1}, \quad a^* = \sqrt{\gamma R^* T^*} = \sqrt{\gamma \frac{p^*}{\rho^*}}. \quad (3.14)$$

### Non-dimensionalization of Navier-Stokes Equations

Equation 3.1 is written in a dimensional form. However it is not suitable to use various flow variables whose orders are different because of inconvenience of a display method and a round-off error. Therefore, in this section, Eq. 3.1 is put into a non-dimensional form.<sup>70</sup>

Flow variables are non-dimensionalized by introducing reference quantity, the density of ambient  $\rho_\infty^*$ , the sound speed of the ambient condition  $a_\infty^*$ , the viscosity coefficient of the ambient condition  $\mu_\infty^*$  and the reference length  $L^*$

$$\begin{aligned} x_i &= \frac{x_i^*}{L^*}, \quad t = \frac{t^*}{L^*/a_\infty^*}, \quad \rho = \frac{\rho^*}{\rho_\infty^*}, \quad u_i = \frac{u_i^*}{a_\infty^*}, \quad e = \frac{e^*}{\rho_\infty^* a_\infty^{*2}}, \\ p &= \frac{p^*}{\rho_\infty^* a_\infty^{*2}} = \frac{p^*}{\gamma p_\infty^*}, \quad \tau_{ij} = \frac{\tau_{ij}^*}{\mu_\infty^* a_\infty^*/L^*}, \quad q_i^* = \frac{q_i^*}{\mu_\infty^* a_\infty^{*2}/L^*}, \end{aligned} \quad (3.15)$$

where no-asterisk variables denote non-dimensional numbers.

Substituting Eq. 3.15 to Eq. 3.1, the non-dimensional Navier-Stokes equations in the Cartesian coordinate system are obtained as follows.

$$\frac{\partial Q}{\partial t} + \frac{\partial E}{\partial x} + \frac{\partial F}{\partial y} + \frac{\partial G}{\partial z} = \frac{1}{Re} \left( \frac{\partial E_v}{\partial x} + \frac{\partial F_v}{\partial y} + \frac{\partial G_v}{\partial z} \right), \quad (3.16)$$

$$Q = \begin{bmatrix} \rho \\ \rho u \\ \rho v \\ \rho w \\ e \end{bmatrix}, \quad E = \begin{bmatrix} \rho u \\ \rho u^2 + p \\ \rho uv \\ \rho uw \\ (e + p)u \end{bmatrix}, \quad F = \begin{bmatrix} \rho v \\ \rho vu \\ \rho v^2 + p \\ \rho vw \\ (e + p)v \end{bmatrix}, \quad G = \begin{bmatrix} \rho w \\ \rho wu \\ \rho wv \\ \rho w^2 + p \\ (e + p)w \end{bmatrix},$$

$$E_v = \begin{bmatrix} 0 \\ \tau_{xx} \\ \tau_{xy} \\ \tau_{xz} \\ \beta_x \end{bmatrix}, \quad F_v = \begin{bmatrix} 0 \\ \tau_{yx} \\ \tau_{yy} \\ \tau_{yz} \\ \beta_y \end{bmatrix}, \quad G_v = \begin{bmatrix} 0 \\ \tau_{zx} \\ \tau_{zy} \\ \tau_{zz} \\ \beta_z \end{bmatrix}, \quad (3.17)$$

$$\beta_x = \tau_{xx}u + \tau_{xy}v + \tau_{xz}w - q_x,$$

$$\beta_y = \tau_{yx}u + \tau_{yy}v + \tau_{yz}w - q_y,$$

$$\beta_z = \tau_{zx}u + \tau_{zy}v + \tau_{zz}w - q_z,$$

$$p = (\gamma - 1) \left\{ e - \frac{1}{2} \rho (u^2 + v^2 + w^2) \right\}, \quad (3.18)$$

where  $Re$  is Reynolds number and  $M_\infty = u_\infty^*/a_\infty^*$  is Mach number as defined below.

$$Re = \frac{\rho_\infty^* a_\infty^* L^*}{\mu_\infty^*} = \frac{1}{M_\infty} \frac{\rho_\infty^* u_\infty^* L^*}{\mu_\infty^*}. \quad (3.19)$$

Here, note that Eq. 3.1 and Eq. 3.16 are identical except for  $1/Re$  in the right hand side.

The non-dimensional viscosity coefficient  $\mu$  is given by

$$\mu = \frac{\mu^*}{\mu_\infty^*} = \mu_0^* \left( \frac{T^*}{T_0^*} \right)^{\frac{3}{2}} \frac{T_0^* + T_1^*}{T^* + T_1^*} \left[ \mu_0^* \left( \frac{T_\infty^*}{T_0^*} \right)^{\frac{3}{2}} \frac{T_0^* + T_1^*}{T_\infty^* + T_1^*} \right]^{-1} = \frac{1 + T_1^*/T_\infty^*}{T + T_1^*/T_\infty^*} (T)^{\frac{3}{2}} \quad (3.20)$$

with  $T_1^* = 111$  [K] for air. Therefore in order to obtain a non-dimensional viscosity coefficient, we need to specify the ambient temperature  $T_\infty^*$ . In the present study,  $T_\infty^*$  is set to 288.15 [K] for the international standard atmosphere (ISA) at the sea-level condition.

### Navier-Stokes Equations in Curvilinear Coordinate System

In order to compute fluid in the domain whose boundary is arbitrary, the Navier-Stokes equations in the Cartesian coordinate system are transformed to the Navier-Stokes equations in the curvilinear coordinate system. A transformation of coordinate system is written as follows.

$$\begin{cases} x = x(\xi, \eta, \zeta, \tau) \\ y = y(\xi, \eta, \zeta, \tau) \\ z = z(\xi, \eta, \zeta, \tau) \\ t = \tau \end{cases} \longleftrightarrow \begin{cases} \xi = \xi(x, y, z, t) \\ \eta = \eta(x, y, z, t) \\ \zeta = \zeta(x, y, z, t) \\ \tau = t \end{cases} \quad (3.21)$$

The differential form of transformation is

$$\begin{cases} dx = x_\xi d\xi + x_\eta d\eta + x_\zeta d\zeta + x_\tau d\tau \\ dy = y_\xi d\xi + y_\eta d\eta + y_\zeta d\zeta + y_\tau d\tau \\ dz = z_\xi d\xi + z_\eta d\eta + z_\zeta d\zeta + z_\tau d\tau \\ dt = t_\xi d\xi + t_\eta d\eta + t_\zeta d\zeta + t_\tau d\tau \end{cases} \rightarrow \begin{bmatrix} dx \\ dy \\ dz \\ dt \end{bmatrix} = \begin{bmatrix} x_\xi & x_\eta & x_\zeta & x_\tau \\ y_\xi & y_\eta & y_\zeta & y_\tau \\ z_\xi & z_\eta & z_\zeta & z_\tau \\ 0 & 0 & 0 & 1 \end{bmatrix} \begin{bmatrix} d\xi \\ d\eta \\ d\zeta \\ d\tau \end{bmatrix}, \quad (3.22)$$

where  $t_\xi = t_\eta = t_\zeta = 0$  and  $t_\tau = 1$ . Similarly the differential form of the inverse transformation is

$$\begin{cases} d\xi = \xi_x dx + \xi_y dy + \xi_z dz + \xi_t dt \\ d\eta = \eta_x dx + \eta_y dy + \eta_z dz + \eta_t dt \\ d\zeta = \zeta_x dx + \zeta_y dy + \zeta_z dz + \zeta_t dt \\ d\tau = \tau_x dx + \tau_y dy + \tau_z dz + \tau_t dt \end{cases} \rightarrow \begin{bmatrix} d\xi \\ d\eta \\ d\zeta \\ d\tau \end{bmatrix} = \begin{bmatrix} \xi_x & \xi_y & \xi_z & \xi_t \\ \eta_x & \eta_y & \eta_z & \eta_t \\ \zeta_x & \zeta_y & \zeta_z & \zeta_t \\ 0 & 0 & 0 & 1 \end{bmatrix} \begin{bmatrix} dx \\ dy \\ dz \\ dt \end{bmatrix}, \quad (3.23)$$

where  $\tau_x = \tau_y = \tau_z = 0$  and  $\tau_t = 1$ .

From the relations between Eq. 3.22 and Eq. 3.23, we obtain metrics  $\xi_x, \xi_y, \xi_z, \xi_t, \dots$  with the derivatives  $x_\xi, x_\eta, \dots$  as follows.

$$\begin{aligned}
\begin{bmatrix} \xi_x & \xi_y & \xi_z & \xi_t \\ \eta_x & \eta_y & \eta_z & \eta_t \\ \zeta_x & \zeta_y & \zeta_z & \zeta_t \\ 0 & 0 & 0 & 1 \end{bmatrix} &= \begin{bmatrix} x_\xi & x_\eta & x_\zeta & x_\tau \\ y_\xi & y_\eta & y_\zeta & y_\tau \\ z_\xi & z_\eta & z_\zeta & z_\tau \\ 0 & 0 & 0 & 1 \end{bmatrix}^{-1} \\
&= J \begin{bmatrix} y_\eta z_\zeta - y_\zeta z_\eta & z_\eta x_\zeta - z_\zeta x_\eta & x_\eta y_\zeta - x_\zeta y_\eta \\ y_\zeta z_\xi - y_\xi z_\zeta & z_\zeta x_\xi - z_\xi x_\zeta & x_\zeta y_\xi - x_\xi y_\zeta \\ y_\xi z_\eta - y_\eta z_\xi & z_\xi x_\eta - z_\eta x_\xi & x_\xi y_\eta - x_\eta y_\xi \\ 0 & 0 & 0 \\ -x_\tau (y_\eta z_\zeta - y_\zeta z_\eta) - y_\tau (z_\eta x_\zeta - z_\zeta x_\eta) - z_\tau (x_\eta y_\zeta - x_\zeta y_\eta) \\ -x_\tau (y_\zeta z_\xi - y_\xi z_\zeta) - y_\tau (z_\zeta x_\xi - z_\xi x_\zeta) - z_\tau (x_\zeta y_\xi - x_\xi y_\zeta) \\ -x_\tau (y_\xi z_\eta - y_\eta z_\xi) - y_\tau (z_\xi x_\eta - z_\eta x_\xi) - z_\tau (x_\xi y_\eta - x_\eta y_\xi) \\ 1 \end{bmatrix}, \quad (3.24)
\end{aligned}$$

where  $J$  is transformation Jacobian from  $(x, y, z, t)$  to  $(\xi, \eta, \zeta, \tau)$ :

$$\begin{aligned}
J &= \frac{\partial (\xi, \eta, \zeta)}{\partial (x, y, z)} = \left( \frac{\partial (x, y, z)}{\partial (\xi, \eta, \zeta)} \right)^{-1} = 1 / \begin{vmatrix} x_\xi & x_\eta & x_\zeta \\ y_\xi & y_\eta & y_\zeta \\ z_\xi & z_\eta & z_\zeta \end{vmatrix} \\
&= \frac{1}{x_\xi y_\eta z_\zeta + x_\eta y_\zeta z_\xi + x_\zeta y_\xi z_\eta - x_\xi y_\zeta z_\eta - x_\eta y_\xi z_\zeta - x_\zeta y_\eta z_\xi}. \quad (3.25)
\end{aligned}$$

To be summarized, the coordinate transformation metrics are obtained as follows:

$$\xi_x/J = y_\eta z_\zeta - y_\zeta z_\eta, \quad \xi_y/J = z_\eta x_\zeta - z_\zeta x_\eta, \quad \xi_z/J = x_\eta y_\zeta - x_\zeta y_\eta, \quad (3.26)$$

$$\eta_x/J = y_\zeta z_\xi - y_\xi z_\zeta, \quad \eta_y/J = z_\zeta x_\xi - z_\xi x_\zeta, \quad \eta_z/J = x_\zeta y_\xi - x_\xi y_\zeta, \quad (3.27)$$

$$\zeta_x/J = y_\xi z_\eta - y_\eta z_\xi, \quad \zeta_y/J = z_\xi x_\eta - z_\eta x_\xi, \quad \zeta_z/J = x_\xi y_\eta - x_\eta y_\xi, \quad (3.28)$$

$$1/J = x_\xi y_\eta z_\zeta - x_\eta y_\xi z_\zeta + x_\zeta y_\xi z_\eta - x_\xi y_\zeta z_\eta + x_\eta y_\zeta z_\xi - x_\zeta y_\eta z_\xi, \quad (3.29)$$

$$\xi_t/J = x_\eta y_\tau z_\zeta - x_\eta y_\zeta z_\tau + x_\zeta y_\eta z_\tau - x_\zeta y_\tau z_\eta + x_\tau y_\zeta z_\eta - x_\tau y_\eta z_\zeta, \quad (3.30)$$

$$\eta_t/J = x_\xi y_\zeta z_\tau - x_\xi y_\tau z_\zeta + x_\zeta y_\tau z_\xi - x_\zeta y_\xi z_\tau + x_\tau y_\xi z_\zeta - x_\tau y_\zeta z_\xi, \quad (3.31)$$

$$\zeta_t/J = x_\eta y_\xi z_\tau - x_\eta y_\tau z_\xi + x_\xi y_\tau z_\eta - x_\xi y_\eta z_\tau + x_\tau y_\eta z_\xi - x_\tau y_\xi z_\zeta, \quad (3.32)$$

which are the conventional forms of metrics, so-called “nonconservative metrics”. Al-

though the expressions of Eqs. 3.26-3.32 are analytically true, the use of high-order finite-difference scheme on their discretization generally causes a “freestream preservation error” as will be explained below (i.e., violation of the “geometric conservation law” for Eqs. 3.51-3.54). Therefore, we do not directly discretize the expressions of Eqs. 3.26-3.32 (nonconservative metrics) but adopt the “symmetric conservative metrics”,<sup>74</sup> which can preserve the freestream in the arbitrary linear high-order finite-difference scheme as well as improving the robustness and accuracy of the computation on high-skewed deforming grids. The symmetric conservative metrics are as follows:

$$\xi_x/J = \{(y_\eta z - z_\eta y)_\zeta - (y_\zeta z - z_\zeta y)_\eta\}/2, \quad (3.33)$$

$$\xi_y/J = \{(z_\eta x - x_\eta z)_\zeta - (z_\zeta x - x_\zeta z)_\eta\}/2, \quad (3.34)$$

$$\xi_z/J = \{(x_\eta y - y_\eta x)_\zeta - (x_\zeta y - y_\zeta x)_\eta\}/2, \quad (3.35)$$

$$\eta_x/J = \{(y_\zeta z - z_\zeta y)_\xi - (y_\xi z - z_\xi y)_\zeta\}/2, \quad (3.36)$$

$$\eta_y/J = \{(z_\zeta x - x_\zeta z)_\xi - (z_\xi x - x_\xi z)_\zeta\}/2, \quad (3.37)$$

$$\eta_z/J = \{(x_\zeta y - y_\zeta x)_\xi - (x_\xi y - y_\xi x)_\zeta\}/2, \quad (3.38)$$

$$\zeta_x/J = \{(y_\xi z - z_\xi y)_\eta - (y_\eta z - z_\eta y)_\xi\}/2, \quad (3.39)$$

$$\zeta_y/J = \{(z_\xi x - x_\xi z)_\eta - (z_\eta x - x_\eta z)_\xi\}/2, \quad (3.40)$$

$$\zeta_z/J = \{(x_\xi y - y_\xi x)_\eta - (x_\eta y - y_\eta x)_\xi\}/2, \quad (3.41)$$

$$\begin{aligned} 1/J = \frac{1}{3} \left\{ \right. & \left[ \frac{1}{2} \{(x_\xi y - y_\xi x)_\eta - (x_\eta y - y_\eta x)_\xi\} z \right]_\zeta + \left[ \frac{1}{2} \{(y_\xi z - z_\xi y)_\eta - (y_\eta z - z_\eta y)_\xi\} x \right]_\zeta \\ & + \left[ \frac{1}{2} \{(z_\xi x - x_\xi z)_\eta - (z_\eta x - x_\eta z)_\xi\} y \right]_\zeta + \left[ \frac{1}{2} \{(x_\zeta y - y_\zeta x)_\xi - (x_\xi y - y_\xi x)_\zeta\} z \right]_\eta \\ & + \left[ \frac{1}{2} \{(y_\zeta z - z_\zeta y)_\xi - (y_\xi z - z_\xi y)_\zeta\} x \right]_\eta + \left[ \frac{1}{2} \{(z_\zeta x - x_\zeta z)_\xi - (z_\xi x - x_\xi z)_\zeta\} y \right]_\eta \\ & + \left[ \frac{1}{2} \{(x_\eta y - y_\eta x)_\zeta - (x_\zeta y - y_\zeta x)_\eta\} z \right]_\xi + \left[ \frac{1}{2} \{(y_\eta z - z_\eta y)_\zeta - (y_\zeta z - z_\zeta y)_\eta\} x \right]_\xi \\ & + \left. \left[ \frac{1}{2} \{(z_\eta x - x_\eta z)_\zeta - (z_\zeta x - x_\zeta z)_\eta\} y \right]_\xi \right\}, \quad (3.42) \end{aligned}$$

$$\begin{aligned}
\xi_t/J = \frac{1}{3} \left\{ \right. & \left[ \frac{1}{2} \{ (x_\tau y - y_\tau x)_\zeta - (x_\zeta y - y_\zeta x)_\tau \} z \right]_\eta + \left[ \frac{1}{2} \{ (y_\tau z - z_\tau y)_\zeta - (y_\zeta z - z_\zeta y)_\tau \} x \right]_\eta \\
& + \left[ \frac{1}{2} \{ (z_\tau x - x_\tau z)_\zeta - (z_\zeta x - x_\zeta z)_\tau \} y \right]_\eta + \left[ \frac{1}{2} \{ (x_\eta y - y_\eta x)_\tau - (x_\tau y - y_\tau x)_\eta \} z \right]_\zeta \\
& + \left[ \frac{1}{2} \{ (y_\eta z - z_\eta y)_\tau - (y_\tau z - z_\tau y)_\eta \} x \right]_\zeta + \left[ \frac{1}{2} \{ (z_\eta x - x_\eta z)_\tau - (z_\tau x - x_\tau z)_\eta \} y \right]_\zeta \\
& + \left[ \frac{1}{2} \{ (x_\zeta y - y_\zeta x)_\eta - (x_\eta y - y_\eta x)_\zeta \} z \right]_\tau + \left[ \frac{1}{2} \{ (y_\zeta z - z_\zeta y)_\eta - (y_\eta z - z_\eta y)_\zeta \} x \right]_\tau \\
& + \left. \left[ \frac{1}{2} \{ (z_\zeta x - x_\zeta z)_\eta - (z_\eta x - x_\eta z)_\zeta \} y \right]_\tau \right\}, \tag{3.43}
\end{aligned}$$

$$\begin{aligned}
\eta_t/J = \frac{1}{3} \left\{ \right. & \left[ \frac{1}{2} \{ (x_\tau y - y_\tau x)_\xi - (x_\xi y - y_\xi x)_\tau \} z \right]_\zeta + \left[ \frac{1}{2} \{ (y_\tau z - z_\tau y)_\xi - (y_\xi z - z_\xi y)_\tau \} x \right]_\zeta \\
& + \left[ \frac{1}{2} \{ (z_\tau x - x_\tau z)_\xi - (z_\xi x - x_\xi z)_\tau \} y \right]_\zeta + \left[ \frac{1}{2} \{ (x_\xi y - y_\xi x)_\zeta - (x_\zeta y - y_\zeta x)_\xi \} z \right]_\tau \\
& + \left[ \frac{1}{2} \{ (y_\xi z - z_\xi y)_\zeta - (y_\zeta z - z_\zeta y)_\xi \} x \right]_\tau + \left[ \frac{1}{2} \{ (z_\xi x - x_\xi z)_\zeta - (z_\zeta x - x_\zeta z)_\xi \} y \right]_\tau \\
& + \left[ \frac{1}{2} \{ (x_\zeta y - y_\zeta x)_\tau - (x_\tau y - y_\tau x)_\zeta \} z \right]_\xi + \left[ \frac{1}{2} \{ (y_\zeta z - z_\zeta y)_\tau - (y_\tau z - z_\tau y)_\zeta \} x \right]_\xi \\
& + \left. \left[ \frac{1}{2} \{ (z_\zeta x - x_\zeta z)_\tau - (z_\tau x - x_\tau z)_\zeta \} y \right]_\xi \right\}, \tag{3.44}
\end{aligned}$$

$$\begin{aligned}
\zeta_t/J = \frac{1}{3} \left\{ \right. & \left[ \frac{1}{2} \{ (x_\eta y - y_\eta x)_\xi - (x_\xi y - y_\xi x)_\eta \} z \right]_\tau + \left[ \frac{1}{2} \{ (y_\eta z - z_\eta y)_\xi - (y_\xi z - z_\xi y)_\eta \} x \right]_\tau \\
& + \left[ \frac{1}{2} \{ (z_\eta x - x_\eta z)_\xi - (z_\xi x - x_\xi z)_\eta \} y \right]_\tau + \left[ \frac{1}{2} \{ (x_\tau y - y_\tau x)_\eta - (x_\eta y - y_\eta x)_\tau \} z \right]_\xi \\
& + \left[ \frac{1}{2} \{ (y_\tau z - z_\tau y)_\eta - (y_\eta z - z_\eta y)_\tau \} x \right]_\xi + \left[ \frac{1}{2} \{ (z_\tau x - x_\tau z)_\eta - (z_\eta x - x_\eta z)_\tau \} y \right]_\xi \\
& + \left[ \frac{1}{2} \{ (x_\xi y - y_\xi x)_\tau - (x_\tau y - y_\tau x)_\xi \} z \right]_\eta + \left[ \frac{1}{2} \{ (y_\xi z - z_\xi y)_\tau - (y_\tau z - z_\tau y)_\xi \} x \right]_\eta \\
& + \left. \left[ \frac{1}{2} \{ (z_\xi x - x_\xi z)_\tau - (z_\tau x - x_\tau z)_\xi \} y \right]_\eta \right\}. \tag{3.45}
\end{aligned}$$

More abbreviated forms can be seen in the reference.<sup>74</sup>

Next, we transform the governing equations 3.16. Here, Eq. 3.16 is rewritten in the



following simple form:

$$\frac{\partial Q}{\partial t} + \frac{\partial \tilde{E}}{\partial x} + \frac{\partial \tilde{F}}{\partial y} + \frac{\partial \tilde{G}}{\partial z} = 0, \quad (3.46)$$

where the right hand side of Eq. 3.16 is summarized in the left hand side. The transformation of each terms is based on the following Chain rule:

$$\begin{aligned} \frac{\partial}{\partial x} &= \xi_x \frac{\partial}{\partial \xi} + \eta_x \frac{\partial}{\partial \eta} + \zeta_x \frac{\partial}{\partial \zeta} + 0, \\ \frac{\partial}{\partial y} &= \xi_y \frac{\partial}{\partial \xi} + \eta_y \frac{\partial}{\partial \eta} + \zeta_y \frac{\partial}{\partial \zeta} + 0, \\ \frac{\partial}{\partial z} &= \xi_z \frac{\partial}{\partial \xi} + \eta_z \frac{\partial}{\partial \eta} + \zeta_z \frac{\partial}{\partial \zeta} + 0, \\ \frac{\partial}{\partial t} &= \xi_t \frac{\partial}{\partial \xi} + \eta_t \frac{\partial}{\partial \eta} + \zeta_t \frac{\partial}{\partial \zeta} + \frac{\partial}{\partial \tau}. \end{aligned} \quad (3.47)$$

Substituting Eq. 3.47 into Eq. 3.46, the following transformation can be conducted:

$$\begin{aligned} &\left( \xi_t \frac{\partial Q}{\partial \xi} + \eta_t \frac{\partial Q}{\partial \eta} + \zeta_t \frac{\partial Q}{\partial \zeta} + \frac{\partial Q}{\partial \tau} \right) + \left( \xi_x \frac{\partial \tilde{E}}{\partial \xi} + \eta_x \frac{\partial \tilde{E}}{\partial \eta} + \zeta_x \frac{\partial \tilde{E}}{\partial \zeta} \right) \\ &+ \left( \xi_y \frac{\partial \tilde{F}}{\partial \xi} + \eta_y \frac{\partial \tilde{F}}{\partial \eta} + \zeta_y \frac{\partial \tilde{F}}{\partial \zeta} \right) + \left( \xi_z \frac{\partial \tilde{G}}{\partial \xi} + \eta_z \frac{\partial \tilde{G}}{\partial \eta} + \zeta_z \frac{\partial \tilde{G}}{\partial \zeta} \right) = 0 \end{aligned} \quad (3.48)$$

$\Longleftrightarrow$

$$\begin{aligned} J \left\{ \left( \frac{\partial J^{-1} \xi_t Q}{\partial \xi} + \frac{\partial J^{-1} \eta_t Q}{\partial \eta} + \frac{\partial J^{-1} \zeta_t Q}{\partial \zeta} + \frac{\partial J^{-1} Q}{\partial \tau} \right) + \left( \frac{\partial J^{-1} \xi_x \tilde{E}}{\partial \xi} + \frac{\partial J^{-1} \eta_x \tilde{E}}{\partial \eta} + \frac{\partial J^{-1} \zeta_x \tilde{E}}{\partial \zeta} \right) \right. \\ \left. + \left( \frac{\partial J^{-1} \xi_y \tilde{F}}{\partial \xi} + \frac{\partial J^{-1} \eta_y \tilde{F}}{\partial \eta} + \frac{\partial J^{-1} \zeta_y \tilde{F}}{\partial \zeta} \right) + \left( \frac{\partial J^{-1} \xi_z \tilde{G}}{\partial \xi} + \frac{\partial J^{-1} \eta_z \tilde{G}}{\partial \eta} + \frac{\partial J^{-1} \zeta_z \tilde{G}}{\partial \zeta} \right) \right\} = 0 \end{aligned} \quad (3.49)$$

$\Longleftrightarrow$

$$\begin{aligned} &\frac{\partial J^{-1} Q}{\partial \tau} + \frac{\partial}{\partial \xi} \left\{ J^{-1} \left( \xi_t Q + \xi_x \tilde{E} + \xi_y \tilde{F} + \xi_z \tilde{G} \right) \right\} \\ &+ \frac{\partial}{\partial \eta} \left\{ J^{-1} \left( \eta_t Q + \eta_x \tilde{E} + \eta_y \tilde{F} + \eta_z \tilde{G} \right) \right\} + \frac{\partial}{\partial \zeta} \left\{ J^{-1} \left( \zeta_t Q + \zeta_x \tilde{E} + \zeta_y \tilde{F} + \zeta_z \tilde{G} \right) \right\} = 0, \end{aligned} \quad (3.50)$$

where the transformation from Eq. 3.48 to Eq. 3.49 is based on the metric identities,

so-called the “geometric conservation law”<sup>74,75</sup> (GCL) as follows:

$$\frac{\partial J^{-1}}{\partial \tau} + \frac{\partial J^{-1}\xi_t}{\partial \xi} + \frac{\partial J^{-1}\eta_t}{\partial \eta} + \frac{\partial J^{-1}\zeta_t}{\partial \zeta} = 0, \quad (3.51)$$

$$\frac{\partial J^{-1}\xi_x}{\partial \xi} + \frac{\partial J^{-1}\eta_x}{\partial \eta} + \frac{\partial J^{-1}\zeta_x}{\partial \zeta} = 0, \quad (3.52)$$

$$\frac{\partial J^{-1}\xi_y}{\partial \xi} + \frac{\partial J^{-1}\eta_y}{\partial \eta} + \frac{\partial J^{-1}\zeta_y}{\partial \zeta} = 0, \quad (3.53)$$

$$\frac{\partial J^{-1}\xi_z}{\partial \xi} + \frac{\partial J^{-1}\eta_z}{\partial \eta} + \frac{\partial J^{-1}\zeta_z}{\partial \zeta} = 0, \quad (3.54)$$

which are analytically true, but not numerically in the generalized high-order finite-difference schemes.<sup>76,77</sup> The GCL identities are often introduced as the sufficient conditions for a freestream preservation, which indicated the freestream (i.e. spatially and temporally uniform flow variables) can satisfy the governing equation 3.50 numerically. On the other hand, the GCL identities can be also regarded as the sufficient conditions for the commutative property of the governing equation between the Cartesian and curvilinear coordinate system in its strong conservation form as is described here, which can be extended to general dimensions as well as the three-dimensional space with one-dimensional time.<sup>74</sup>

Equation 3.50 is the strong conservation form of the compressible Navier-Stokes equations on the general curvilinear coordinate system, which can be rewritten as follows:

$$\frac{\partial \hat{Q}}{\partial \tau} + \frac{\partial \hat{E}}{\partial \xi} + \frac{\partial \hat{F}}{\partial \eta} + \frac{\partial \hat{G}}{\partial \zeta} = \frac{1}{Re} \left( \frac{\partial \hat{E}_v}{\partial \xi} + \frac{\partial \hat{F}_v}{\partial \eta} + \frac{\partial \hat{G}_v}{\partial \zeta} \right), \quad (3.55)$$

where

$$\begin{aligned}
\hat{Q} &= J^{-1} \begin{bmatrix} \rho \\ \rho u \\ \rho v \\ \rho w \\ e \end{bmatrix}, \quad \hat{E} = J^{-1} \begin{bmatrix} \rho U \\ \rho u U + \xi_x p \\ \rho v U + \xi_y p \\ \rho w U + \xi_z p \\ (e + p) U - \xi_t p \end{bmatrix}, \quad \hat{F} = J^{-1} \begin{bmatrix} \rho V \\ \rho u V + \eta_x p \\ \rho v V + \eta_y p \\ \rho w V + \eta_z p \\ (e + p) V - \eta_t p \end{bmatrix} \\
\hat{G} &= J^{-1} \begin{bmatrix} \rho w \\ \rho u W + \zeta_x p \\ \rho v W + \zeta_y p \\ \rho w W + \zeta_z p \\ (e + p) W - \zeta_t p \end{bmatrix}, \quad \hat{E}_v = J^{-1} \begin{bmatrix} 0 \\ \xi_x \tau_{xx} + \xi_y \tau_{xy} + \xi_z \tau_{xz} \\ \xi_x \tau_{yx} + \xi_y \tau_{yy} + \xi_z \tau_{yz} \\ \xi_x \tau_{zx} + \xi_y \tau_{zy} + \xi_z \tau_{zz} \\ \xi_x \beta_x + \xi_y \beta_y + \xi_z \beta_z \end{bmatrix} \\
\hat{F}_v &= J^{-1} \begin{bmatrix} 0 \\ \eta_x \tau_{xx} + \eta_y \tau_{xy} + \eta_z \tau_{xz} \\ \eta_x \tau_{yx} + \eta_y \tau_{yy} + \eta_z \tau_{yz} \\ \eta_x \tau_{zx} + \eta_y \tau_{zy} + \eta_z \tau_{zz} \\ \eta_x \beta_x + \eta_y \beta_y + \eta_z \beta_z \end{bmatrix}, \quad \hat{G}_v = J^{-1} \begin{bmatrix} 0 \\ \zeta_x \tau_{xx} + \zeta_y \tau_{xy} + \zeta_z \tau_{xz} \\ \zeta_x \tau_{yx} + \zeta_y \tau_{yy} + \zeta_z \tau_{yz} \\ \zeta_x \tau_{zx} + \zeta_y \tau_{zy} + \zeta_z \tau_{zz} \\ \zeta_x \beta_x + \zeta_y \beta_y + \zeta_z \beta_z \end{bmatrix} \quad (3.56)
\end{aligned}$$

$U$ ,  $V$  and  $W$  are so-called contra-variant velocities along the  $\xi$ ,  $\eta$  and  $\zeta$  direction as defined follow.

$$\begin{aligned}
U &= \xi_x u + \xi_y v + \xi_z w \\
V &= \eta_x u + \eta_y v + \eta_z w \\
W &= \zeta_x u + \zeta_y v + \zeta_z w
\end{aligned} \quad (3.57)$$

### 3.1.3 Numerical Schemes

#### Discretization of Governing Equations

A temporal and spatial discretization of governing equations is required to numerically solve these equations whose form is partial differential. Using finite difference operators, Eq. 3.55 is becomes as follow.

$$\left( \delta_\tau \hat{Q} \right) \Big|_{j,k,l} + \left( \delta_\xi \hat{E} + \delta_\eta \hat{F} + \delta_\zeta \hat{G} \right) \Big|_{j,k,l} = \frac{1}{Re} \left( \delta_{v\xi} \hat{E}_v + \delta_{v\eta} \hat{F}_v + \delta_{v\zeta} \hat{G}_v \right) \Big|_{j,k,l}, \quad (3.58)$$

where  $\delta_\tau$ ,  $\delta_\xi$ ,  $\delta_\eta$ ,  $\delta_\zeta$ ,  $\delta_{v\xi}$ ,  $\delta_{v\eta}$  and  $\delta_{v\zeta}$  are finite difference operators, and  $j$ ,  $k$  and  $l$  subscripts are indices of discrete points. When the same discretization scheme is used for advection terms and viscous terms, Eq. 3.58 can be rewritten as flow.

$$\left(\delta_\tau \hat{Q}\right) \Big|_{j,k,l} = \left[ \delta_\xi \left( -\hat{E} + \frac{1}{Re} \hat{E}_v \right) + \delta_\eta \left( -\hat{F} + \frac{1}{Re} \hat{F}_v \right) + \delta_\zeta \left( -\hat{G} + \frac{1}{Re} \hat{G}_v \right) \right]_{j,k,l} \quad (3.59)$$

The temporal and spatial accuracy depend on the evaluation of the finite difference operators. For example, when the Euler explicit scheme is used for the time integration and numerical fluxes are introduced, Eq. 3.58 becomes

$$\begin{aligned} \hat{Q}_{j,k,l}^{n+1} = \hat{Q}_{j,k,l}^n - \Delta t & \left[ \frac{\tilde{E}_{j+\frac{1}{2},k,l} - \tilde{E}_{j-\frac{1}{2},k,l}}{\Delta \xi} + \frac{\tilde{F}_{j,k+\frac{1}{2},l} - \tilde{F}_{j,k-\frac{1}{2},l}}{\Delta \eta} + \frac{\tilde{G}_{j,k,l+\frac{1}{2}} - \tilde{G}_{j,k,l-\frac{1}{2}}}{\Delta \zeta} \right. \\ & \left. - \frac{1}{Re} \left( \frac{\tilde{E}_{v;j+\frac{1}{2},k,l} - \tilde{E}_{v;j-\frac{1}{2},k,l}}{\Delta \xi} + \frac{\tilde{F}_{v;j,k+\frac{1}{2},l} - \tilde{F}_{v;j,k-\frac{1}{2},l}}{\Delta \eta} + \frac{\tilde{G}_{v;j,k,l+\frac{1}{2}} - \tilde{G}_{v;j,k,l-\frac{1}{2}}}{\Delta \zeta} \right) \right]^n. \end{aligned} \quad (3.60)$$

In this equation, the temporal accuracy is first-order and the spacial accuracy depends on numerical fluxes. In this study, a second-order backward-difference implicit scheme is used for the temporal discretization. Partial differential equation Eq. 3.55 is discretized as follow:

$$\begin{aligned} & \underbrace{\frac{3\hat{Q}^{n+1} - 4\hat{Q}^n + \hat{Q}^{n-1}}{2\Delta t}}_{\text{Second-order backward-difference}} + \mathcal{O}(\Delta t^2) \\ & = - \underbrace{\left[ \partial_\xi \hat{E} + \partial_\eta \hat{F} + \partial_\zeta \hat{G} - \frac{1}{Re} \left( \partial_\xi \hat{E}_v + \partial_\eta \hat{F}_v + \partial_\zeta \hat{G}_v \right) \right]^{n+1}}_{\text{Next time step (n+1) values for an implicit time integration}}, \end{aligned} \quad (3.61)$$

where the symbols  $\partial_\xi$ ,  $\partial_\eta$  and  $\partial_\zeta$  denote the partial differential operators  $\partial/\partial\xi$ ,  $\partial/\partial\eta$  and  $\partial/\partial\zeta$  respectively. To solve this implicit equation, the fluxes in the advection and viscous terms are linearized by Taylor expansion in the time direction as follow:

$$\hat{E}^{n+1} = \hat{E}^n + \left( \frac{\partial \hat{E}}{\partial \hat{Q}} \right)^n \left( \hat{Q}^{n+1} - \hat{Q}^n \right) + \mathcal{O}(\Delta t^2) = \hat{E}^n + \hat{A}^n \Delta \hat{Q}^n + \mathcal{O}(\Delta t^2), \quad (3.62)$$

where  $\Delta\hat{Q}^n = \hat{Q}^{n+1} - \hat{Q}^n$  (delta-form approximate-factorization<sup>78</sup>), and  $\hat{A}$ ,  $\hat{B}$ ,  $\hat{C}$ ,  $\hat{A}_v$ ,  $\hat{B}_v$  and  $\hat{C}_v$  are flux Jacobian matrices which are defined as follows:

$$\hat{A} = \frac{\partial \hat{E}}{\partial \hat{Q}}, \quad \hat{B} = \frac{\partial \hat{F}}{\partial \hat{Q}}, \quad \hat{C} = \frac{\partial \hat{G}}{\partial \hat{Q}}, \quad \hat{A}_v = \frac{\partial \hat{E}_v}{\partial \hat{Q}}, \quad \hat{B}_v = \frac{\partial \hat{F}_v}{\partial \hat{Q}}, \quad \hat{C}_v = \frac{\partial \hat{G}_v}{\partial \hat{Q}}, \quad (3.63)$$

By substituting Eq. 3.62 and  $\Delta\hat{Q}^n$  into Eq. 3.61, the following equation is obtained:

$$\begin{aligned} & \left[ I + \frac{2\Delta t}{3} \partial_\xi \left( \hat{A} \Delta\hat{Q}^n \right) + \partial_\eta \left( \hat{B} \Delta\hat{Q}^n \right) + \partial_\zeta \left( \hat{C} \Delta\hat{Q}^n \right) \right. \\ & \quad \left. - \frac{2\Delta t}{3Re} \partial_\xi \left( \hat{A}_v \Delta\hat{Q}^n \right) + \partial_\eta \left( \hat{B}_v \Delta\hat{Q}^n \right) + \partial_\zeta \left( \hat{C}_v \Delta\hat{Q}^n \right) \right]^n + \mathcal{O}(\Delta t^2) \\ & = \frac{\hat{Q}^n - \hat{Q}^{n-1}}{3} - \frac{2\Delta t}{3} \left[ \partial_\xi \left( \hat{E} - \frac{1}{Re} \hat{E}_v \right) + \partial_\eta \left( \hat{F} - \frac{1}{Re} \hat{F}_v \right) + \partial_\zeta \left( \hat{G} - \frac{1}{Re} \hat{G}_v \right) \right]^n, \end{aligned} \quad (3.64)$$

We have to solve the Eq. 3.64 to obtain the solution of next time step. However obvious difficulty is expected to solve this equation, and solving it is not realistic because of enormous computational costs. Thus, generally, this equation is not solved directly but solved using approximate factorization. In this study, ADI-SGS factorization is used with Newton-Raphson iteration (which is often called as the sub-iteration<sup>79,80</sup>). These details are explained following sections.

### Newton-Raphson iteration

Generally, approximate factorizations do not guarantee the time discretization accuracy. Thus, in order to guarantee the time discretization accuracy, Newton-Raphson iteration is used with approximate factorizations. Multiplying by  $2\Delta t/3$ , we define the function  $f(Q)$  to obtain the nonlinear equation system for the unknown  $Q = Q^{n+1}$  in Eq. 3.61

$$\begin{aligned} f(\hat{Q}) &= \frac{3\hat{Q}^{n+1} - 4\hat{Q}^n + \hat{Q}^{n-1}}{3} + \frac{2\Delta t}{3} \left[ \partial_\xi \hat{E} + \partial_\eta \hat{F} + \partial_\zeta \hat{G} - \frac{1}{Re} \left( \partial_\xi \hat{E}_v + \partial_\eta \hat{F}_v + \partial_\zeta \hat{G}_v \right) \right]^{n+1} \\ &= \frac{3\hat{Q} - 4\hat{Q}^n + \hat{Q}^{n-1}}{3} + f_a(\hat{Q}) + f_v(\hat{Q}) \\ &= 0, \end{aligned} \quad (3.65)$$

where

$$\begin{aligned} f_a(\hat{Q}) &= \frac{2\Delta t}{3} \left[ \partial_\xi \hat{E}(\hat{Q}) + \partial_\eta \hat{F}(\hat{Q}) + \partial_\zeta \hat{G}(\hat{Q}) \right]^{n+1}, \\ f_v(\hat{Q}) &= -\frac{2\Delta t}{3Re} \left[ \partial_\xi \hat{E}_v(\hat{Q}) + \partial_\eta \hat{F}_v(\hat{Q}) + \partial_\zeta \hat{G}_v(\hat{Q}) \right]^{n+1}, \end{aligned} \quad (3.66)$$

$f_a(\hat{Q})$  and  $f_v(\hat{Q})$  are the advection term and the viscous term at the  $n + 1$  time step, which are functions of  $\hat{Q}$ . The numerical solution of the Eq 3.65 can be done using Newton's method. One Newton step is given by:

$$\left. \frac{\partial f(\hat{Q})}{\partial \hat{Q}} \right|^{(m)} \Delta \hat{Q}^{(m)} = -f(\hat{Q}^{(m)}), \quad (3.67)$$

where the superscript  $(m)$  is a Newton iteration (which is often called as a sub-iteration) index, and  $\Delta \hat{Q}^{(m)} = \hat{Q}^{(m+1)} - \hat{Q}^{(m)}$  is a delta form of the unknown  $\hat{Q}$  in Newton iteration. We solve this linear equation system iteratively with system matrix  $\left. \frac{\partial f(\hat{Q})}{\partial \hat{Q}} \right|^{(m)}$  using ADI-SGS factorization until the  $\Delta \hat{Q}^{(m)}$  of the Eq. 3.67 converges. The system matrix  $\left. \frac{\partial f(\hat{Q})}{\partial \hat{Q}} \right|^{(m)}$  is written as follow:

$$\left. \frac{\partial f(\hat{Q})}{\partial \hat{Q}} \right|^{(m)} = I + \left. \frac{\partial f_a(\hat{Q})}{\partial \hat{Q}} \right|^{(m)} + \left. \frac{\partial f_v(\hat{Q})}{\partial \hat{Q}} \right|^{(m)}, \quad (3.68)$$

where

$$\begin{aligned} \left. \frac{\partial f_a(\hat{Q})}{\partial \hat{Q}} \right|^{(m)} &= \left[ \partial_\xi \frac{\partial \hat{E}(\hat{Q})}{\partial \hat{Q}} + \partial_\eta \frac{\partial \hat{F}(\hat{Q})}{\partial \hat{Q}} + \partial_\zeta \frac{\partial \hat{G}(\hat{Q})}{\partial \hat{Q}} \right]^{(m)}, \\ \left. \frac{\partial f_v(\hat{Q})}{\partial \hat{Q}} \right|^{(m)} &= -\frac{1}{Re} \left[ \partial_\xi \frac{\partial \hat{E}_v(\hat{Q})}{\partial \hat{Q}} + \partial_\eta \frac{\partial \hat{F}_v(\hat{Q})}{\partial \hat{Q}} + \partial_\zeta \frac{\partial \hat{G}_v(\hat{Q})}{\partial \hat{Q}} \right]^{(m)}. \end{aligned} \quad (3.69)$$

By substituting Eq. 3.63 and Eq. 3.69, Eq. 3.68 is rewritten as follow:

$$\left. \frac{\partial f(\hat{Q})}{\partial \hat{Q}} \right|^{(m)} = I + \frac{2\Delta t}{3} \left[ \partial_\xi \hat{A} + \partial_\eta \hat{B} + \partial_\zeta \hat{C} \right]^{(m)} - \frac{2\Delta t}{3Re} \left[ \partial_\xi \hat{A}_v + \partial_\eta \hat{B}_v + \partial_\zeta \hat{C}_v \right]^{(m)} \quad (3.70)$$

By substituting Eq. 3.70, Eq. 3.67 is rewritten as follow:

$$\begin{aligned}
& \left[ I + \frac{2\Delta t}{3} \left( \partial_\xi \hat{A} + \partial_\eta \hat{B} + \partial_\zeta \hat{C} \right) - \frac{2\Delta t}{3Re} \left( \partial_\xi \hat{A}_v + \partial_\eta \hat{B}_v + \partial_\zeta \hat{C}_v \right) \right]^{(m)} \Delta \hat{Q}^{(m)} \\
&= -\frac{1}{3} \left( 3\hat{Q}^{(m)} - 4\hat{Q}^n + \hat{Q}^{n-1} \right) - \frac{2\Delta t}{3} \left[ \partial_\xi \hat{E} + \partial_\eta \hat{F} + \partial_\zeta \hat{G} - \frac{1}{Re} \left( \partial_\xi \hat{E}_v + \partial_\eta \hat{F}_v + \partial_\zeta \hat{G}_v \right) \right]^{(m)} \\
&\equiv (RHS)
\end{aligned} \tag{3.71}$$

The multiple sub-iterations of  $(m)$  are conducted in the Eq. 3.71. If  $\Delta \hat{Q}^{(m)}$  converges to 0, by multiplying  $3/2\Delta t$ , the right hand side of Eq. 3.71 can be rewritten as follow:

$$\begin{aligned}
& \lim_{m \rightarrow \infty} \frac{3}{2\Delta t} (RHS) = \\
& -\frac{3\hat{Q}^{n+1} - 4\hat{Q}^n + \hat{Q}^{n-1}}{2\Delta t} - \left[ \partial_\xi \hat{E} + \partial_\eta \hat{F} + \partial_\zeta \hat{G} - \frac{1}{Re} \left( \partial_\xi \hat{E}_v + \partial_\eta \hat{F}_v + \partial_\zeta \hat{G}_v \right) \right]^{n+1} = 0,
\end{aligned} \tag{3.72}$$

where

$$\hat{Q}^{(m)0} = \hat{Q}^n, \quad \hat{Q}^{(m)\infty} = \hat{Q}^{n+1}, \tag{3.73}$$

$$\lim_{(m) \rightarrow \infty} \hat{Q}^{(m+1)} = \lim_{(m) \rightarrow \infty} \hat{Q}^{(m)} = \hat{Q}^{n+1}, \quad \lim_{(m) \rightarrow \infty} \Delta \hat{Q}^{(m)} = 0. \tag{3.74}$$

The Eq. 3.72 corresponds to Eq. 3.61, and clearly satisfies unsteady Navier-Stokes equations which provide the flow variables fluctuating in time and space. That is, no matter what approximation is introduced into the left hand side of the equation 3.72 to inverse the implicit operator efficiently, exact temporal accuracy is realized if the sub-iterations converge. Thus, in the current research, second-order temporal accuracy is guaranteed by the three-level backward-differencing formula.

### Spacial Difference Scheme

In this section, the compact difference scheme,<sup>81</sup> which is used in this study, is explained.

The compact difference scheme is proposed by Lele<sup>81</sup> and is extended to curvilinear coordinate system by Gaitonde and Visbal.<sup>82,83</sup> A high-order central difference discretization with spectral-like resolution that minimizes dispersive and dissipative numerical errors is preferable for LES. Due to their spectral-like resolution, high-order compact difference scheme<sup>81</sup> is an attractive choice for reducing dispersion, anisotropy and dissipation errors associated with the spatial discretization. Recently, the compact

difference scheme is applied to several engineering problems such as vortical flow over delta and double-delta wings,<sup>84–88</sup> the unsteady flow over a wing section near stall condition.,<sup>89–92</sup> bypass transitional boundary Layer<sup>93–95</sup> and, analysis of noise sources inside the high speed flow over a bump.<sup>96,97</sup>

Note that spatial resolution of sixth-order compact difference scheme<sup>81</sup> is in general much finer than conventional second or third-order scheme (Total variation diminishing (TVD) scheme,<sup>98–100</sup> monotonic upstream scheme for conservation laws (MUSCL)<sup>101,102</sup> scheme) in each direction. Our experience<sup>85,92</sup> indicates that the results by the present method would correspond to that by the conventional method with 50 to 100 times more grids points in the vortical flows. The advantage of the compact difference scheme<sup>81</sup> was shown for the vortical flows compared with the conventional second or third-order scheme (TVD scheme,<sup>98–100</sup> MUSCL<sup>101,102</sup> scheme). In this study, the spatial derivatives of advection terms and viscous terms, metrics, and Jacobian are evaluated by the sixth-order compact difference scheme in order to efficiently solve the boundary layer and shear layer.

First, the compact difference scheme for the approximation of a first differential is explained. Second, tri-diagonal filter which suppress the numerical oscillation is noted. Third, the compact difference scheme for the approximation of a second differential is explained. Finally the evaluation of metrics is explained.

### Compact Difference Scheme for First Differential

In this study the sixth order compact scheme<sup>81</sup> is used. The sixth order compact scheme is written as follows.

$$\begin{aligned} \beta_{cmpt}\phi'_{i-2} + \alpha_{cmpt}\phi'_{i-1} + \phi'_i + \alpha_{cmpt}\phi'_{i+1} + \beta_{cmpt}\phi'_{i+2} = & \frac{a_{cmpt}}{2\Delta h}(\phi_{i+1} - \phi_{i-1}) \\ & \frac{b_{cmpt}}{4\Delta h}(\phi_{i+2} - \phi_{i-2}) \\ & \frac{c_{cmpt}}{6\Delta h}(\phi_{i+3} - \phi_{i-3}) \end{aligned} \quad (3.75)$$

Here,  $\Delta h$  shows discretization step size. The relations between the coefficients  $\alpha$ ,  $\beta$ ,  $a$ ,  $b$  and  $c$  are derived by matching the Taylor series coefficients of various orders.

$$\phi'_{i\pm 1} = \sum_{n=0}^{\infty} \frac{(\pm h)^n}{n!} \phi_i^{n+1}, \phi'_{i\pm 2} = \sum_{n=0}^{\infty} \frac{(\pm 2h)^n}{n!} \phi_i^{n+1} \quad (3.76)$$



$$\phi'_{i\pm 1} = \sum_{n=0}^{\infty} \frac{(\pm h)^n}{n!} \phi_i^n, \phi'_{i\pm 2} = \sum_{n=0}^{\infty} \frac{(\pm 2h)^n}{n!} \phi_i^n \quad (3.77)$$

The first unmatched coefficient determines the formal truncation error of the approximation (3.75). These constraints are:

$$1 + 2\alpha + 2\beta = a + b + c \quad (\text{second - order}) \quad (3.78)$$

$$2\frac{3!}{2!}(a + 2^2\beta) = a + 2^2b + 3^2c \quad (\text{fourth - order}) \quad (3.79)$$

$$2\frac{5!}{4!}(a + 2^4\beta) = a + 2^4b + 3^4c \quad (\text{sixth - order}) \quad (3.80)$$

$$2\frac{7!}{6!}(a + 2^6\beta) = a + 2^6b + 3^6c \quad (\text{eighth - order}) \quad (3.81)$$

$$2\frac{9!}{8!}(a + 2^8\beta) = a + 2^8b + 3^8c \quad (\text{tenth - order}) \quad (3.82)$$

The general relation (3.75) with (3.76), (3.77) can be regarded as a three-parameter family of fourth-order schemes. If the schemes are restricted to  $\beta = 0$  a variety of tri-diagonal systems are obtained. For  $\beta \neq 0$  penta-diagonal schemes are generated. If the additional constraint of sixth-order formal accuracy is imposed, a two-parameter family of sixth-order penta-diagonal schemes is obtained. These may be further specialized into a one-parameter family of eighth-order penta-diagonal schemes or a single tenth-order scheme. First the tri-diagonal schemes are described. These are generated by  $\beta = 0$  to avoid inversion of penta-diagonal matrix. If a further choice of  $c = 0$  is made to reduce a stencil of right hand side of (3.75), a one-parameter ( $a$ ) family of fourth-order tri-diagonal schemes is obtained.

$$\beta = 0, a = \frac{2}{3}(\alpha + 2), b = \frac{1}{3}(4\alpha - 1), c = 0 \quad (3.83)$$

As  $\alpha \rightarrow 0$  this family merges into the well-known fourth-order central difference scheme. Similarly for  $\alpha = \frac{1}{4}$  the classical Padé scheme is recovered.

Furthermore, forth order error term diminish by the coefficient of  $\alpha = \frac{1}{3}$ , because in case of (3.83) truncation error of first term is  $(\frac{4}{5!}(3\alpha - 1)h^4 f^{(5)})$ . Finally, the compact difference scheme have only even-order error. the scheme is formally sixth-order accurate because next error term of forth-order is sixth-order. These coefficients are

	$\alpha$	$\beta$	$a$	$b$	$c$
4th order	1/4	0	3/2	0	0
6th order	1/3	0	14/9	1/9	0
8th order	4/9	1/36	40/27	25/24	0
10th order	1/2	1/20	17/12	101/150	1/100

Table 3.1: Coefficients of compact difference scheme

$$\alpha = \frac{1}{3}, \beta = 0, a = \frac{14}{9}, b = \frac{1}{9}, c = 0 \quad (3.84)$$

These coefficients are used in this study. Typical coefficients are presented in Table 3.1. Maximum order of (3.75) is tenth-order.

Eq. 3.75 is solved as follows. Replacing the right hand side of Eq. 3.75 with  $RHS(i)$ , following expression is obtained.

$$\alpha_{cmpt} \phi'_{i-1} + \phi'_i + \alpha_{cmpt} \phi'_{i+1} = RHS(i) \quad (3.85)$$

A matrix form of Eq. 3.85 is

$$\begin{bmatrix}
 1 & \alpha_{cmpt} & & & & & & & \\
 \alpha_{cmpt} & 1 & \alpha_{cmpt} & & & & & & \\
 & \alpha_{cmpt} & 1 & \alpha_{cmpt} & & & & & \\
 & & \ddots & \ddots & \ddots & \ddots & & & \\
 & & & \ddots & \ddots & \ddots & \ddots & & \\
 & & & & \ddots & \ddots & \ddots & \ddots & \\
 & & & & & \ddots & \ddots & \ddots & \\
 & & & & & & \alpha_{cmpt} & 1 & \alpha_{cmpt} \\
 & & & & & & \alpha_{cmpt} & 1 & \alpha_{cmpt} \\
 & & & & & & & \alpha_{cmpt} & 1
 \end{bmatrix}
 \begin{bmatrix}
 \phi'_3 \\
 \phi'_4 \\
 \phi'_4 \\
 \vdots \\
 \vdots \\
 \vdots \\
 \phi'_{imax-4} \\
 \phi'_{imax-3} \\
 \phi'_{imax-2}
 \end{bmatrix}
 =
 \begin{bmatrix}
 RHS(3) - \alpha_{cmpt}\phi_2 \\
 RHS(4) \\
 RHS(5) \\
 \vdots \\
 \vdots \\
 \vdots \\
 RHS(imax - 4) \\
 RHS(imax - 3) \\
 RHS(imax - 2) - \alpha_{cmpt}\phi_{imax-1}
 \end{bmatrix} \quad (3.86)$$

First, the right hand side of Eq. 3.86 is computed at every stencil. Then, this tri-diagonal or penta-diagonal matrix in the left hand side is inversed using LU decomposition which is a kind of direct methods. Finally, first derivative is evaluated. In the case that the advection terms are evaluated with this compact difference scheme, numerical fluxes are constructed at every grid point, and then these numerical fluxes are substituted into Eq. 3.85 which is solved with the procedure discussed above. As the scheme above has five stencils in the right hand side and three stencils in the left hand side.

### Treatment near the boundary

The sixth-order compact difference scheme can not be applied to near the boundary region, since the scheme above has five stencils in the right hand side and three stencils in the left hand side of 3.75. Though Visbal and Gaitonde<sup>103</sup> propose the evaluation

method of first difference which maintain form of tri-diagonal or penta-diagonal matrix of the left hand side of 3.75 near the boundary region, the second order explicit difference schemes<sup>104</sup> are used near the boundary due to the emphasisization of stable computation. ( $\phi_{jmax-1}$ - $\phi_{jmax}$  are computed symmetrically. )

second order:

$$\begin{aligned}\phi'_1 &= \frac{1}{2}(-3\phi_1 + 4\phi_2 - \phi_3), \\ \phi'_2 &= \frac{1}{12}(\phi_1 - \phi_3)\end{aligned}\tag{3.87}$$

fourth order:

$$\begin{aligned}\phi'_1 &= \frac{1}{12}(-25\phi_1 + 48\phi_2 - 36\phi_3 + 16\phi_4 - 3\phi_5), \\ \phi'_2 &= \frac{1}{12}(-3\phi_1 - 10\phi_2 + 18\phi_3 - 6\phi_4 + \phi_5)\end{aligned}\tag{3.88}$$

Though the accuracy decrease near the boundary region by the second order explicit difference schemes,<sup>104</sup> this treatment does not matter because the grid points are clustered near the boundary.

### Tri-diagonal Filter

The compact difference scheme is a central difference one which needs the filtering procedure for suppressing numerical oscillations except for in direct numerical simulations in which physical viscosities can suppress numerical oscillations. In this study, the following implicit tenth order tri-diagonal filter<sup>83,105</sup> is used.

$$\alpha_f \phi'_{i-1} + \phi'_i + \alpha_f \phi'_{i+1} = \sum_{n=0}^5 \frac{a_f^n}{2} (\phi_{i+n} + \phi_{i-n})\tag{3.89}$$

where the superscript acute ( $\acute{\phi}$ ) denotes a filtered quantity. The coefficients  $\alpha_f$  are shown in table 3.2. If  $\alpha_f = 0$  is used, this filter becomes explicit filter and does not to be solved tri-diagonal matrix.

Note that the near boundary formulation is

$$\alpha_f \phi'_{i-1} + \phi'_i + \alpha_f \phi'_{i+1} = \sum_{n=1}^{11} a_f^n (\phi_i)\tag{3.90}$$

(Near jmax, these values are evaluated symmetrically.) Coefficients are shown in Table

**3.3.**  $\alpha_f$  varies from  $-0.5$  to  $0.5$ . The resolution of the filter becomes higher as  $\alpha_f$  approaches to  $0.5$ , while this filter is becoming not to be able to suppress numerical oscillations simultaneously. In this study  $\alpha_f$  is set to be  $0.45$ . Equations **3.89-3.90** can be solved in a similar way as the previous section. Replacing the right hand side of Eq. **3.89** with  $RHS(i)$ , following expression is obtained.

$$\alpha_f \phi'_{i-1} + \phi'_i + \alpha_f \phi'_{i+1} = RHS(i) \quad (3.91)$$

A matrix form of Eq. **3.91** is

$$\begin{bmatrix} 1 & \alpha_f & & & & & \\ \alpha_f & 1 & \alpha_f & & & & \\ & \alpha_f & 1 & \alpha_f & & & \\ & & \ddots & \ddots & \ddots & & \\ & & & \ddots & \ddots & \ddots & \\ & & & & \ddots & \ddots & \ddots \\ & & & & & \alpha_f & 1 & \alpha_f \\ & & & & & \alpha_f & 1 & \alpha_f \\ & & & & & & \alpha_f & 1 \end{bmatrix} \begin{bmatrix} \phi'_2 \\ \phi'_3 \\ \phi'_4 \\ \vdots \\ \vdots \\ \vdots \\ \phi'_{imax-3} \\ \phi'_{imax-2} \\ \phi'_{imax-1} \end{bmatrix} = \begin{bmatrix} RHS(2) - \alpha\phi_1 \\ RHS(3) \\ RHS(4) \\ \vdots \\ \vdots \\ \vdots \\ RHS(imax-3) \\ RHS(imax-2) \\ RHS(imax-1) - \alpha\phi_{imax} \end{bmatrix} \quad (3.92)$$

First, the right hand side of Eq. **3.92** are computed at every stencil. Then, the tri-diagonal matrix in left hand side is inversed using LU decomposition which is a kind of direct methods. This filtering procedures in  $\xi$ ,  $\eta$  and  $\zeta$  directions are used for each conservative value for suppressing numerical oscillations once per a time step (not per a sub-iteration of inner iteration ) after time integration.

Table 3.2: Coefficients  $a_{f,n}$  in tenth order tri-diagonal filtering.

$a_f^0$	$a_f^1$	$a_f^2$	$a_f^3$	$a_f^4$	$a_f^5$
$\frac{193+126\alpha_f}{256}$	$\frac{105+302\alpha_f}{256}$	$\frac{-15+30\alpha_f}{64}$	$\frac{45-90\alpha_f}{512}$	$\frac{-5+10\alpha_f}{256}$	$\frac{1-2\alpha_f}{512}$

Table 3.3: Coefficients  $a_{f,k}^n$  in tenth order tri-diagonal filtering.

k	$a_{f,k}^1$	$a_{f,k}^2$	$a_{f,k}^3$	$a_{f,k}^4$	$a_{f,k}^5$	$a_{f,k}^6$	$a_{f,k}^7$	$a_{f,k}^8$	$a_{f,k}^9$	$a_{f,k}^{10}$	$a_{f,k}^{11}$
2	$\frac{1+1022\alpha_f}{1024}$	$\frac{507+10\alpha_f}{512}$	$\frac{45+934\alpha_f}{1024}$	$\frac{-15+30\alpha_f}{128}$	$\frac{105-210\alpha_f}{512}$	$\frac{-63+126\alpha_f}{256}$	$\frac{105-210\alpha_f}{512}$	$\frac{-15+30\alpha_f}{128}$	$\frac{45-90\alpha_f}{1024}$	$\frac{-5+10\alpha_f}{512}$	$\frac{1-2\alpha_f}{1024}$
3	$\frac{-1+2\alpha_f}{1024}$	$\frac{5+502\alpha_f}{512}$	$\frac{979+90\alpha_f}{1024}$	$\frac{15+98\alpha_f}{128}$	$\frac{-105+210\alpha_f}{512}$	$\frac{63-126\alpha_f}{256}$	$\frac{-105+210\alpha_f}{512}$	$\frac{15-30\alpha_f}{128}$	$\frac{-45+90\alpha_f}{1024}$	$\frac{5-10\alpha_f}{512}$	$\frac{-1+2\alpha_f}{1024}$
4	$\frac{1-2\alpha_f}{1024}$	$\frac{-5+10\alpha_f}{512}$	$\frac{45+930\alpha_f}{1024}$	$\frac{113-30\alpha_f}{128}$	$\frac{105+302\alpha_f}{512}$	$\frac{-63+126\alpha_f}{256}$	$\frac{105-210\alpha_f}{512}$	$\frac{-15+30\alpha_f}{128}$	$\frac{45-90\alpha_f}{1024}$	$\frac{-5+10\alpha_f}{512}$	$\frac{1-2\alpha_f}{1024}$
5	$\frac{-1+2\alpha_f}{1024}$	$\frac{5-10\alpha_f}{512}$	$\frac{-45+90\alpha_f}{1024}$	$\frac{15+98\alpha_f}{128}$	$\frac{407+210\alpha_f}{512}$	$\frac{63+130\alpha_f}{256}$	$\frac{-105+210\alpha_f}{512}$	$\frac{15-30\alpha_f}{128}$	$\frac{-45+90\alpha_f}{1024}$	$\frac{5-10\alpha_f}{512}$	$\frac{-1+2\alpha_f}{1024}$

### Evaluation of Metrics

All the metrics and Jacobian are expressed in the symmetric conservative forms of Appendix A of the reference.<sup>74</sup> Here, the discretization of metrics and Jacobian in Eq. 3.71 are described in terms of the temporal direction. The spatial discretization is based on the sixth-order compact scheme in Eqs. 3.86, 3.87, and 3.88.

For the conciseness, the one-dimensional case is explained without losing generality. Equation 3.71 includes the metrics and Jacobian at the sub-iteration step of  $m$ , i.e.,  $J^{(m)}$ ,  $\xi_t^{(m)}$ , and  $\xi_x^{(m)}$ . The solution at the sub-iteration steps of  $m$  and  $m + 1$  is the approximation of that at the time step of  $n + 1$ . Therefore, all the metrics and Jacobian with the superscripts of  $m$  and  $m + 1$  should be computed from the grid at the time step of  $n + 1$ , e.g.,  $J^{(m)} = J^{(m+1)} = J^{n+1}$ , where the grid motion is assumed to be analytically determined in the current thesis. Note that the time metrics  $\xi_t^{(m)}$  includes the first differential of the coordinate value in the temporal direction, e.g.,  $x_\tau^{(m)}$ , that is discretized as

$$x_\tau^{(m)} \simeq \frac{3x^{n+1} - 4x^n + x^{n-1}}{2\Delta t}. \quad (3.93)$$

The important point is that the temporal differential of the coordinate values appearing in the time metrics should be discretized in the same manner as that used for the temporal discretization of the governing equations, i.e., second-order backward-difference scheme in the current thesis.

### Viscous Terms

In the following, the evaluation of viscous terms is explained. Viscous fluxes are evaluated with the second difference operator. Though Lele evaluated viscous fluxes with the second difference operator,<sup>81</sup> in this way the viscous terms are evaluated with twice operations of the difference operator.

Nagarajan *et al.*<sup>106</sup> reported that a more robust scheme can be constructed using the second difference operator, or the evaluation of viscous terms on cell-centers because the viscous terms can be evaluated up to a very high wave number. However, in this study, viscous terms are not evaluated in these ways because the compact difference scheme with the filtering is adopted which is stable enough.

The following sixth order compact difference scheme is used.

$$\begin{aligned} \beta\phi''_{i-2} + \alpha\phi''_{i-1} + \phi''_i + \alpha\phi''_{i+1} + \beta\phi''_{i+2} = & \frac{a}{2h} (\phi'_{i+1} - \phi'_{i-1}) \\ & + \frac{b}{4h} (\phi'_{i+2} - \phi'_{i-2}) \\ & + \frac{c}{6h} (\phi'_{i+3} - \phi'_{i-3}) \end{aligned} \quad (3.94)$$

Note that Eq. 3.87 are used near boundary region. On the other hand, the compact difference scheme is used for the evaluation of advection terms, the sixth order compact difference scheme (Eq. 3.75 and Eq. 3.87) is also used for the evaluation of viscous terms.

First, approximate  $\xi$ ,  $\eta$ ,  $\zeta$  direction first differential values of  $u$ ,  $v$ ,  $w$  and  $q$  are evaluated the difference operator. Then, these differential values are transformed into  $x$ ,  $y$ ,  $z$  direction differential ones of  $u$ ,  $v$ ,  $w$  and  $q$ . This transform is based on the chain rule of the partial differential which is written with general function  $\phi$  as follows,

$$\begin{aligned} \phi_x &= \xi_x \phi_\xi + \eta_x \phi_\eta + \zeta_x \phi_\zeta \\ \phi_y &= \xi_y \phi_\xi + \eta_y \phi_\eta + \zeta_y \phi_\zeta \\ \phi_z &= \xi_z \phi_\xi + \eta_z \phi_\eta + \zeta_z \phi_\zeta \end{aligned} \quad (3.95)$$

The viscous tensor is constructed with  $x$ ,  $y$ ,  $z$  direction differential values, and then the viscous flux in Eq. 3.55 is calculated at each grid points. Finally, the viscous flux is differenced with the difference operator Eq. 3.95. The same coefficients of first difference operator are used in second difference operator.

Though above procedure does not have the effect of suppression of high frequency oscillation in viscous term, the above procedure does not matter due to using the filtering at the same time in this study.

## Time integration

The numerical scheme which has higher temporal accuracy is preferable for the analysis of the temporal behaviour of the flow field using LES. The choice of the time integration scheme is the trade-off between the temporal accuracy and total simulation time. There are mainly two choices of the time integration scheme; one is the explicit time integration method, and the other is the implicit time integration method. The explicit time marching method is one choice. Even the simplest Euler explicit scheme has at least first-order temporal accuracy, and it is easy to extend temporal accuracy of the explicit



schemes using Runge-Kutta method.<sup>107</sup> However, the time step size  $\Delta t$  for the explicit schemes is strongly restricted by the local Courant-Friedrichs-Lewy (CFL) number,<sup>108</sup> and the restriction becomes very strict when the grid clustered near the wall to resolve the boundary layer. The restriction derives the long total simulation time, and it is almost impossible to simulate the phenomena considered in the current research. The flow field considered here is essentially unsteady, and it is necessary to resolve unsteady flows both in time and space for the LES.

### ADI-SGS factorization algorithm

Alternative direction implicit-symmetric gauss seidel (ADI-SGS) implicit scheme is used for the time integration in this study to overcome the restriction of the time step size  $\Delta t$ . Although ADI-SGS implicit time integration scheme is numerically efficient, the temporal accuracy of the scheme is less than first-order due to the errors of linearization, alternative direction implicit and etc. Therefore, multiple sub-iterations (Newton-Raphson iteration)<sup>79,80</sup> are adopted and the errors due to the linearization, alternative direction implicit and etc. are eliminated. With regard to time integration, an alternative direction implicit-symmetric gauss seidel (ADI-SGS) implicit scheme<sup>109–111</sup> is employed.

This algorithm uses the same type of idea as a four-factor symmetric Gauss-Seidel (FF-SGS) method,<sup>112</sup> which uses both lower-upper symmetric alternating direction implicit (LU-ADI) methods<sup>61–64</sup> and lower-upper symmetric Gauss-Seidel (LU-SGS) methods.<sup>113,114</sup> Concretely, the spectral radius is used to obtain the upwind difference in each direction of the LU-ADI scheme.

When we consider the first-order Euler implicit scheme, the Navier-Stokes equations can be written as

$$\hat{Q}^{n+1} - \hat{Q}^n = -\Delta t \left[ \frac{\partial \hat{E}}{\partial \xi} + \frac{\partial \hat{F}}{\partial \eta} + \frac{\partial \hat{G}}{\partial \zeta} - \frac{1}{Re} \left( \frac{\partial \hat{E}_v}{\partial \xi} + \frac{\partial \hat{F}_v}{\partial \eta} + \frac{\partial \hat{G}_v}{\partial \zeta} \right) \right]^{n+1} \quad (3.96)$$

Then the flux vectors in the time direction are linearized by Taylor series expansion<sup>78</sup>,

and  $\hat{E}$ ,  $\hat{F}$  and  $\hat{G}$  is described as:

$$\begin{aligned}\hat{E}^{n+1} &= \hat{E}^n + \left( \frac{\partial \hat{E}}{\partial \hat{Q}} \right)^n (\hat{Q}^{n+1} - \hat{Q}^n) + O(\Delta t^2) \\ \hat{F}^{n+1} &= \hat{F}^n + \left( \frac{\partial \hat{F}}{\partial \hat{Q}} \right)^n (\hat{Q}^{n+1} - \hat{Q}^n) + O(\Delta t^2) \\ \hat{G}^{n+1} &= \hat{G}^n + \left( \frac{\partial \hat{G}}{\partial \hat{Q}} \right)^n (\hat{Q}^{n+1} - \hat{Q}^n) + O(\Delta t^2)\end{aligned}\quad (3.97)$$

By substituting Eq. 3.1.3 for Eq. 3.96 and importing  $\Delta \hat{Q} = \hat{Q}^{n+1} - \hat{Q}^n$  (delta-form approximate-factorization<sup>78</sup>), The followings are obtained:

$$\Delta \hat{Q}^n = -\Delta t \left[ \frac{\partial}{\partial \xi} (\hat{E} + \hat{A} \Delta \hat{Q}) + \frac{\partial}{\partial \eta} (\hat{F} + \hat{B} \Delta \hat{Q}) + \frac{\partial}{\partial \varsigma} (\hat{G} + \hat{C} \Delta \hat{Q}) - Q \left( \frac{1}{J} \right)_\tau \right]^n \quad (3.98)$$

where  $\hat{A}$ ,  $\hat{B}$ ,  $\hat{C}$  are called flux Jacobian matrices and are described as:

$$\hat{A} = \frac{\partial \hat{E}}{\partial \hat{Q}}, \hat{B} = \frac{\partial \hat{F}}{\partial \hat{Q}}, \hat{C} = \frac{\partial \hat{G}}{\partial \hat{Q}}, \hat{A}_v = \frac{\partial \hat{E}_v}{\partial \hat{Q}}, \hat{B}_v = \frac{\partial \hat{F}_v}{\partial \hat{Q}}, \hat{C}_v = \frac{\partial \hat{G}_v}{\partial \hat{Q}} \quad (3.99)$$

and given by

$$\begin{aligned} & \hat{A} \text{ or } \hat{B} \text{ or } \hat{C} \\ &= \begin{bmatrix} \kappa_t & \kappa_x & \kappa_y \\ \kappa_x \phi^2 - v\theta & \kappa_t + \theta - (\gamma - 2)\kappa_x u & \kappa_x u - (\gamma - 1)\kappa_y v \\ \kappa_y \phi^2 - v\theta & \kappa_x v - (\gamma - 1)\kappa_y u & \kappa_t + \theta - (\gamma - 2)\kappa_y v \\ \kappa_z \phi^2 - w\theta & \kappa_x w - (\gamma - 1)\kappa_z u & \kappa_y w - (\gamma - 1)\kappa_z v \\ -\theta(\frac{\gamma^e}{\rho} - 2\phi^2) & \kappa_x(\frac{\gamma^e}{\rho} - \phi^2) - (\gamma - 1)\theta u & \kappa_y(\frac{\gamma^e}{\rho} - \phi^2) - (\gamma - 1)\theta v \\ & \kappa_z & 0 \\ & \kappa_z u - (\gamma - 1)\kappa_x w & (\gamma - 1)\kappa_x \\ & \kappa_z v - (\gamma - 1)\kappa_y w & (\gamma - 1)\kappa_y \\ & \kappa_t + \theta - (\gamma - 2)\kappa_z w & (\gamma - 1)\kappa_z \\ & \kappa_z(\frac{\gamma^e}{\rho} - \phi^2) - (\gamma - 1)\theta w & \kappa_t + \gamma\theta \end{bmatrix} \quad (3.100)\end{aligned}$$

where

$$\begin{aligned}\theta &= \kappa_u + \kappa_y v + \kappa_z w \\ \phi^2 &= \frac{1}{2}(\gamma - 1)(u^2 + v^2 + w^2)\end{aligned}\tag{3.101}$$

with  $\kappa = \xi, \eta$  or  $\zeta$  for  $\hat{A}, \hat{B}, \hat{C}$ , respectively. The term of  $\hat{Q}^n$  is moved to the left hand side,

$$\begin{aligned}&\left[ I + \Delta t \left( \frac{\partial \hat{A}}{\partial \xi} + \frac{\partial \hat{B}}{\partial \eta} + \frac{\partial \hat{C}}{\partial \zeta} \right) - \frac{\Delta t}{Re} \left( \frac{\partial \hat{A}_v}{\partial \xi} + \frac{\partial \hat{B}_v}{\partial \eta} + \frac{\partial \hat{C}_v}{\partial \zeta} \right) \right]^n \Delta \hat{Q}^n \\ &= -\Delta t \left[ \frac{\partial \hat{E}}{\partial \xi} + \frac{\partial \hat{F}}{\partial \eta} + \frac{\partial \hat{G}}{\partial \zeta} - \frac{1}{Re} \left( \frac{\partial \hat{E}_v}{\partial \xi} + \frac{\partial \hat{F}_v}{\partial \eta} + \frac{\partial \hat{G}_v}{\partial \zeta} \right) \right]^n\end{aligned}\tag{3.102}$$

By ignoring the viscous terms in the left-hand side of Eq. 3.102, assuming that they can be dealt with explicitly.<sup>115,116</sup>

$$\begin{aligned}&\left[ I + \Delta t \left( \frac{\partial \hat{A}}{\partial \xi} + \frac{\partial \hat{B}}{\partial \eta} + \frac{\partial \hat{C}}{\partial \zeta} \right) \right]^n \Delta \hat{Q}^n \\ &= -\Delta t \left[ \frac{\partial \hat{E}}{\partial \xi} + \frac{\partial \hat{F}}{\partial \eta} + \frac{\partial \hat{G}}{\partial \zeta} - \frac{1}{Re} \left( \frac{\partial \hat{E}_v}{\partial \xi} + \frac{\partial \hat{F}_v}{\partial \eta} + \frac{\partial \hat{G}_v}{\partial \zeta} \right) \right]^n\end{aligned}\tag{3.103}$$

The implicit operator (ADI operator) inside [ ] of the left hand side of 3.103 is sparse but block non-band matrix, and it is a tough work to inverse it. Here, ADI factorization is a good choice;

$$\begin{aligned}&\left[ I + \Delta t \left( \frac{\partial \hat{A}}{\partial \xi} + \frac{\partial \hat{B}}{\partial \eta} + \frac{\partial \hat{C}}{\partial \zeta} \right) \right]^n \Delta \hat{Q}^n \\ &\rightarrow \left( I + \Delta t \frac{\partial \hat{A}}{\partial \xi} \right)^n \left( I + \Delta t \frac{\partial \hat{B}}{\partial \eta} \right)^n \left( I + \Delta t \frac{\partial \hat{C}}{\partial \zeta} \right)^n \Delta \hat{Q}^n + O(\Delta t^2)\end{aligned}\tag{3.104}$$

The implicit operator of 3.103 can be factored by the approximate factorization<sup>78</sup> as

$$\begin{aligned}
& \left( I + \Delta t \frac{\partial \hat{A}}{\partial \xi} \right)^n \left( I + \Delta t \frac{\partial \hat{B}}{\partial \eta} \right)^n \left( I + \Delta t \frac{\partial \hat{C}}{\partial \zeta} \right)^n \Delta \hat{Q}^n \\
&= -\Delta t \left[ \frac{\partial \hat{E}}{\partial \xi} + \frac{\partial \hat{F}}{\partial \eta} + \frac{\partial \hat{G}}{\partial \zeta} - \frac{1}{Re} \left( \frac{\partial \hat{E}_v}{\partial \xi} + \frac{\partial \hat{F}_v}{\partial \eta} + \frac{\partial \hat{G}_v}{\partial \zeta} \right) \right]^n = -\Delta t \cdot R_j^n \quad (3.105)
\end{aligned}$$

This reduces the complex inversion of Matrix to three stages of one dimensional Matrix inversion. If we apply second order central differences for spatial derivatives, each of three matrices will be a tri-diagonal matrix with its components as flux Jacobians. where,  $\delta\xi$ ,  $\delta\eta$  and  $\delta\zeta$  which are the finite difference operator for each direction are applied to the left hand side of Eq. 3.105,

$$\begin{aligned}
& \left( I + \Delta t \frac{\partial \hat{A}}{\partial \xi} \right)^n \left( I + \Delta t \frac{\partial \hat{B}}{\partial \eta} \right)^n \left( I + \Delta t \frac{\partial \hat{C}}{\partial \zeta} \right)^n \\
&= \left( I + \Delta t \delta_\xi \hat{A} \right)^n \left( I + \Delta t \delta_\eta \hat{B} \right)^n \left( I + \Delta t \delta_\zeta \hat{C} \right)^n \quad (3.106)
\end{aligned}$$

The following is obtained:

$$\begin{aligned}
& \left( I + \Delta t \delta_\xi \hat{A} \right)^n \left( I + \Delta t \delta_\eta \hat{B} \right)^n \left( I + \Delta t \delta_\zeta \hat{C} \right)^n \Delta \hat{Q}^n \\
&= -\Delta t \left[ \frac{\partial \hat{E}}{\partial \xi} + \frac{\partial \hat{F}}{\partial \eta} + \frac{\partial \hat{G}}{\partial \zeta} - \frac{1}{Re} \left( \frac{\partial \hat{E}_v}{\partial \xi} + \frac{\partial \hat{F}_v}{\partial \eta} + \frac{\partial \hat{G}_v}{\partial \zeta} \right) \right]^n \quad (3.107)
\end{aligned}$$

Approximate Lower-Diagonal-Upper (LDU) factorization,<sup>78</sup> which is more stable than simple Lower-Upper (LU) factorization<sup>117</sup> due to diagonally dominant, is applied to the operator in the left hand side of Eq. 3.107. This basic idea of LDU factorization is proposed as DDADI factorization by Lombard et al.<sup>118</sup>

$$\begin{aligned}
& \left( I + \Delta t \delta_\xi \hat{A} \right) \left( I + \Delta t \delta_\eta \hat{B} \right) \left( I + \Delta t \delta_\zeta \hat{C} \right) \\
&= [L_\xi + D_\xi + U_\xi][L_\eta + D_\eta + U_\eta][L_\zeta + D_\zeta + U_\zeta] \quad (3.108) \\
&\approx [(L_\xi + D_\xi) D_\xi^{-1} (D_\xi + U_\xi)] [(L_\eta + D_\eta) D_\eta^{-1} (D_\eta + U_\eta)] [(L_\zeta + D_\zeta) D_\zeta^{-1} (D_\zeta + U_\zeta)]
\end{aligned}$$

Then, equation 3.107 can be rewritten as

$$\begin{aligned}
& [(L_\xi + D_\xi) D_\xi^{-1} (D_\xi + U_\xi)] [(L_\eta + D_\eta) D_\eta^{-1} (D_\eta + U_\eta)] [(L_\zeta + D_\zeta) D_\zeta^{-1} (D_\zeta + U_\zeta)] \Delta \hat{Q}^n \\
&= (RHS) \quad (3.109)
\end{aligned}$$

where  $I$ ,  $L$ ,  $D$  and  $U$  are the identity matrix, the left-lower triangle, the diagonal and the right-upper triangle of the matrix, respectively as

$$\begin{aligned} L_\xi &= -\Delta t \hat{A}_{j-1}, \quad D_\xi = I + \Delta t \left[ \left( \hat{A}^+ - \hat{A}^- \right) / \Delta \xi \right], \quad U_\xi = \Delta t \hat{A}_{j+1}^+ \\ L_\eta &= -\Delta t \hat{B}_{j-1}, \quad D_\eta = I + \Delta t \left[ \left( \hat{B}^+ - \hat{B}^- \right) / \Delta \eta \right], \quad U_\eta = \Delta t \hat{B}_{j+1}^+ \\ L_\zeta &= -\Delta t \hat{A}_{j-1}, \quad D_\zeta = I + \Delta t \left[ \left( \hat{A}^+ - \hat{A}^- \right) / \Delta \zeta \right], \quad U_\zeta = \Delta t \hat{C}_{j+1}^+ \end{aligned} \quad (3.110)$$

$$\begin{aligned} L_\xi + D_\xi &= I + \Delta t \left( \delta_\xi^- \hat{A}^+ - \hat{A}^- / \Delta \xi \right) \\ D_\xi &= I + \Delta t \left[ \left( \hat{A}^+ - \hat{A}^- \right) / \Delta \xi \right] \\ D_\xi + U_\xi &= I + \Delta t \left( \delta_\xi^+ \hat{A}^- - \hat{A}^+ / \Delta \xi \right) \end{aligned} \quad (3.111)$$

$$\begin{aligned} L_\eta + D_\eta &= I + \Delta t \left( \delta_\eta^- \hat{B}^+ - \hat{B}^- / \Delta \eta \right) \\ D_\eta &= I + \Delta t \left[ \left( \hat{B}^+ - \hat{B}^- \right) / \Delta \eta \right] \\ D_\eta + U_\eta &= I + \Delta t \left( \delta_\eta^+ \hat{B}^- - \hat{B}^+ / \Delta \eta \right) \end{aligned} \quad (3.112)$$

$$\begin{aligned} L_\zeta + D_\zeta &= I + \Delta t \left( \delta_\zeta^- \hat{C}^+ - \hat{C}^- / \Delta \zeta \right) \\ D_\zeta &= I + \Delta t \left[ \left( \hat{C}^+ - \hat{C}^- \right) / \Delta \zeta \right] \\ D_\zeta + U_\zeta &= I + \Delta t \left( \delta_\zeta^+ \hat{C}^- - \hat{C}^+ / \Delta \zeta \right) \end{aligned} \quad (3.113)$$

As for the Jacobian matrix of the convective numerical fluxes,  $\hat{A}^\pm$ ,  $\hat{B}^\pm$  and  $\hat{C}^\pm$ , the eigenvalues of "+" matrices are nonnegative and those of "-" matrices are nonpositive.<sup>119</sup> Finite difference operators of  $\delta_\xi^+$ ,  $\delta_\eta^+$  and  $\delta_\zeta^+$  are first-order forward difference operators and  $\delta_\xi^-$ ,  $\delta_\eta^-$  and  $\delta_\zeta^-$  are first-order backward difference operators using the idea of 1st upwind difference, as follows:

$$\delta_{\xi}^+ \hat{A}^- = \frac{\hat{A}_{j+1,k,l}^- - \hat{A}_{j,k,l}^-}{\Delta \xi}, \quad \delta_{\xi}^- \hat{A}^+ = \frac{\hat{A}_{j,k,l}^+ - \hat{A}_{j-1,k,l}^+}{\Delta \xi} \quad (3.114)$$

$$\delta_{\eta}^+ \hat{B}^- = \frac{\hat{B}_{j,k+1,l}^- - \hat{B}_{j,k,l}^-}{\Delta \eta}, \quad \delta_{\eta}^- \hat{B}^+ = \frac{\hat{B}_{j,k,l}^+ - \hat{B}_{j,k-1,l}^+}{\Delta \eta} \quad (3.115)$$

$$\delta_{\zeta}^+ \hat{C}^- = \frac{\hat{C}_{j,k+1,l}^- - \hat{C}_{j,k,l}^-}{\Delta \zeta}, \quad \delta_{\zeta}^- \hat{C}^+ = \frac{\hat{C}_{j,k,l}^+ - \hat{C}_{j,k-1,l}^+}{\Delta \zeta} \quad (3.116)$$

In the solution process, operation of the equation (3.109) using the finite difference operators of the equations (3.116) consists of three steps for each direction (a number of total steps are nine times).

### $\xi$ direction

First step

$$\left[ I + \Delta t \left( \hat{A}_{j,k,l}^+ - \hat{A}_{j,k,l}^- \right) \right] \Delta \hat{Q}_{j,k,l}^* = (RHS) + \Delta t \left( \hat{A}^+ \Delta \hat{Q}^* \right)_{j-1,k,l} \quad (3.117)$$

where

$$\Delta \hat{Q}_{j,k,l}^* = D_{\xi}^{-1} [D_{\xi} + U_{\xi}] \Delta \hat{Q}_{j,k,l}^{**}$$

Second step

$$\left[ I + \Delta t \left( \hat{A}_{j,k,l}^+ - \hat{A}_{j,k,l}^- \right) \right]^{-1} \Delta \hat{Q}_{j,k,l}^{**} = \Delta \hat{Q}_{j,k,l}^* \quad (3.118)$$

where

$$\Delta \hat{Q}_{j,k,l}^{**} = D_{\xi}^{-1} [D_{\xi} + U_{\xi}] \Delta \hat{Q}_{j,k,l}^{***}$$

Third step

$$\left[ I + \Delta t \left( \hat{A}_{j,k,l}^+ - \hat{A}_{j,k,l}^- \right) \right] \Delta \hat{Q}_{j,k,l}^{***} = \Delta \hat{Q}_{j,k,l}^{**} - \Delta t \left( \hat{A}^- \Delta \hat{Q}^{***} \right)_{j+1,k,l} \quad (3.119)$$

### $\eta$ direction

Fourth step

$$\left[ I + \Delta t \left( \hat{B}_{j,k,l}^+ - \hat{B}_{j,k,l}^- \right) \right] \Delta \hat{Q}_{j,k,l}^{***} = (RHS) + \Delta t \left( \hat{B}^+ \Delta \hat{Q}^{***} \right)_{j,k-1,l} \quad (3.120)$$

where

$$\Delta \hat{Q}_{j,k,l}^{***} = D_{\eta}^{-1} [D_{\eta} + U_{\eta}] \Delta \hat{Q}_{j,k,l}^{****}$$

Fifth step

$$\left[ I + \Delta t \left( \hat{B}_{j,k,l}^+ - \hat{B}_{j,k,l}^- \right) \right]^{-1} \Delta \hat{Q}_{j,k,l}^{****} = \Delta \hat{Q}_{j,k,l}^{***} \quad (3.121)$$

where

$$\Delta \hat{Q}_{j,k,l}^{****} = D_{\eta}^{-1} [D_{\eta} + U_{\eta}] \Delta \hat{Q}_{j,k,l}^{*****}$$

Sixth step

$$\left[ I + \Delta t \left( \hat{B}_{j,k,l}^+ - \hat{B}_{j,k,l}^- \right) \right] \Delta \hat{Q}_{j,k,l}^{*****} = \Delta \hat{Q}_{j,k,l}^{****} - \Delta t \left( \hat{B}^- \Delta \hat{Q}^{*****} \right)_{j,k+1,l} \quad (3.122)$$

$\zeta$  direction

Seventh step

$$\left[ I + \Delta t \left( \hat{C}_{j,k,l}^+ - \hat{C}_{j,k,l}^- \right) \right] \Delta \hat{Q}_{j,k,l}^{*****} = (RHS) + \Delta t \left( \hat{C}^+ \Delta \hat{Q}^{*****} \right)_{j,k,l-1} \quad (3.123)$$

where

$$\Delta \hat{Q}_{j,k,l}^{*****} = D_{\zeta}^{-1} [D_{\zeta} + U_{\zeta}] \Delta \hat{Q}_{j,k,l}^n$$

Eighth step

$$\left[ I + \Delta t \left( \hat{C}_{j,k,l}^+ - \hat{C}_{j,k,l}^- \right) \right]^{-1} \Delta \hat{Q}_{j,k,l}^{*****} = \Delta \hat{Q}_{j,k,l}^{****} \quad (3.124)$$

where

$$\Delta \hat{Q}_{j,k,l}^{*****} = D_{\zeta}^{-1} [D_{\zeta} + U_{\zeta}] \Delta \hat{Q}_{j,k,l}^n$$

Ninth step

$$\left[ I + \Delta t \left( \hat{C}_{j,k,l}^+ - \hat{C}_{j,k,l}^- \right) \right] \Delta \hat{Q}_{j,k,l}^n = \Delta \hat{Q}_{j,k,l}^{*****} - \Delta t \left( \hat{C}^- \Delta \hat{Q}^n \right)_{j,k,l+1} \quad (3.125)$$

where  $\Delta \xi = \Delta \eta = \Delta \zeta = 1$  for simplicity. There are several ways to evaluate such as Steger-Warming FVS<sup>119</sup> etc., though, following definition is much easier and cost effective. To reduce the computational cost, The idea of LU-SGS<sup>113, 114</sup> or Lax-Friedrich scheme<sup>120</sup> is employed instead of the diagonal form<sup>121</sup> of LU-ADI. Therefore, in the ADI-SGS implicit time integration scheme, the following approximation is then applied to the

Jacobian matrices,  $\hat{A}^\pm$ ,  $\hat{B}^\pm$  and  $\hat{C}^\pm$ ,

$$\begin{aligned}\hat{A}^\pm &= \frac{\hat{A} + \sigma(\hat{A})I}{2} \\ \sigma(\hat{A}) &= \max_i \left( |\lambda_{\hat{A};i}| \right) \\ &= |\xi_t + U| + a\sqrt{\xi_x^2 + \xi_y^2 + \xi_z^2}\end{aligned}\tag{3.126}$$

$$\begin{aligned}\hat{B}^\pm &= \frac{\hat{B} + \sigma(\hat{B})I}{2} \\ \sigma(\hat{B}) &= \max_i \left( |\lambda_{\hat{B};i}| \right) \\ &= |\eta_t + V| + a\sqrt{\eta_x^2 + \eta_y^2 + \eta_z^2}\end{aligned}\tag{3.127}$$

$$\begin{aligned}\hat{C}^\pm &= \frac{\hat{C} + \sigma(\hat{C})I}{2} \\ \sigma(\hat{C}) &= \max_i \left( |\lambda_{\hat{C};i}| \right) \\ &= |\zeta_t + W| + a\sqrt{\zeta_x^2 + \zeta_y^2 + \zeta_z^2}\end{aligned}\tag{3.128}$$

where  $\sigma(\hat{A})$ ,  $\sigma(\hat{B})$  and  $\sigma(\hat{C})$  represent the maximum eigen values of the Jacobian matrices, so-called spectral radius.  $\lambda_{\hat{A};i}$ ,  $\lambda_{\hat{B};i}$  and  $\lambda_{\hat{C};i}$  are  $i$ th eigen value of  $\hat{A}$ ,  $\hat{B}$  and  $\hat{C}$ . Then, the left hand side of equations (3.117)-(3.125) becomes

$$\left[ I + \Delta t \left( \hat{A}_{j,k,l}^+ - \hat{A}_{j,k,l}^- \right) \right] = \left[ 1 + \Delta t \sigma(\hat{A}) \right] I \tag{3.129}$$

$$\left[ I + \Delta t \left( \hat{B}_{j,k,l}^+ - \hat{B}_{j,k,l}^- \right) \right] = \left[ 1 + \Delta t \sigma(\hat{B}) \right] I \tag{3.130}$$

$$\left[ I + \Delta t \left( \hat{C}_{j,k,l}^+ - \hat{C}_{j,k,l}^- \right) \right] = \left[ 1 + \Delta t \sigma(\hat{C}) \right] I \tag{3.131}$$

These procedures turns matrix inversion to scalar division.

The inversion of the implicit operator of Eq. 3.109 requires only one forward sweep for the inversion of  $L_\xi + D_\xi$  and one backward sweep for that of  $D_\xi^{-1}(L_\xi + D_\xi)$ .

Finally, the ADI-SGS scheme can be described by using the similar decomposition for the other implicit operators of the other directions  $\eta$  and  $\zeta$  in 3.109,

The equations 3.125-3.125 can be rewritten from three steps and two steps and the sweeps are conducted below to each factor (i.e., 6 times in total per iteration) as follow



$$\begin{aligned}
& \left( I + \Delta t \sigma(\hat{A}) \right) \Delta \hat{Q}_{j,k,l}^* - \Delta t \hat{A}_{j,k,l}^+ \Delta \hat{Q}_{j-1,k,l}^* = (RHS) \quad \text{:forward sweep} \\
& \Delta \hat{Q}_{j,k,l}^{**} + \frac{1}{1 + \Delta t \sigma(\hat{A})} \Delta t \hat{A}_{j,k,l}^- \Delta \hat{Q}_{j-1,k,l}^{**} = \Delta \hat{Q}_{j,k,l}^* \quad \text{:backward sweep}
\end{aligned} \tag{3.132}$$

$$\begin{aligned}
& \left( I + \Delta t \sigma(\hat{B}) \right) \Delta \hat{Q}_{j,k,l}^{**} - \Delta t \hat{B}_{j,k,l}^+ \Delta \hat{Q}_{j,k-1,l}^{**} = (RHS) \quad \text{:forward sweep} \\
& \Delta \hat{Q}_{j,k,l}^{***} + \frac{1}{1 + \Delta t \sigma(\hat{B})} \Delta t \hat{B}_{j,k,l}^- \Delta \hat{Q}_{j,k-1,l}^{***} = \Delta \hat{Q}_{j,k,l}^{**} \quad \text{:backward sweep}
\end{aligned} \tag{3.133}$$

$$\begin{aligned}
& \left( I + \Delta t \sigma(\hat{C}) \right) \Delta \hat{Q}_{j,k,l}^{***} - \Delta t \hat{C}_{j,k,l}^+ \Delta \hat{Q}_{j,k,l-1}^{***} = (RHS) \quad \text{:forward sweep} \\
& \Delta \hat{Q}_{j,k,l}^n + \frac{1}{1 + \Delta t \sigma(\hat{C})} \Delta t \hat{C}_{j,k,l}^- \Delta \hat{Q}_{j,k,l-1}^n = \Delta \hat{Q}_{j,k,l}^{***} \quad \text{:backward sweep}
\end{aligned} \tag{3.134}$$

This implicit method is highly suitable for Vector/Parallel hybrid architecture because along a direction in being swept, there still remain two directions free that can be vectorized/parallelized, for three-dimensional case, while in general a Gauss-Seidel relaxation is not suitable for Vector/Parallel hybrid system. The ADI-SGS scheme eliminates the need for the inversions of block diagonal matrices, as seen in the LU-ADI scheme, without using a diagonalization procedure, and can achieve further reduction of calculation processes compared to the LU-ADI scheme. In addition, the ADI-SGS scheme is more diagonally dominant, i.e., more stable than the LU-ADI scheme due to the approximation of the split Jacobian matrices with those spectral radius. The ADI-SGS scheme introduces several approximation (e.g. linear approximation and approximate factorization) to inverse the implicit operator efficiently. Especially for the approximation of the Eqs. 3.126-3.128, the numerical dissipation corresponding to the eigen values of each wave is added, and the excessive numerical dissipation may introduce to a specific wave. Therefore its temporal accuracy is less than the first-order. In the current study, multiple sub-iterations are adopted and the errors are eliminated.

### Treatment of Viscous Term in the Time Integration

Though it is assumed above that the viscous terms in the left-hand side of Eq. 3.98 can be dealt with explicitly, it is possible to add the viscous terms to the left-hand side as implicit operators.<sup>122,123</sup> However, the operators on the left-hand side are variously approximated, and the strictness of these approximations is not specially needed. There-

fore, for practical use, it is known that the viscous terms can be put only in the right-hand side and dealt with explicitly.<sup>115,116</sup> However, in the calculation of low Reynolds number (i.e., less than  $10^4$ ), it is known that the calculation diverges because of the disagreement of left- and right- hand sides, then some kinds of approximation operators are indispensable. In the current research, a comparatively high Reynolds number are dealt, in the turbulent boundary layer, the viscosity becomes very high, and the Reynolds number virtually seems to decrease.

For simplicity and efficiency, in the current study, the following approximate operator of the viscous terms introduced by Obayashi *et al.*<sup>124</sup> which is similar to the implicit MacCormack scheme<sup>125</sup> is added in the diagonal matrix in the left hand side of the Eqs. 3.126, 3.127 and 3.128. Thus, to add the effect of the viscosity, the equations are modified by:

$$\begin{aligned}
 \sigma_\xi &= |\xi_t + U| + c\sqrt{\zeta_x^2 + \zeta_y^2 + \zeta_z^2} + 2\hat{\nu} \\
 \hat{\nu} &= \frac{\mu(\xi_x^2 + \xi_y^2 + \xi_z^2)}{Re \cdot \rho \cdot \Delta\xi} \\
 \sigma_\eta &= |\eta_t + V| + c\sqrt{\eta_x^2 + \eta_y^2 + \eta_z^2} + 2\hat{\nu} \\
 \hat{\nu} &= \frac{\mu(\eta_x^2 + \eta_y^2 + \eta_z^2)}{Re \cdot \rho \cdot \Delta\eta} \\
 \sigma_\zeta &= |\zeta_t + W| + c\sqrt{\zeta_x^2 + \zeta_y^2 + \zeta_z^2} + 2\hat{\nu} \\
 \hat{\nu} &= \frac{\mu(\zeta_x^2 + \zeta_y^2 + \zeta_z^2)}{Re \cdot \rho \cdot \Delta\zeta}
 \end{aligned} \tag{3.135}$$

### Turbulence Modeling

Large-eddy simulation (LES) is adopted in the study to resolve the three-dimensional fine vortex structures of the flow inside and outside the cavity, turbulent boundary layer and separated shear layer. Direct numerical simulation (DNS) is not used because the present computational resources are not sufficient for DNS, and the analysis of vortex structure that can be resolved using LES is sufficient for understanding the flow control mechanism. LES does not solve the full range of scales (unlike DNS), but it solves a much larger range of scales than RANS. Hence, LES is potentially more accurate than RANS, since less modeling errors are introduced. In LES approaches, required resolution is coarser than in DNS, while much finer resolution is needed than in RANS.

Large eddy simulation (LES) is a popular technique for simulating turbulent flows. An implication of Kolmogorov's theory of self similarity is that the large eddies of the flow

are dependant on the geometry while the smaller scales more universal.<sup>126</sup> This feature allows one to explicitly solve for the large eddies in a calculation and implicitly account for the small eddies by using a subgrid-scale model (SGS model) such as Smagorinsky model.<sup>127</sup>

With a traditional LES approach, physical dissipation at the Kolmogorov scale is not represented. For spatially non-dissipative numerical schemes, without use of SGS models, this leads to an accumulation of energy at high mesh wave numbers, and ultimately to numerical instability. Explicitly added SGS models are then employed as a means to dissipate this energy.

In this study, the implicit LES (ILES) is used instead of SGS model. The ILES approach which any explicit sub-grid scale terms are not used while numerical viscosity (dissipation and dispersion) or high-order filtering procedure<sup>128–130</sup> are used to dissipate the small waves compared with grid size. As a result, reasonable energy spectra are obtained with the ILES approaches. In the present methodology, the effect of the smallest fluid structures is accounted for by an ILES technique, which has been successfully utilized for a number of turbulent and transitional computations, some of which will subsequently be described. The ILES approach is an alternative to conventional methodologies, and is predicated upon the high-order compact differencing and low-pass spatial filtering schemes, without the inclusion of additional SGS modeling. This technique is similar to monotonically integrated large-eddy simulation (MILES)<sup>131</sup> in that it relies upon the numerical solving procedure to provide the dissipation of upwinding scheme<sup>131–134</sup> that is typically supplied by traditional SGS models. Unlike MILES however, dissipation is contributed only at high spatial wave numbers where the solution is poorly resolved, by the aforementioned high-order Padé -type low-pass filter. This allows a mechanism for the turbulence energy to be dissipated at scales that cannot be accurately resolved on a given mesh system, in a fashion similar to sub-grid modeling. For purely laminar flows, filtering may be required to maintain numerical stability and preclude a transfer of energy to high-frequency spatial modes due to spurious numerical events. The ILES methodology thereby permits a seamless transition from large-eddy simulation to direct numerical simulation as the resolution is increased. In the ILES approach, the unfiltered governing equations may be employed, and the computational expense of evaluating sub-grid models, which can be substantial, is avoided. Therefore, ILES is sufficient stable and the computational cost is small compared with an explicit LES. The procedure, which uses unfiltered governing equations, also enables the unified simulation of flow-fields where laminar, transitional, and turbulent regions simultaneously coexist.

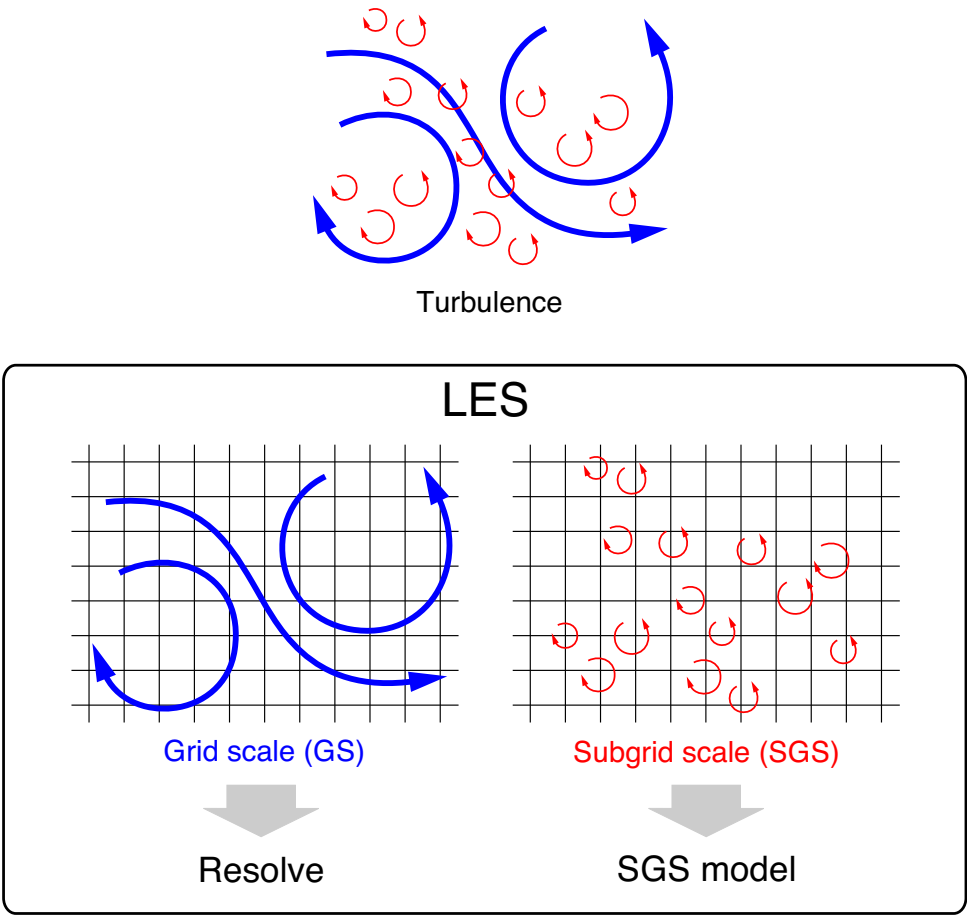


Figure 3.2: Concept of LES.

### 3.1.4 Computational Domain, Grid System, and Time Step Size

The zonal method<sup>135</sup> is employed to treat the small DBD plasma actuator region. Figure 3.3 shows the computational grids and coordinates, where the DBD plasma actuator model is applied at 0% or 15% chord length from the leading edge. Every four grid points in each direction are presented in this figure. The grids for ILES consist of two parts. The blue grid (Zone 1) is the grid for the flow around the airfoil and the red grid (Zone 2) is the fine grid for the flow around the DBD plasma actuator. Computation procedure consists of the following three steps. At first, the body force is calculated with Suzen model on the green grid (actuator grid) corresponding to the DBD plasma actuator model region. Then, the body force is mapped to the Zone 2 grid from the actuator grid. The Zone 1 is the C type grid and the length from the wing surface to the exterior boundary is 20 times chord length. The length of the computational region in span direction ( $y$ -direction) is 0.2. The numbers of grid points in the each case of different actuator location are shown in Table 3.4. The Zone 2 is overlapped with the Zone 1, and the flow variables are interpolated at the seven grid points on the edge of the Zone 2 from the Zone 1. In the same way, the flow variables are interpolated at the Zone 1 from the Zone 2 except the seven grid points of the edge. The computational time step is  $\Delta t = 5.0 \times 10^{-4}$  in non-dimensional time and the maximum Courant-Friedrichs-Lewy (CFL) number becomes approximately 20. With this  $\Delta t$ , the wall-unit criteria  $\Delta t^+$  is approximately 0.2, and this satisfies the criterion proposed by Choi.<sup>136</sup> At the outflow boundary, all variables are extrapolated from one point front of the outflow boundary. On the airfoil surface, no-slip conditions are adopted. Periodic boundary condition is applied to the spanwise boundaries and the flow variables of five grid points are directly exchanged without any interpolation.

### 3.1.5 Modeling of airfoil pitching motion

In this thesis, the airfoil dynamically rotates around its quarter-chord location from the leading edge with time. This pitching motion is modeled by the change in metrics with time; the grid rotates in a rigid manner. As aforementioned, the metrics are computed at every time step and this can be a model of the pitching motion.

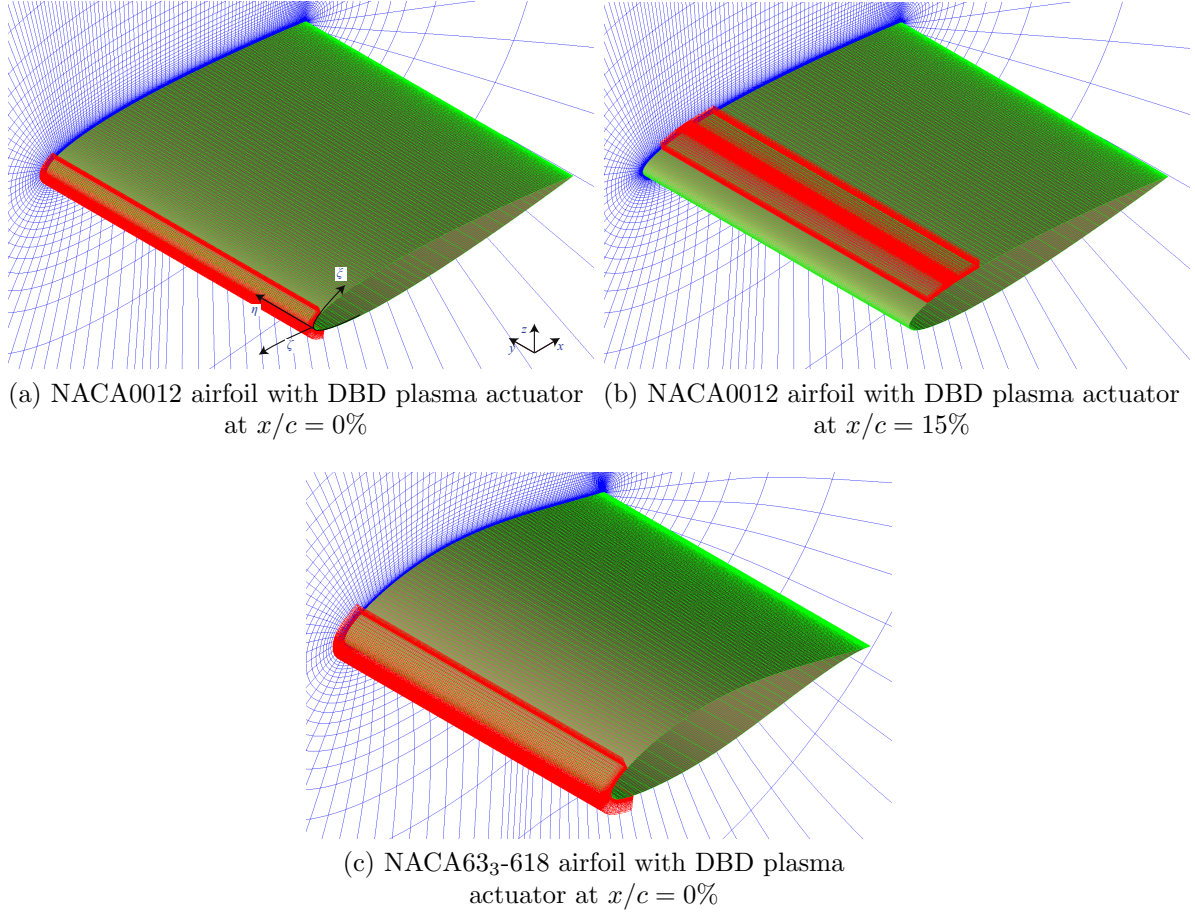


Figure 3.3: Computational grids. Every forth line is visualized here.

Table 3.4: Grid points.

DBD plasma actuator location	Zone 1 (for airfoil) ( $N_\xi \times N_\eta \times N_\zeta$ )	Zone 2 (for actuator) ( $N_\xi \times N_\eta \times N_\zeta$ )	Total Grid points
NACA0012 airfoil			
N/A	$680 \times 687 \times 205$	N/A	95,767,800
$x/c = 0\%$	$680 \times 687 \times 205$	$445 \times 687 \times 201$	157,216,515
$x/c = 15\%$	$680 \times 687 \times 205$	$441 \times 687 \times 201$	156,664,167
NACA63 <sub>3</sub> -618 airfoil			
N/A	$680 \times 687 \times 205$	N/A	95,767,800
$x/c = 0\%$	$680 \times 687 \times 205$	$445 \times 687 \times 201$	157,216,515

### 3.1.6 Boundary Conditions

In this subsection, the boundary conditions used in fluid analyses are explained.

#### Far-Fields Condition

Here the far-fields condition is explained. With regard to the condition at the second point of the boundary, two cases are switched. In this procedure, contra-variant velocity is used for the switching.

If the flow is going out from the computational domain, flow variables at far fields boundaries are fixed to the ambient condition as follows.

$$Q_{far-field} = Q_{\infty}. \quad (3.136)$$

If the flow is coming into computational domain, flow variables at the far field boundary are extrapolated from the inner computational domain except for the static pressure.

$$\begin{bmatrix} \rho \\ \rho u \\ \rho v \\ \rho w \\ e \end{bmatrix}_{far-field} = \begin{bmatrix} \rho|_{inner} \\ \rho u|_{inner} \\ \rho v|_{inner} \\ \rho w|_{inner} \\ \frac{p_{subsonic/supersonic}}{\gamma-1} + \frac{1}{2}\rho(u^2 + v^2 + w^2) \end{bmatrix}, \quad (3.137)$$

where  $p_{subsonic/supersonic}$  is switched on a local Mach number at second point of the boundary as follows,

$$p_{subsonic/supersonic} = \begin{cases} p_{\infty} & \text{flow is subsonic} \\ p_{inner} & \text{flow is supersonic.} \end{cases} \quad (3.138)$$

Basically, a local Mach number of the second point of the boundary is less than unity due to the buffer region as discussed below. In addition, the simple one-point first order extrapolation is used in Eq. 3.137.

With this boundary condition, non-physical waves, such as reflected waves, occurs. However, in this study grid-stretching is used in buffer region and unsteady motion of fluids and acoustics are dumped until these motion reaches to the boundary. The grid stretching ratio is decided with several a prior tests because very large grid stretching ratio may cause unphysical acoustic waves. (If we use even the more advanced methods, such as perfect matched layer<sup>137,138</sup> or absorbing layers<sup>139</sup> to dump the waves or vortices,

we must conduct a priori tests to avoid non-physical waves.<sup>140)</sup>

## Wall Condition

The wall condition is used at the synthetic jet and backward-facing step wall. There are many evaluation methods for a wall condition.<sup>141</sup> In this study, we adopt the wall condition proposed by Rizzi.<sup>142</sup>

Solid wall boundary at the surface of the body is treated as "non-slip" wall, and the velocity components at the wall are given as

$$u = x_\tau, v = y_\tau, w = z_\tau \quad (3.139)$$

where  $x_\tau$ ,  $y_\tau$  and  $z_\tau$  represent the velocities of the grid point at the wall. The density is extrapolated from an adjacent node,

$$\rho_{l=1} = \rho_{l=2} \quad (3.140)$$

Static pressure is defined from the equilibrium condition of the momentum normal to the wall ("normal momentum equation"),

$$\frac{\partial p}{\partial n} = -\rho \frac{u_\parallel^2}{R} \quad (3.141)$$

where  $n$  is the unit vector normal to the wall,  $u_\parallel$  is the velocity component parallel to the wall, and  $R$  is the radius of the curvature of the wall. Equation 3.141 is expressed in the generalized coordinate system as follows

$$A \frac{\partial p}{\partial \xi} + B \frac{\partial p}{\partial \eta} + \frac{\partial p}{\partial \zeta} = C \quad (3.142)$$

where



$$\begin{cases} A = \frac{1}{D}\xi_x\zeta_x + \xi_y\zeta_y + \xi_z\zeta_z \\ B = \frac{1}{D}\eta_x\zeta_x + \eta_y\zeta_y + \eta_z\zeta_z \\ C = \frac{1}{D}\left[\rho\left(\frac{\partial\zeta_t}{\partial\tau} + u\frac{\partial\zeta_x}{\partial\tau} + v\frac{\partial\zeta_y}{\partial\tau} + w\frac{\partial\zeta_z}{\partial\tau}\right) - \rho U\left(\zeta_x\frac{\partial u}{\partial\xi} + \zeta_y\frac{\partial v}{\partial\xi} + \zeta_z\frac{\partial w}{\partial\xi}\right) - \rho V\left(\zeta_x\frac{\partial u}{\partial\eta} + \zeta_y\frac{\partial v}{\partial\eta} + \zeta_z\frac{\partial w}{\partial\eta}\right)\right] \\ D = \zeta_x^2 + \zeta_y^2 + \zeta_z^2 \end{cases} \quad (3.143)$$

Here, the wall is  $\zeta = \text{const}$  plane. The first term of  $C$  in the right hand side of the equation 3.143 is the term due to accelerated motion and deformation of grid. In the present study,  $x_\tau$ ,  $y_\tau$  and  $z_\tau$  are calculated from Eq. . Unknown variables in the equation 3.141 are only differential terms of pressure, and pressure distribution over the flow field ( $l \geq 2$ ) is known. Second-order one sided differencing is applied to the difference operator in  $\zeta$  direction,

$$Ap_\xi + Bp_\eta + \frac{-p_{j,k,3} + 4p_{j,k,2} - 3p_{j,k,1}}{2\Delta\zeta} = C. \quad (3.144)$$

$\Longleftrightarrow$

$$-\frac{2\Delta\zeta}{3}(Ap_\xi + Bp_\eta) + p_{j,k,1} = -\frac{2}{3}\Delta\zeta\left(C - \frac{-p_{j,k,3} + 4p_{j,k,2}}{2\Delta\zeta}\right) \quad (3.145)$$

The following approximate factorization is applied to the operator in the left hand side of equation 3.145,

$$\left[I - \frac{2}{3}\Delta\zeta A\delta_\xi\right]\left[I - \frac{2}{3}\Delta\zeta B\delta_\eta\right]p_{j,k,1} = -\frac{2}{3}\Delta\zeta\left(C - \frac{-p_{j,k,3} + 4p_{j,k,2}}{2\Delta\zeta}\right) \quad (3.146)$$

where the difference operators in  $\xi$  and  $\eta$  directions are second-order central difference operators as

$$p_\xi = \frac{p_{j+1,k,1} - p_{j-1,k,1}}{2\Delta\xi}, p_\eta = \frac{p_{j,k,1+1} - p_{j,k,1-1}}{2\Delta\eta} \quad (3.147)$$

The tri-diagonal equation 3.146 can be solved by LU decomposition which is a kind

of direct methods through a sequence of operations, and pressure  $p_{j,k,1}$  on the wall is given then.

### Periodic Condition

The periodic conditions are used in the  $\eta(k)$  direction boundary. The ten points of the both sides are overlapped. Flow variables are exchanged as follows.

$$\begin{aligned}
 Q_{k=1} &\leftarrow Q_{k=k_{max}-9} \\
 Q_{k=2} &\leftarrow Q_{k=k_{max}-8} \\
 Q_{k=3} &\leftarrow Q_{k=k_{max}-7} \\
 Q_{k=4} &\leftarrow Q_{k=k_{max}-6} \\
 Q_{k=5} &\leftarrow Q_{k=k_{max}-5} \\
 Q_{k=6} &\rightarrow Q_{k=k_{max}-4} \\
 Q_{k=7} &\rightarrow Q_{k=k_{max}-3} \\
 Q_{k=8} &\rightarrow Q_{k=k_{max}-2} \\
 Q_{k=9} &\rightarrow Q_{k=k_{max}-1} \\
 Q_{k=10} &\rightarrow Q_{k=k_{max}}
 \end{aligned}$$

### Zonal Interface

On the Zone 2 , the flow variables at the ten grid points at the outer boundary are replaced with the variables of the Zone 1 as the boundary conditions with interpolations.<sup>135</sup> On the other hand, the flow variables at the inner grid points of the Zone 2 are sent to the corresponding grid points of the Zone 1, and the variables at the grid points of the Zone 1 are replaced with the high-accuracy solutions of the Zone 2. This procedure is used for each conservative value for suppressing numerical oscillations per each time steps (including per each sub-iterations of inner iteration ).

## 3.2 DBD Plasma Actuator Modeling

The momentum addition by the plasma discharge to fluid can be introduced to the fluid governing equations as a body force. Some DBD plasma actuator models are proposed to couple the plasma effect with fluid governing equations. Shyy et al.<sup>143</sup> propose a most simple model. They assume the body force distribution as a triangle shape. Corke et al.<sup>144,145</sup> They model discharge of the DBD plasma actuator as capacitors of electric circuit.

In this study, DBD plasma actuator is introduced as a body force to Navier-Stokes equations. The body force is obtained by a model designed by Suzen and Huang (S-H model),<sup>146–149</sup> which is relatively simple but physically-based model.

### 3.2.1 Suzne and Huang Model

The working principle of the S-H model stems from the splitting of the electric potential into two governing modes; one describing the effects of electric field and the other characterizing the effects of surface charge density.

The S-H model studied the implication of splitting the total electric potential term ( $\Phi$ ) into two parts: one being influenced by external electric field ( $\varphi$ ), and the other potential affected by the net charge density ( $\phi$ ).

$$\nabla \cdot (\epsilon_r \nabla \phi) = 0, \quad (3.148)$$

$$\nabla \cdot (\epsilon_r \nabla \varphi) = \rho_c / \epsilon_0, \quad (3.149)$$

where  $\epsilon_0$  is the vacuum permittivity,  $\epsilon_r$  is the relative permittivity, and  $\rho_c$  is the surface charge potential.

The net charge density potential ( $\varphi$ ) can be eliminated by utilizing the Debye length ( $\lambda_D$ ) which relates  $\varphi$  to  $\rho_c$  through

$$\rho_c / \epsilon_0 = (-1 / \lambda_D^2) \varphi, \quad (3.150)$$

which combined with Eq. 3.149 yields

$$\nabla \cdot (\epsilon_r \nabla \rho_c) = (\rho_c / \lambda_D^2). \quad (3.151)$$

Thus, the model consists of solving Eqs. 3.148 and 3.151 with suitable boundary conditions. Finally, the Lorentz body force which is used in the Navier-Stokes equations

is obtained through

$$F_b = \rho_c(-\nabla\phi). \quad (3.152)$$

The two equations (Eqs. (3.148) and (3.151) above) defining the electric field potential ( $\phi$ ) and the surface charge potential ( $\rho_c$ ) can be solved initially before the Navier-Stokes equation as these equations do not contain a time derivative term.

### 3.2.2 Coupling with Fluid Governing Equations

In the non-dimensional form, governing equations with the source terms of DBD plasma actuator are represented as follows:

$$\frac{\partial \rho}{\partial t} + \frac{\partial \rho u_k}{\partial x_k} = 0 \quad (3.153)$$

$$\frac{\partial \rho u_i}{\partial t} + \frac{\partial (\rho u_i u_k + p \delta_{ik})}{\partial x_k} = \frac{1}{Re} \frac{\partial \tau_{ik}}{\partial x_k} + D_c F_{bi} \quad (3.154)$$

$$\frac{\partial e}{\partial t} + \frac{\partial ((e+p)u_k)}{\partial x_k} = \frac{1}{Re} \frac{\partial u_l \tau_{kl}}{\partial x_k} + \frac{1}{(\gamma-1)PrReM_\infty^2} \frac{\partial q_k}{\partial x_k} + D_c u_k F_{bk} \quad (3.155)$$

In Eq. (3.154), (3.155),  $D_c F_{bi}$  term and  $D_c u_k F_{bk}$  term represent the momentum and energy provided by plasma actuator.

The body force  $F_{bi}$  induced by the DBD plasma actuator is obtained by Eq. (3.152)  $D_c$  is the non-dimensional number relating to the electromagnetic force, and determines the magnitude of the body force. In this study,  $F_{bi}$  is determined by S-H model on the steady boundary condition, and unsteadiness is added simply as follow;

$$F_{bi} = F_{bmax,i} \sin^2(2\pi f_{base} t) \quad (3.156)$$

where  $F_{bmax,i}$  is calculated by the S-H model when the exposed electrode potential is positive constant value and insulated electrode potential is zero. The value of  $D_c$  is determined so that the induced velocity is close to the induced velocity in the experiment. The consideration on  $D_c$  will be presented in each Chapter.

The instantaneous force vector distribution of S-H model is shown in Fig. 3.4. Contour surface is body force magnitude and yellow vectors show body force direction. The two white lines are the electrodes.

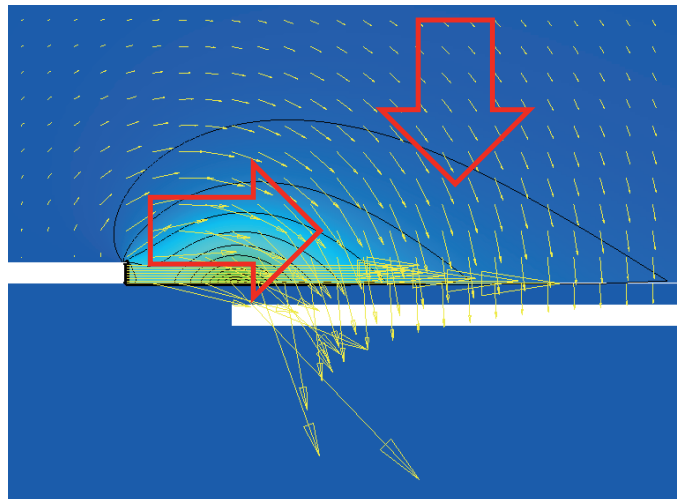


Figure 3.4: Force vectors obtained by the Suzen-Huang model.

### 3.3 Data Processing

#### 3.3.1 Data acquisition

Calculations for the cases without flow control is initiated with all the grid points have uniform distribution of physical quantities with of freestream at  $tu_\infty/c = 0$ . The example of the history of an aerodynamic performance is presented in Figure 3.5. In this figure, the curves during the 1st, 2nd, and 3rd pitching cycle are depicted. Here, the origin is reset to 0 for each cycle in this figure. At the initial stage of the computation, the computational results are discarded until before the effect of the impulsive start of the computation diminishes. The duration until the effect of the impulsive start of the computation diminishes is, approximately  $10tu_\infty/c$  under the current configuration, as seen by the aerodynamic performance come to on the 2nd and 3rd pitching values. After this, the data acquisition is began and used to be analysis.

With regard to the cases with flow control, the computation starts from the flowfield without flow control at  $35tu_\infty/c$ . The flowfield in this time is in the stalled state, and the control effect does not much appears to the flowfield. The data acquisition start from  $50tu_\infty/c$ .

The phase-averaged value in the current study comprises two cycles of the pitching motion. Therefore, calculations are continued until the acquired data duration reaches two cycles. All the phase-averaged values are also averaged in the spanwise direction.

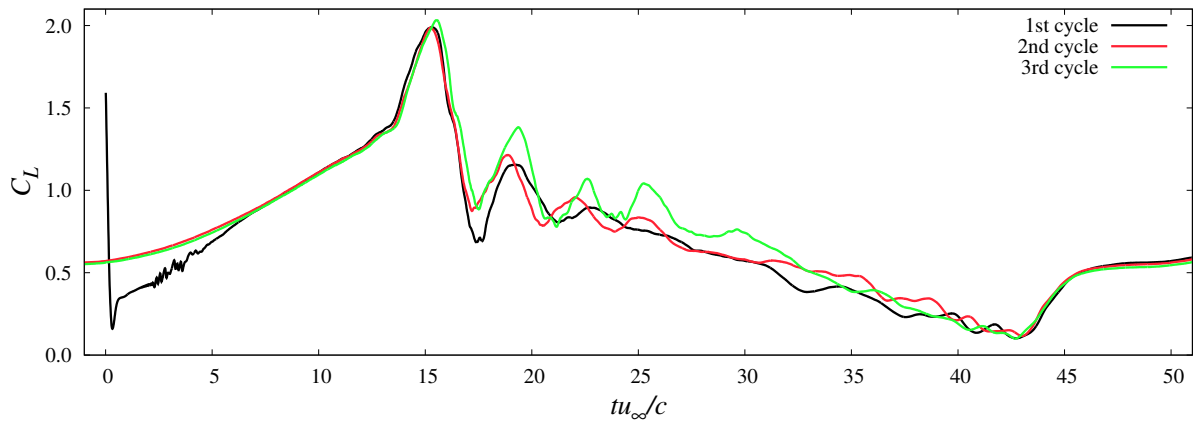


Figure 3.5: Example of time history of aerodynamic performance from the start of the computation.

### 3.3.2 Phase-averaging

To draw the phase-averaged flowfield, the acquired flowfield data are phase-averaged. The pitching cycle is divided into  $N$  phases and the instantaneous data is sorted into this  $N$  phases. Then the data in each phase is averaged to comprise the phase-averaged data. In the current research,  $N$  is set as 180. Each instantaneous data is sorted into  $i$ th phase according its  $AoA$ ; the instantaneous data is sorted into  $i$ th phase if its  $AoA$  satisfies the following relation.

$$\alpha_{min} + \alpha_{amp}(1 - \cos(2\pi i/N)) - \alpha_{tol} \leq \alpha < \alpha_{min} + \alpha_{amp}(1 - \cos(2\pi i/N)) + \alpha_{tol}, i = 1, \dots, N \quad (3.157)$$

where  $\alpha_{min}$ ,  $\alpha_{amp}$  are the minimum  $AoA$  and the pitching amplitude, and so these are respectively  $5^\circ$  and  $10^\circ$ .  $\alpha_{tol}$  is the tolerance for  $AoA$  range and is set to  $0.5^\circ$ .





# Chapter 4

## Verification and validation

### 4.1 Outline

In the current research, verification and validation of the computational method are conducted. The flowfield used for the verification and validation is the dynamic flowfield around a pitching NACA0012 airfoil under the baseline flow conditions.

The validation of modeling of the DBD plasma actuator is conducted on the reference,<sup>150</sup> and is not addressed in this research.

### 4.2 Validation and verification of spanwise length

With regard to the flowfield in post-stall regime, visualizations of the stalled flowfield around a sufficiently spanwise-long wing revealed the existence of a spanwise cellular pattern with narrow attached regions between the separated cells<sup>151,152</sup> (called as a “stall cell”). Yon et al. investigated the unsteady behaviour of the flowfield with stall cells and they suggested that the interaction between the airfoil surface and the leading edge and trailing edge shear layers is responsible for the low-frequency fluctuations of the flowfield.<sup>152</sup>

With regard to such stall-cell-like spanwise structure, sufficient large spanwise computational domain is required to resolve the spanwise-distributed flow structures. Validation study of the spanwise length is conducted by Almutairi et al.<sup>153</sup> and they concludes that the spanwise length of 50% of the chord length is sufficient while Eisenbach et al.<sup>154</sup> reported the spanwise length of 100% length of the chord is necessary. The common opinion among those references is that, the flow has no physical space to develop its structures with insufficient spanwise length. Frère et al.<sup>155</sup> suggested the importance

to address the spanwise length in order to clarify the importance of the stall-cell like three dimensional structure. Considering that the dynamicity or the time-scale of the flow structure become more important in dynamic flowfields, it is surely important to address the sufficient spanwise length to resolve the spanwise structures. The importance of this spanwise length can be seen in the papers in which comparison of the CFD results with experimental results is conducted;<sup>156,157</sup> these paper show that there are significant inconsistencies between the LES. These CFD results have the same features that the aerodynamic forces show good agreement before dynamic stall, however, show unanticipated oscillation after dynamic stall which is not observed in experimental results. As is not mentioned in their report, but it would be possible to be said that these discrepancies come from the shortage of the spanwise length. The same characteristics are observed also in the preliminary study of the current research and later it is clarified that the discrepancies are mainly due to the shortage of the spanwise length, as presented in this chapter.

In the current research, to address the sufficient spanwise length for LES on dynamic flowfields, verification and validation of the spanwise length is conducted by comparing the LES result and the experimental result.<sup>2</sup> First, preliminary considerations on the spanwise length is conducted on a stationary flowfield. Then the validation of the spanwise length and verification on a dynamic flowfield is conducted.

The computational grid used in the validation study of the spanwise length is listed in Table 4.1. The spanwise length is varied by the cases.

Not presented here, but preliminary studies are also conducted to investigate the effect of freestream Mach number and sub-grid scale model. The results are that the choice of freestream Mach number of 0.2 and ILES is reasonable for the current research.

### 4.2.1 Verification of spanwise length on stationary flowfield

The results for the stationary flowfields at  $AoA$  of  $10^\circ$ , and then at  $25^\circ$  are presented in this order.

#### Stationary cases at $AoA$ of $10^\circ$

Figure 4.1 shows the surface pressure coefficient  $C_p$  and friction coefficient  $C_f$  distributions for time- and span-averaged flowfields of the stationary cases at  $AoA$  of  $10^\circ$ . From this figure, no significant difference is observed. At this  $AoA$ , the flow separates near the leading edge and soon reattaches at approximately  $x/c = 9\%$  as observed in the  $C_f$  distribution. The region between the separation point and reattachment point corresponds

Table 4.1: Grids used for verification of spanwise length

Case name	Spanwise length (relative to the chord length)	Grid points ( $N_\xi \times N_\eta \times N_\zeta$ )
Stationary cases		
S0.2c	0.2	$680 \times 154 \times 205$
S1.0c	1.0	$680 \times 687 \times 205$
S5.0c	5.0	$680 \times 3354 \times 205$
Dynamic cases		
D0.2c	0.2	$680 \times 154 \times 205$
D1.0c	1.0	$680 \times 687 \times 205$
D2.0c	2.0	$680 \times 1354 \times 205$

Table 4.2:  $C_L$  for the stationary flowfield at  $AoA$  of  $10^\circ$ .

Case name	average of $C_L$	standard deviation of $C_L$
S0.2c	0.945	$2.83 \times 10^{-3}$
S1.0c	0.947	$1.35 \times 10^{-3}$

to LSB, as observed in Figure 4.2 which depicts the time- and span-averaged chordwise velocity field.

The time- and span-averaged lift coefficients  $C_L$  and its standard deviation are summarized in Table 4.2. Here, the average duration is  $tu_\infty/c = 15$  after calculation is steadied down. From the time-averaged values, spanwise length effect is not obviously observed in the averaged  $C_L$  whereas the unsteady  $C_L$  deviation is a little low in the longer spanwise length case. To investigate this, the autocorrelation is calculated. Figure 4.3 shows the spanwise autocorrelation  $R$  of chordwise velocity at a selected sampling point inside LSB. The spanwise distributions of the autocorrelation are almost the same with each other case. This result suggests that the spanwise length of approximately  $0.02c$  is sufficient, for the spanwise distance where the autocorrelation becomes zero is approximately  $0.01c$ . This suggests that the reason that the unsteady  $C_L$  deviation decreases as the spanwise length increases is just an increase of the amount of the spatial sample.

### Stationary cases at $AoA$ of $25^\circ$

Next presented are the results of the stationary flowfields at  $AoA$  of  $25^\circ$ . Figure 4.4 provides the time- and span-averaged chordwise velocity flowfields in the quasi-steady

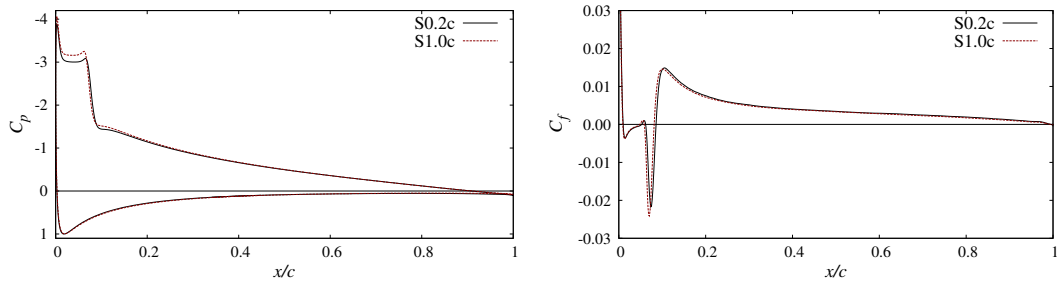


Figure 4.1:  $C_p$  and  $C_f$  distributions for the stationary flowfields at  $AoA$  of  $10^\circ$ .

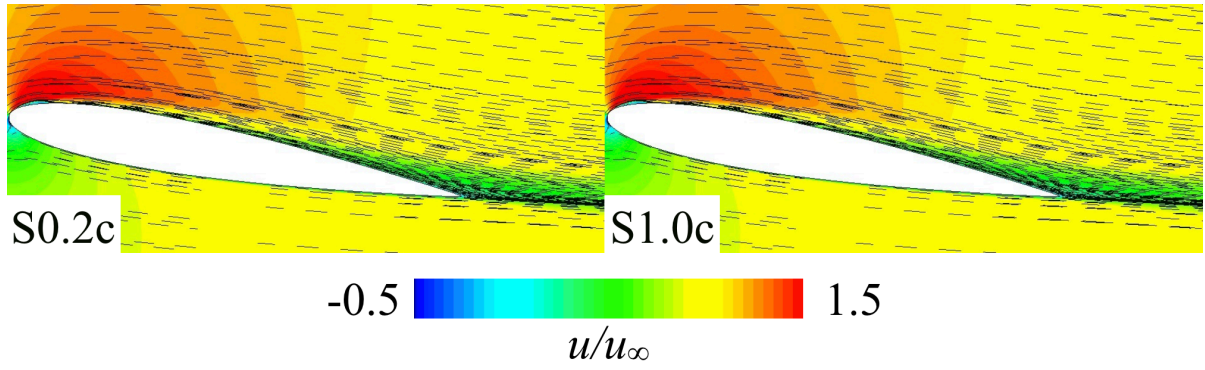


Figure 4.2: Time- and span-averaged chordwise velocity flowfields for the stationary cases at  $AoA$  of  $10^\circ$ .

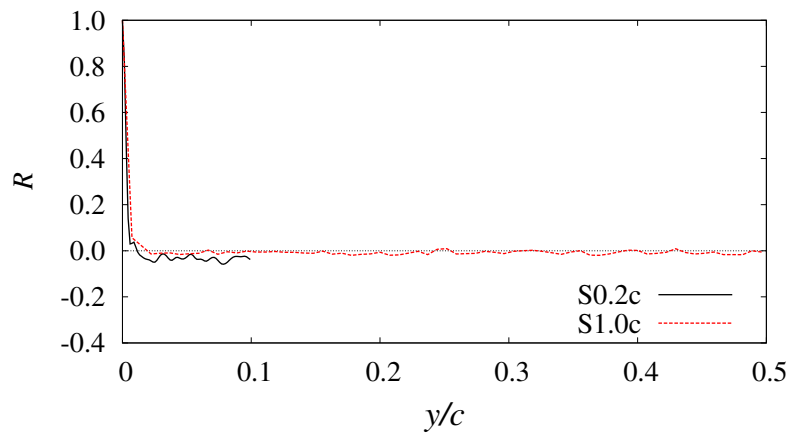


Figure 4.3: Autocorrelation of chordwise velocity for the stationary cases at  $AoA$  of  $10^\circ$ .

state and Figure 4.5 presents the time history of the lift coefficient  $C_L$  in the quasi-steady state. Here the time axis in Figure 4.5 is scaled properly but not coordinated because the time for flow to reach quasi-steady state differs from case by case, as mentioned later. Comparing the cases, a large discrepancy is observed; full-stalled flowfield is observed for the case of S1.0c and S5.0c whereas the flowfield for the case of S0.2c seems to separate from leading-edge and reattach near the trailing edge. Figure 4.4 also shows a large discrepancy as observed by the contrast between the steadied down  $C_L$  in the case of S1.0c and S5.0c and the highly oscillating  $C_L$  in the case of S0.2c.

To investigate this phenomena, Figure 4.6 presents the time history of  $C_L$  in the early stage of the computation. As aforementioned, the calculation is initiated with all the grid points have uniform distribution of physical quantities with of freestream at  $tu_\infty/c = 0$ .  $AoA$  is fixed to  $25^\circ$ , and thus a unphysical large vortex is formed from the leading edge as soon as the computation begins. The large oscillation in  $C_L$  observed in Figure 4.5 is now observed in all the cases. In the cases with longer spanwise length, however, the aerodynamic effects by these large vortices gradually decreases. The transient flowfields of the case of S1.0c in the early stage of the computation are shown in Figure 4.7. First, a large vortex is formed from the leading edge, whose formation is due to the impulsive start of the computation. Then the large vortex convect toward the downstream. When the large vortex come close to the trailing edge, a large trailing vortex is induced. The final subfigure shows the formation of the other large leading vortex. This formation and convection of the large vortices from the leading edge and the trailing edge is repeated some times until the flowfield steadies down. Now it can be said that the large oscillation in  $C_L$  is caused by the continuous formation and convection of large vortices. In the longer spanwise length cases, the amplitude of the oscillation in  $C_L$  gradually decreases as the repeated times. Here it can be said that the large  $C_L$  oscillation for the case of S0.2c in the quasi-steady state observed in Figure 4.5 is due to the not-steadied-down repeated convection and formation of the large vortices.

### Spanwise length effects

The flowfield and aerodynamic performances showed large differences between the cases with different spanwise length. Here, the phenomena of the spanwise length effects are discussed. Quantitative analyses such as spatial autocorrelation analysis which is often employed to discuss the spatial coherency are very sensitive to the sample position.<sup>158</sup> Due to many difficulties of quantitative analyses, current study is conducted through discussing on the results of the qualitative investigations.

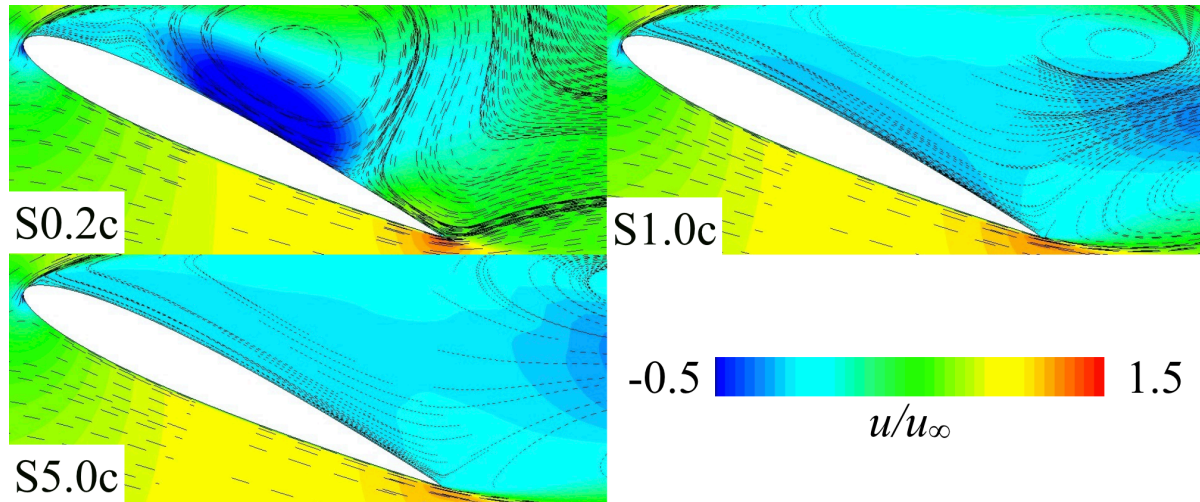


Figure 4.4: Time- and span-averaged chordwise velocity flowfield for the stationary cases at  $AoA$  of  $25^\circ$ .

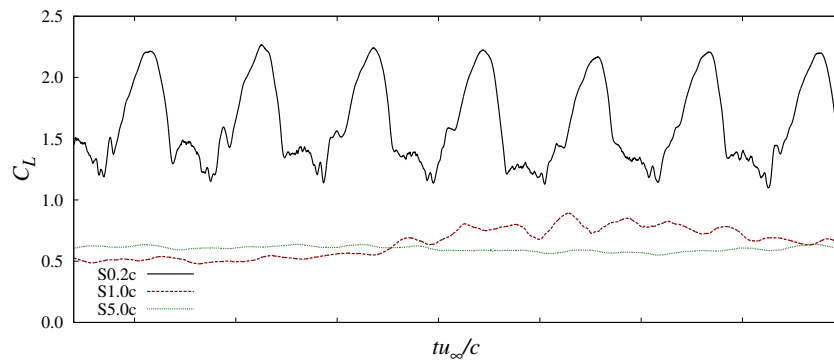


Figure 4.5: Temporal development of  $C_L$  in the quasi-steady state for the stationary cases at  $AoA$  of  $25^\circ$ .

Tics for horizontal axis is for  $t u_\infty/c$  of 5.

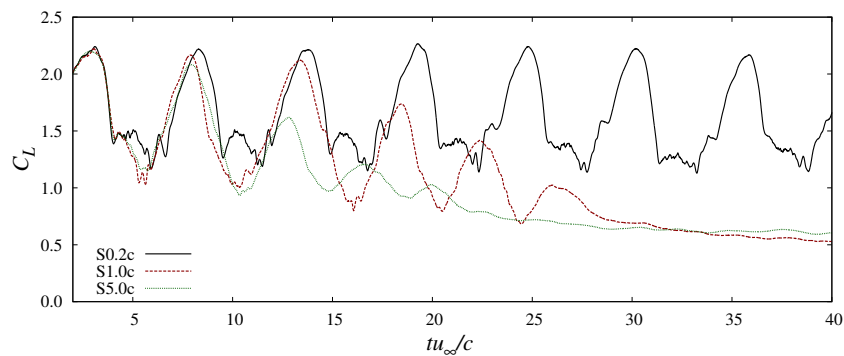


Figure 4.6: Temporal development of  $C_L$  in the early stage of the computation for the stationary cases at  $AoA$  of  $25^\circ$ .



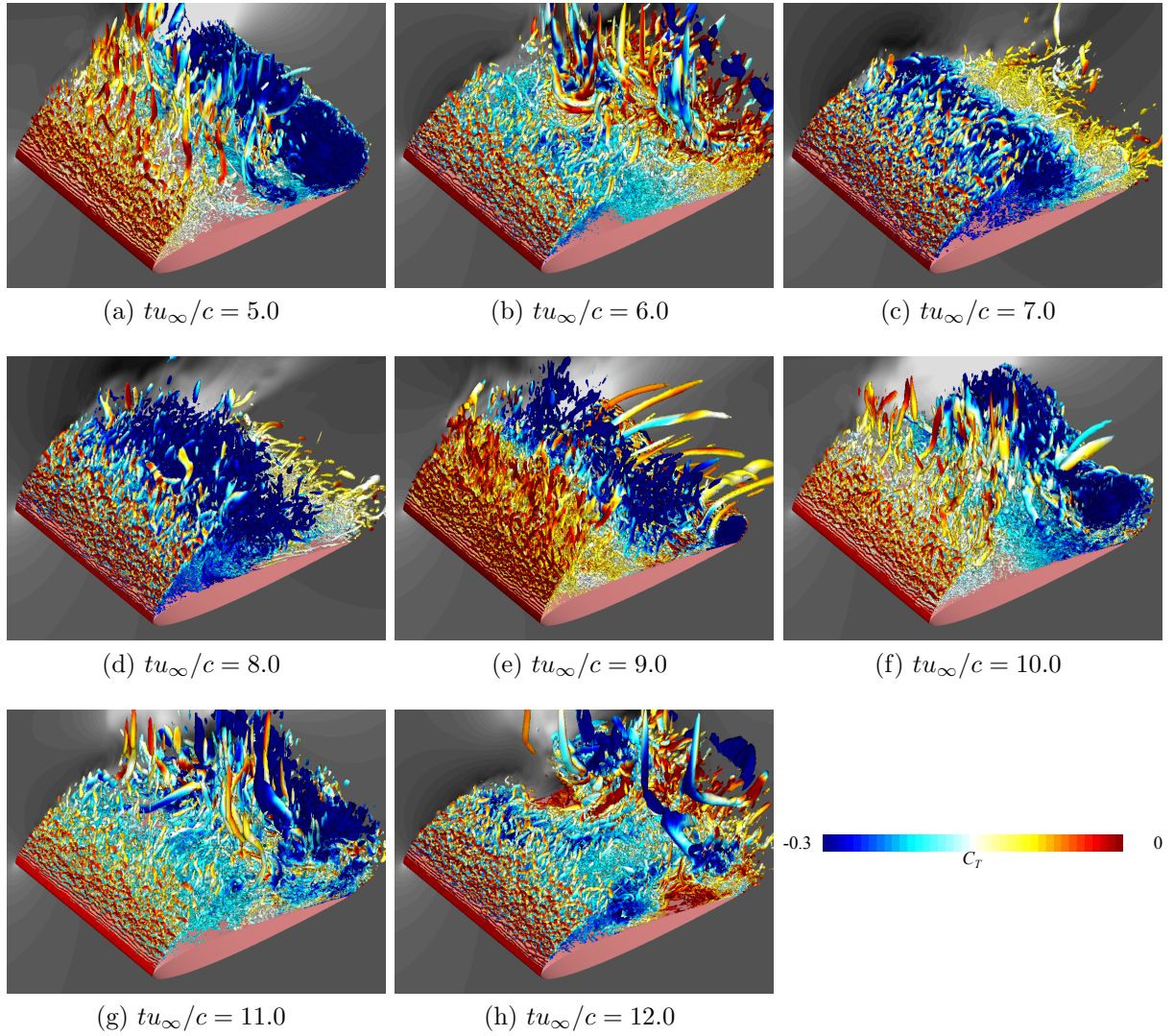


Figure 4.7: Snapshots of instantaneous flowfield for stationary flowfield at  $25^\circ$ . The iso-surfaces indicate the second invariant of the velocity gradient tensor colored by total pressure coefficient.

The references in that spanwise length effects are discussed have common remarks that the spanwise length is important in resolving the relatively long-scaled flow structure in spanwise direction.<sup>153–155,159,160</sup> The long flow structure in spanwise direction with spanwise distribution decays the coherence of the spanwise-axised vortex and so whether if such the structure can be resolved might be the point of the argument. To investigate this, Figure 4.8 depicts the snapshots of the instantaneous isosurface of total-pressure coefficient  $C_T$  colored by wall-normal vorticity from front of the airfoil with the chord direction. The subfigures in Figure 4.8 depict (a)formation of leading edge vortex, (b)formation of trailing edge vortex, and (c)formation of secondary vortices which follow on the interaction of the leading edge vortex and the trailing edge vortex. The case of S0.2c exhibits no clear spanwise structure or undulation of large vortices for all the instants. The case of S1.0c and S5.0c, on the other hand, the leading edge vortex and trailing edge vortex show themselves undulating as soon as they organize. As for the secondary vortices, they organize intermittently in spanwise direction. Investigating qualitatively, the undulation of both leading edge vortex and trailing edge vortex has spanwise wavelength of approximately  $1.0c$  and  $2.5c$  for the case of S1.0c and S5.0c respectively. As for the secondary vortices, the intermittent interval is approximately  $0.5c$  for the case of S1.0c. For the case of S5.0c, the intermittent interval is observed not uniformly in spanwise direction, as observed in Figure 4.8(c). These difference between the case of S1.0c and S5.0c suggests some phenomena are not resolved even in the case of S1.0c. However,  $C_L$  for the case of S1.0c and S5.0c shows a little difference in time-averaged value but a good agreement generally. In this point of view, spanwise length of  $1.0c$  is sufficient to evaluate the aerodynamic performances. Above investigations suggest that spanwise length of  $1.0c$  cannot resolve some phenomena, however, it is not necessary to have the spanwise length to resolve the whole physical phenomena in order to estimate aerodynamic performances.

### 4.2.2 Validation and verification of spanwise length on dynamic flowfield

In the stationary flowfields, the effects of spanwise length is observed as the extent of the attenuation of the large vortices. For dynamic flowfields, such attenuation are more important than for stationary flowfields considering the attenuation of the vortices directly affect the time scale of the flowfield.



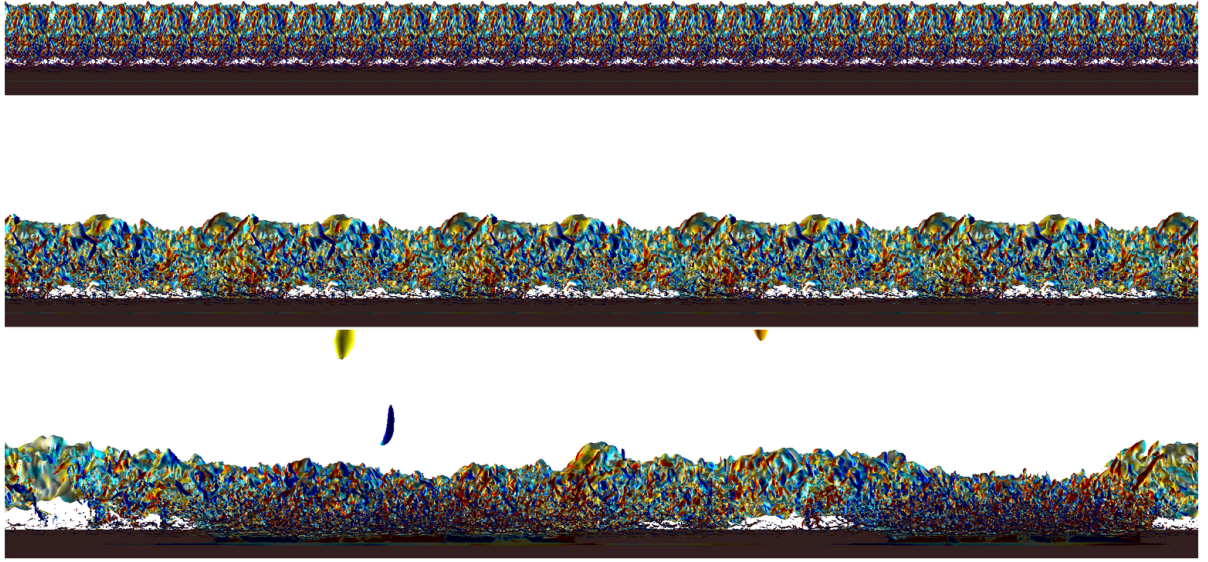
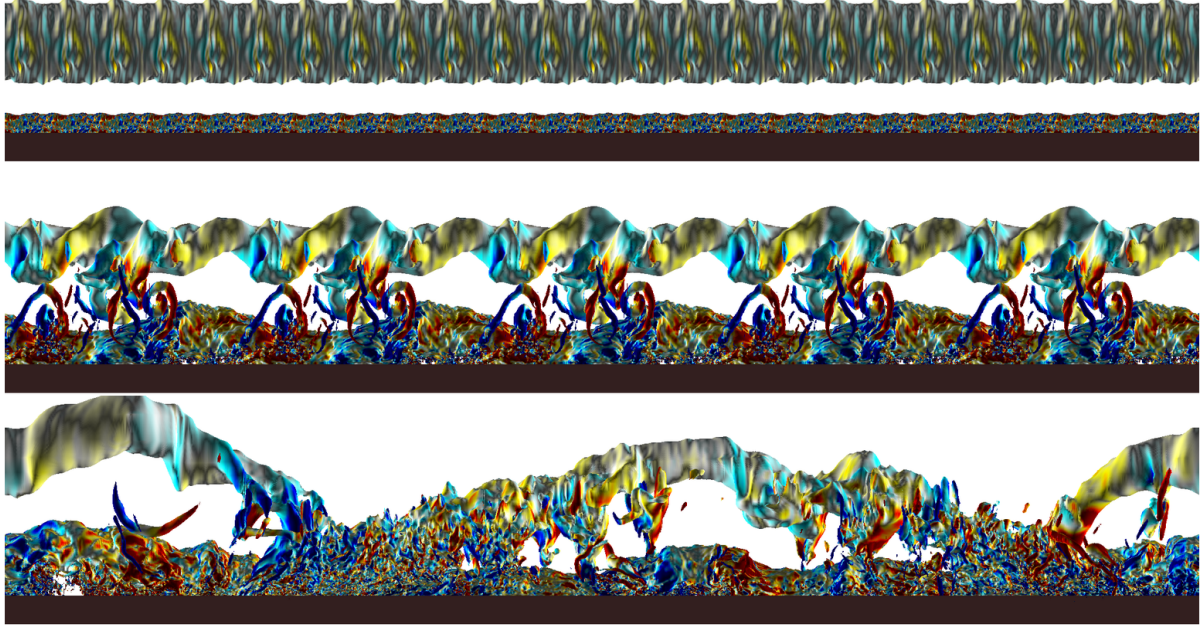
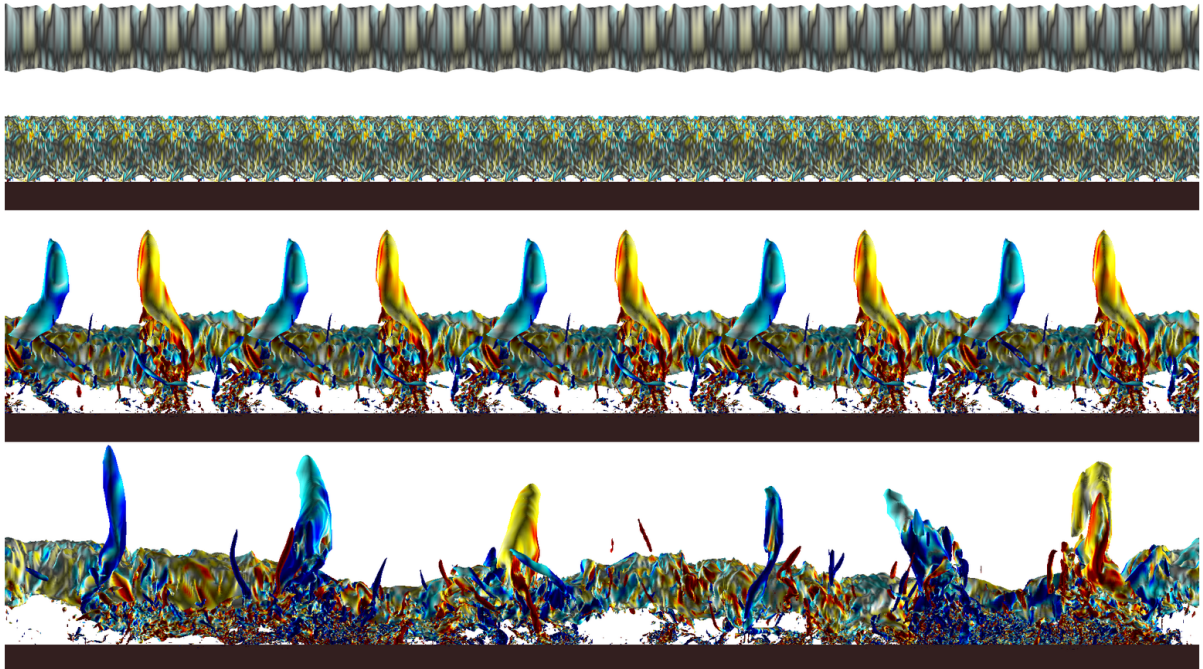
(a) Formation of leading edge vortex( $tu_{\infty}/c=7.7$ )

Figure 4.8: Snapshots of instantaneous flowfields for the stationary cases at  $AoA$  of  $25^\circ$ . Isosurface of total-pressure colored by wall-normal vorticity is depicted from the chord-wise view direction. For the case of S0.2c and S1.0c, flowfield is duplicated periodically for the comparison with the case of S5.0c. Every 5 point of LES calculation grid is visualized here.

From top to bottom: S0.2, S1.0c and S5.0c.



(b) Formation of trailing edge vortex ( $tu_\infty/c = 9.8$ ). A vortex near the airfoil surface is trailing edge vortex, and the other large vortex is highly deformed leading edge vortex.



(c) Formation of the secondary vortices ( $tu_\infty/c = 11.2$ ). Trailing edge vortex is also observed in back of the secondary vortices.

Figure 4.8: *Continued.*

### Phase-averaged flowfield and aerodynamic forces

Figure 4.9 presents the phase- and span-averaged aerodynamic performances; lift coefficient  $C_L$ , drag coefficient  $C_D$ , and moment coefficient  $C_M$  against the pitching  $AoA$ . The black solid line is the experimental result from the reference.<sup>2</sup> The phase- and span-averaged chordwise velocity field is depicted in Figure 4.10 for the selected phases. As discussed in the reference, general dynamic-stall process can be described as follows. (a) Flow separates from the leading edge and an LSB is formed near the leading edge ( $AoA \lesssim 15^\circ$ ). (b) Above an  $AoA$  ( $\sim 12^\circ$ ), the LSB breaks down into a consequent dynamic stall vortex (DSV), producing large aerodynamic force as seen in rapid increase/decrease in the aerodynamic performances. (c) Once a DSV is formed, the DSV convects toward trailing edge. (d) After the DSV sheds into the wake, the flow above the airfoil is of full-stall ( $AoA \gtrsim 24^\circ$ ). (e) As  $AoA$  becomes low, the flow begin to reattach near the leading edge ( $AoA \sim 9^\circ$ ). The detailed description of the flowfield will be given the next chapter. Above description is applicable to the LES results for the cases of D1.0c and D2.0c in Figure 4.9 and 4.10. On the other hand, the results of the case of D0.2c after dynamic stall are very different from these of the cases of D1.0c and D2.0c. The first difference is that of the peak value of the aerodynamic forces at the moment of dynamic stall process. The second difference is the large oscillation of the aerodynamic forces after dynamic stall. Similar to the case of S0.2c, the flowfield of D0.2c after dynamic stall is characterized by the repeated formation and shedding of large vortices from the leading edge and the trailing edge.

Here, validation of the LES results is conducted by comparing the LES results with the experimental results. The small  $C_L$  fluctuations during the pitching down are somewhat overpredicted in the LES result and the mean value of  $C_L$  during the pitching down show significant difference with that of the experiment. In spite of the discrepancies, the LES results successfully evaluate the aerodynamic performances well. Considering that  $AoA$  at which dynamic stall occurs is sensitive in this Reynolds number regime, this comparison shows that our computational code is capable of predicting the dynamic stall angle.

### Spanwise length effects

The flowfields of D0.2c and S0.2c are similar to each other as exhibiting large oscillations in aerodynamic forces. Here the same visualizations with Figure 4.8 for the dynamic cases are presented in Figure 4.11. The undulation of leading edge vortex and trailing edge vortex has spanwise wavelength that corresponds to the spanwise domain length

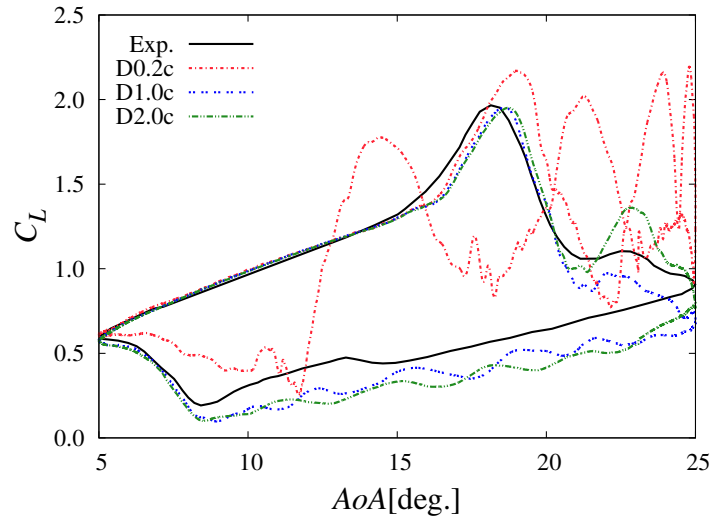
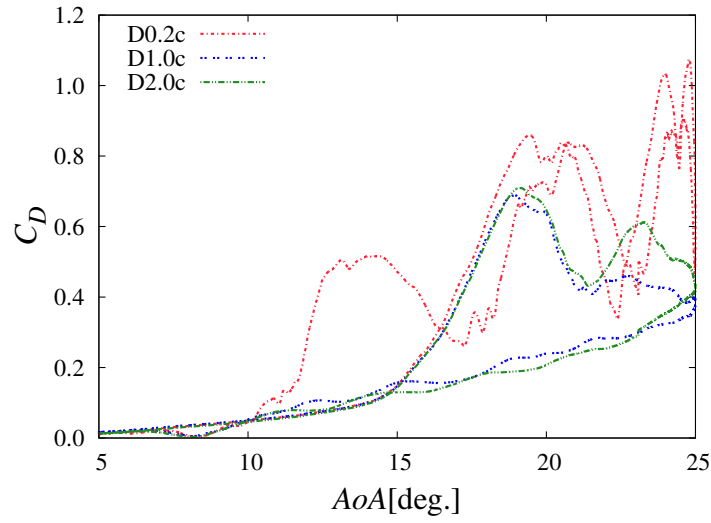
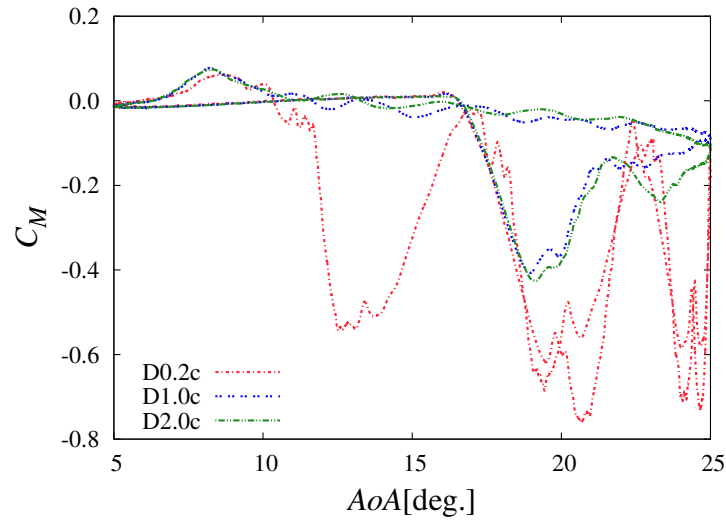
(a)  $C_L$ (b)  $C_D$ (c)  $C_M$ 

Figure 4.9:  $C_L$ ,  $C_D$ , and  $C_M$  against the pitching angle for the dynamic cases. The experimental result<sup>2</sup> is plotted in the  $C_L$  plot.



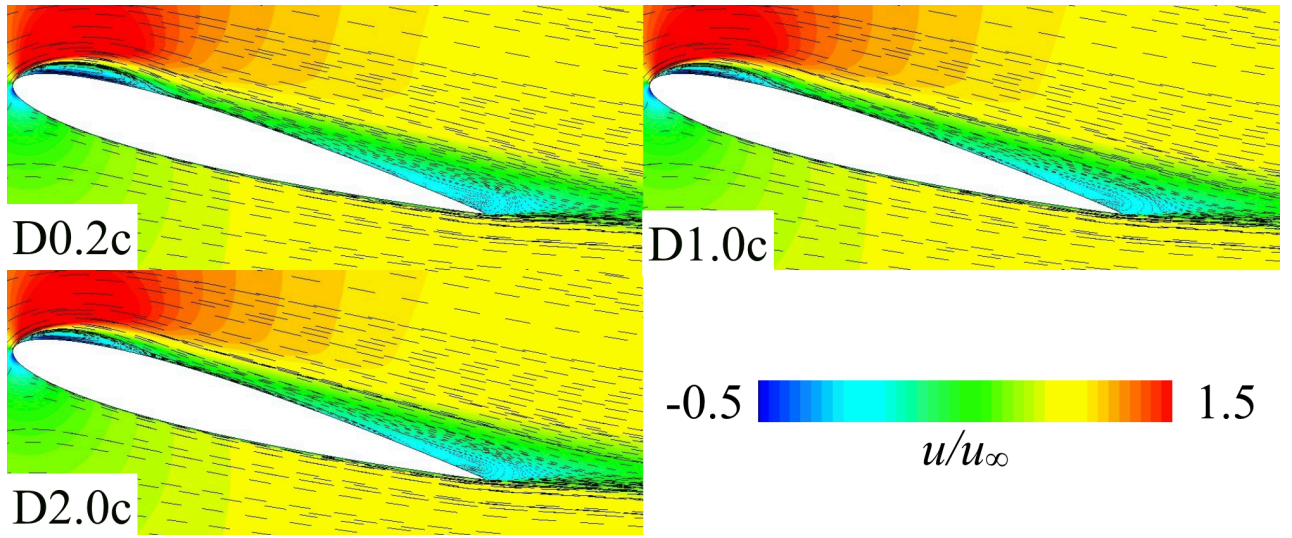
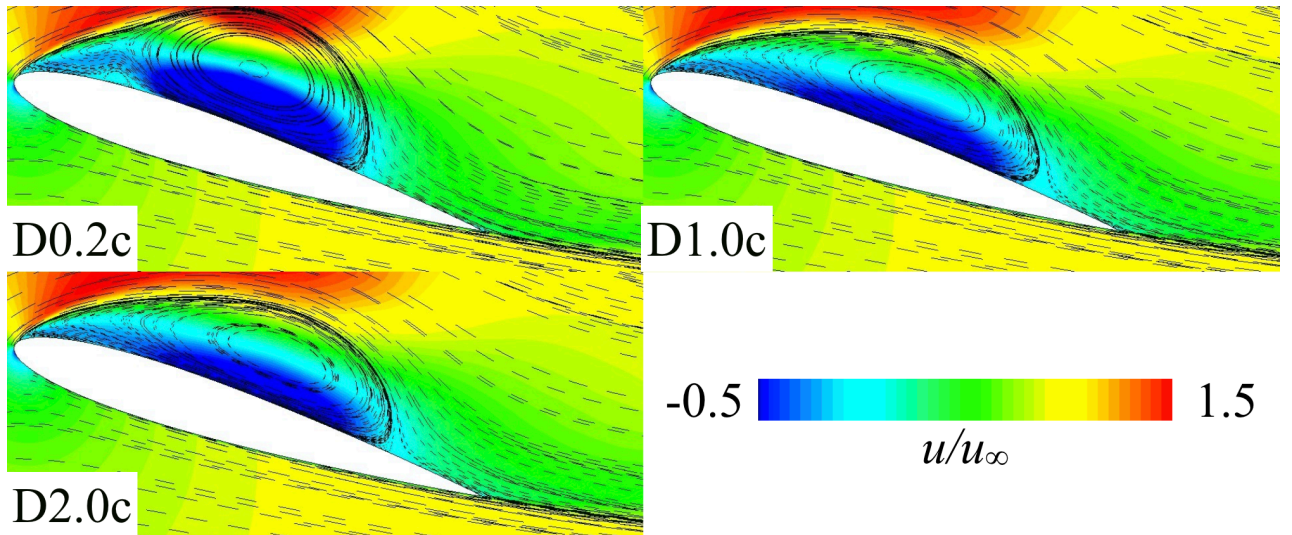
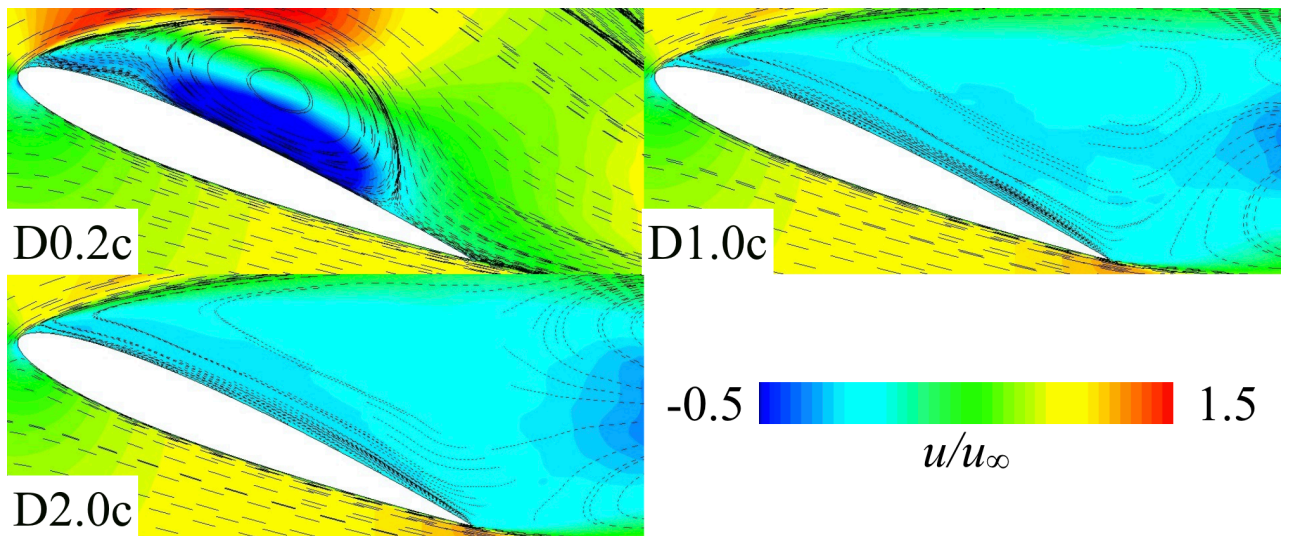
(a)  $AoA = 15.2^\circ$  (pitching up)(b)  $AoA = 17.6^\circ$  (pitching up)(c)  $AoA = 22.2^\circ$  (pitching down)

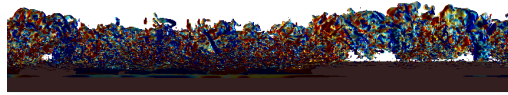
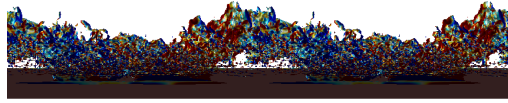
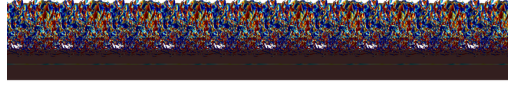
Figure 4.10: Phase- and span-averaged chordwise velocity flowfield for the dynamic cases.

of each case. As for the secondary vortices, the intermittent formation of the secondary vortices has the interval of the same with the spanwise length of each dynamic case. These results suggest that all the cases does not fully resolve the phenomena of the undulation of leading edge vortex and trailing edge vortex nor the formation of the secondary vortices because the length scale is restricted to the computational spanwise domain length. Considering the  $C_L$  curve of the case of D1.0c shows good agreement with the experimental result, the intermittent interval seems to have less significant effects on the aerodynamic forces or their attenuation. Then comparing the case of D0.2c and the cases of D1.0c and D2.0c, which are the cases with or without the large oscillation in aerodynamic forces, the undulation of leading edge vortex and trailing edge vortex is the difference between the cases. Here it is assumed that the key flow structure is the undulation of these large vortices and that the spanwise length should have the sufficient length enough to resolve the undulation with regard to the estimation of the aerodynamic forces.

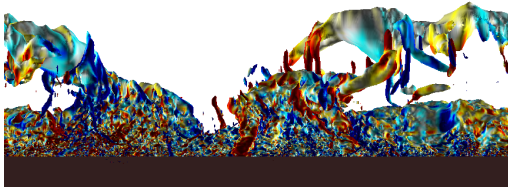
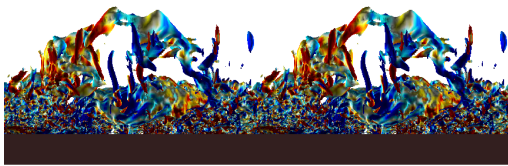
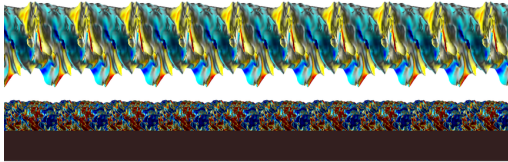
### 4.2.3 Discussions

By investigating the flowfields of the stationary and dynamic cases, two thresholds for the spanwise length is suggested. The first threshold is the spanwise length with which the undulation of leading edge vortex and trailing edge vortex can simply organize, and the second is the spanwise length with which the undulation of leading edge vortex and trailing edge vortex can organize with its physical ( natural ) length scale. Under the current flow conditions in this study, the first threshold is between the spanwise length of  $0.2c$  and  $1.0c$ , and the second threshold is between  $1.0c$  and  $5.0c$ . Note that these thresholds would depend on the flow conditions and airfoils. In the current study, the spanwise length effects appear as the time for the large vortices to attenuate. The time scales of the flow structures are more important for the dynamic cases, however, the spanwise length above the first threshold is sufficient for estimating the aerodynamic forces. This indicates that the undulation itself is the important factor of the spanwise length effect.

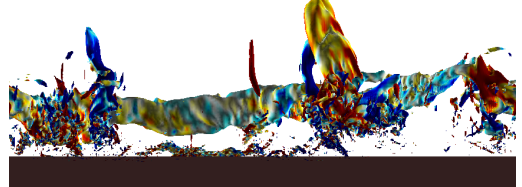
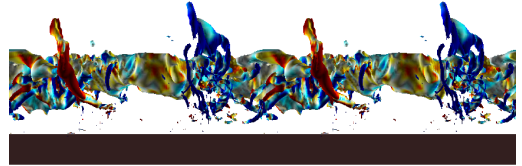
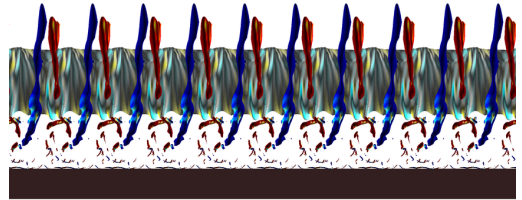
Next, the mechanism of the undulation of leading edge vortex and trailing edge vortex is discussed here. In the current investigations, the undulation of leading edge vortex and trailing edge vortex and the secondary vortices are focused on as the long flow structure in the spanwise direction. The secondary vortices are observed only after leading edge vortex and trailing edge vortex approaches each other and are observed only around leading edge vortex and trailing edge vortex. Thus behaviour of the leading edge



(a) Formation of leading edge vortex ( $AoA = 17.2^\circ$ )



(b) Formation of trailing edge vortex ( $AoA = 20.4^\circ$ )



(c) Formation of the secondary vortices ( $AoA = 21.2 \sim 22^\circ$ )

Figure 4.11: Snapshots of instantaneous flowfields for the dynamic cases. Isosurface of total-pressure colored by wall-normal vorticity is depicted from the chordwise view direction. For the case of D0.2c and D1.0c, flowfield is duplicated periodically for the comparison with the case of D2.0c. Every 5 point of LES calculation grid is visualized here.

From top to bottom: D0.2, D1.0c and D2.0c.

Table 4.3: Grid points

Grid designation	Grid points ( $N_\xi \times N_\eta \times N_\zeta$ )	Spanwise length (relative to the chord length)
Coarse	$487 \times 497 \times 146$	1.0
Medium	$680 \times 687 \times 205$	1.0
Fine	$948 \times 956 \times 287$	1.0

vortex and trailing edge vortex as a vortex pair is deduced as one of the mechanisms of the spanwise length effects. With regard to the behaviour of a vortex pair, Widnall instability<sup>161</sup> and Crow instability<sup>162</sup> are well-known. The aspect of the ununiformity of the undulation of the trailing edge vortex as observed in the case of S5.0c in Figure 4.8(c) is similar to that of the vortex pair which is displaced due to the interaction of the Widnall and Crow instability.<sup>163</sup> In addition to this, the observed facts that the intermittent formation of the secondary vortices also have ununiformity in spanwise direction and that the vorticity of the secondary vortices have not regular pattern in spanwise distribution supports that some phenomena more than two are involved. Here, these instabilities are of a vortex pair generally, however, a sole vortex and wall (in this case, airfoil surface) can be regarded as a counter-rotating vortex pair.<sup>164</sup> Now, the reason why the intermittent interval of the secondary vortices differed between the stationary and dynamic cases can be explained the difference in the distance of the vortex pair, as the Widnall instability grows less as the distance increases. For comparing the dynamic case with the stationary case, the distance of the vortex pair or the vortex and the airfoil surface get away from each other due to the pitching motion of the airfoil. Further investigations are required to verify the above arguments.

The current investigations conclude that the spanwise length of  $1.0c$  is sufficient to estimate the aerodynamic forces in the flowfield with large vortex structures. Therefore, all the cases calculated hereafter have spanwise length of  $1.0c$ .

### 4.3 Verification of grid spacing

Verification study of grid spacing is conducted on the dynamic flowfield around a NACA0012 airfoil. Also in this verification study, the spanwise length is fixed to  $1.0c$ . The cases for the verification study of grid spacing are listed in Table 4.3.

The cycle-integrated  $C_L$ ,  $C_D$ , and  $L/D$  are presented in Table 4.4. The difference between the Medium case and Fine case is 5.6% in  $C_L$ , 9.6% in  $C_D$ , and 3.6% in  $L/D$



Table 4.4: Cycle-averaged aerodynamic performances.

Resolution	$C_L$	$C_D$	$L/D$
Coarse	0.829	0.216	3.84
Medium	0.709	0.198	3.58
Fine	0.749	0.217	3.45

while the difference between the Medium case and Coarse case is 16.9% in  $C_L$ , 9.1% in  $C_D$ , and 7.3% in  $L/D$ . Figure 4.12 presents the  $C_L$  and  $C_D$  curves against  $AoA$ . The aerodynamic curves for the Medium and Fine case show good agreement with each other whereas the Coarse grid shows large discrepancy from the other results. Considering that there is large variation in aerodynamic performances in each calculation cycle (prominent from the formation of a DSV until its shed into the wake), the disagreement shown in Table 4.4 can be considered to be within the permissible range.

The chordwise distributions of  $C_p$  and  $C_f$  are presented in Figure 4.13. In this figure, the distributions at the phase at which the LSB breaks down are depicted. The  $C_p$  and  $C_f$  distributions of the Medium and Fine grid show good agreement with each other. The distributions of the chordwise velocity, turbulent kinetic energy (TKE), and Reynolds stress along the wall-normal direction are presented in Figure 4.14. Although some discrepancies are observed between the Medium and Fine grid, the shape of wall-normal distributions are well-comparable. Considering that the shape of the LSB is well-captured in Figure 4.13 and the stall characteristics show good agreement with each other, the grid resolution of Medium is sufficient to resolve the behaviour of the LSB in dynamic flowfields.

## 4.4 Verification of time step size

In the main case, time step size  $\Delta t$  is set as  $5 \times 10^{-4}$  in nondimensional value, where the maximum CFL corresponds to approximately 20. In the verification study of time step size, the results with  $\Delta t$  of  $1.0 \times 10^{-3}$ ,  $5.0 \times 10^{-4}$ , and  $2.5 \times 10^{-4}$  are compared with each other.

The cycle-integrated  $C_L$ ,  $C_D$ , and  $L/D$  are presented in Table 4.5. The difference between the case with  $\Delta t$  of  $2.5 \times 10^{-4}$  and the case with  $\Delta t$  of  $5.0 \times 10^{-4}$  is 2.1% in  $C_L$ , 1.6% in  $C_D$ , and 0.58% in  $L/D$  while the difference between the case with  $\Delta t$  of  $5.0 \times 10^{-4}$  and the case with  $\Delta t$  of  $1.0 \times 10^{-3}$  is 1.3% in  $C_L$ , 3.3% in  $C_D$ , and 4.4% in  $L/D$ .

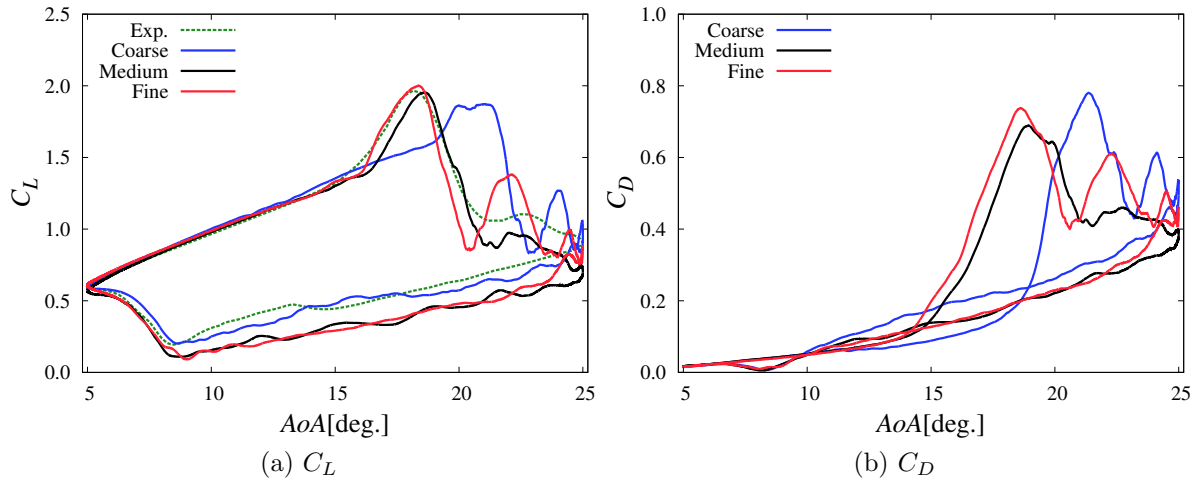


Figure 4.12: Aerodynamic performances against  $AoA$ .

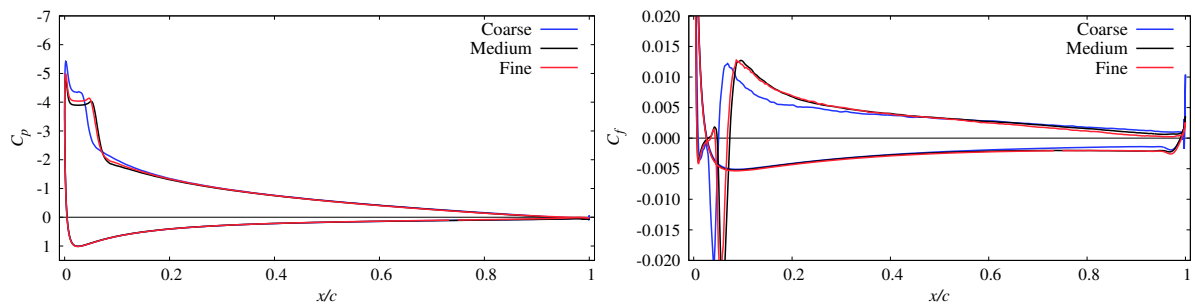
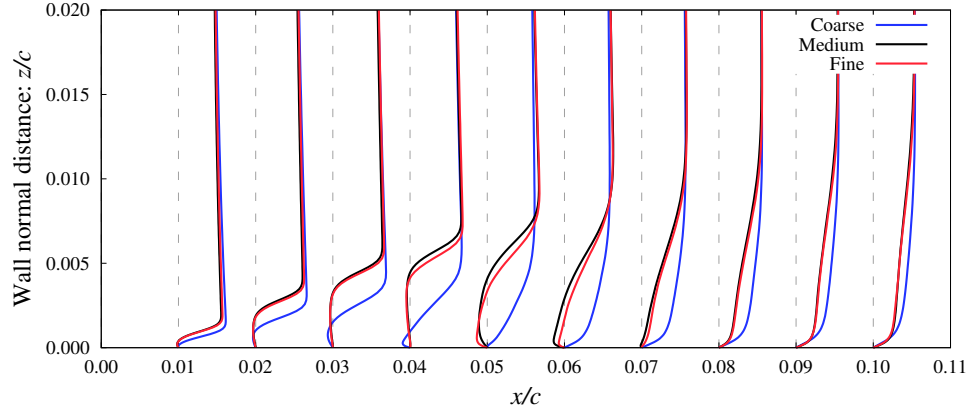
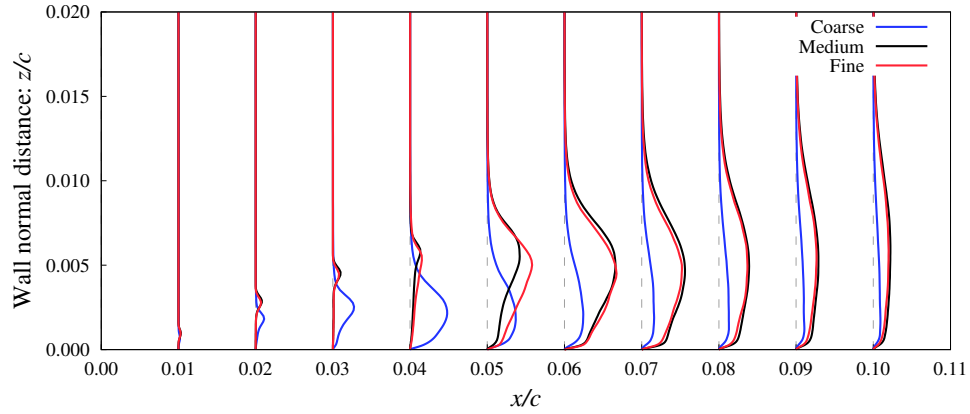


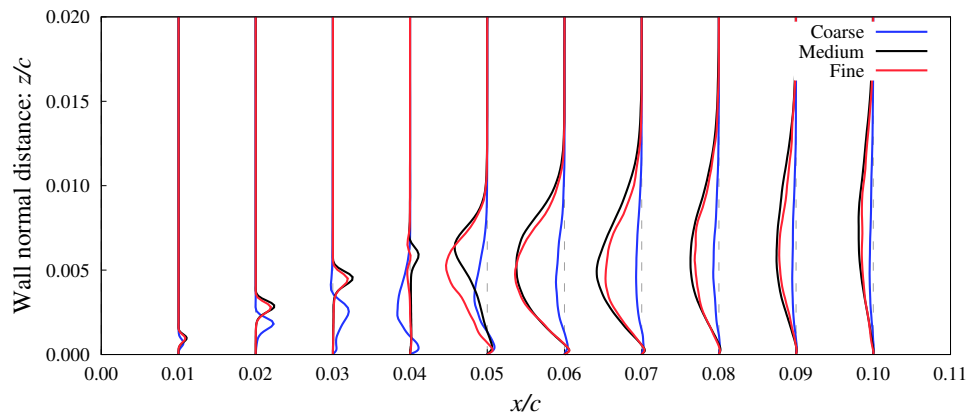
Figure 4.13: Chordwise  $C_p$  and  $C_f$  distributions for pitching NACA0012 airfoil at *phase* of  $76^\circ$  ( $AoA$  of  $12.5^\circ$ ).



(a) Chordwise velocity



(b) TKE



(c) Reynolds stress

Figure 4.14: Phase- and span-averaged distributions of chordwise velocity, TKE, and Reynolds stress near the leading edge at *phase* of  $76^\circ$  (*AoA* of  $12.5^\circ$ ).

Table 4.5: Cycle-averaged aerodynamic performances.

Time step size	$C_L$	$C_D$	$L/D$
$\Delta t = 1.0 \times 10^{-3}$	0.829	0.204	4.06
$\Delta t = 5.0 \times 10^{-4}$	0.709	0.198	3.58
$\Delta t = 2.5 \times 10^{-4}$	0.724	0.201	3.60

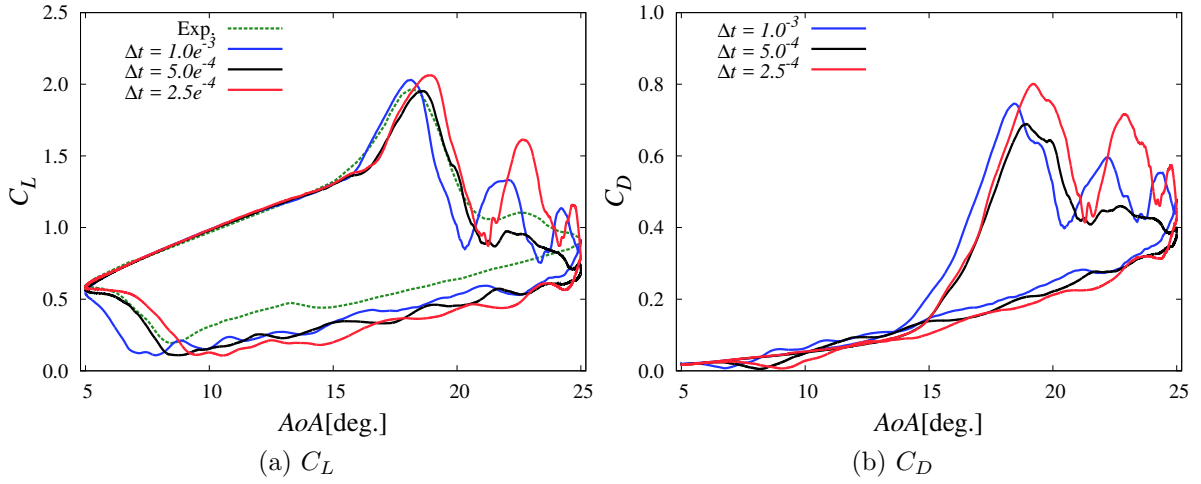
Figure 4.15: Aerodynamic performances against  $AoA$ .

Figure 4.16 and Figure 4.17 respectively presents the chordwise distributions of  $C_p$  and  $C_f$  and the distributions of the chordwise velocity, TKE, and Reynolds stress along the wall-normal direction at the phase at which the LSB breaks down. At this phase, results of the case with  $\Delta t$  of  $5.0 \times 10^{-4}$  and  $\Delta t$  of  $2.5 \times 10^{-4}$  are well-comparable.

Figure 4.15 presents the  $C_L$  and  $C_D$  curve against  $AoA$ . The curves of the case with  $\Delta t$  of  $5.0 \times 10^{-4}$  and  $\Delta t$  of  $2.5 \times 10^{-4}$  shows good agreement with each other around the phase before dynamic stall. The curves around the phase at which the flow begin to reattach show some discrepancies between all the cases. The  $AoA$  where the flow reattaches are  $7.8^\circ$ ,  $9.4^\circ$ , and  $10.3^\circ$  respectively for the case with  $\Delta t$  of  $1.0 \times 10^{-3}$ ,  $5.0 \times 10^{-4}$ , and  $2.5 \times 10^{-4}$ ; the difference between the case with  $5.0 \times 10^{-4}$  and  $2.5 \times 10^{-4}$  is half of that between  $\Delta t$  of  $1.0 \times 10^{-3}$  and  $5.0 \times 10^{-4}$ . These results shows that it is reasonable to employ the time step size  $\Delta t$  of  $5.0 \times 10^{-4}$  considering that the  $C_L$  curve of the case with  $\Delta t$  of  $5.0 \times 10^{-4}$  already shows good agreement that of the experiment around the phase where the flow reattaches and the behaviour of the LSB around the phase before the dynamic stall is well-resolved.

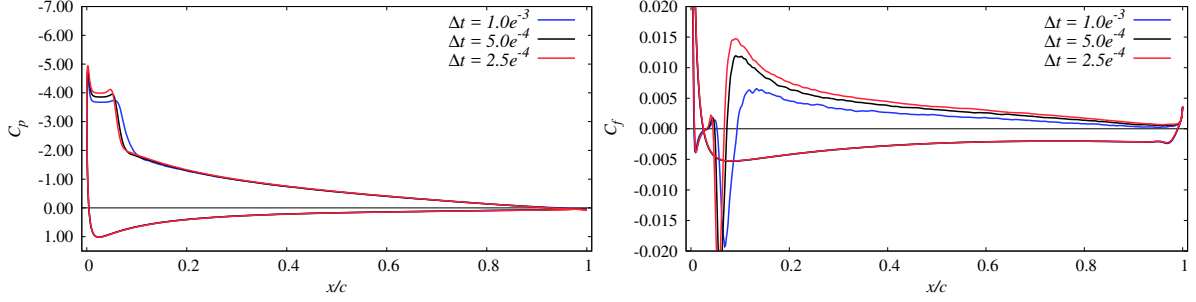


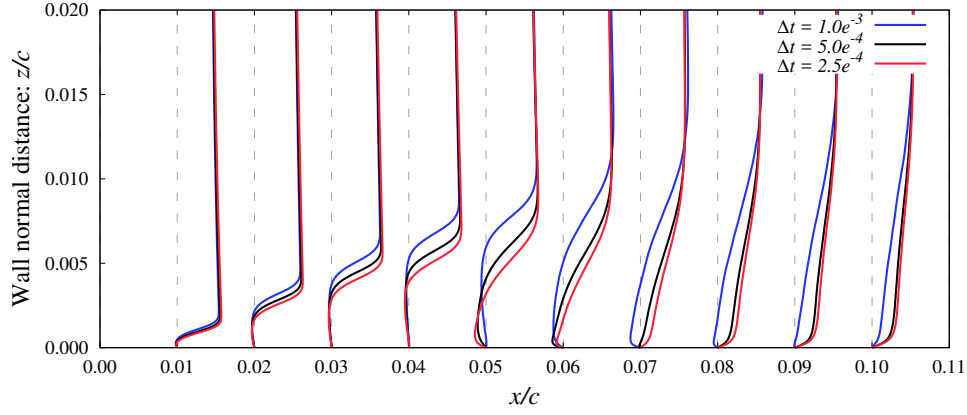
Figure 4.16: Chordwise  $C_p$  and  $C_f$  distribution for pitching NACA0012 airfoil at *phase* of  $76^\circ$  (*AoA* of  $12.5^\circ$ ).

## 4.5 Summary

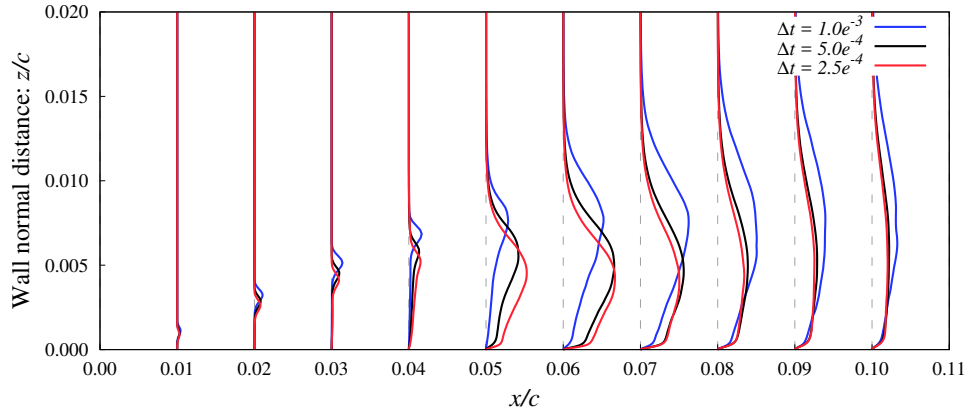
In this chapter, verification and validation of the computational method are conducted.

First, the effects of the spanwise length of the computational domain on stationary flowfields and dynamic flowfields are investigated. The spanwise length has no noticeable effects to the flowfield before stall. The spanwise length effects become significant after stall, as observed as the attenuation of the large vortices. It is suggested that the key phenomenon of this spanwise length effects is the undulation of large vortices. To resolve the undulation of large vortices, it is clarified that spanwise length of  $1.0c$  is sufficient to estimate the aerodynamic performances for the current conditions.

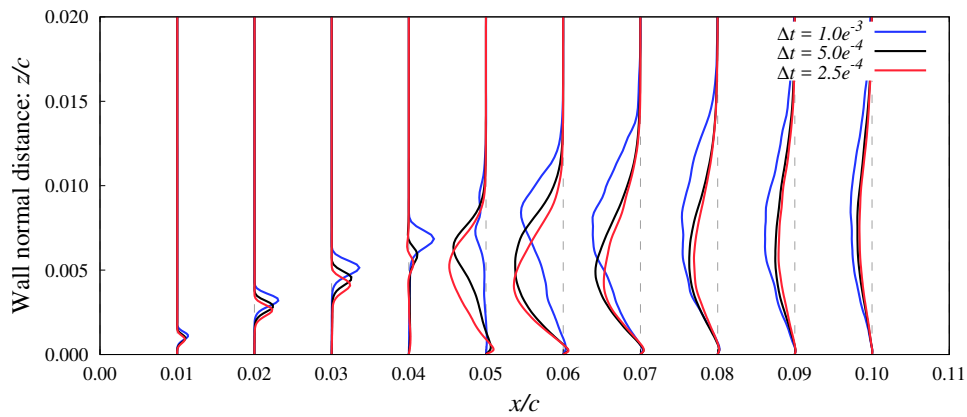
With clarified spanwise length, verification studies of grid resolution and time step size are conducted. Although full convergence in time step size is not achieved, the results show that the main case in this thesis has reasonable spatial and temporal resolution for the flowfield in dynamic stall.



(a) Chordwise velocity



(b) TKE



(c) Reynolds stress

Figure 4.17: Phase- and span-averaged distributions of chordwise velocity, TKE, and Reynolds stress near the leading edge at *phase* of  $76^\circ$  (*AoA* of  $12.5^\circ$ ).

# Chapter 5

## Arrangement of effective control mechanisms of DBD plasma actuator on dynamic flowfields

### 5.1 Outline

In this chapter, effective control mechanisms of DBD plasma actuator on dynamic flowfields are investigated and arranged. The objective airfoil used in this study is NACA0012 airfoil so that previous knowledge of effective control mechanisms for stationary flowfields can be applied on the controlled case.

First, flowfields without control are investigated and some considerations on control of the dynamic flowfields are given. Then the investigation results and the previous findings about effective control mechanisms are integrated in order to determine the DBD plasma actuator parameters. Next, controlled flowfields are investigated to clarify the effective control mechanisms.

### 5.2 Investigation on flowfield without control

#### 5.2.1 Stationary flowfield

First, stationary flowfields around a NACA0012 airfoil are investigated. The flow conditions for stationary flowfields are summarized in Table 5.1; angle of attack ( $AoA$ ) ranges from  $5^\circ$  to  $25^\circ$  and Reynolds number is set as constant of  $2.56 \times 10^5$ . These parameters are determined so that the results can be compared with the results in the dynamic flowfields.

Table 5.1: Cases for stationary NACA0012 airfoil without control.

Reynolds number	Angle of attack	Reduced frequency
$2.56 \times 10^5$	5, 10, 12, 13, 14, 15, 20, 25°	N/A

Table 5.2: Case for pitching NACA0012 airfoil without control.

Reynolds number	Angle of attack	Reduced frequency
$2.56 \times 10^5$	$5 \sim 25^\circ$	$0.02\pi$

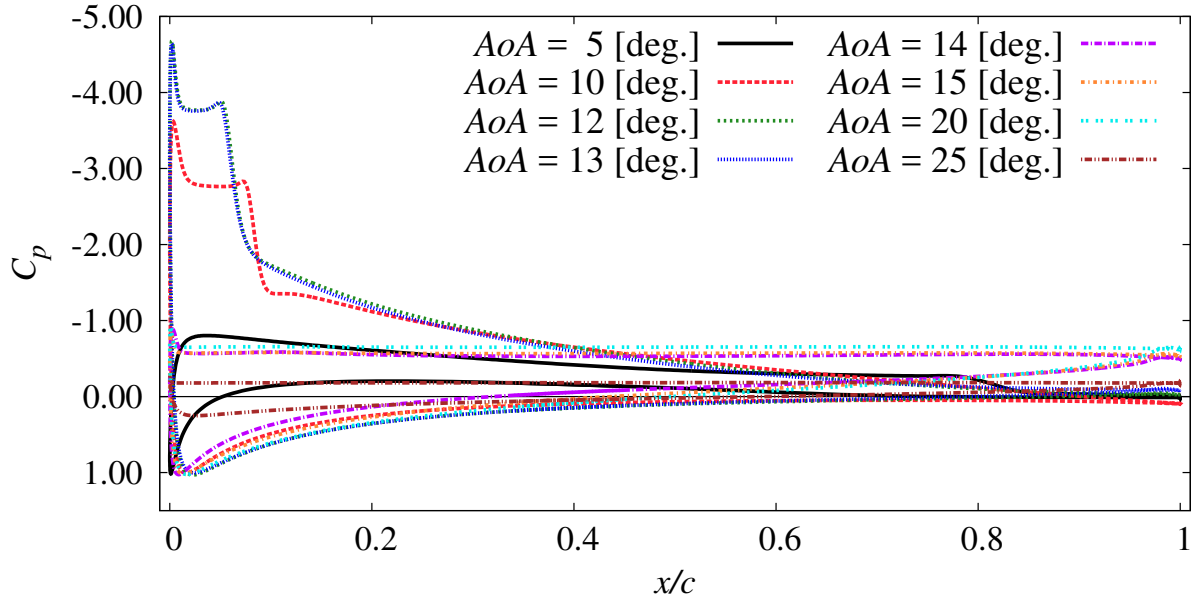
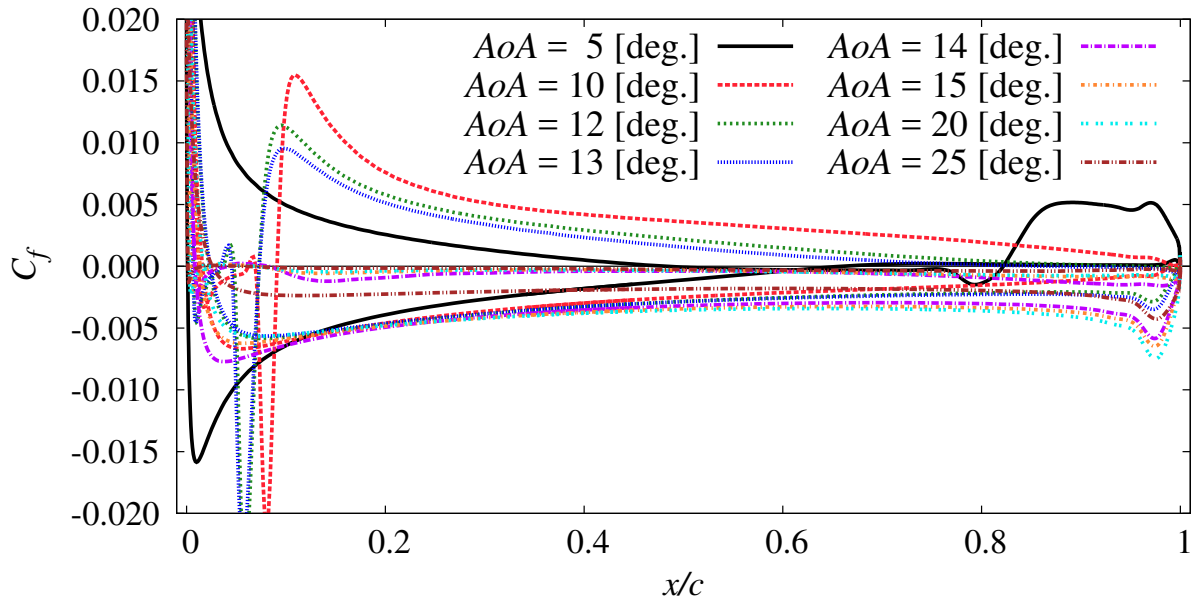
Figure 5.1 shows the surface pressure coefficient  $C_p$  and friction coefficient  $C_f$  distributions of time- and span-averaged flowfield. The time- and span-averaged streamwise velocity fields are depicted in Figure 5.2. At  $AoA$  of  $5^\circ$ , the flow separates around the mid-chord and reattaches near the trailing edge as observed in the  $C_f$  distribution. As  $AoA$  increases, the region between the separation and the reattachment point, which can be regarded as an laminar separation bubble (LSB), come to show a clear recirculation region in Figure 5.2. The existence of LSB is also observed by the  $C_p$  distribution as a plateau near the leading edge. Beyond  $AoA$  of  $14^\circ$ , the flow massively separates near the leading edge over the entire airfoil surface.

Figure 5.3 shows  $C_L$ ,  $C_D$ , and  $C_M$  against  $AoA$ . Stall is observed between  $AoA$  of  $12^\circ$  and  $13^\circ$ . Here, the stall angle is defined as the first drop in  $C_L$  against increasing  $AoA$ .<sup>165</sup> Beyond the stall  $AoA$ , large drop in  $C_L$ , rise in  $C_D$ , and drop in  $C_M$  is observed between  $AoA$  of  $13^\circ \sim 14^\circ$ . Here, the slight drop in  $C_L$  observed just before the rapid drop and this is due to the trailing edge separation as seen in Figure 5.1 and Figure 5.2(d). Drastic changes in the flow near the leading edge is observed at and after  $AoA$  of  $14^\circ$ ; the flow does not reattaches and massively separates from the leading edge.

### 5.2.2 Dynamic flowfield

Next, dynamic flowfields around a pitching NACA0012 airfoil is discussed. The flow condition for the dynamic flowfield without control is shown in Table 5.2;  $AoA$  ranges from  $5^\circ$  to  $25^\circ$ , which is dependent variable of time, and Reynolds number is set as constant of  $2.56 \times 10^5$ .



(a)  $C_p$ (b)  $C_f$ Figure 5.1: Chordwise  $C_p$  and  $C_f$  distributions of stationary NACA0012 airfoil.

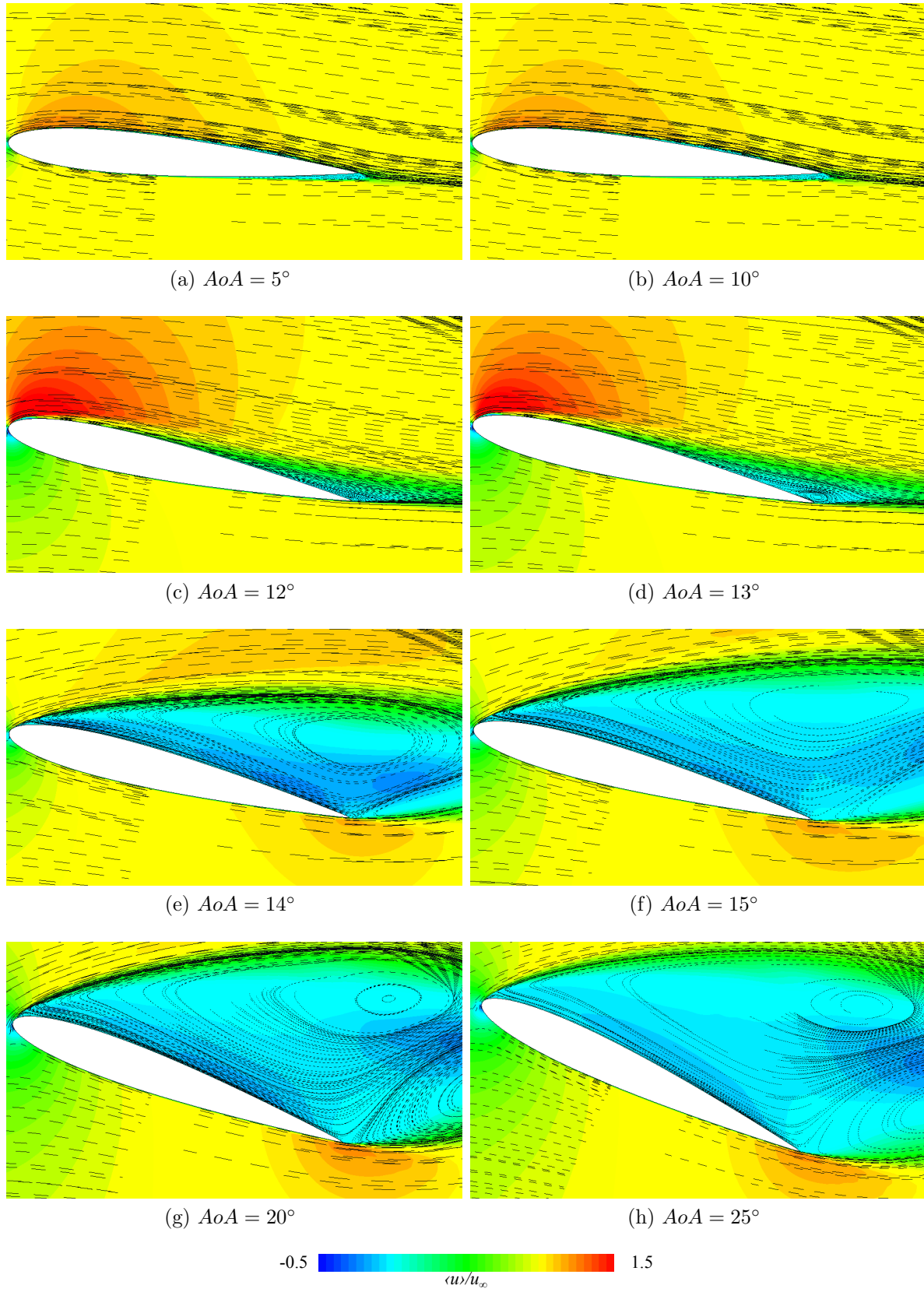


Figure 5.2: Time- and span-averaged streamwise velocity flowfield with streamline of stationary NACA0012 airfoil.

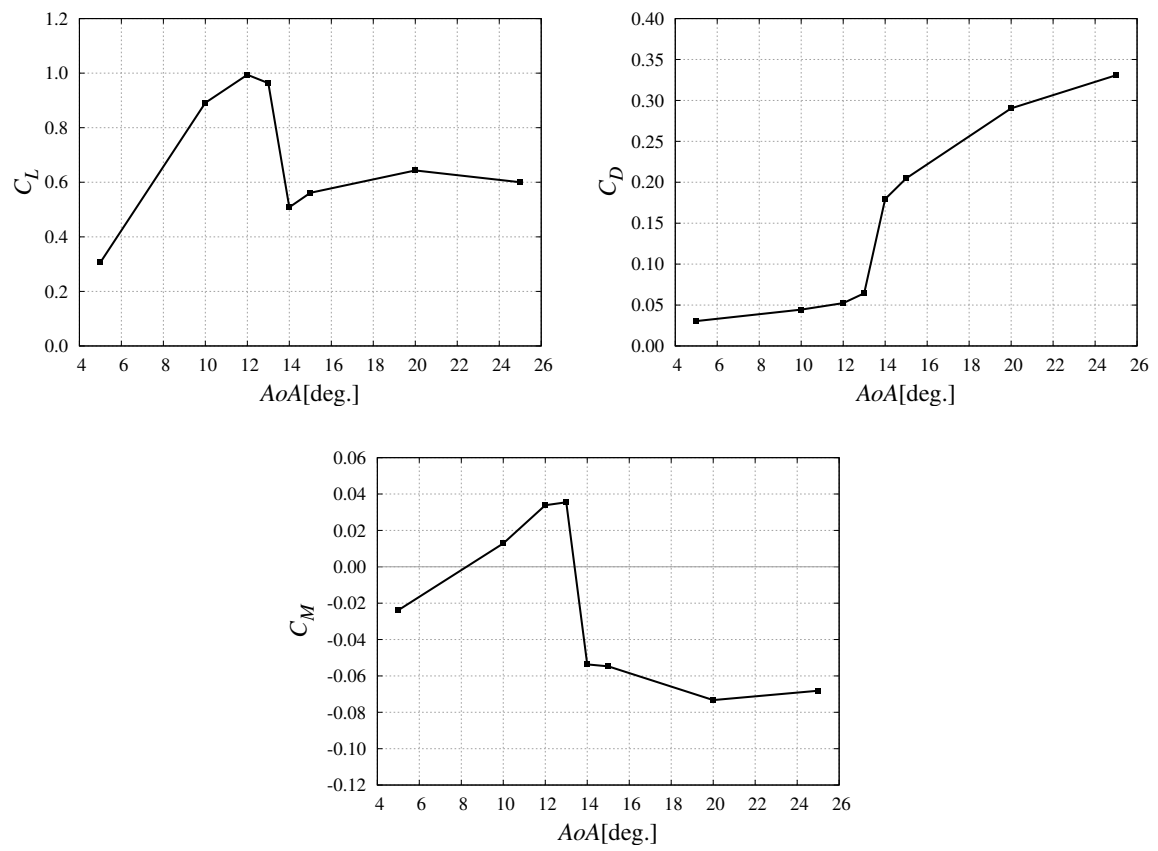


Figure 5.3: Aerodynamic performances of stationary NACA0012 airfoil.

### Phase-averaged and instantaneous flowfield

The phase- and span-averaged flowfields around a pitching airfoil at selected phases are presented in Figure 5.4 with  $C_p$  distribution. The instantaneous flowfields of the corresponding  $AoA$  to the subfigures of Figure 5.4 are presented in Figure 5.5. In the phase-averaged flowfields, the LSB and the dynamic stall vortex (DSV) observed in the instantaneous flowfields are observed as clearly organized flow structures; the formation of this LSB starts from  $AoA$  of approximately  $9^\circ$  during the pitching down (after Figure 5.4 and 5.5(i)), where the separated flow come to reattach near the leading edge. As the pitching motion proceeds, the LSB come to be observed more clearly and the level of the plateau in negative  $C_p$  near the leading edge rises by this grow-up of the LSB (Figure 5.4 and 5.5(b)).

Then the LSB breaks down and it corresponds to the onset of dynamic stall; the LSB grows into a DSV in a continuous manner. The flowfield at the phase at which the LSB breaks down is depicted in Figure 5.4 and 5.5(c). Due to its strong circulation and large size, the DSV produces large aerodynamic forces with large undulation as apparent in the chordwise  $C_p$  distribution (Figure 5.4 and 5.5(d), (e)). Not only the DSV, but subsequent formation of an other large vortex from the trailing edge (Figure 5.4 and 5.5(f)) and then another large vortex from the leading edge are also observed. This tertiary vortex (secondary large vortex from the leading edge) is not clearly observed in the phase-averaged flowfield, but its effect can be observed in the aerodynamic performances presented in next subsection. After these large vortices shed, where is around the maximum  $AoA$ , the separated flow from the leading edge is observed without any prominent flow structure and the  $C_p$  distribution become flat along the entire chord (Figure 5.4 and 5.5(g)). Note that  $C_f$  on the suction side near the leading edge becomes positive although the flow separates from the leading edge separation as seen in Figure 5.4 and 5.5(c)~(h). This is because of the obverse (counterclockwise in these figures) circulation region formed inside the circulation (clockwise) region and this is not regarded as the reattachment point in the current research. This fully stalled state continues until  $AoA$  decreases to around  $9^\circ$ ; then the separated flow come to reattach and an LSB begin to form (Figure 5.4 and 5.5(h), (i)).

### Aerodynamic performances

The phase-averaged lift coefficient  $C_L$ , drag coefficient  $C_D$ , moment coefficient  $C_M$ , and torque coefficient  $C_Q$  against  $AoA$  are shown in Figure 5.6. At relatively low  $AoA$  during the pitching up, the slopes of all the aerodynamic performances against  $AoA$  are gentle.

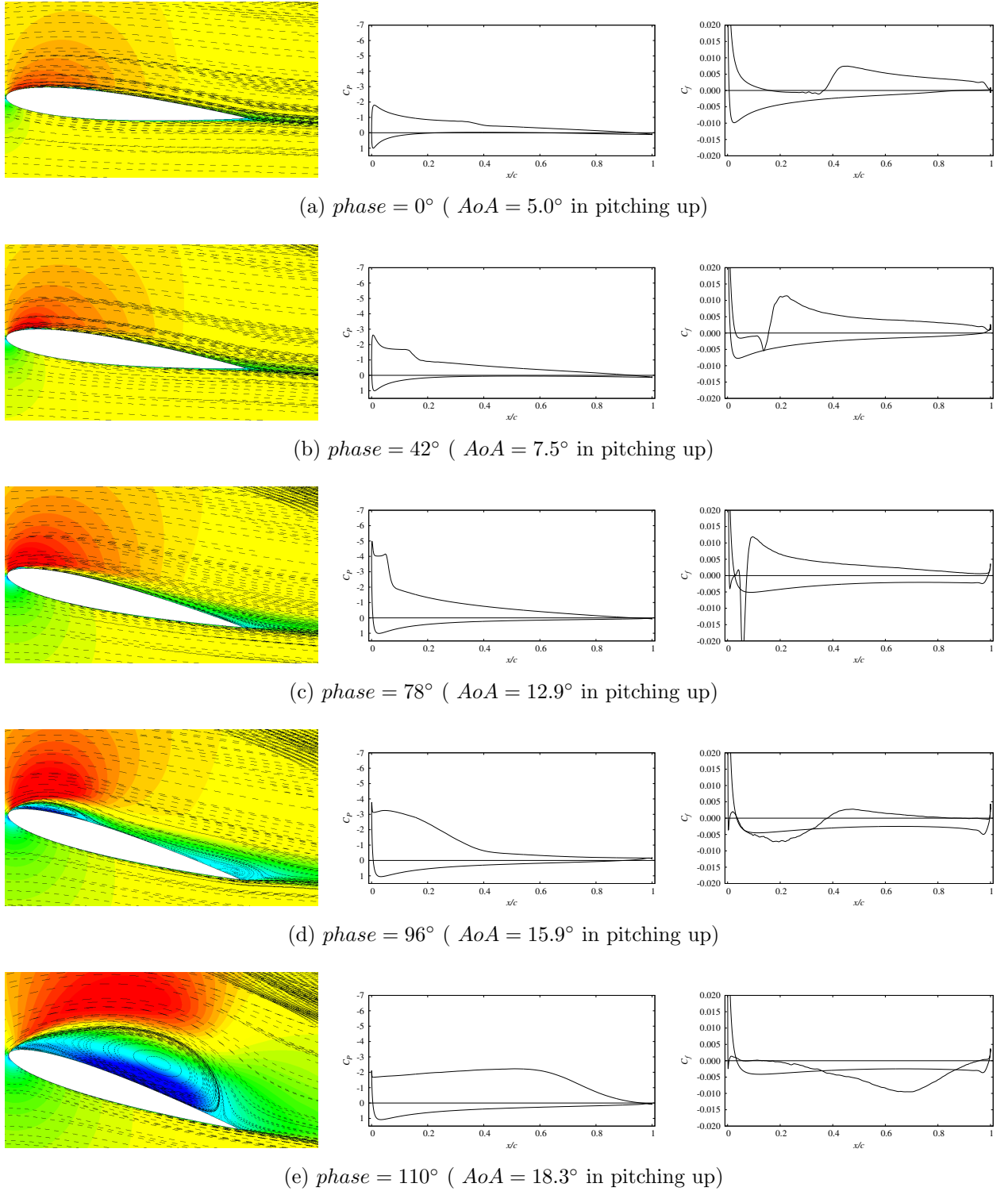
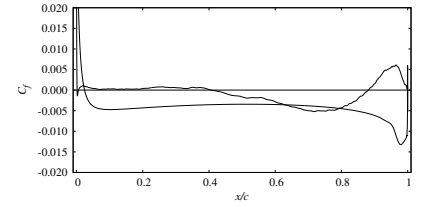
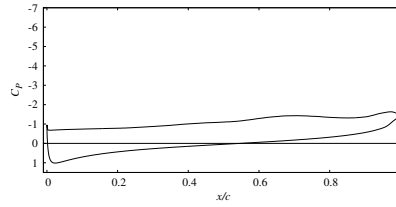
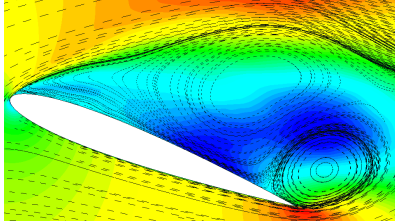
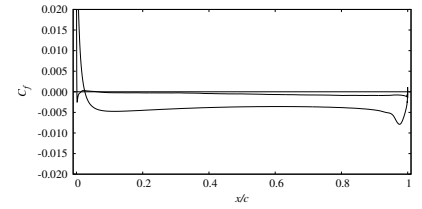
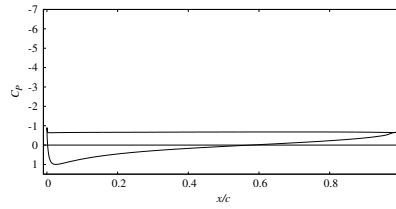
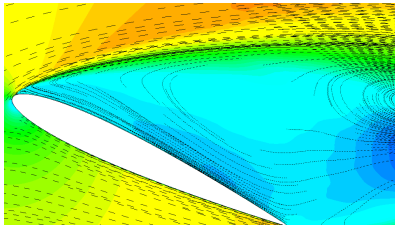


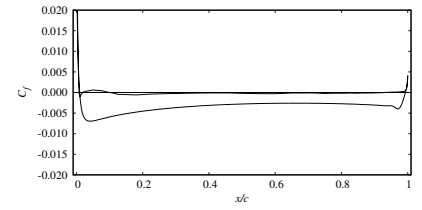
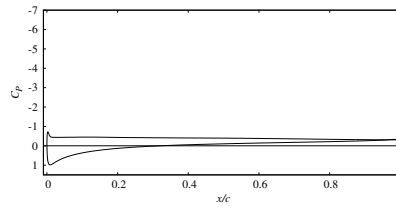
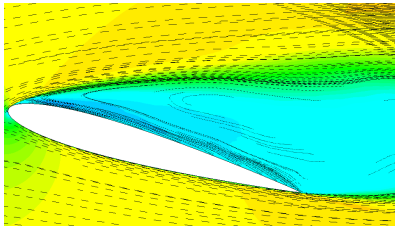
Figure 5.4: Phase- and span-averaged flowfield for pitching NACA0012 airfoil without control.



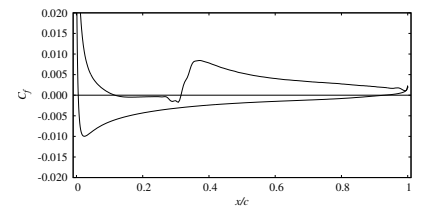
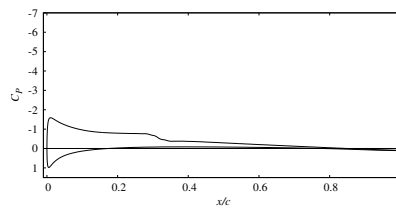
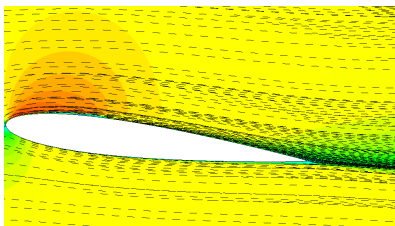
(f)  $phase = 126^\circ$  (  $AoA = 20.7^\circ$  in pitching up)



(g)  $phase = 180^\circ$  (  $AoA = 25.0^\circ$  )



(h)  $phase = 268^\circ$  (  $AoA = 15.4^\circ$  in pitching down)



(i)  $phase = 306^\circ$  (  $AoA = 9.3^\circ$  in pitching down)

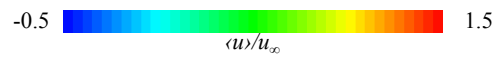


Figure 5.4: *Continued.*

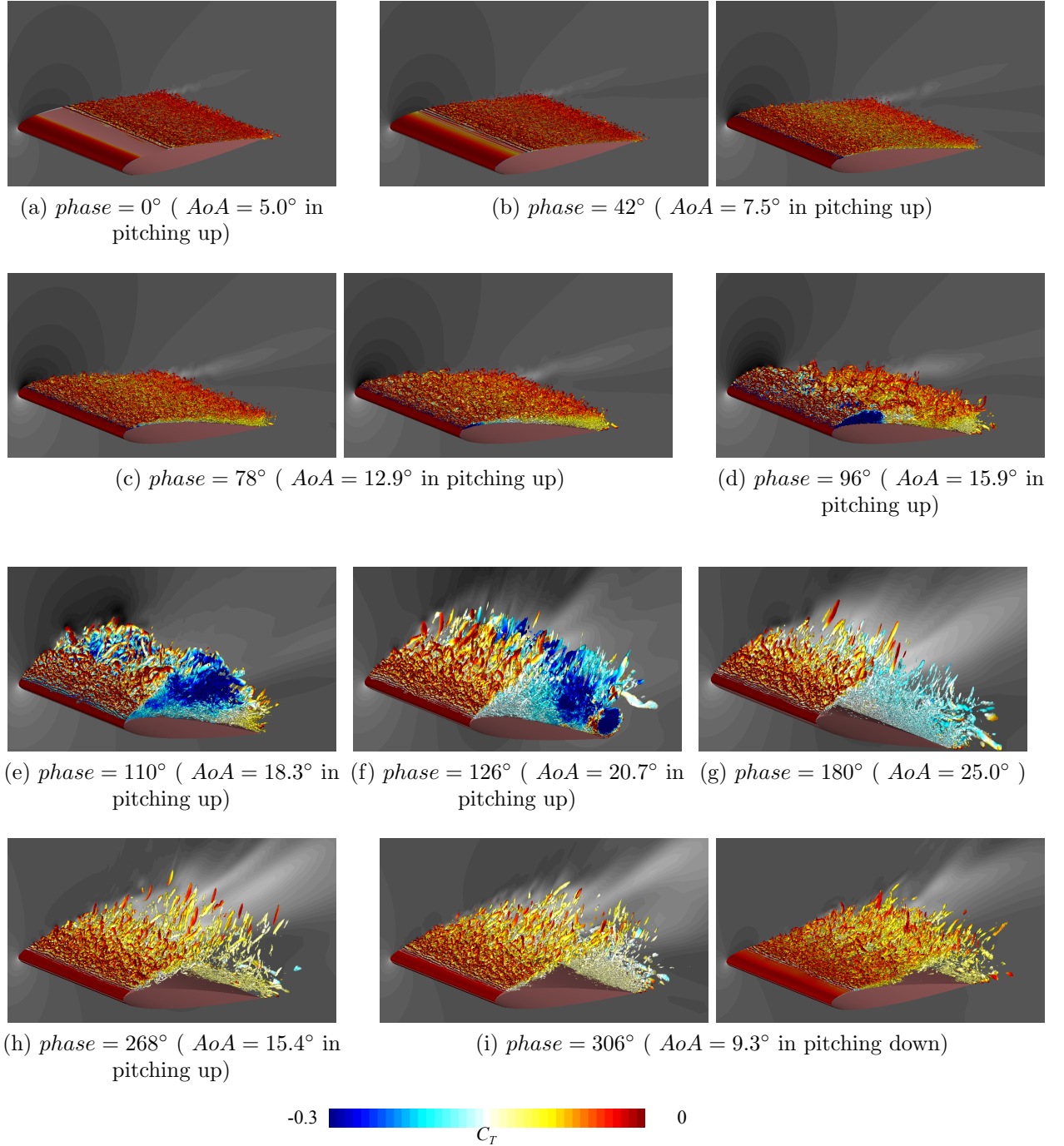


Figure 5.5: Snapshots of instantaneous flowfield for pitching NACA0012 airfoil without control. The iso-surfaces indicate the second invariant of the velocity gradient tensor colored by total pressure coefficient.



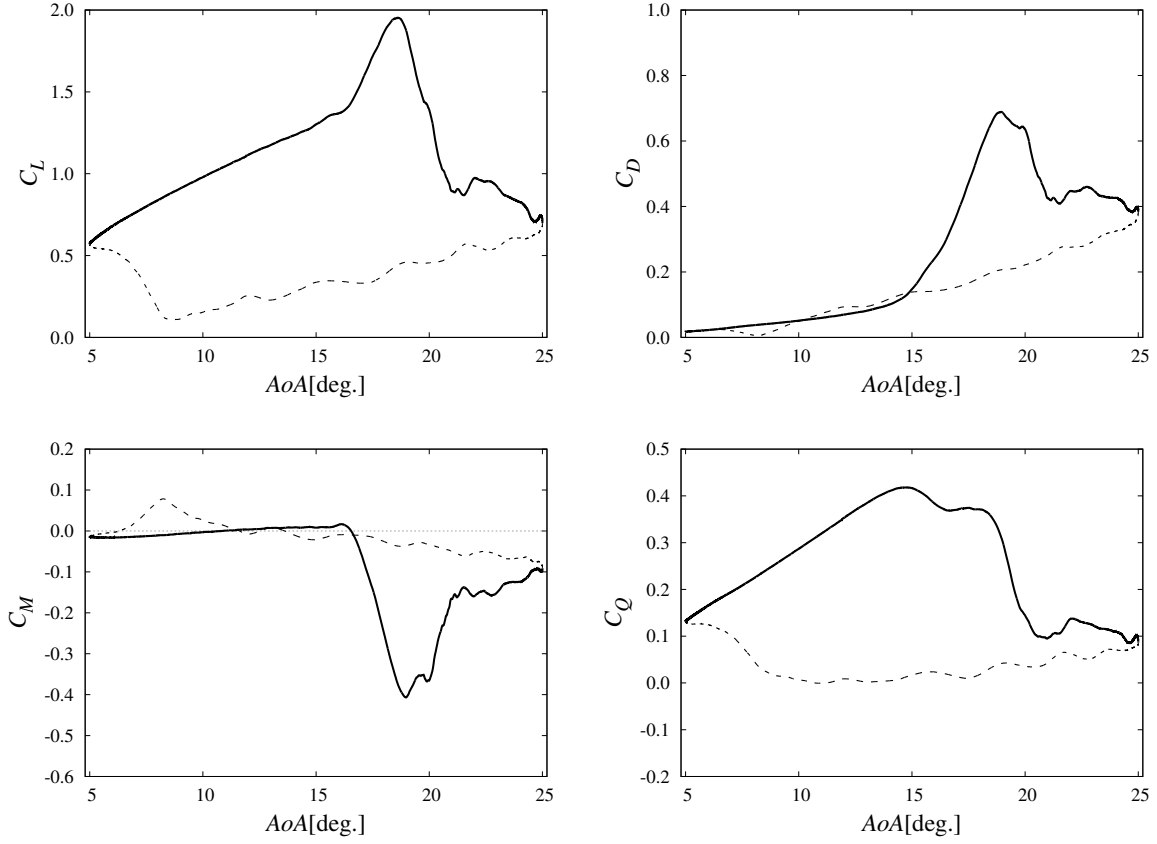


Figure 5.6: Aerodynamic performances for pitching NACA0012 airfoil without control. Solid lines denote increasing  $AoA$ , dashed lines decreasing  $AoA$ .

As the pitching motion proceeds, sudden and drastic increase in  $C_L$ , increase in  $C_D$ , and decrease in  $C_M$  are observed around  $AoA$  of  $16 \sim 17^\circ$  during the pitching up and soon the aerodynamic performances show their maximum/minimum value around  $AoA$  of  $18 \sim 19^\circ$ . Another small extremum is observed after this peak of the aerodynamic performances near  $AoA$  of  $22^\circ$  and these two peaks of the aerodynamic performances are due to the aforementioned two large vortices from the leading edge. When the peaks take each extremum, the first and second large vortex from the leading edge is observed around the mid-chord, respectively. After the large vortices shed, the aerodynamic performances show gentle slope against  $AoA$  during large portion of the pitching down as can be seen during  $AoA$  of  $25^\circ \sim 10^\circ$  in pitching down. Around the final stage of the pitching down, rapid increase in  $C_L$ , decrease in  $C_D$ , and decrease in  $C_M$  are observed at around  $AoA$  of  $9^\circ$  due to the recovery to the attached state.



### Characteristic angles in dynamic stall

The stall angle is defined as the  $AoA$  where first drop in  $C_L$  against increasing  $AoA$  is observed.<sup>165</sup> By this definition, the stall angle is between  $AoA$  of  $12 \sim 13^\circ$  in the stationary case and  $AoA$  of  $18.6^\circ$  in the dynamic case.

In the dynamic case for NACA0012 airfoil, the first drop in  $C_L$  is brought by the DSV. Considering that the formation of DSV is triggered by the breakdown of LSB, the  $AoA$  at which the LSB breaks down always precedes the  $AoA$  at which drop in  $C_L$  is observed. Here, according to references,<sup>166</sup> NACA0012 airfoil exhibits a combined stall type of trailing edge stall and leading edge stall at intermediate Reynolds number. This combined type of stall characteristic can be observed in Figure 5.4; as seen in this Figure, the extent of the trailing edge separation is relatively small and the trailing edge separation and the breakdown of LSB take place almost at the same time. As the result, the effects by this trailing edge separation on the aerodynamic performances are lost among the large effects of DSV. This suggests that the effects by the trailing edge separation on the aerodynamic performances can appear in the aerodynamic performance if, for example, the extent of trailing edge separation is enough big or the temporal relation between the trailing edge separation and the breakdown of LSB is not close. In such cases, two different characteristic  $AoA$  related to drop in  $C_L$  can be defined; one is the  $AoA$  at which first drop in  $C_L$  is observed, which is the traditional definition of stall  $AoA$ , and the other is the  $AoA$  at which drop in  $C_L$  associated to dynamic stall is observed.

With regard to the definition of  $AoA$  for dynamic stall onset, the stall onset  $AoA$  is defined as the  $AoA$  at which the maximum leading edge suction peak in  $C_p$  is observed in some previous researches.<sup>167</sup>

To sum these up, four stall-related characteristic  $AoA$  can be defined in dynamically stalled flowfields as follows;

- (1)  $AoA$  at which first drop in  $C_L$  is observed; hereafter denoted as  $AoA_{LD}$  (Lift Drop)
- (2)  $AoA$  at which LSB breaks down; hereafter denoted as  $AoA_{BD}$  (Break Down)
- (3)  $AoA$  at which maximum leading edge suction peak in  $C_p$  is observed; hereafter denoted as  $AoA_{DS}$  (Dynamic Stall)
- (4)  $AoA$  at which drop in  $C_L$  associated to dynamic stall is observed; hereafter denoted as  $AoA_{LDDS}$  (Lift Drop associated to Dynamic Stall)

In stationary flowfields, the  $AoA$  at which the leading edge stall occurs may correspond to the  $AoA$  where the LSB breaks down. On the other hand, it is not always true in

dynamic flowfields; in the dynamic case, the leading edge stall occurs far later than the breakdown of the LSB and after the convection of the DSV.

The other possible characteristic  $AoA$  in dynamic stall is  $AoA$  at which the flow starts to reattach around the final stage of the pitching down and this  $AoA$  is hereafter denoted as  $AoA_{RA}$  (ReAttach).

To give further definitions to the characteristic  $AoA$ , Figure 5.7 presents the transition of the separation, reattachment, and secondary separation points against the pitching phase estimated by the surface friction. Enlarged figure focused on the breakdown of LSB is presented in Figure 5.7(b) with regard to  $AoA_{BD}$ . Both for the stationary and dynamic case, the reattachment point moves toward the leading edge as  $AoA$  (and/or the pitching phase) increases as a typical short bubble. As  $AoA$  increases, however, the reattachment point turn to move toward the trailing edge and this means the reattachment point has an extremum against  $AoA$ . The  $AoA$  at which this extremum is observed in the reattachment point is used as the definition  $AoA_{BD}$  and as the  $AoA$  for dynamic stall onset in this thesis. For example,  $AoA_{BD}$  for the dynamic case is  $AoA$  of  $12.6^\circ$  (which corresponds to the *phase* of  $76.2^\circ$ ) for the dynamic case. Note that exceeding  $AoA_{BD}$  does not always mean the LSB breaks down; for the stationary case,  $AoA_{BD}$  is between  $AoA$  of  $12 \sim 13^\circ$  whereas the LSB breaks down above  $AoA$  of  $13^\circ$ ; therefore, this definition of  $AoA_{BD}$  may include slight changes of the LSB before the breakdown. It is suggested that  $AoA_{BD}$  is the better indicator of dynamic stall onset rather than  $AoA_{DS}$  for the flowfield with unsteady actuation because the control effects on the LSB is mainly observed as the change in the reattachment point as presented later and  $C_p$  at the leading edge is directly affected by the DBD plasma actuator. With regard to the definition of dynamic stall onset, other definitions of dynamic stall onset based on the investigation of the aerodynamic performances are proposed by several researchers.<sup>168–171</sup> However, the definitions based on the aerodynamic forces, which are calculated by integrating the force along the entire chord, cannot indicate slight changes in the behaviour of LSB brought by the DBD plasma actuator.

With respect to  $AoA_{RA}$ , the reattachment point around the final stage of dynamic stall appears suddenly as seen around *phase* of  $300^\circ$  in Figure 5.7. Therefore,  $AoA_{RA}$  may be simply defined as the  $AoA$  where reattachment is observed first around the final stage of the dynamic stall for the result processed in the phase-averaged flowfield. For example, in the current study,  $AoA_{RA}$  for the dynamic case is  $AoA$  of  $9.4^\circ$ . Here  $AoA_{RA}$  for the stationary case is not available in the current calculation. With regard to the secondary separation point, the secondary separation point is located very close to the trailing edge and is observed in very limited phase right before (and/or after, in the

controlled case) the dynamic stall.

### 5.2.3 Classification of dynamic stall process

Observations on the flowfield suggest that the process in the dynamic stall can be classified into some stages according to the flow features which describes the flowfield most at that time.

Stage 1 : Formation of LSB

The stage in which a LSB near the leading edge is observed

Stage 2 : Breakdown of LSB and formation of DSV

The stage in which the LSB breaks down and grows into a DSV

Stage 3 : Convection of DSV

The stage in which the DSV convects toward the trailing edge with large undulation of the aerodynamic performances

Stage 4 : Full-stall from leading edge

The stage in which the flow separates near the leading edge without any prominent flow structures

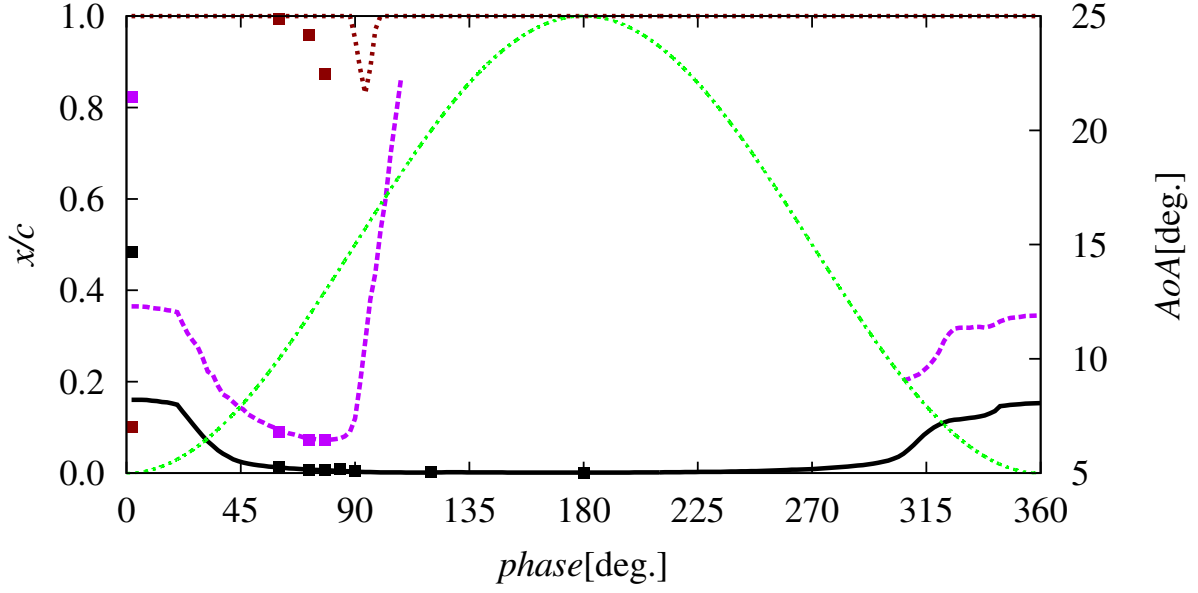
Stage 5 : Recovery to attached state

The stage in which the flow come to reattach

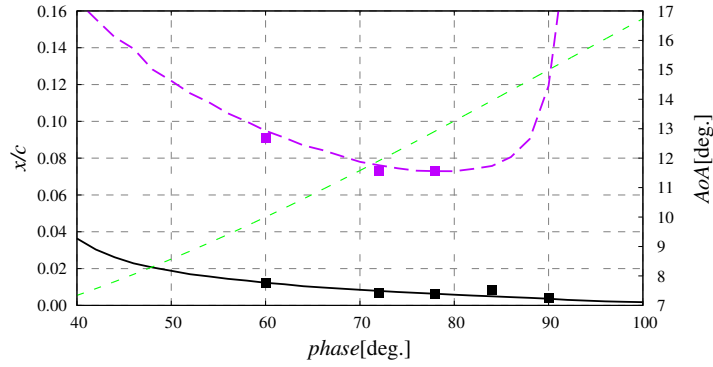
The characteristic snapshots of the phase- and span-averaged flowfield and the instantaneous flowfield in each stage are presented in Figure 5.8. Note that the events observed through the whole dynamic stall process and the classification are consistent with these given by Carr<sup>4</sup> or Leishman<sup>172</sup> although Reynolds number and the reduced frequency differs. Here, their conditions are Reynolds number is above  $1.0 \times 10^6$  and the reduced frequency is above 0.1. Considerations on this classification under various flow conditions are given in Chapter 6.

### 5.2.4 Consideration on DBD plasma actuator parameters

As introduced in Chapter 1, many previous researches on flow control around various airfoils by a DBD plasma actuator have been conducted and now knowledge about effective control mechanisms of the DBD plasma actuator is getting established. The previous knowledge about the effective control mechanisms are utilized in order to determine the DBD plasma actuator parameters to be examined.



(a) Overall pitching phase



(b) Closed-up of moment of breakdown of LSB

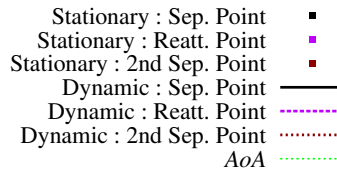


Figure 5.7: Separation, reattachment, and secondary separation points against pitching phase for stationary and pitching NACA0012 airfoil without control. Corresponding AoA is plotted with right axis.

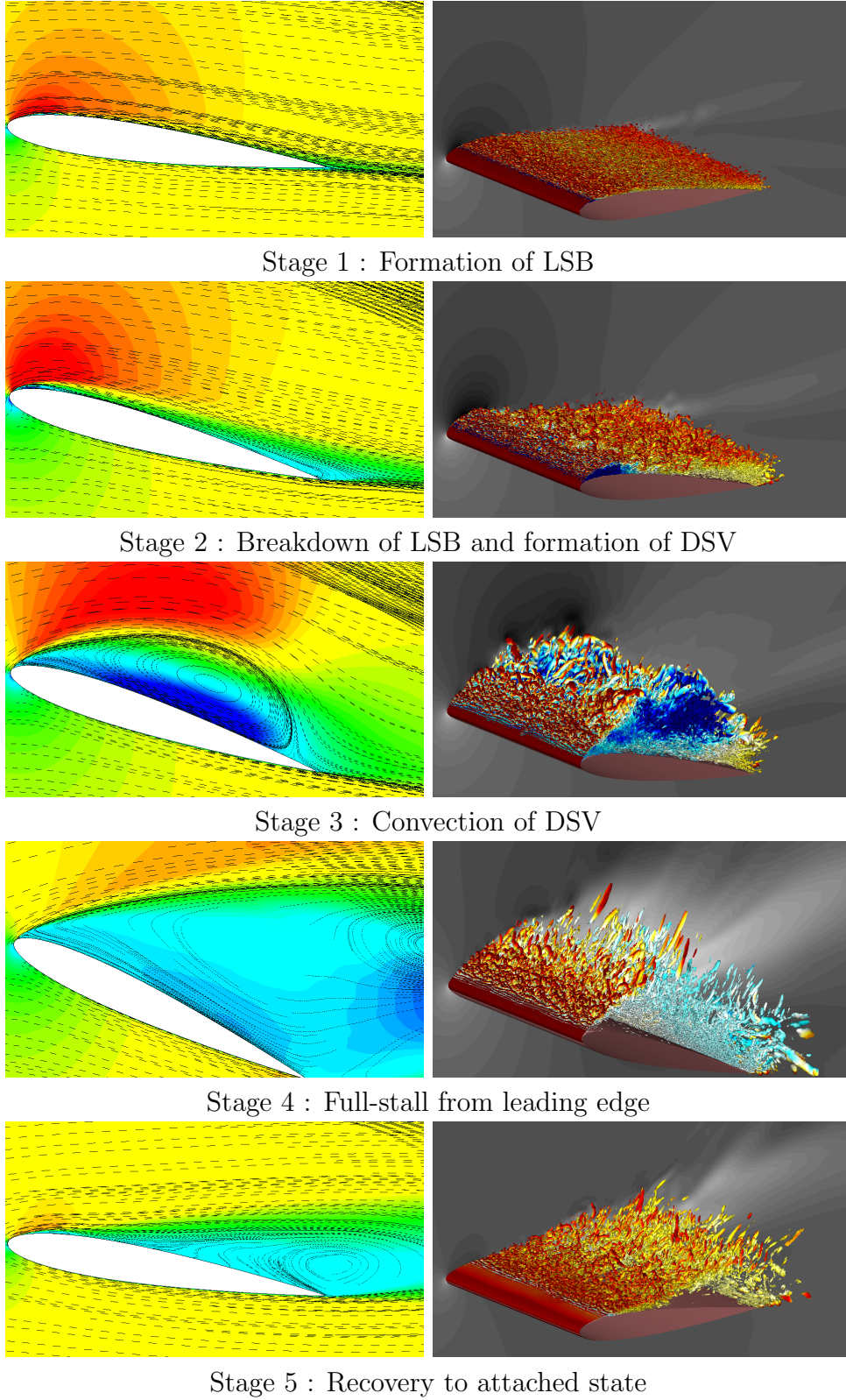


Figure 5.8: Characteristic flowfields in each classified dynamic stall process. Left column: Phase- and span-averaged chordwise velocity field. Right column: Instantaneous flowfield. The iso-surfaces indicate the second invariant of the velocity gradient tensor colored by spanwise vorticity.

### Investigation on installation position

The installation position of the DBD plasma actuator is chosen based on the observation of the transitions of the flow structures and the separation points. The separation and reattachment points are plotted in Figure 5.7. In the current study, the plasma actuator are installed at  $x/c = 0\%$  (leading edge), and 15%. Ideas as for the installation position are based on the knowledge that the effective installation position of the plasma actuator is in the vicinity of the separation point,<sup>173</sup> although this knowledge is obtained by the studies on stationary flowfields. The position of  $x/c = 15\%$  is upstream of the most upstream point of the separation point around minimum  $AoA$ . The installation position of  $x/c = 0\%$  is chosen based on references<sup>2,20</sup> and the position of  $x/c = 0\%$  corresponds the chordwise position where the flow separates right before and during dynamic stall.

### Investigation on unsteady actuation parameters

As introduced in Chapter 1, control mechanisms of the separated flow can be classified to “direct momentum injection” and “freestream momentum induction”.<sup>42</sup> In this study, to save the energy consumption by the DBD plasma actuator, the idea of utilizing the mechanism of direct momentum injection is not emphasized. Now the control mechanism of freestream momentum induction can be divided into “use of large-scale vortex” and “use of turbulent vortex”. Here, making use of these two mechanisms are proven to be effective even on the dynamic stall.<sup>20,45</sup>

With regard to the mechanism of use of large-scale vortex,  $F^+$  of unity is generally said to be effective.<sup>20,38</sup> To control the dynamic flowfields, a lot of researches have been conducted with the  $F^+$  range of order of unity.<sup>11,20,38,174</sup> The effective  $F^+$  varies depends on the airfoil geometry, Reynolds number, Mach number, or the pitching frequency, but many of the researches conclude the best  $F^+$  is between  $0.3 \sim 1.0$ . Here, Mitsuo et al. conducted experimental research on controlling the flowfield around a NACA0012 airfoil using a DBD plasma actuator installed at the leading edge. They explored the best  $F^+$  among the range of  $0.2 \sim 1$ , and found that  $F^+$  of 0.5 is the best for enhancing the cycle-integrated  $C_L$ . Their investigation suggested that the  $F^+$  of 0.5 corresponds to the frequency normalized by the characteristic vortex length and velocity of unity. The consideration for  $F^+$  based on this relation between  $F^+$  and the vortex scale is reconsidered in the current study. There is some kind of “large vortex” in the current flowfield, the large vortex emanates from the leading edge is focused on as the “large vortex” in the current study. The result of the preliminary calculation showed that the convection speed of the large vortex ranges from  $0.3u_\infty \sim 0.6u_\infty$  depending on its

chordwise position. The averaged velocity is approximately  $0.5u_\infty$  ( $= u_{lv}$ ), which is consistent result with the reference.<sup>2</sup> As for the characteristic length of the large vortex ( $c_{lv}$ ), the large vortex emanates from the leading edge and keep growing until reaches to the trailing edge. Therefore, its maximum size is considered to be limited to the length from the emanation point to the trailing edge, i.e., the chord length. Here, this definition of the estimated vortex size is effective to arrange the effective  $F^+$ .<sup>38</sup> Then the effective frequency nondimensionalized by the characteristic velocity ( $u_{lv}$ ) and the length ( $c_{lv}$ ) of the large vortex is;  $F_{eff} = f_{eff}c_{lv}/u_{lv} = 1$  and finally  $F^+$  is obtained as  $F^+ = f_{eff}c/u_\infty = 0.5$ .

The effective  $F^+$  related to the other mechanism of use of turbulent vortices has some options as for the way of transition to turbulence; Kelvin-Helmholtz instability, Tollmien-Schlichting instability, or the bypass transition. In dynamic stall flowfields, dynamic stall is triggered by the breakdown of LSB, thus the most feasible choice for the path to the turbulence will be K-H instability of the leading edge shear layer. Then, the effective  $F^+$  for stimulating the K-H instability frequency is said to be the subharmonics of the instability frequency.<sup>6,42,175</sup> Based on this findings, the effective  $F^+$  is studied by frequency analyses. Figure 5.9 shows power spectrum density (PSD) of the chordwise velocity for the pitching case. In this analysis, PSD is calculated at the points where the spanwise vorticity takes maximum at each chordwise position at each time step, and then the calculated PSD is span-averaged. This sampling method is employed because the flow structure above the airfoil surface is subject to move with the motion of the airfoil and sampling at a certain fixed location cannot track a certain flow feature. Here, the duration of the frequency analysis is set as short as possible in order to exclude the effects of the pitching motion and the resolution of  $St$  is approximately 1.5. At low  $AoA$  of Figure 5.9(a), the flow separates around  $x/c = 15\%$  and the turbulent transition occurs around  $x/c = 35\%$ . Around this transition point, prominent peak around  $St = 12 \sim 20$  is observed. By observing the flowfield, it is revealed that this peak corresponds to the frequency of the shedding of the vortices from the shear layer. At  $AoA$  right before the breakdown of LSB, the instability frequency is observed around  $St$  of 90 (Figure 5.9(b) and (c)). In the full-stalled stage, the instability frequency is observed around  $St$  of  $30 \sim 70$  around the *phase* of  $225^\circ$  (Figure 5.9(d)). It can be also observed that this peak corresponds to the frequency of the shedding of the vortices from the shear layer from the flowfield (not shown). The frequency of the vortex shedding from the shear layer corresponds to this  $St$  range of  $30 \sim 70$ . During the full-stalled stage, the peak frequency of the vortex shedding gradually shifts toward lower frequency, showing peak around  $St$  of  $30 \sim 60$  around the *phase* of  $256^\circ$  (5.9(e)). Around the final stage of pitching motion



where the flow begin to reattach, the center of instability frequency shifts to around  $St$  of 30. (Figure 5.9(f)). Here, all of these instability frequency agrees well with of the estimated frequency of the inviscid instability of the shear layer.<sup>176</sup>

One of the aims of flow control is to energize LSB in order to delay its breakdown. Therefore, the target is set to the flowfield right before the breakdown of LSB. To promote the instability mode,  $F^+$  of 50 is employed as the subharmonics<sup>175</sup> of  $St = 90$ , which is the instability frequency right before the breakdown of the LSB ((Figure 5.9(b) and (c))). Here, actuation with  $F^+$  of 50 shows its good control performance in several previous reports<sup>6,17,46</sup> at Reynolds number in the order of  $10^5$  both for stationary and dynamic flowfield.

In addition to  $F^+$  of 0.5 and 50, the control effect of  $F^+ = 6$  is also examined. Aono et al.<sup>17</sup> report that  $F^+$  of 6 has good control performance even though it is reported that the effectiveness of  $F^+ = 6$  is less than that of the high-frequency ( $F^+ = 50$ ) case both in the references.<sup>6,17</sup> The effect of these three  $F^+$  are investigated with the installation position of  $x/c = 0\%$ .

Here, the effect of the DBD plasma actuator installed at  $x/c = 15\%$  is also investigated. In this case, the control target is set to the flowfield at low  $AoA$  so as to control the flowfield in the phase at which the separation point is near the installation position. The flowfield at low  $AoA$  is characterized by formation of LSB near the mid-chord, and then its move toward to the leading edge. The aim is to delay the move of LSB and consequently delay the dynamic stall. With respect to this aim, it is considered to be important to control the behaviour of LSB and so  $F^+$  is determined so as stimulate the instability frequency of the shear layer. The instability frequency is observed around  $St = 12$  as seen in Figure 5.9(a), therefore its highest subharmonics of  $F^+ = 6$  is employed.

## 5.3 Control effects

### 5.3.1 Case description

Based on the considerations presented in the previous section, four cases are prepared as the cases with DBD plasma actuator control. The cases with control for the flowfield around a pitching NACA0012 airfoil is summarized in Table 5.3.

With regard to the other parameters of the DBD plasma actuator than the installation position and  $F^+$ , BR is set as constant of 10%, which is widely employed in previous researches and is often concluded to be a better choice. With the same value of  $D_c$  and



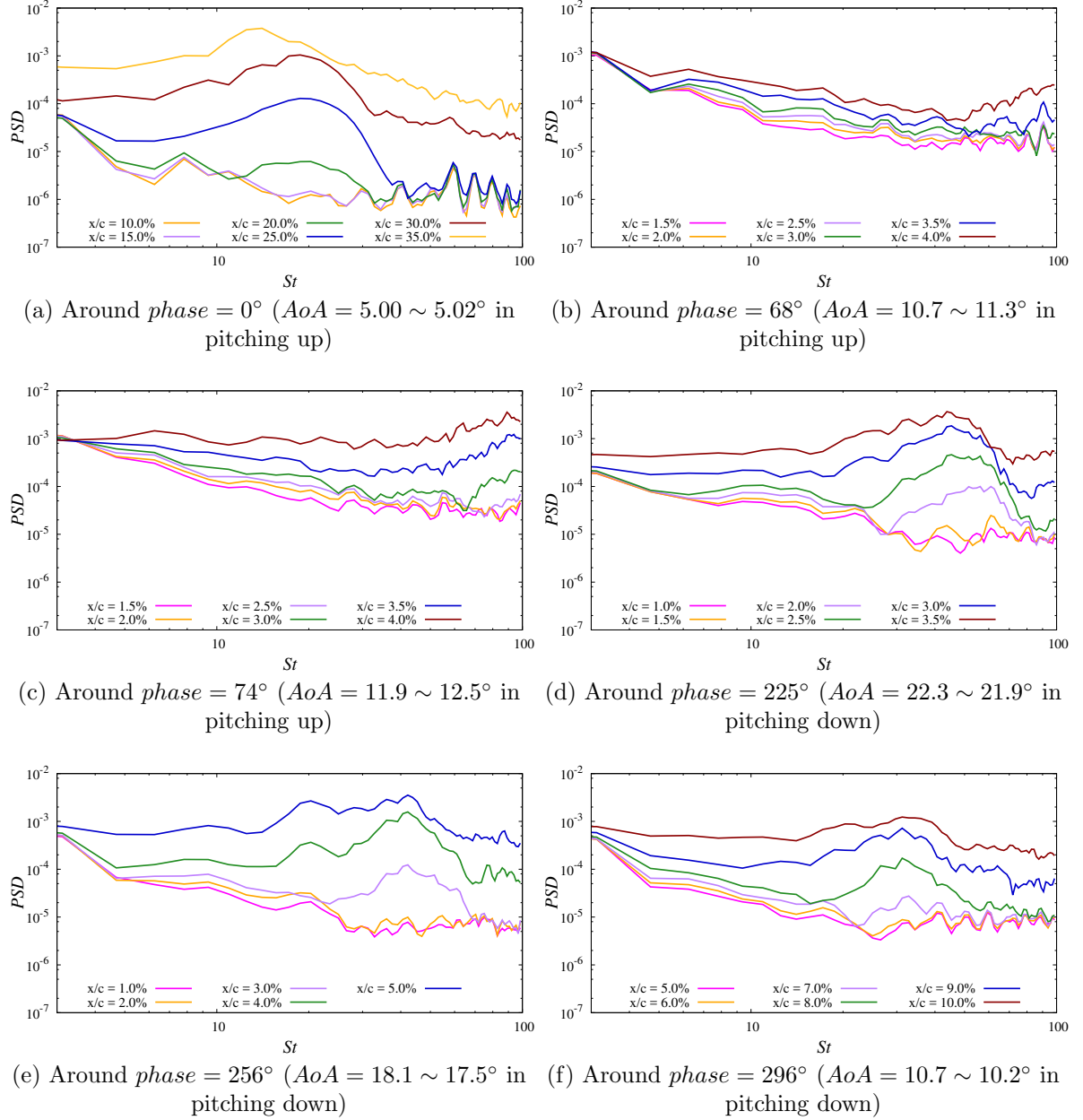


Figure 5.9: PSD of chordwise velocity on shear layer for pitching NACA0012 airfoil without control.

Table 5.3: Cases for pitching NACA0012 airfoil.

Case name	Installation position	$F^+$	$D_c$	$f_{base}$	$BR$
OFF	N/A	N/A	N/A	N/A	N/A
ON $F^+ = 0.5$	$x/c = 0\%$	0.5	0.25	70	0.1
ON $F^+ = 6$	$x/c = 0\%$	6	0.25	240	0.1
ON $F^+ = 50$	$x/c = 0\%$	50	0.25	200	0.1
ON $15\%F^+ = 6$	$x/c = 15\%$	6	0.25	240	0.1

BR, net momentum induced by a DBD plasma actuator become identical. The value of  $D_c$  is set as constant of 0.25 among all control cases in this thesis. This value of  $D_c$  is determined so that the maximum velocity induced by the DBD plasma actuator corresponds to that in the experiment;<sup>2</sup> in the experiment, the maximum velocity is between  $1 \sim 2$  [m/s] in quiescence field. In the current calculations, the maximum velocity induced by the DBD plasma actuator is approximately 1.4 [m/s] with  $D_c$  of 0.25 and BR of 10%. Then the momentum coefficient  $C_\mu$  is calculated as  $3.8 \times 10^{-5}$ . With regard to  $f_{base}$ , it is said that  $f_{base}$  has less effect on the characteristics of the induced flow compared with the other parameters. Here, the  $f_{base}$  for the case of ON  $F^+ = 0.5$  is set as the same value as the experiment<sup>2</sup> of 70. In the other cases, first, the  $f_{base}$  for the case of ON  $F^+ = 50$  is set so that an integer number of base waves is included in a burst wave. The  $f_{base}$  with  $F^+ = 6$  for the case of ON  $F^+ = 6$  and ON  $15\%F^+ = 6$  is set in the same way as in the case of ON  $F^+ = 50$  and chosen as close to the value in the case of ON  $F^+ = 50$  as possible. As the result, the values of  $f_{base}$  in the case with  $F^+$  of 50 and 6 are set as 200 and 240, respectively.

### 5.3.2 Control effects on cycle-averaged aerodynamic performances

Table 5.4 shows the cycle-averaged aerodynamic performances. In terms of enhancing  $C_L$  and  $C_Q$ , the best case is the case of ON  $F^+ = 0.5$  where  $C_L$  and  $C_Q$  are respectively enhanced by 15.8% and 21.3% compared with the case without control. However, the case of ON  $F^+0.5$  also considerably increases  $C_D$  and this results in moderate increase in  $L/D$ . When focus is on  $L/D$ , the best cases are the case of ON  $F^+ = 6$  and ON  $F^+ = 50$ . These two cases successfully enhances  $C_L$  without significant increase in  $C_D$  unlike the case of ON  $F^+ = 0.5$ . In the best cases with regard to  $L/D$ ,  $L/D$  is enhanced by 4.2% compared with the case without control. The torque coefficient  $C_Q$  is enhanced most in the case of ON  $F^+ = 0.5$ , the enhancement is 21.3%. The case of ON  $15\%F^+ = 6$  does

Table 5.4: Cycle-averaged aerodynamic performances.

Case name	$C_L$	$C_D$	$L/D$	$C_Q$	$\zeta_d$
OFF	0.709	0.198	3.58	0.136	0.0723
ON $F^+ = 0.5$	0.821	0.226	3.63	0.165	0.0520
ON $F^+ = 6$	0.772	0.207	3.73	0.159	0.0847
ON $F^+ = 50$	0.772	0.207	3.73	0.159	0.0749
ON 15% $F^+ = 6$	0.734	0.211	3.48	0.140	0.0830

not show better control effects on the cycle-averaged aerodynamic performances. With regard to the pitch damping  $\zeta_d$ , the case of ON  $F^+ = 6$  is the best and the case of ON  $F^+ = 0.5$  is the worst. Here,  $\zeta_d$  tend to decrease as the increase of reduced frequency. With the reduced frequency  $k$  of  $0.02\pi$ ,  $\zeta_d$  is always positive in all the cases.

### 5.3.3 Control effects on phase-averaged flowfield

Figure 5.10 presents the phase- and span-averaged chordwise velocity field with  $C_p$  and  $C_f$  distributions. In stage 1, where the formation of LSB is observed, the separation is suppressed most in the case of  $F^+ = 6$  or delayed in the other controlled cases as observed by  $C_f$  distributions (Figure 5.10(a), (b)). Delay of the separation leads to the delay in formation of LSB and thus rise in negative  $C_p$  around the LSB is also delayed (Figure 5.10(b)). However, once an LSB is formed, the size of LSB is reduced and the negative  $C_p$  peak by the LSB is enhanced in the controlled cases other than the case of ON 15% $F^+ = 6$  (Figure 5.10(c)). In the case of ON 15% $F^+ = 6$ , the peak  $C_p$  near the LSB is decreased and it may be caused by the delayed formation of the LSB, or by the upstream-propagating effect of the DBD plasma actuator.

As  $AoA$  increases and the stage comes into 2, the LSB breaks down in the cases other than the case of ON  $F^+ = 50$  and the consequent DSV convects toward downstream (Figure 5.10(d)).

Figure 5.10(e) and (f) respectively depicts the phase at which  $C_L$  takes the largest and the second largest peak for the case of OFF (stage 3). The control effects in this stage are not clear due to the large oscillation by the DSV.

After the DSV sheds into the wake, the flowfield is in full-stall. In the case of ON  $F^+ = 0.5$ , however, the DBD plasma actuator promotes the formation of large vortices from the leading edge while the other cases show no significant changes in the flowfield (stage 4, Figure 5.10(g)).

In stage 4 after  $AoA$  sufficiently decreases, the flow begins to reattach from around  $x/c = 10\% \sim 20\%$  and soon the reattachment point moves toward downstream. The cases with DBD plasma actuator control promote the reattachment as shown in Figure 5.10(h). The most significant control effect is observed in the case of ON  $F^+ = 6$ ; in this case, the reattachment is so promoted that the effect begin to be observed even in Figure 5.10(g), at  $AoA$  of  $15.1^\circ$ .

### 5.3.4 Control effects on phase-averaged aerodynamic performances

To see the control effects in details, the aerodynamic performances and the separation and reattachment points against the pitching phase or  $AoA$  are investigated. Figure 5.11 presents the phase-averaged aerodynamic performances against  $AoA$ .

First, in the stage 1 where an LSB forms near the leading edge, control effects are observed as slight decreases in all the aerodynamic performances among all the cases due to the delay of the formation of LSB.

In the stage 2, which is associated to the breakdown of LSB, the  $AoA$  at which rapid changes in aerodynamic performances are observed become higher in all the controlled cases. This corresponds to delaying the dynamic stall. This delay effect is clearly observed in the aerodynamic performance curves, for example in  $C_L$  or  $C_M$  curve; the best case with regard to this effect is the case of ON  $F^+ = 50$  and then the second best is the case of ON  $F^+ = 6$ . Here, delaying the dynamic stall onset itself is a good effect because it can extend the operation condition of the fluid machineries or the aircrafts. Delaying the stall onset also works positively to all the aerodynamic performances because delaying stall simply means prolonging the duration out of stall, where sever deterioration in aerodynamic performances are experienced. The control effects that the cases of ON  $F^+ = 6$  and ON  $F^+ = 50$  gained large increase in  $C_L$  without large increase in  $C_D$  are contributed by this effect.

With respect to the stage 3 where the DSV convects over the airfoil surface affecting drastic changes to all the aerodynamic performances, the precise evaluation of the control effect in this stage is difficult. This is because the behaviours of large vortices have large variations in each different pitching cycle and so lots of cycles are needed for the phase-averaged characteristics to converge. Thus, in this thesis, control effects in the stage 3 are put out of scope of the investigations.

After all large vortices shed, the undulation of the aerodynamic performances caused by large vortices is not observed any longer and so the phase-averaged characteristics

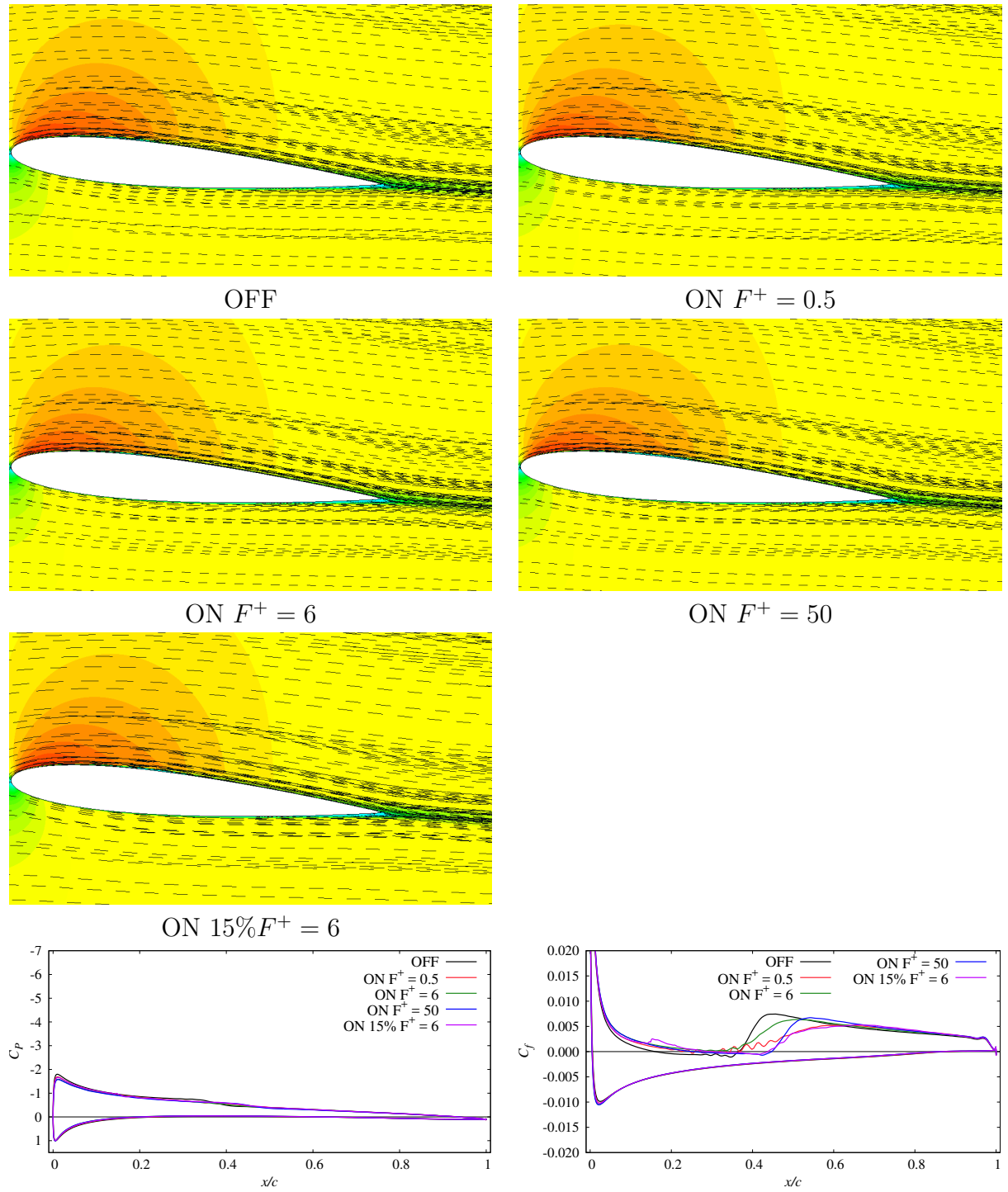
(a)  $phase = 0^\circ$  ( $AoA = 5.0^\circ$  in pitching up)

Figure 5.10: Top three rows: Phase- and span-averaged chordwise velocity field for pitching NACA0012 airfoil.

Bottom row : Phase-averaged  $C_p$  and  $C_f$  distributions.

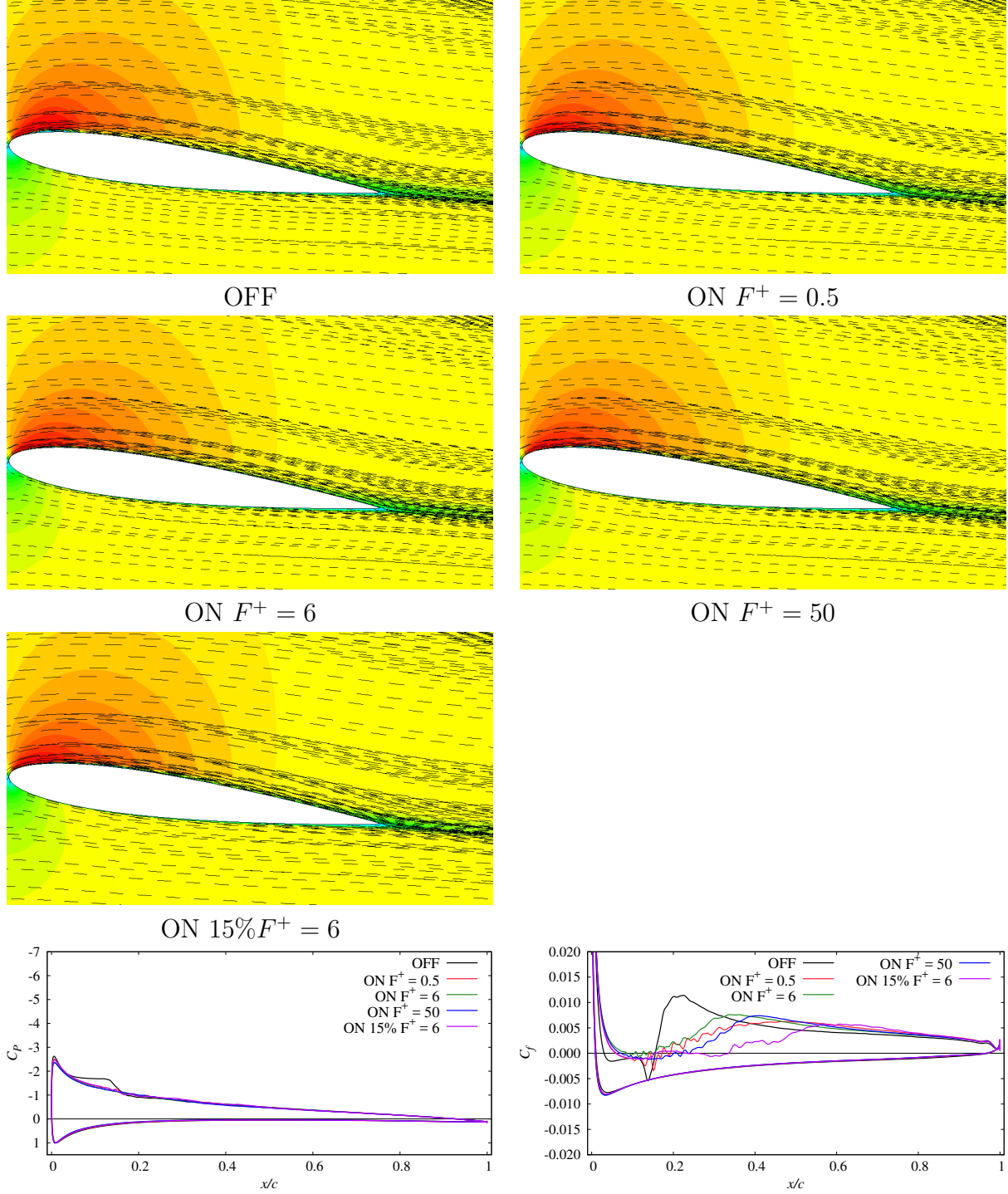
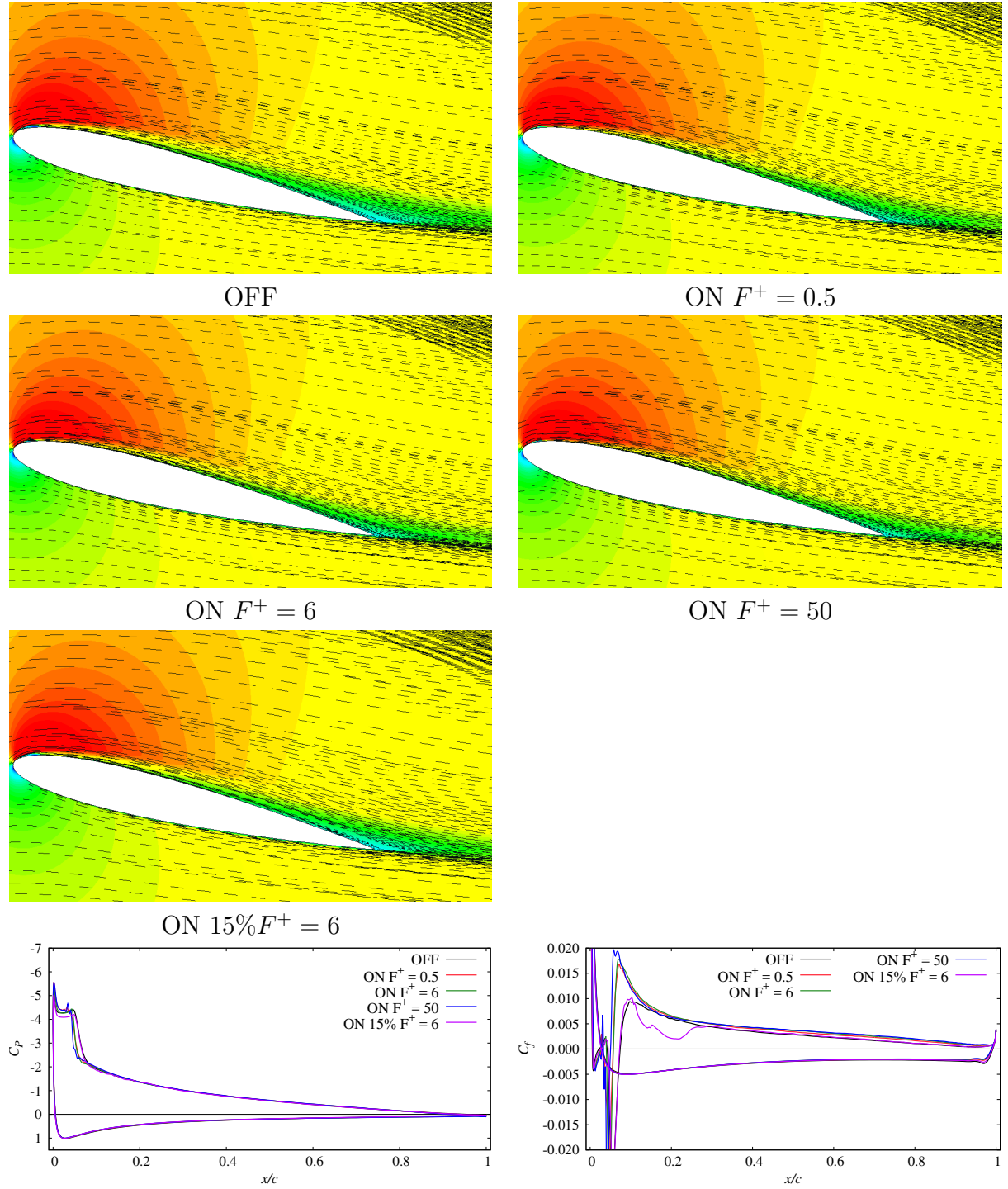
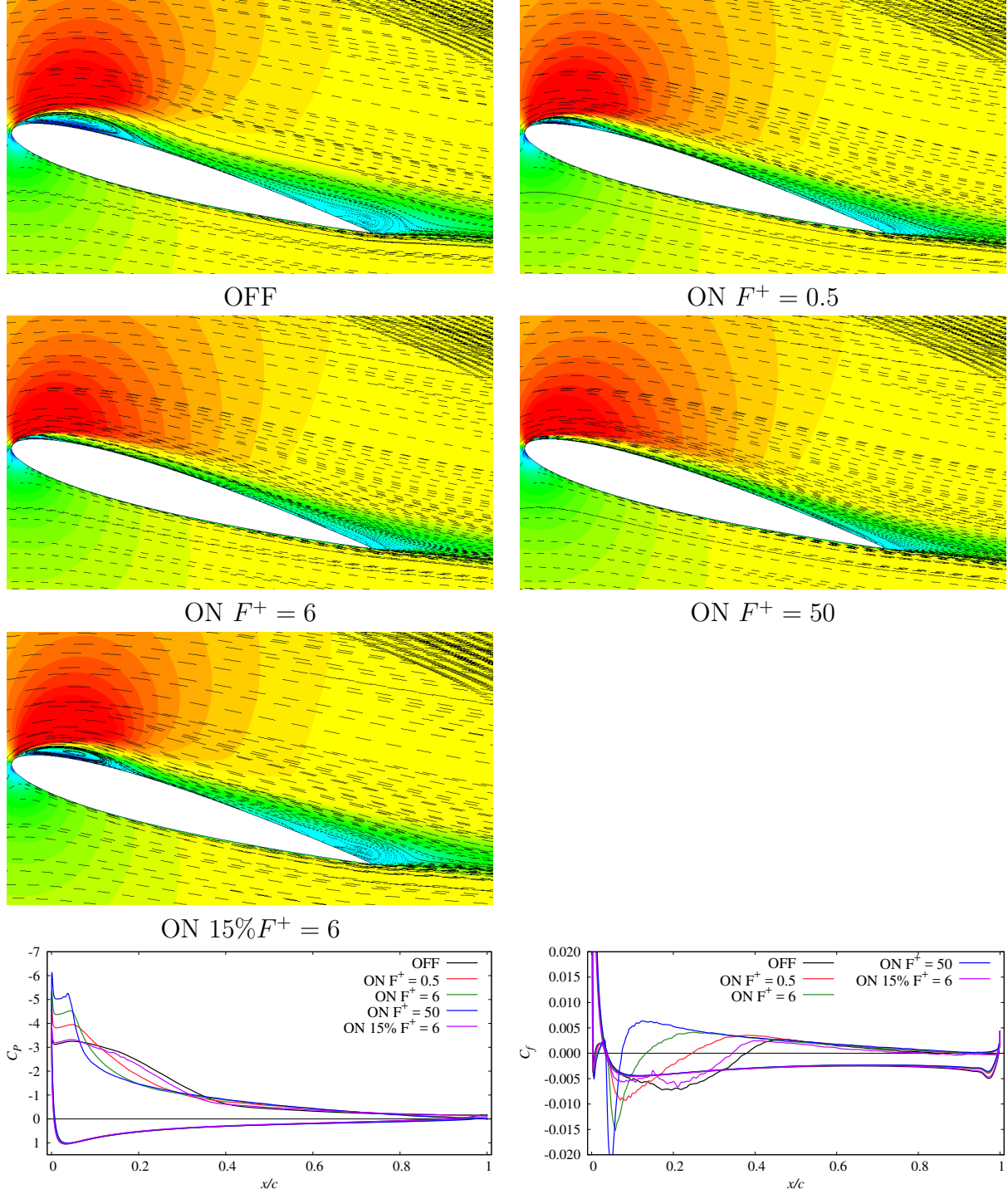


Figure 5.10: *Continued.*

(c)  $phase = 82^\circ$  (AoA =  $12.9^\circ$  in pitching up)Figure 5.10: *Continued.*

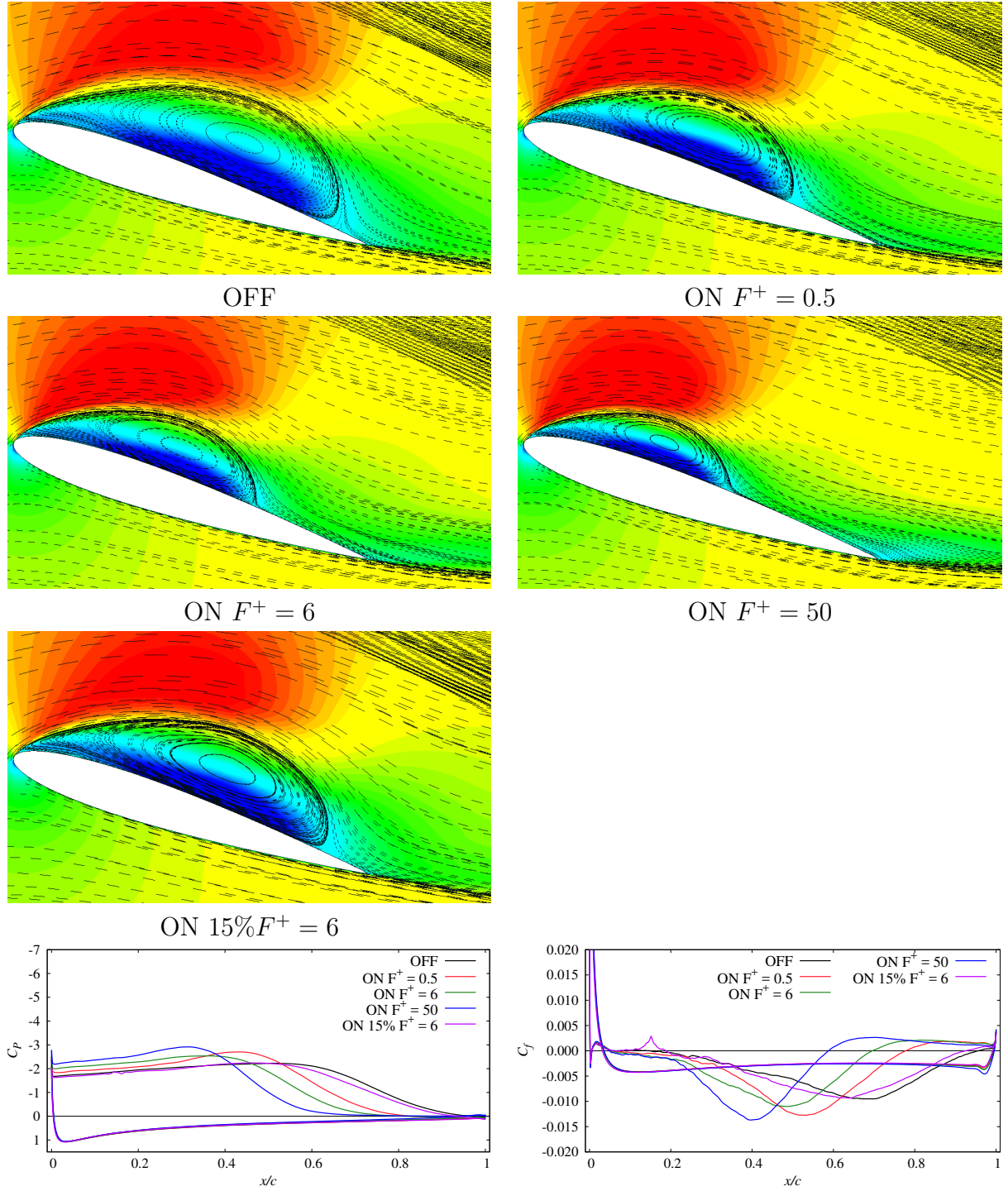


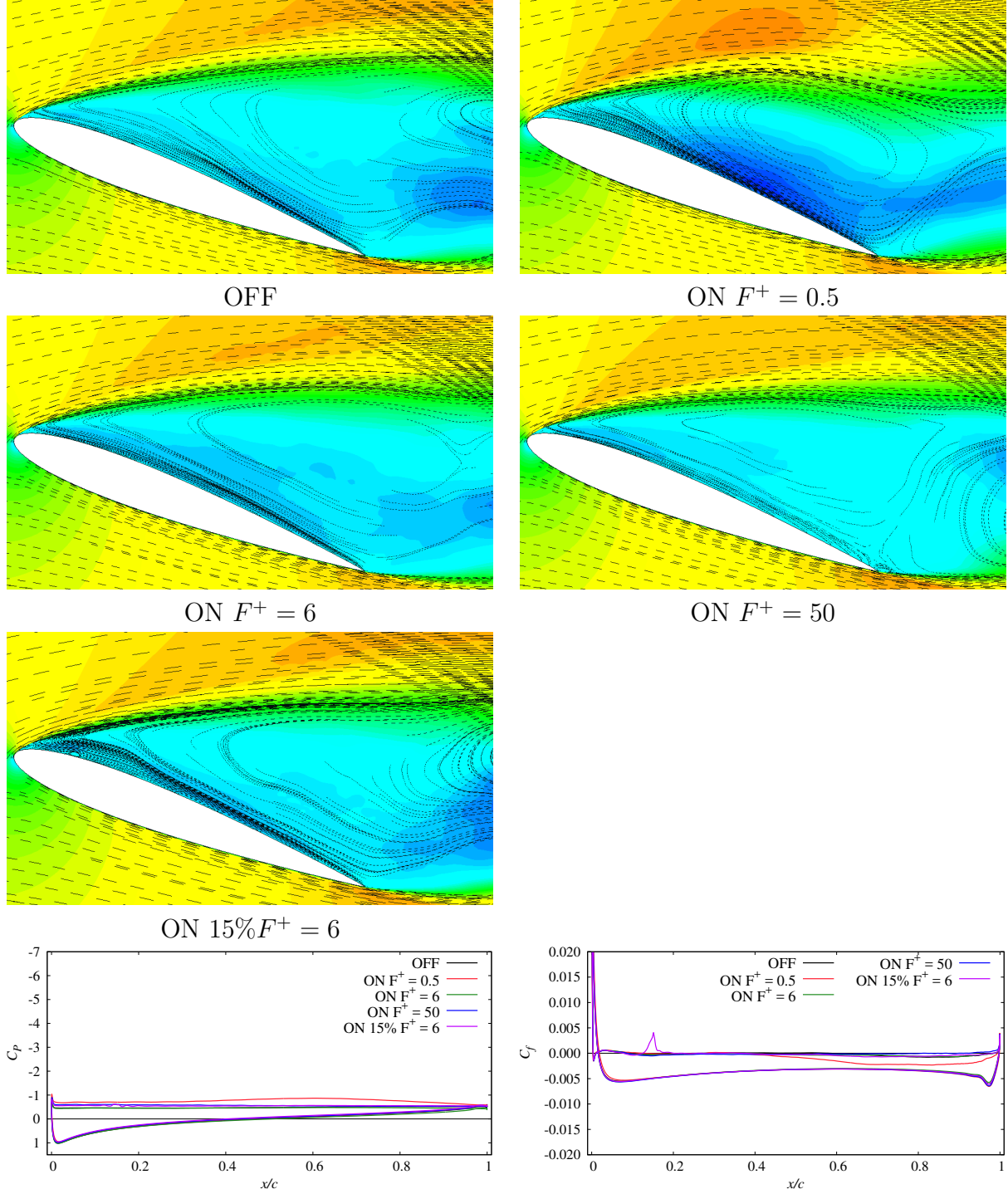


(d)  $phase = 96^\circ$  (AoA =  $15.9^\circ$  in pitching up)

Figure 5.10: *Continued.*

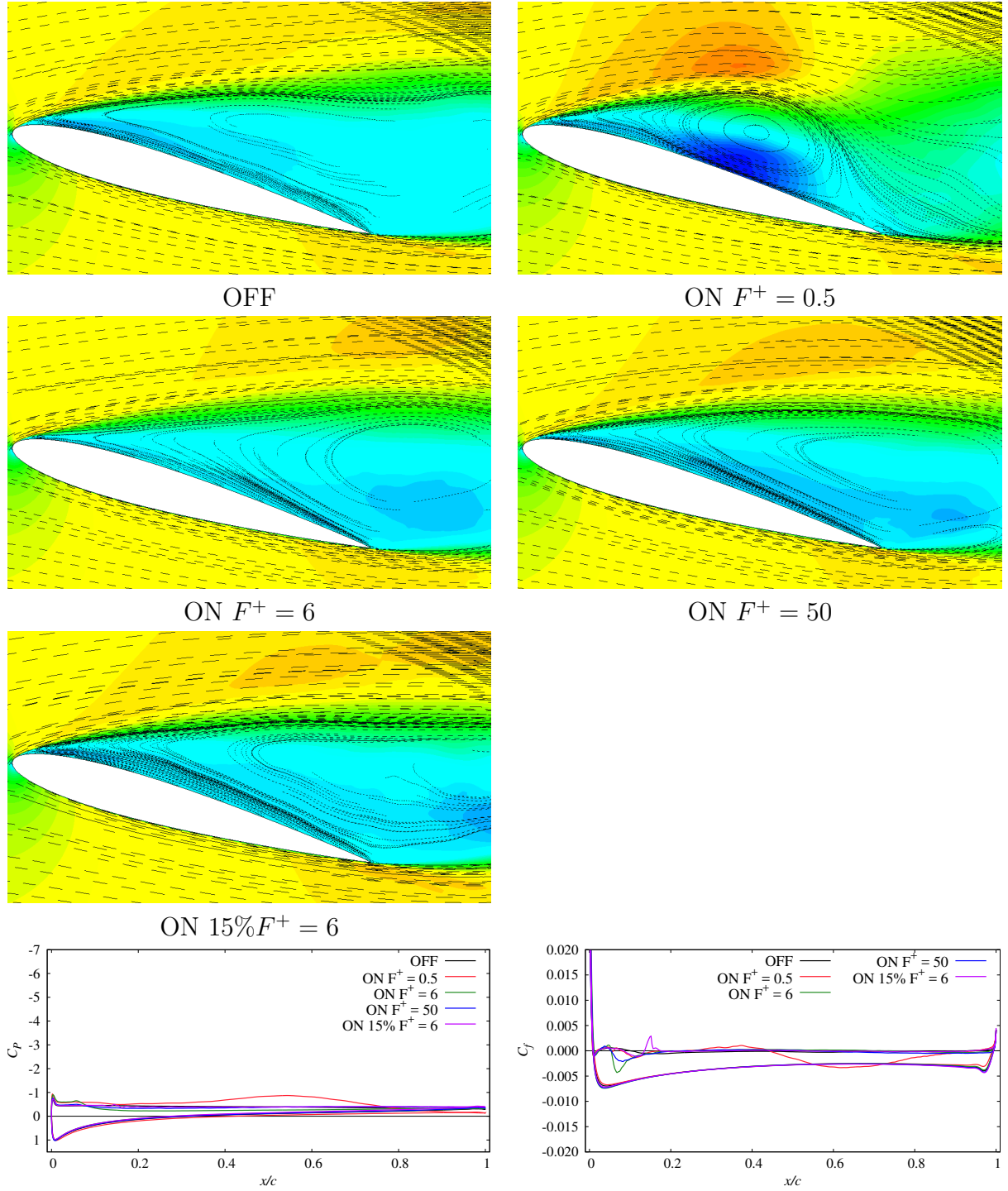


(e)  $phase = 110^\circ$  ( AoA =  $18.3^\circ$  in pitching up)Figure 5.10: *Continued.*



(f)  $phase = 238^\circ$  (  $AoA = 20.3^\circ$  in pitching down)

Figure 5.10: *Continued.*

(g)  $phase = 270^\circ$  (  $AoA = 15.1^\circ$  in pitching down)Figure 5.10: *Continued.*

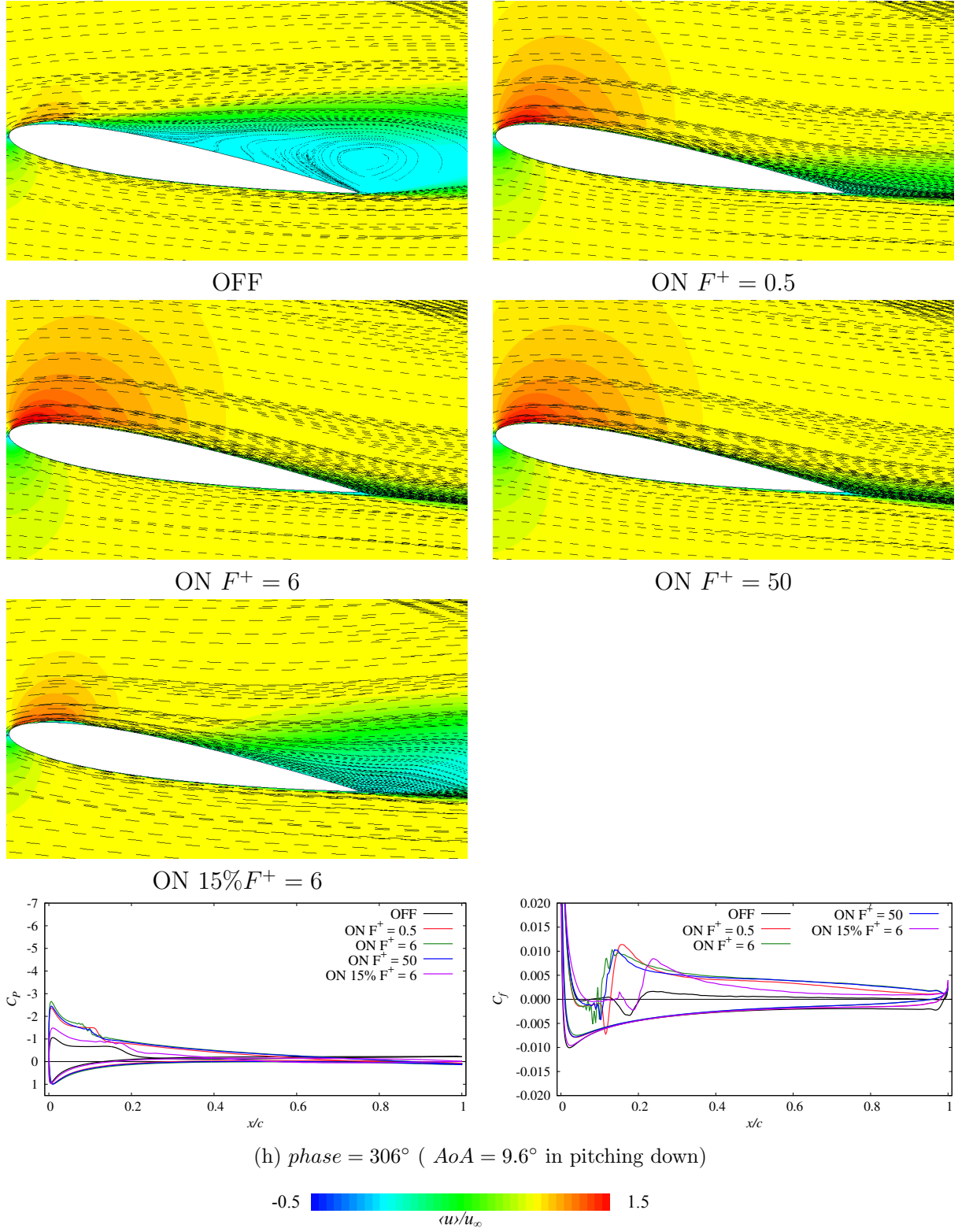
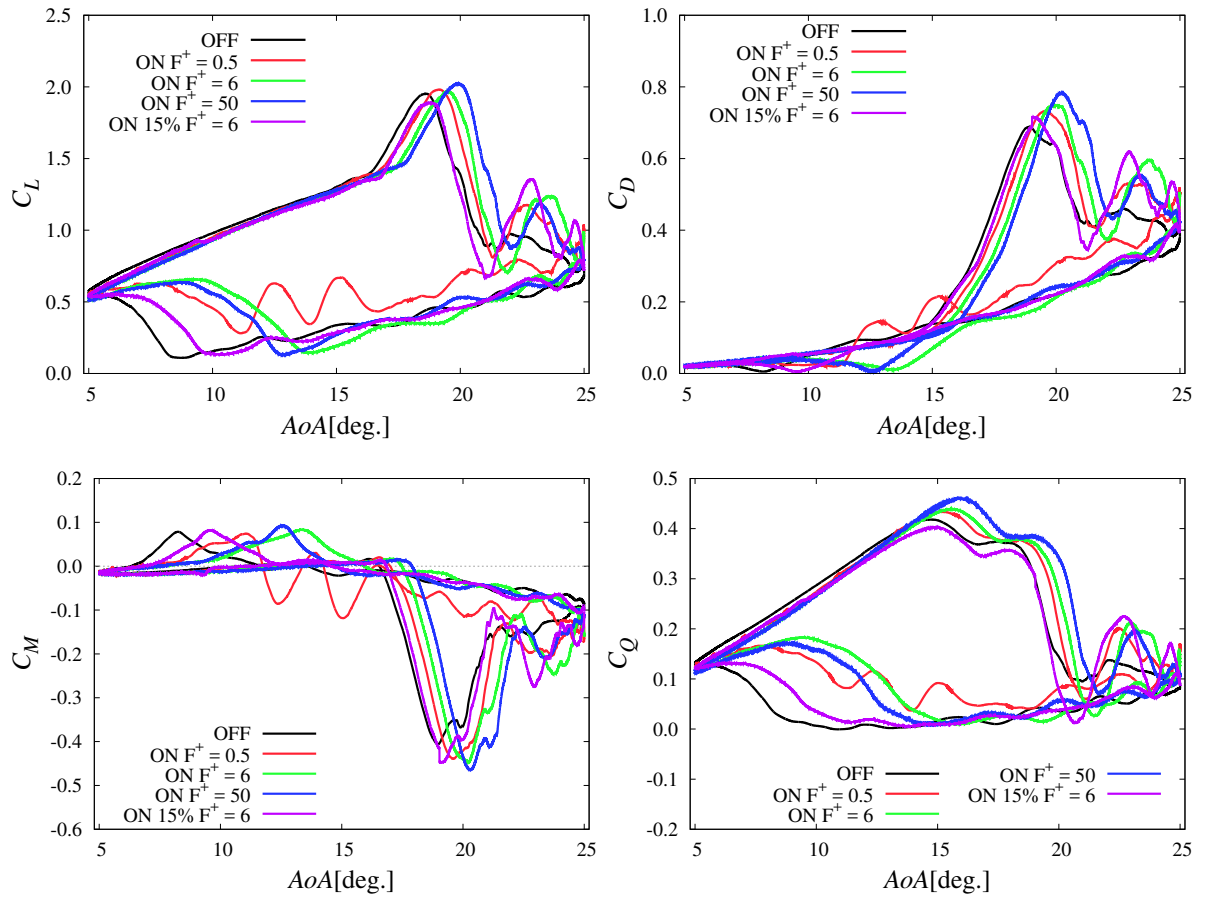


Figure 5.10: *Continued.*

Figure 5.11: Aerodynamic performances against  $AoA$  for pitching NACA0012 airfoil.

can be discussed. In this study, stage 4 corresponds to the  $AoA$  from approximately  $25^\circ$  to around  $12^\circ$ . In this stage, only the case of ON  $F^+ = 0.5$  has outstanding control effect that all the aerodynamic performances are considerably affected with undulation. Comparing the flowfield for the case of OFF and ON  $F^+ = 0.5$  depicted in Figure 5.10(g) suggests that this effect is brought by the large vortices induced by the DBD plasma actuator. Considering the other control effects of the case of ON  $F^+ = 0.5$  are not so significant, it can be said that the large portion of the change in the cycle-averaged aerodynamic performances owes to this effect.

In the final stage of the dynamic stall, the largest control effect is observed here. For example, the  $C_L$  curve shows rapid increase around  $AoA$  of  $9^\circ$  in the case of OFF while this is advanced to  $AoA$  of around  $15^\circ$  in the case of ON  $F^+ = 50$ . As aforementioned, the rapid increase in  $C_L$  around the final stage of the pitching down is due to the recovery to the attached state and so the control effect here is the effect that the recovery to the attached state is promoted. Here, the case with the fastest increase in  $C_L$  is observed is the case of ON  $F^+ = 6$ , followed by the case of ON  $F^+ = 50$ . The control effect by the promotion of the reattachment also prolongs the duration out of stall; large portion of the increase in  $C_L$  without increase in  $C_D$  in the cycle-averaged value in the cases of ON  $F^+ = 6$  and ON  $F^+ = 50$  would be made by this effect.

### 5.3.5 Control effects on phase-averaged separation and reattachment point

The aerodynamic performances are calculated by integrating the aerodynamic forces along the entire airfoil chord and the chordwise features are diminished. Next, to evaluate the control effects on the chordwise features, the transient of the separation, reattachment, and secondary separation points against the pitching phase are depicted with the chordwise distribution of  $C_p$  on the upper surface (suction side) in Figure 5.12. The lowest values of  $C_p$  are observed around the LSB around *phase* of  $45 \sim 90^\circ$ . The aforementioned control effects can be seen here; the negative  $C_p$  area around the LSB is enhanced its negative value or broadened out to the phase-wise direction, the negative  $C_p$  level during the dynamic stall are risen up by large vortices, and/or the relatively weak negative  $C_p$  area during the dynamic stall is narrowed down.

The separation, reattachment, secondary separation points help us to evaluate the control effects quantitatively. Here,  $AoA_{BD}$  and  $AoA_{RA}$  can be indicators of the control effect of delaying the stall onset and promoting the reattachment, respectively.  $AoA_{BD}$ ,  $AoA_{DS}$ ,  $AoA_{LD}$ ,  $AoA_{LDDS}$ , and  $AoA_{RA}$  for each case are presented in Table 5.5. Here,



Table 5.5: Control effects on  $AoA_{BD}$ ,  $AoA_{DS}$ ,  $AoA_{LD}$ , and  $AoA_{RA}$  for pitching NACA0012 airfoil.

$AoA_{BD}$  for the case of ON  $F^+ = 0.5$  is obtained by rough estimation.

$AoA_{BD}$ ,  $AoA_{DS}$ , and  $AoA_{LD}$  are in the pitching up and  $AoA_{RA}$  is in the pitching down.

Case name	$AoA_{BD}$	$AoA_{DS}$	$AoA_{LD}$	$AoA_{LDDs}$	$AoA_{RA}$
OFF	12.6°	14.2°	18.6°	18.6°	9.4°
ON $F^+ = 0.5$	(13.0°)	14.6°	19.2°	19.2°	12.6°
ON $F^+ = 6$	13.1°	15.2°	19.5°	19.5°	15.0°
ON $F^+ = 50$	13.7°	15.5°	19.9°	19.9°	14.3°
ON 15% $F^+ = 6$	13.0°	14.6°	18.8°	18.8°	11.2°

$AoA_{BD}$  for the case of ON  $F^+ = 0.5$  cannot be calculated precisely because of the large oscillation of the reattachment point induced by the DBD plasma actuator and so rough estimation is listed in the table instead. The most effective case in delaying the stall onset is the case of ON  $F^+ = 50$ , followed by the case of ON  $F^+ = 6$ , ON  $F^+ = 0.5$ , and ON 15% $F^+ = 6$ . In the most effective case,  $AoA_{BD}$  is delayed by 1.1°,  $AoA_{DS}$  is delayed by 1.3°, and  $AoA_{LD}$  is delayed by 1.3°. Here,  $AoA_{LD}$  and  $AoA_{LDDs}$  is identical to the flowfield around NACA0012 airfoil under the current condition. Here, similar to the discussion on the stage 3, the behaviour of the DSV have large variations between the pitching cycles and so the effect on  $AoA_{LDDs}$  itself is not investigated in this thesis. In terms of promoting the reattachment, the most effective case is the case of ON  $F^+ = 6$ , followed by the case of ON  $F^+ = 50$ , ON  $F^+ = 0.5$ , and ON 15% $F^+ = 6$ .

Note that DBD plasma actuator has a certain level of capability of controlling the separation in the dynamic flowfield as observed in Figure 5.12, especially for the case of  $F^+ = 6$ , although this appears as the diminished plateau of  $C_p$  near the LSB as shown in Figure 5.10(b) in this case.

### 5.3.6 Summary on control effects

To conclude the results on control effects presented in this section, the control effects on aerodynamic performances can be arranged as the following three major control effects.

1. Delaying dynamic stall onset
2. Enhancing aerodynamic forces during full-stall
3. Promoting reattachment

In the following section, the mechanisms for each control effects are investigated.

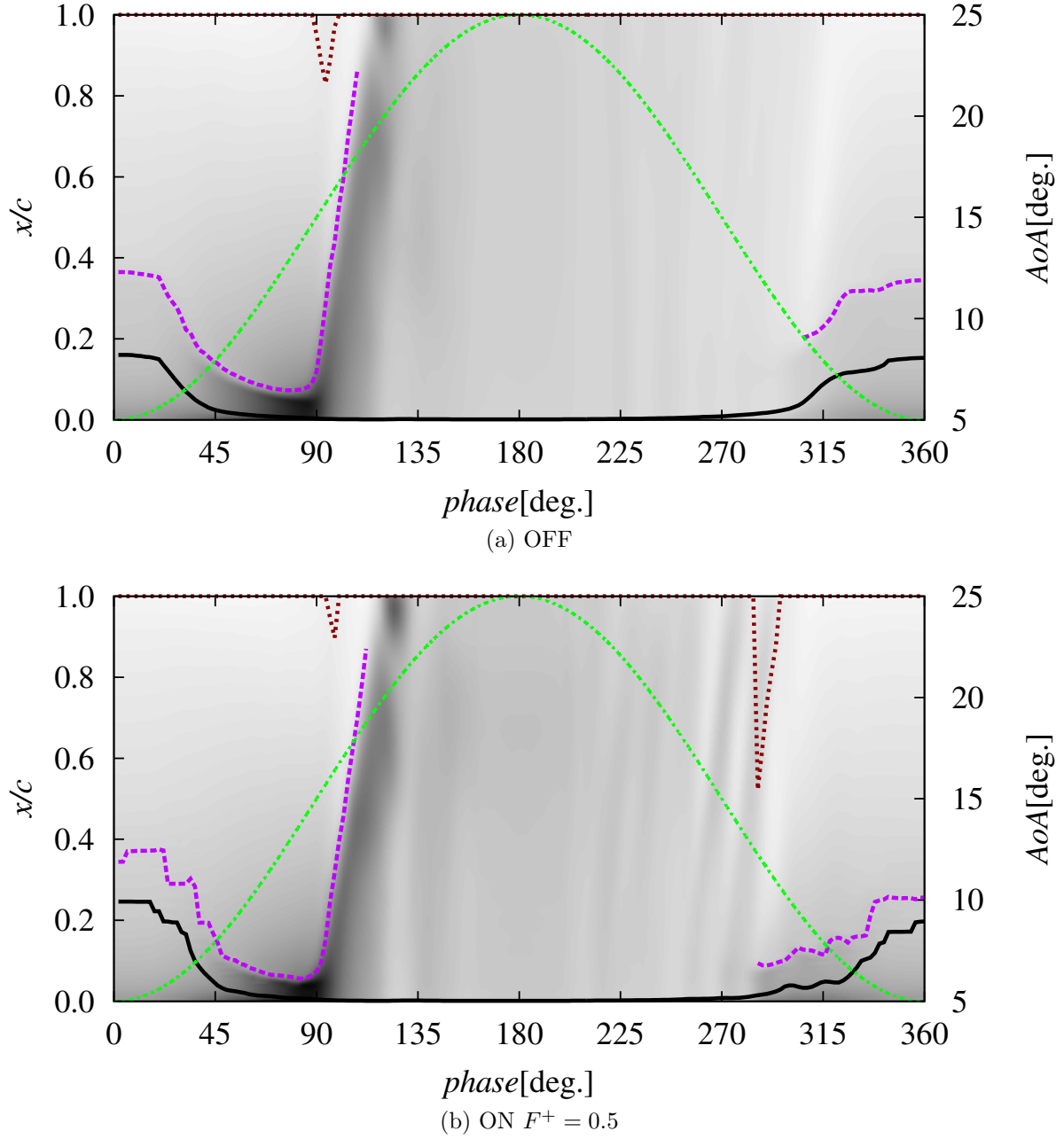
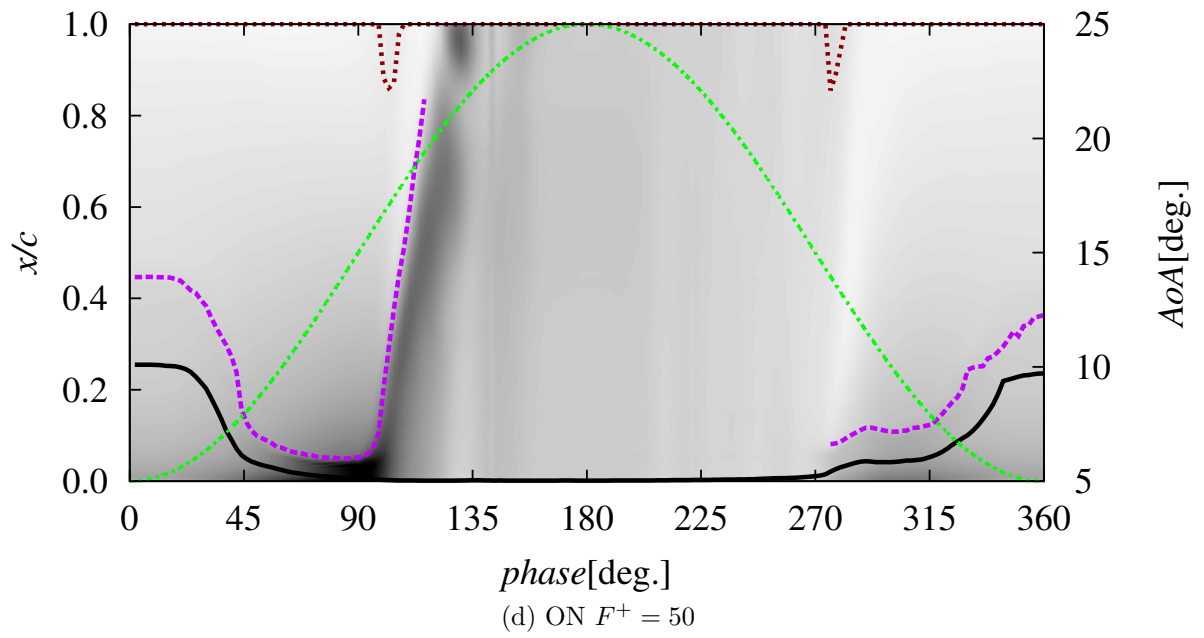
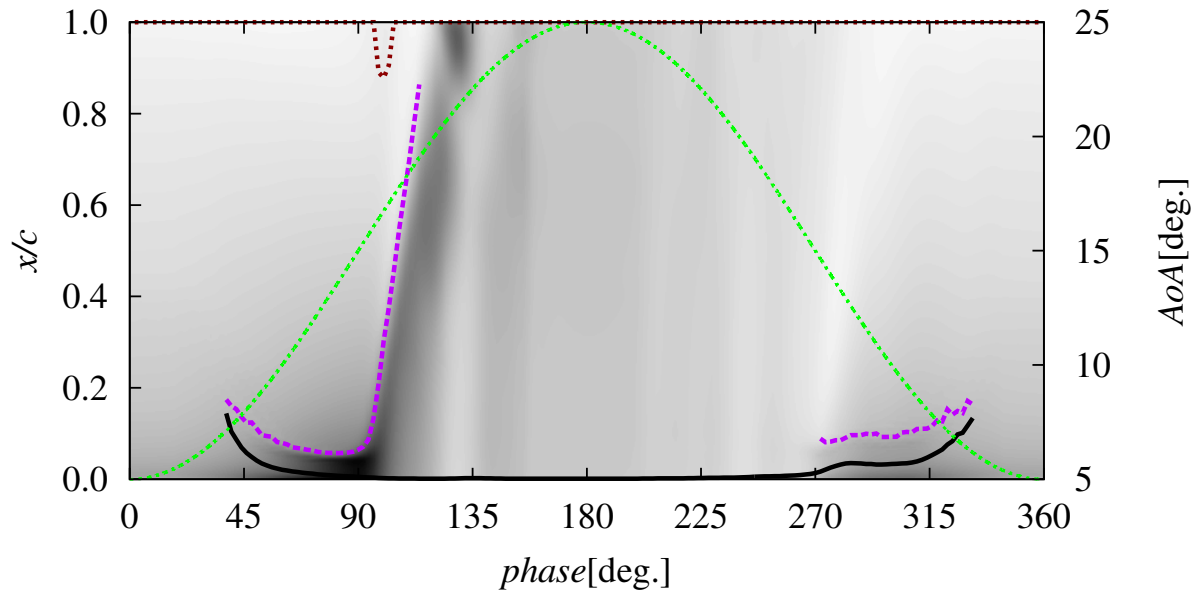


Figure 5.12: Separation, reattachment, and secondary separation points against pitching phase for NACA0012 airfoil. Corresponding  $AoA$  is plotted with right axis. Background color depicts phase- and span-averaged  $C_p$  distribution.



Figure 5.12: *Continued.*

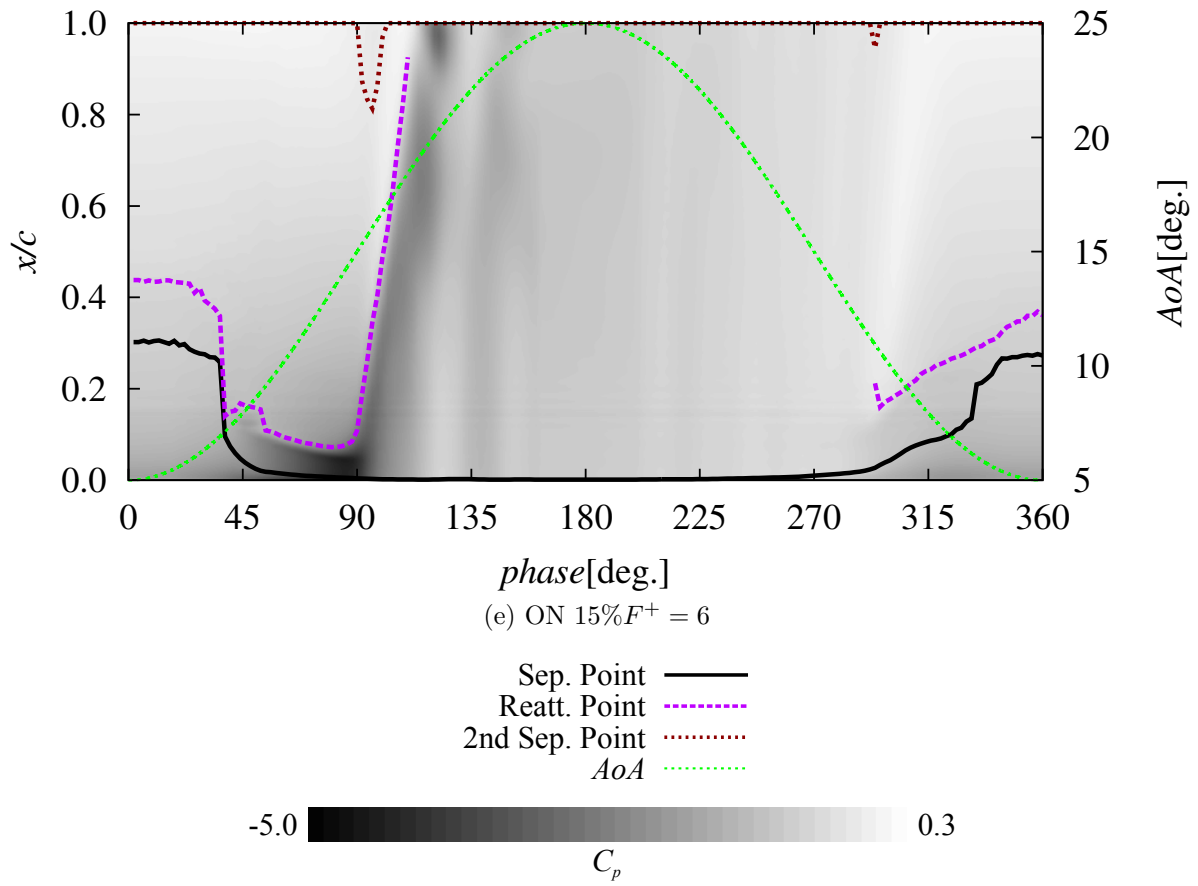


Figure 5.12: *Continued.*

## 5.4 Control mechanisms

### 5.4.1 Mechanisms on delaying dynamic stall onset

First discussed is the control mechanisms on the control effect of delaying the dynamic stall onset. With regard to delay of the dynamic stall onset, Visbal et al. conducted LESs of the control of the dynamic flowfield around a pitching NACA0012 airfoil at Reynolds number of  $2.0 \times 10^5 \sim 5.0 \times 10^5$  with a focus of delaying the dynamic stall onset.<sup>6, 45, 46</sup> In these references, the control is implemented by a zero-net mass flow control device with high frequency of  $6.25 \sim 150.0$  and the results are that the dynamic stall onset is delayed more in the case with higher  $F^+$ . Their conclusions in there references can be summarized that the control mechanism is related to the receptivity of the LSB, whose most instable frequency ranges between  $St$  of  $60 \sim 120$  depending on  $AoA$  and Reynolds number, and the cases with higher  $F^+$  can delay the dynamic stall onset more by effectively feeding energy into the LSB. Here, the result that the case with higher  $F^+$  is better is consistent with the result obtained in the current study and it suggests that the mechanism as for delaying the dynamic stall onset is consider to be same with each other, considering the airfoil and Reynolds number are identical or comparable. Therefore, the focus of the analyses on this mechanism is put on the investigation on the behaviour of LSB.

#### Investigation on phase-averaged flowfield

Figure 5.13 presents the phase- and span-averaged chordwise velocity field near the leading edge right before the breakdown of LSB. The size of LSB is significantly reduced in the controlled case, especially in the case of ON  $F^+ = 50$ . The difference can be also observed in Figure 5.14; the cases with better control effect shows smaller size of the LSB both in height and chordwise length.

To observe the effect of turbulent transition and the momentum mixing on the LSB size, TKE and Reynolds stress fields at the same phase with Figure 5.13 are presented in Figure 5.15 and 5.16, respectively. The area where TKE takes maximum value locates more upstream and/or closer to the airfoil in more effective cases. The same can be said on the maximum value of negative Reynolds stress; where the negative Reynolds stress takes maximum locates more upstream and/or closer to the airfoil surface in more effective cases. With regard to the maximum TKE and negative Reynolds stress values, the effective cases have lower maximum value of TKE and negative Reynolds stress values over the entire flowfield, compared with less effective cases. More precise visualization

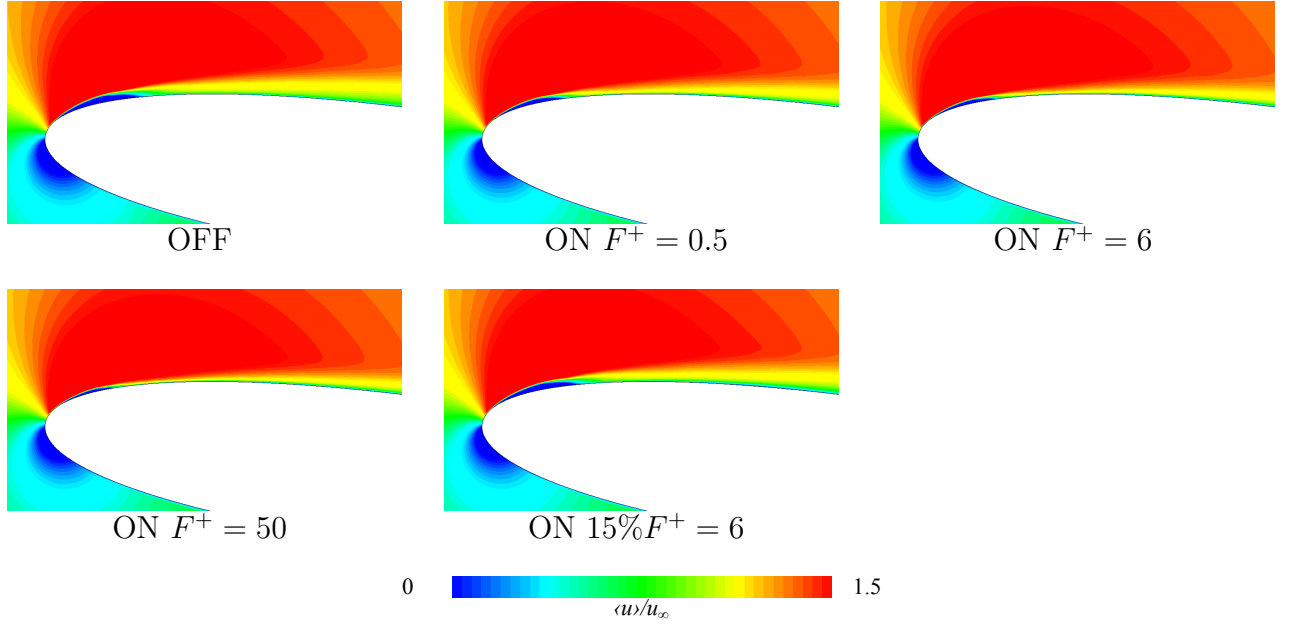


Figure 5.13: Phase- and span-averaged chordwise velocity field near the leading edge at the *phase* of  $76^\circ$  ( $AoA = 12.5^\circ$ )

of the wall-normal distributions of TKE and Reynolds stress near the LSB is presented in Figure 5.17. As observed in the flowfield, the maximum value of TKE is higher and that of negative Reynolds stress is lower in the effective cases. When the focus is on  $x/c = 4\%$  in Figure 5.17, however, the case with the highest value in TKE and the lowest value in negative Reynolds stress is rather the case of  $ON F^+ = 50$ . These suggest that what important for the size of LSB is not only the maximum strength of the turbulent fluctuation over the field as represented by the maximum value of TKE and minimum value of Reynolds stress but also the local strength in upstream region near the airfoil surface.

### Investigation on instantaneous flowfield

To investigate the control mechanism, instantaneous flowfields are investigated next. Figure 5.18 shows the instantaneous flowfields near the leading edge. The sequence of figures covers before and after the actuation timing for the case of  $ON F^+ = 0.5$ . In all the controlled cases with the DBD plasma actuator at  $x/c = 0\%$ , small spanwise-coherent vortices are shed from the leading edge shear layer in synchronization with the actuation timing, whereas no significant spanwise-coherent structures are observed in the case of OFF and  $ON 15\%F^+ = 6$ . Figure 5.19 shows the side-views of the

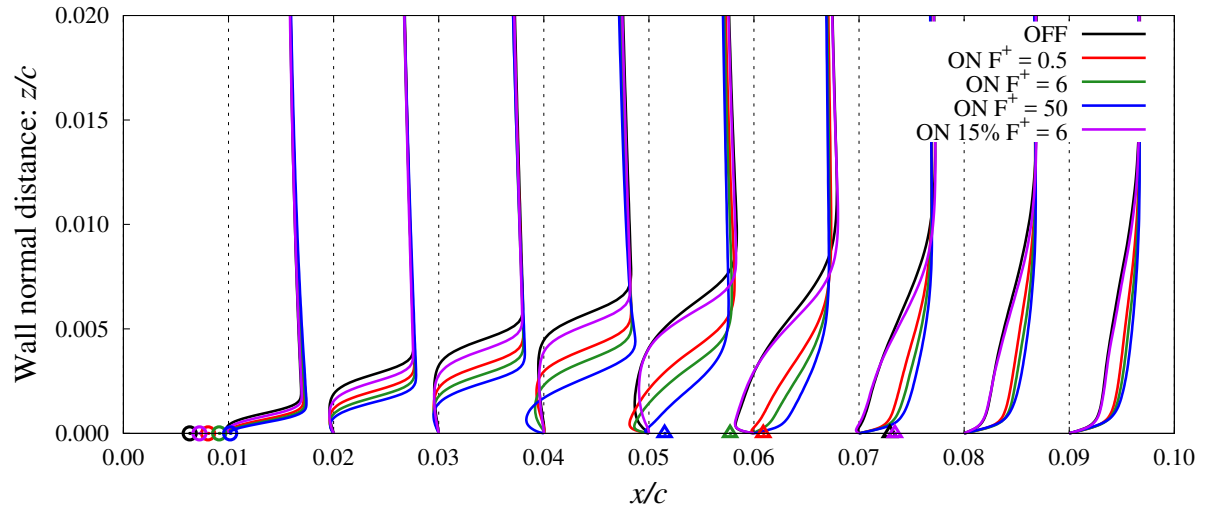


Figure 5.14: Phase- and span-averaged chordwise velocity distributions near the leading edge at the *phase* of  $76^\circ$  ( $AoA = 12.5^\circ$ ). Separation and reattachment points are presented respectively with circles and triangles.

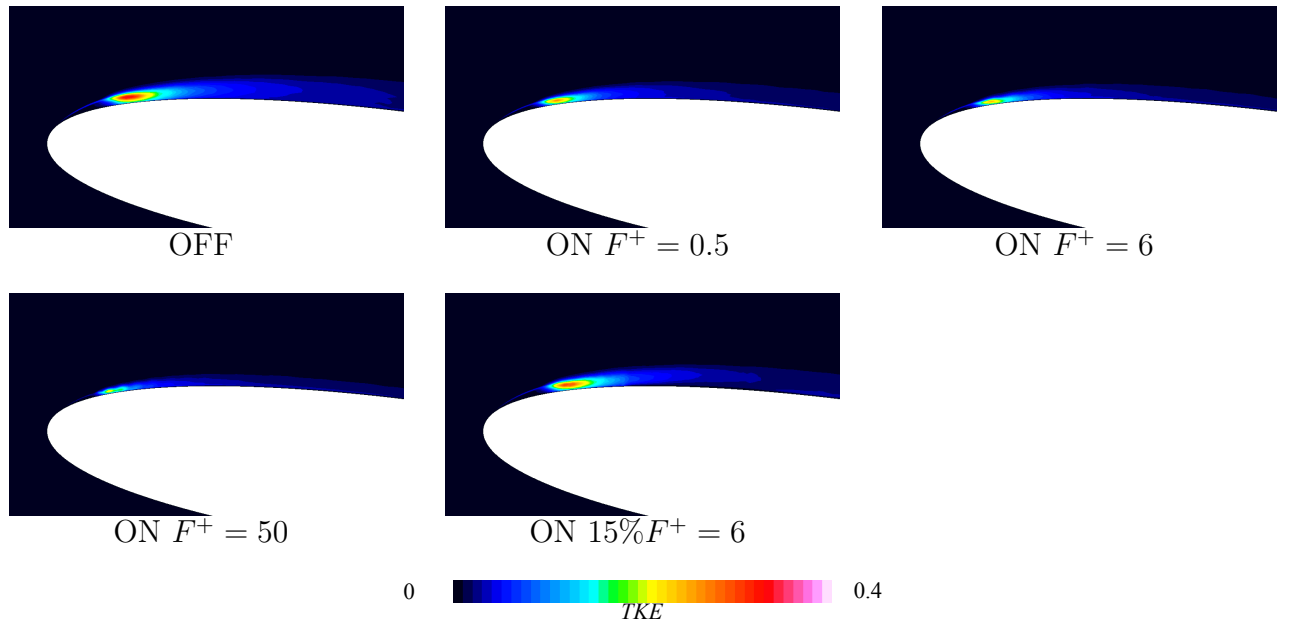


Figure 5.15: Phase- and span-averaged TKE field near the leading edge at the *phase* of  $76^\circ$  ( $AoA = 12.5^\circ$ )

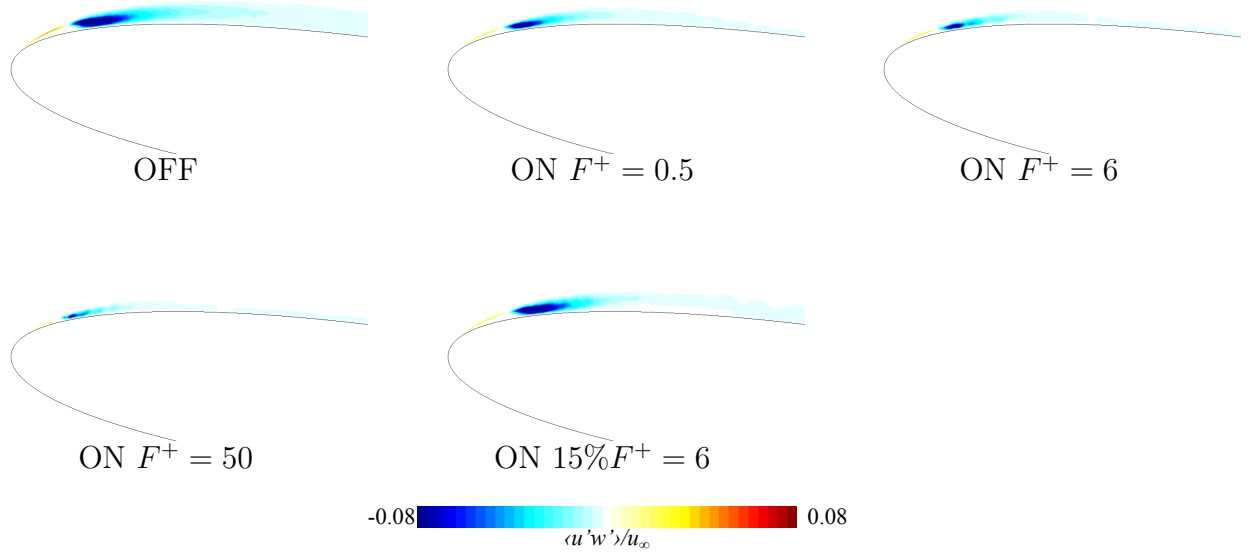
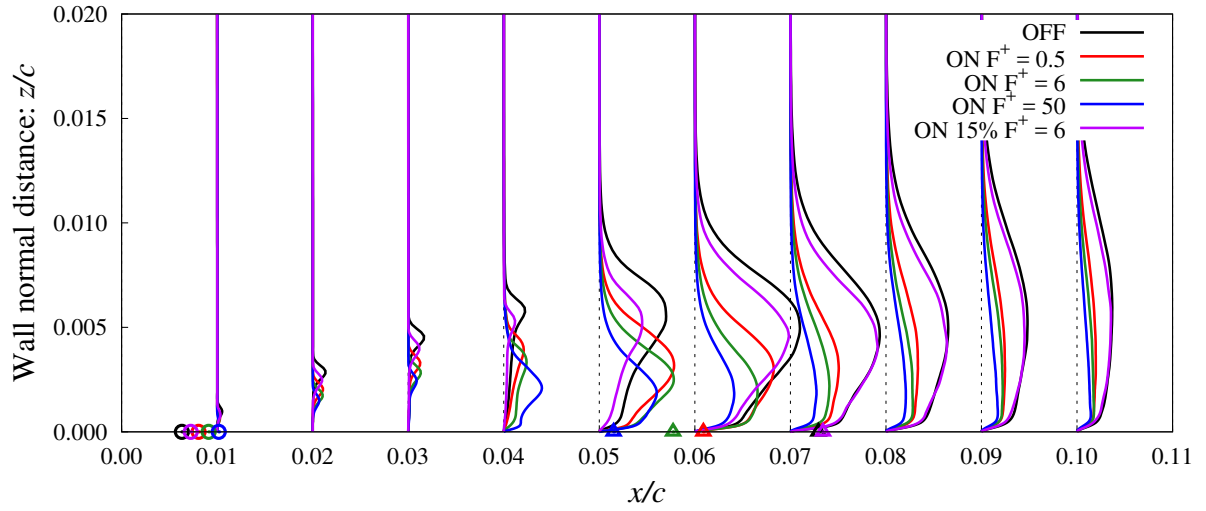


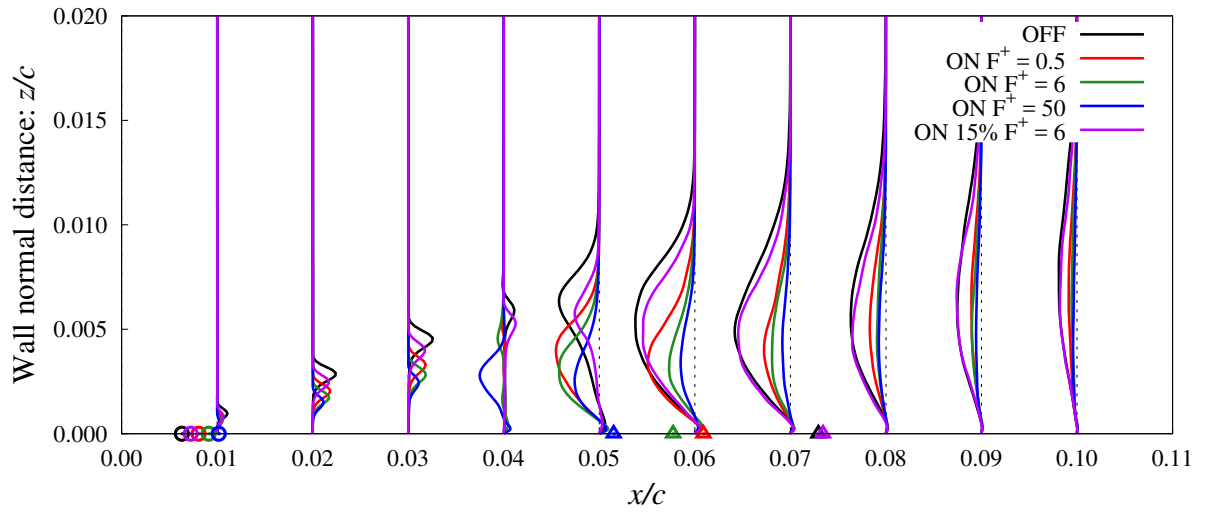
Figure 5.16: Phase- and span-averaged Reynolds stress field near the leading edge at the *phase* of  $76^\circ$  ( $AoA = 12.5^\circ$ )

flowfields at a spanwise cross-section around the same phase with Figure 5.18. While the DBD plasma actuator is turned on, a series of vortices shed from the leading edge show well-aligned behaviour unlike these shed when the actuator is off. These vortices are spanwise-coherent as shown in Figure 5.18 and convect toward downstream with their roller-like shape, but soon decays into three dimensional fine vortex structure. These coherent vortices stop forming as soon as the DBD plasma actuator is turned off and then the shear layer goes back to where the shear layer were right before the actuation. This temporal behaviour of the coherent vortices and the shear layer is apparent in the case of  $ON F^+ = 0.5$  and  $ON F^+ = 6$ . On the other hand, the frequency of  $F^+ = 50$  is so high that no significant time-varying aspect is observed within the time span presented here. Here, no significant changes can be observed by both of these visualizations in the case of  $ON 15\%F^+ = 6$ .

The quantitative analysis on the phase-averaged flowfield helps us to understand the gross control effect easily. On the other hand, the effects of unsteady actuation are averaged out. To investigate the effects of unsteady actuation, the results of quantitative analyses on the instantaneous flowfield are presented. Here, the following analyses are processed on the span-averaged instantaneous flowfield and then the results are phase-averaged. Figure 5.20 presents the behaviour of the separation and reattachment points and the shear layer near the leading edge around the phase of the breakdown of LSB



(a) TKE



(b) Reynolds stress

Figure 5.17: Phase- and span-averaged chordwise TKE and Reynolds stress distributions near the leading edge at the *phase* of  $76^\circ$  ( $AoA = 12.5^\circ$ ). Separation and reattachment points are presented respectively with circles and triangles.



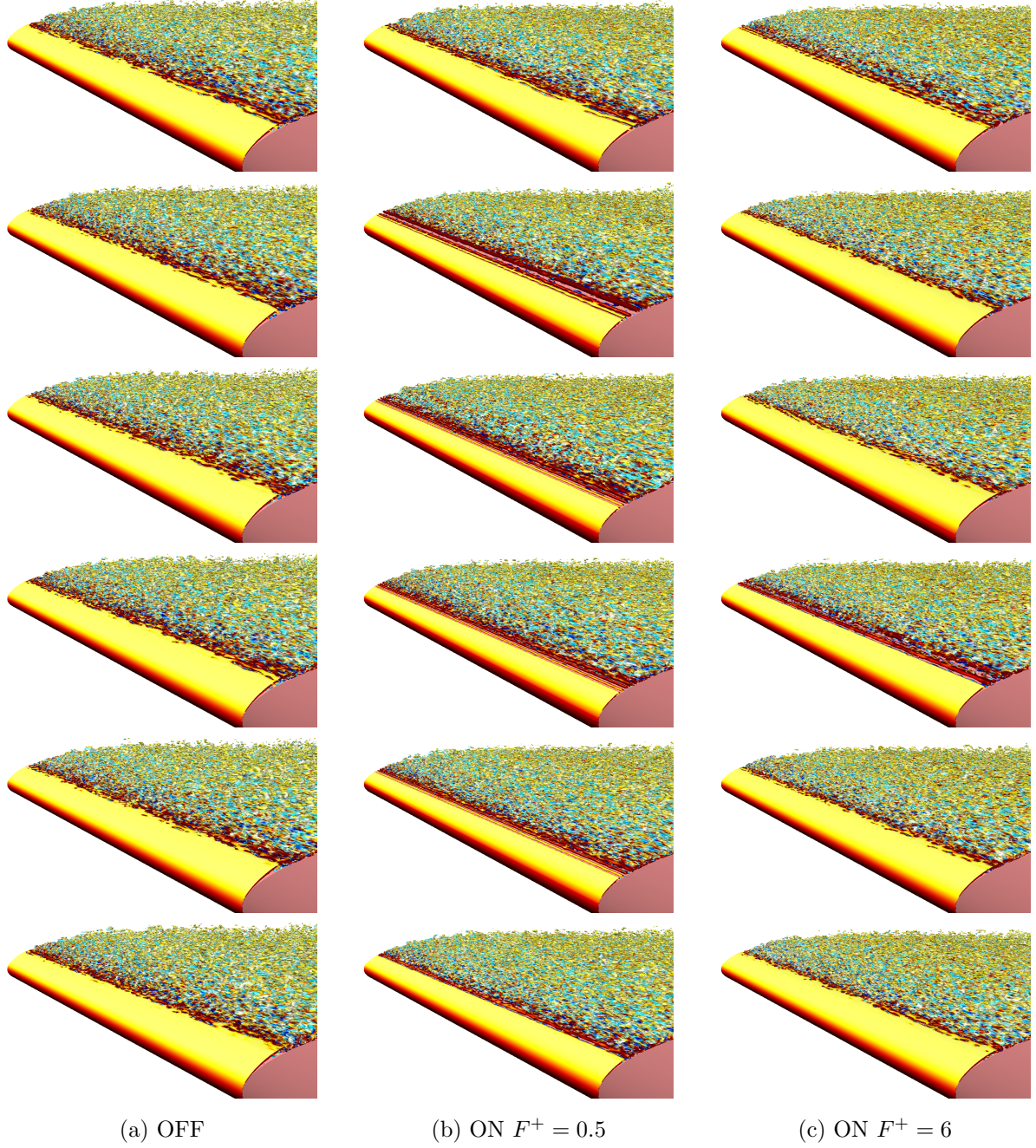


Figure 5.18: Snapshots of instantaneous flowfields around  $AoA$  of  $10^\circ$  in the *phase* of  $65^\circ$  for pitching NACA0012 airfoil. The iso-surfaces indicate the second invariant of the velocity gradient tensor colored by spanwise vorticity. Time lapses from top to bottom with time increment of  $tu_\infty/c = 0.05$ .



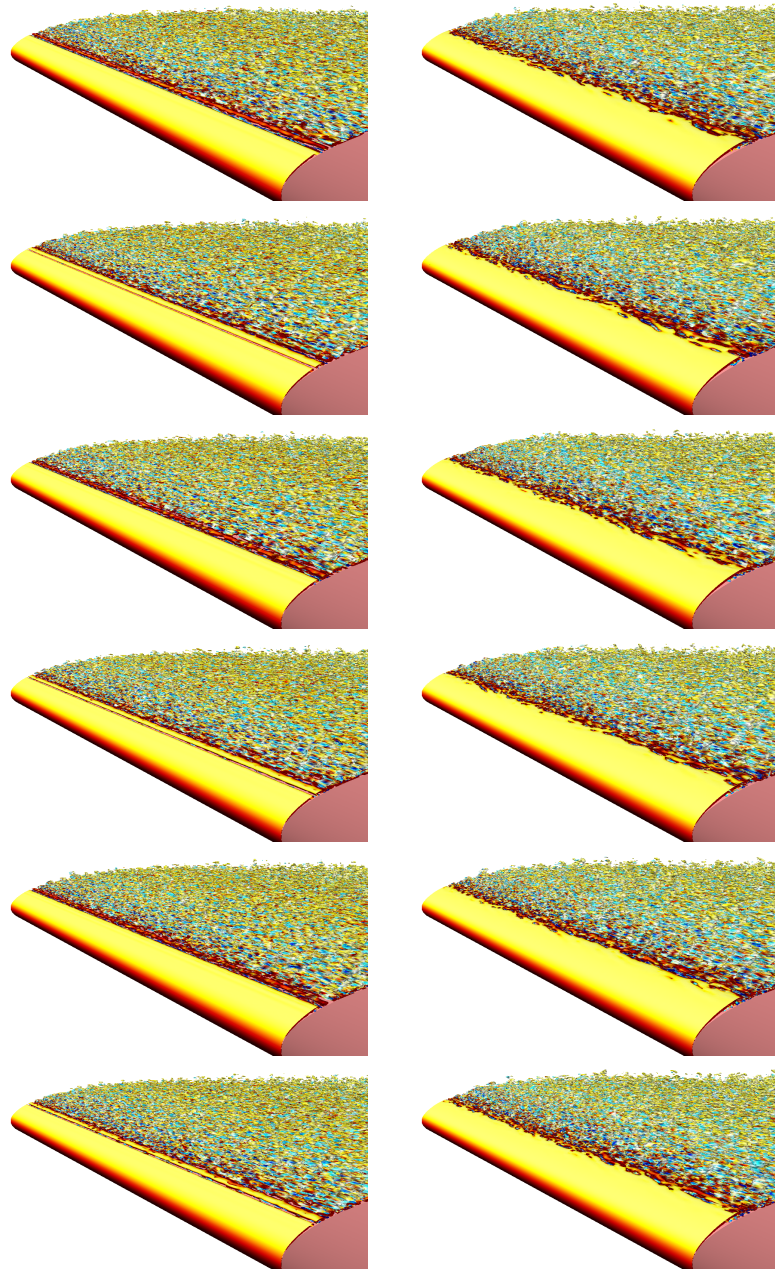
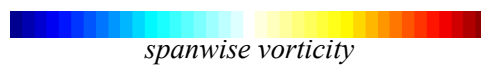
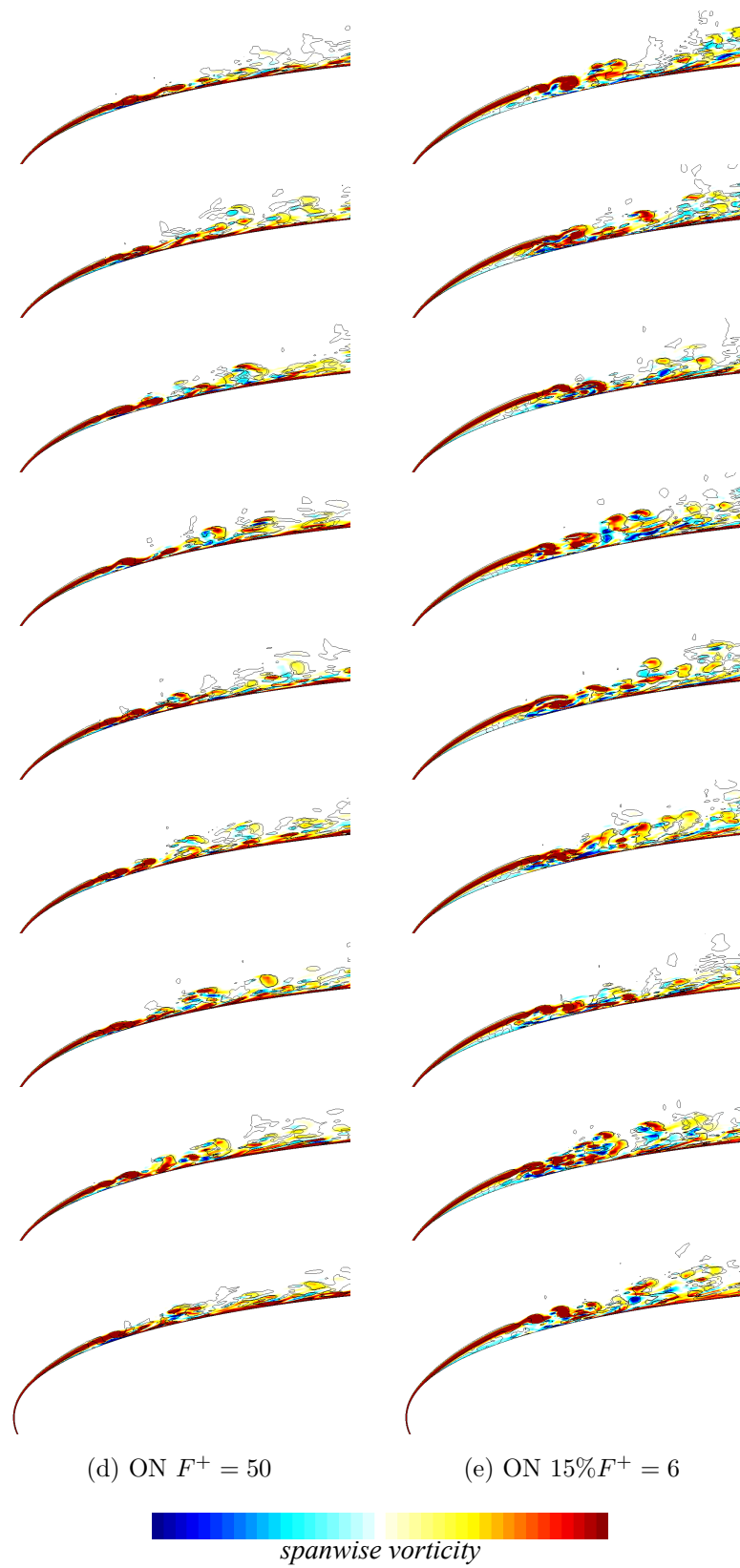
(d) ON  $F^+ = 50$ (e) ON  $15\%F^+ = 6$ *spanwise vorticity*Figure 5.18: *Continued.*



Figure 5.19: Side-view for instantaneous flowfield around the leading edge shear layer in the *phase* of  $65^\circ$ . The black line contour depicts the second invariant of the velocity gradient tensor, and color contour depicts the spanwise vorticity. Time lapses from top to bottom with time increment of  $tu_\infty/c = 0.065$ .

Figure 5.19: *Continued.*

against the pitching phase. Here, the angle of the shear layer is defined by the angle between the airfoil surface and the line which is defined where the spanwise vorticity take maximum at each chordwise location. The  $AoA$  at which the LSB breaks down are listed in Table 5.5 in section 5.3.5, and these  $AoA$  corresponds to the *phase* of  $76.2^\circ$  in the case of OFF, approximately  $78^\circ$  in the case of ON  $F^+ = 0.5$ ,  $79.1^\circ$  in the case of ON  $F^+ = 6$ ,  $82.5^\circ$  in the case of ON  $F^+ = 50$ , and  $78.2^\circ$  in the case of ON  $15\%F^+ = 6$ , respectively. Around the *phase* of  $70 \sim 90^\circ$  in Figure 5.20, the difference in the separation points among all the cases are relatively small compared with the reattachment points and therefore the reduction in the LSB length seen in Figure 5.13 is brought by the advancement of reattachment points. The best case of ON  $F^+ = 50$  has the reattachment points closest to the leading edge. The second best case of ON  $F^+ = 6$  has also advanced reattachment point compared with the case of OFF. The same can be observed by the case of ON  $F^+ = 0.5$ . Soon after the actuation, however, the reattachment position goes back to the almost same chordwise position before the actuation. The actuation with  $F^+$  of 0.5 is very intermittent and only three times of burst actuation take place within the phase range depicted in this figure. Here, the duration that the DBD plasma actuator is turned off in the case of ON  $F^+ = 0.5$  is as long as  $tu_\infty/c = 1.8$ , which is considerably large compared with the possible time scale of the behaviour of LSB. However, the reattachment point does not go back to the chordwise position without the control. This suggests that the behaviour of LSB is considerably affected by the history of the flowfield, not just by the flowfield at the moment. As for the case of ON  $15\%F^+ = 6$ , the chordwise position of the reattachment point is not so advanced because the DBD plasma actuator locates in downstream of the separation point and reattachment point is less affected by the DBD plasma actuator.

From the observation of the reattachment points, there is a the general trend that the effective cases in delaying the dynamic stall onset have advanced reattachment point (ON  $F^+ = 0.5$ , ON  $F^+ = 6$ , and ON  $F^+ = 50$ ). In Figure 5.20(b), the similar trend can be observed; the shear layer is displaced toward more the airfoil surface in more effective cases. Here, The control effect of the case of ON  $15\%F^+ = 6$  can be found in the angle of the shear layer in Figure 5.20(b). In the case of ON  $15\%F^+ = 6$ , the reattachment point crosses the actuator position at the *phase* of around  $48^\circ$ . At this phase, the reattachment point is highly oscillated and at the same time the shear layer is displaced upward and then downward. After this oscillation, the angle of the shear layer keeps lower angle compared with the case of OFF although the anteroposterior relation between the reattachment point and the DBD plasma actuator is reversed. As will be presented in the following section, the DBD plasma actuator have significant

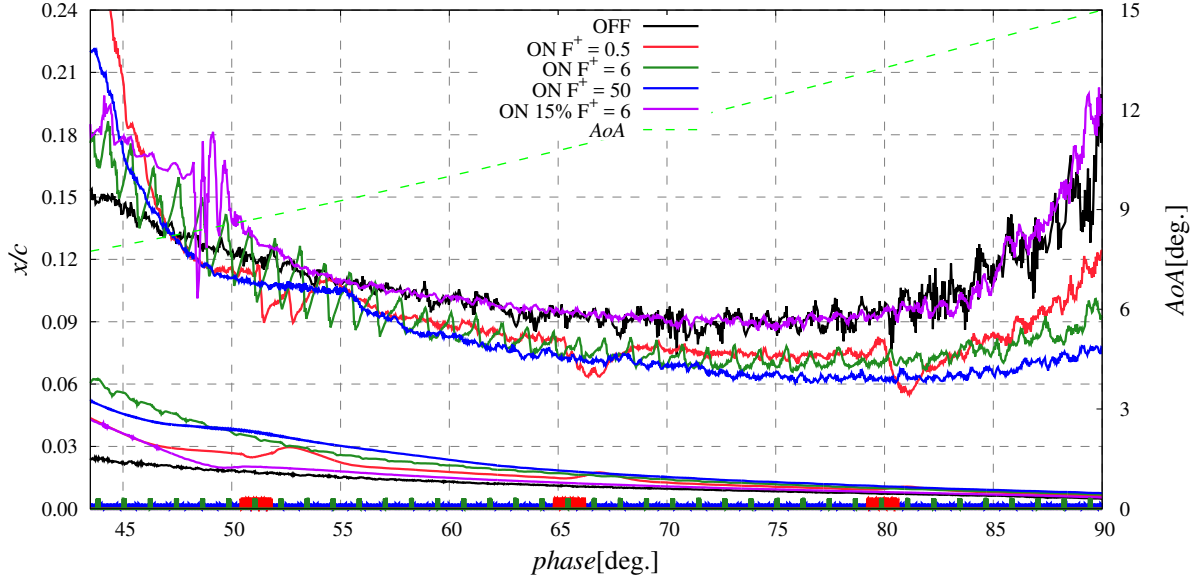
capability of stimulating the shear layer, even when the DBD plasma actuator is located in downstream of the shear layer. The control effect of the case of ON 15%  $F^+ = 6$  may owe to the effect of changing the “history” of the flowfield as shown in the case of ON  $F^+ = 0.5$ , or the upstream-propagating effect of the actuator, or both of them. Even though these cannot be completely discriminated on the current control effect.

PSD of the chordwise velocity in the *phase* of  $68^\circ$ , right before the breakdown of LSB, at several position on the leading edge shear layer is presented in Figure 5.21. Here PSD is calculated by the same method used in Figure 5.9. The instability frequency in the case without control is observed around  $St$  of 90, as presented in the previous subsection. The actuation with  $F^+$  of 50 can effectively stimulate this  $St$  with its harmonics and the corresponding frequency is already amplified before as upstream as  $x/c = 1.5\%$ . The actuation with  $F^+$  of 0.5, whose case have  $f_{base}$  of 70, have amplified frequency around  $St$  of 70 or higher. Here, the duration of frequency analysis is so short that the effect of  $F^+$  of 0.5 cannot be resolved. The actuation with  $F^+$  of 6 shows relatively slow amplification of the unstable frequency around  $St$  of 90. When focusing on  $St$  around 90, the cases with higher  $F^+$  or  $f_{base}$  can amplify the instability frequency of 90 earlier.

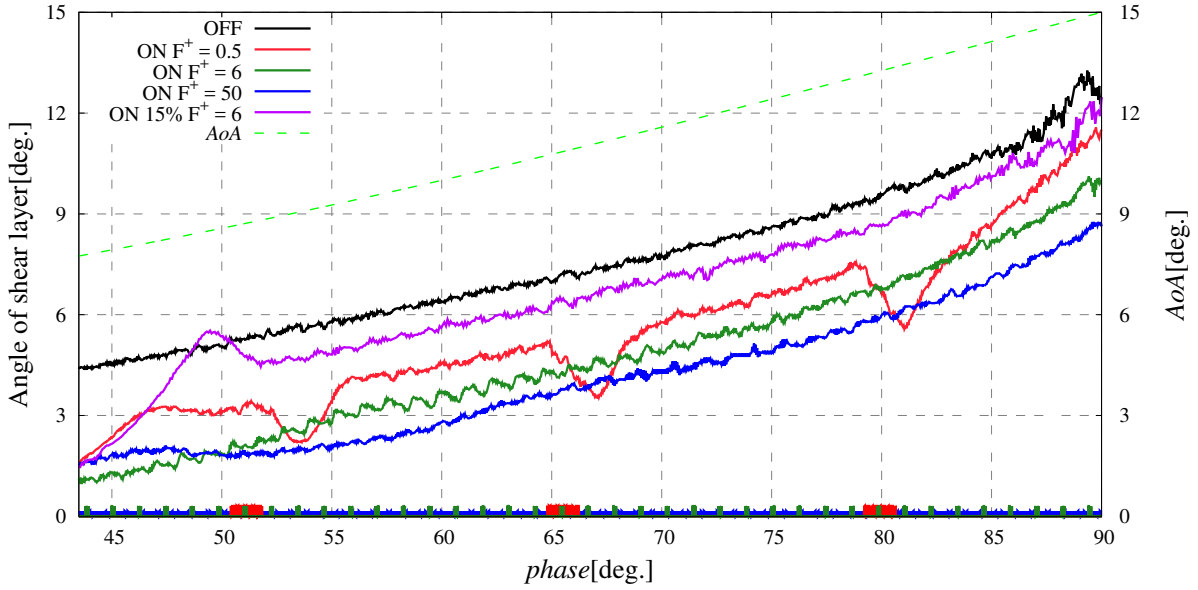
Observing the slope of PSDs, it seems that there is other amplified frequencies above  $St$  of 100, although not resolved in the current study. With control, it is considered that the instability frequency shifts toward higher frequency due to the decreased vorticity thickness.<sup>176</sup> Considering that the instability frequency of LSB is as high as  $St$  of 100 or maybe above, the cases with high actuation frequency whose low order harmonics can stimulate the instability frequency would have better control effect on delaying the dynamic stall onset. Here, as seen in Figure 5.20, the case of ON  $F^+ = 0.5$  has better capability of stimulating the instability frequency thanks to its high  $f_{base}$  at the timing of actuation. The reason why the case of ON  $F^+ = 0.5$  shows poor control effect in delaying the dynamic stall onset would be due to the low frequency of  $F^+$ , which cannot follow up the speed of increase of  $AoA$ .

### 5.4.2 Mechanisms on enhancing aerodynamic forces during full-stall

Control mechanisms of enhancing the aerodynamic forces during the full-stall is investigated next. The effect is observed apparently only in the case of ON  $F^+ = 0.5$  as shown in Figure 5.11. Mitsuo et al.<sup>2</sup> conducted experiments to control of the flowfield under the same flow condition and with the same  $F^+$ , as partially introduced in Chapter 4. The exact same control effect of enhancing the aerodynamic forces is clearly observed



(a) Separation and reattachment points



(b) Angle of leading edge shear layer

Figure 5.20: Closed-up of separation and reattachment points and angle of shear layer around the breakdown of LSB against pitching phase for NACA0012 airfoil. The actuation timing is presented at the bottom.



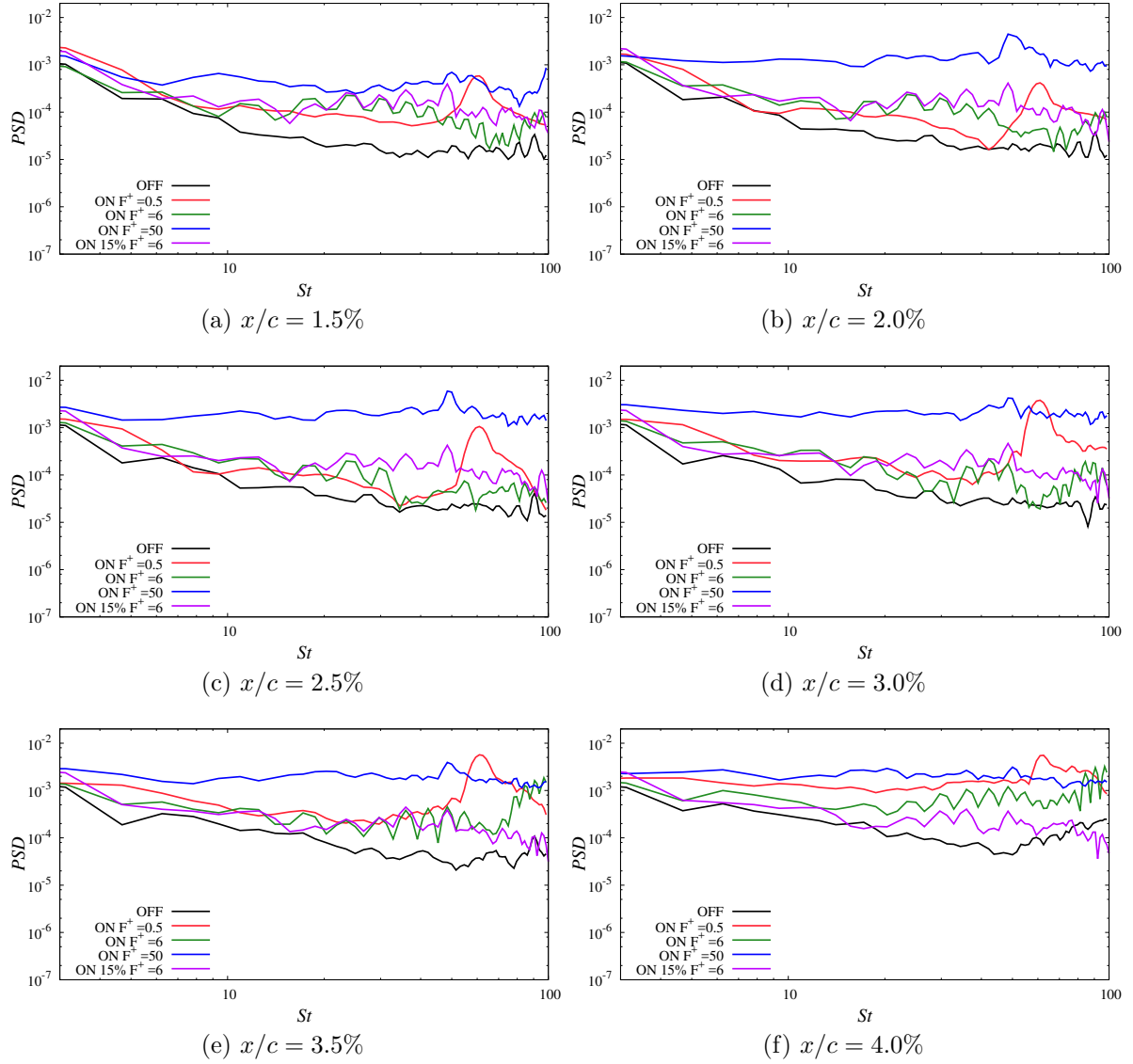


Figure 5.21: PSD of chordwise velocity on shear layer for pitching NACA0012 airfoil around the *phase* of  $68^\circ$  ( $AoA$ :  $10.7 \sim 11.3^\circ$  during pitching up).

in the reference and they conclude that the enhancement is brought by the large vortices and these large vortices are of grown from the vortex kernels induced by the DBD plasma actuator.<sup>2</sup> The mechanisms analysed herein are consistent with their conclusion. Hereafter the vortex which is likely to grow into a large vortex is called as a “kernel vortex” after Mitsuo et al..

### Investigation on phase-averaged flowfield

The phases in which the corresponding control effect is observed are from the phase after the large vortices have shed to the phase right before the flow begin to reattach. The flowfield in these the phases is characterized by the full-stall (stage 5); this stage corresponds to the *phase* of  $152^\circ \sim 290^\circ$  and *AoA* of  $23.7^\circ$  during the pitching up  $\sim 11.7^\circ$  during the pitching down, although the start of this phase range cannot be clearly defined. The flowfields in the stage 4 for the case of OFF, ON  $F^+ = 0.5$ , and ON  $F^+ = 6$  are presented in Figure 5.22. In this figure, field of total-pressure coefficient  $C_T$  is depicted to draw the existence of vortices. The case of ON  $F^+ = 6$  represents the less effective cases. The flowfields the cases other than the case of ON  $F^+ = 0.5$  show no prominent flow structures over the airfoil. In Figure 5.22(a) for the case of ON  $F^+ = 0.5$ , a relatively small vortex near the leading edge and another large vortex near the trailing edge are observed. In Figure 5.22(b), the vortex near the leading edge moves to the mid-chord and the other vortex located near the trailing edge moves right above the trailing edge, with inducing another trailing edge vortex. Not shown here, but the similar behaviour of large vortices of continuous formation and shedding can be observed until the flow at the leading edge reattaches only in the case of ON  $F^+ = 0.5$ . The chordwise distributions of  $C_p$  and  $C_f$  have their negative peak under these large vortices, whereas the other cases have relatively flat distributions both in  $C_p$  and  $C_f$ . This indicates that the enhancement in the aerodynamic forces are the result of the suction force produced by these large vortices.

### Investigation on instantaneous flowfield

Figure 5.23 presents the snapshots of instantaneous flowfields in the *phase* of  $223 \sim 244^\circ$ , where the characteristic flow features are observed in the case of ON  $F^+ = 0.5$ . The DBD plasma actuator for the case of ON  $F^+ = 0.5$  is turned on at the moment of the first subfigure and turned off at the moment of the second subfigure. The DBD plasma actuator for the cases with  $F^+$  of 6 or higher is turned on and off between the subfigures; time increment between the subfigures corresponds 1.2 times to the burst



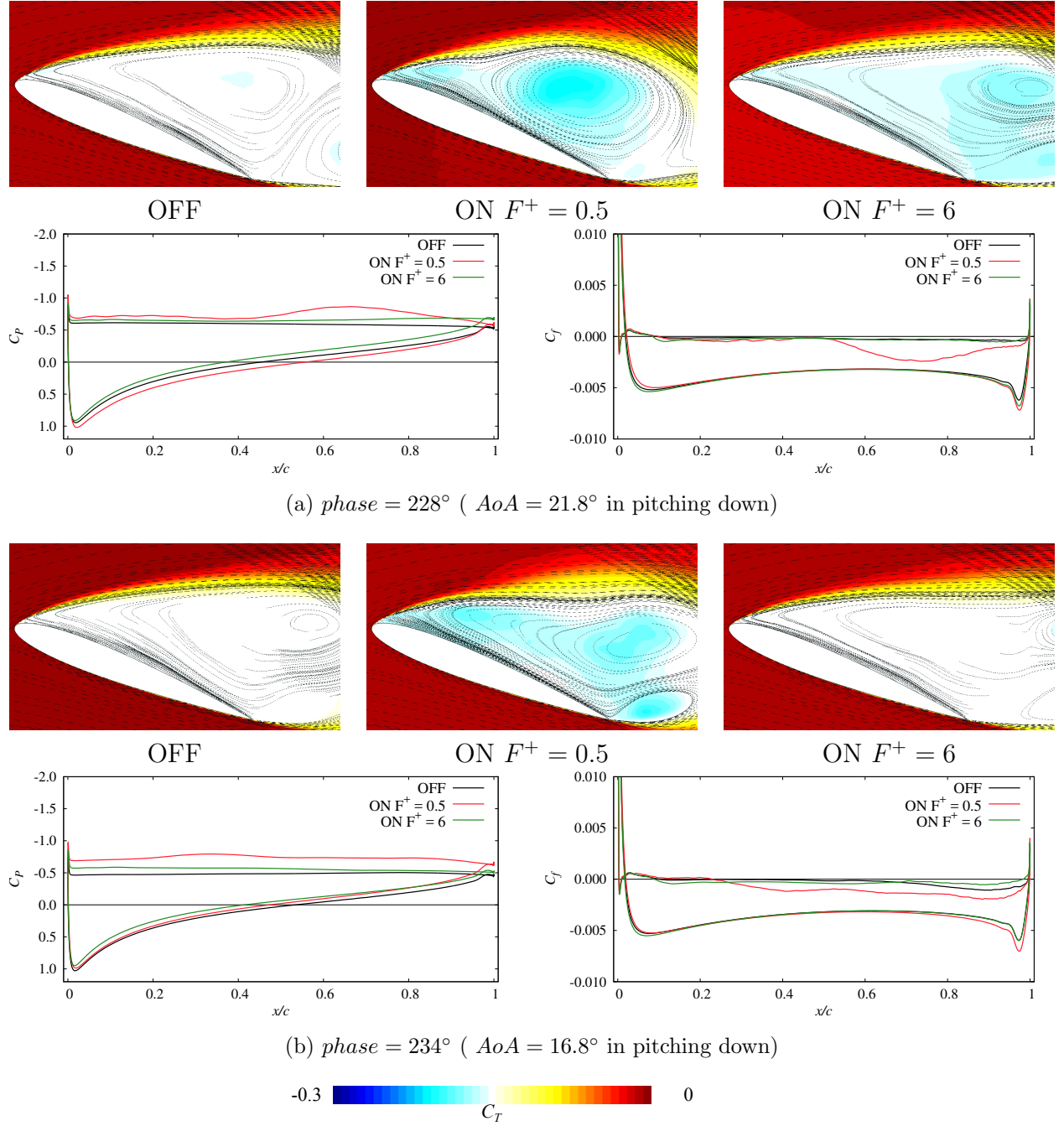


Figure 5.22: Top row: Phase- and span-averaged total-pressure coefficient fields. Bottom row : Phase-averaged  $C_p$  and  $C_f$  distributions.

actuation period of  $F^+$  of 6 and 10 times to the burst actuation period of  $F^+$  of 50. The leading edge shear layer is sheet-like when the DBD plasma actuator is off, and then is divided by the actuation, as is apparent in the case of ON  $F^+ = 0.5$  and ON  $F^+ = 6$ . In the case of ON  $F^+ = 0.5$ , the vortices form from the front edge of the upstream part of the divided shear layer act as a kernel of the consequent large vortex. This grown-up large vortex is the “large vortex” mentioned in the investigation on the phase-averaged flowfield. Here, another large vortex formed by the previous burst actuation is observed by the most blue flow structure above the mid-chord in the first subfigure of the case of ON  $F^+ = 0.5$ . The convective velocity of these large vortices is approximately one-third to half of the freestream velocity, and as a result the burst actuation with  $F^+$  of 0.5 can keep at least two large vortices over the airfoil at once. To make use of the aerodynamic forces of large vortices, this capability of  $F^+ = 0.5$  would be advantageous. As is not obvious as the case of ON  $F^+ = 0.5$ , the case of ON  $F^+ = 6$  also have kernel vortices at each tip of the divided sheet-like shear layer.

The behaviour of the shear layer is depicted in Figure 5.24. In this figure, the phase history of the distance between the separation point and the tip of the shear layer (denoted as  $s_{shed}$ ) and the angle of the shear layer are presented. The location of the tip of the shear layer is defined as the first point where the second invariant of the velocity gradient tensor becomes zero along the center line of the shear layer. This second invariant of the velocity gradient tensor, is also called as Q criterion,<sup>177</sup> identifies not only vortex structures but also shear layers and thus can be an indicator of the point of the vortex shedding from the shear layer. The relation of the vortices and the shear layer is visualized in Figure 5.19. In the figure, contour line of the second invariant of the velocity gradient tensor of zero is depicted with the spanwise vorticity. It is shown that the second invariant of the velocity gradient tensor can be a reasonable identifier of the tip of the shear layer, i.e., the point at which the vortex sheds from the leading edge. Here, data in Figure 5.24 is analysed on the span-averaged instantaneous flowfield and then are phase-averaged. On each burst actuation with  $F^+$  of 0.5, the shear layer is affected twice; the first is triggered by the turning on of the actuation and the second is by the turning off. On the other hand, the cases with higher  $F^+$  than 6, the shear layer moves only at the timing of the actuator on; this might because the frequency higher  $F^+$  than  $St$  of 6 is too fast for the shear layer to follow up. The similar trend is also observed in the angle of the shear layer; the shear layer is displaced toward the airfoil surface and the vortex shedding point is advanced by the DBD plasma actuator. Comparing the cases with the same  $F^+$ , i.e., the cases of ON  $F^+ = 6$  and ON 15% $F^+ = 6$ , the behaviour of the shear layer shows similar trend with a little phase lag.

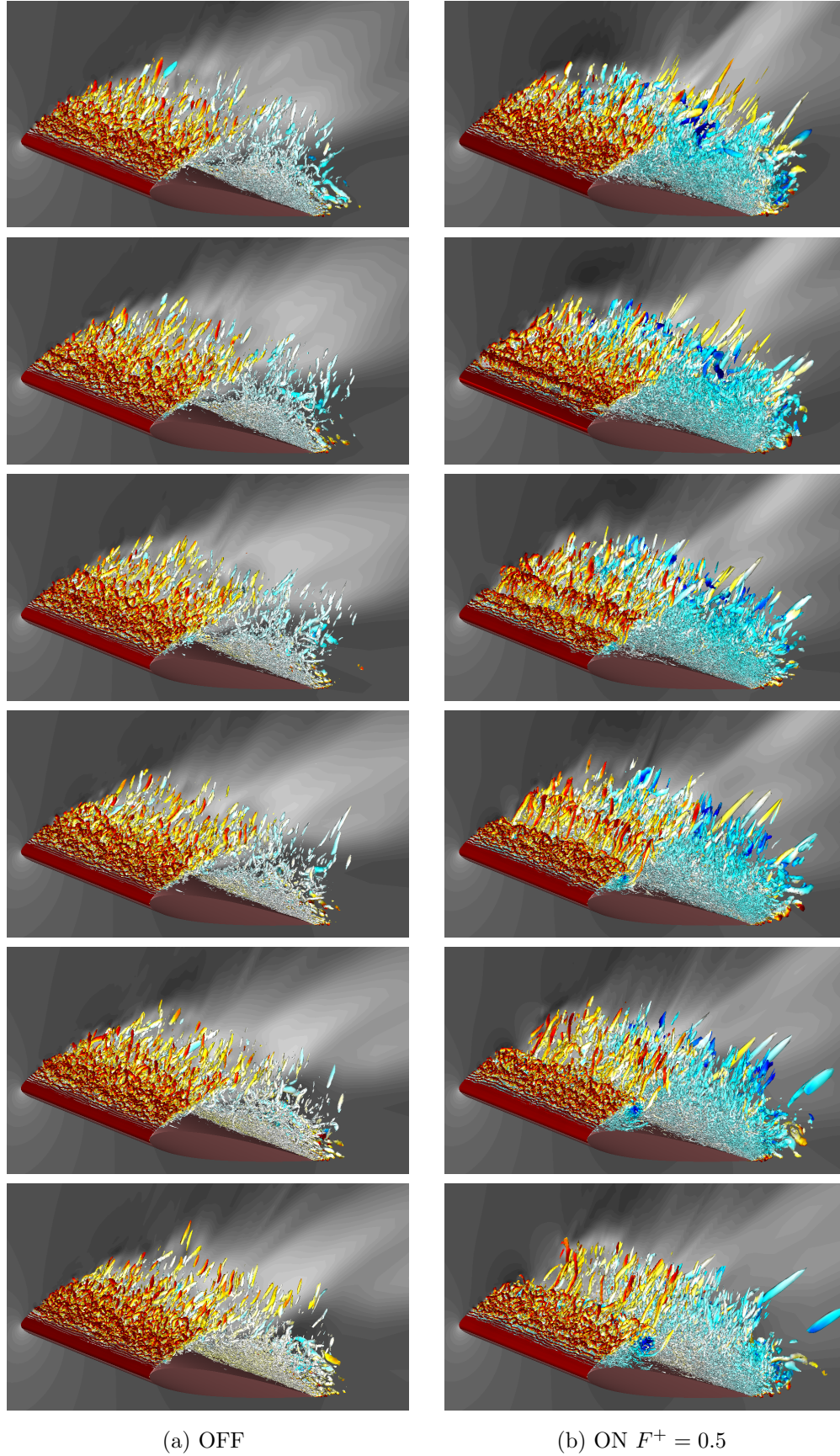
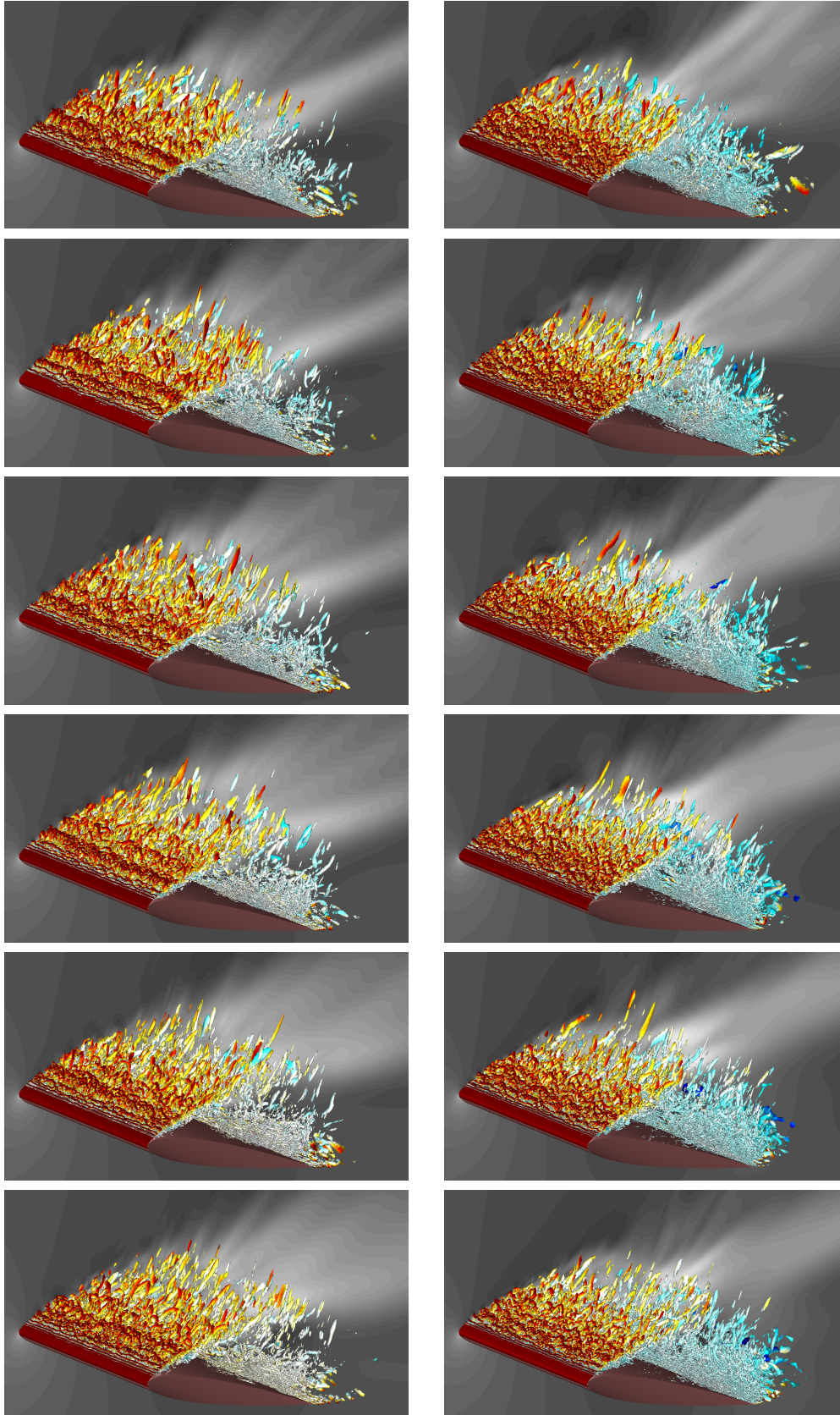


Figure 5.23: Snapshots of instantaneous flowfields in the *phase* of  $223 \sim 244^\circ$ . The iso-surfaces indicate the second invariant of the velocity gradient tensor colored by total-pressure coefficient.

Time lapses from top to bottom with time increment of  $tu_\infty/c = 0.2$ .

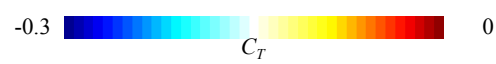
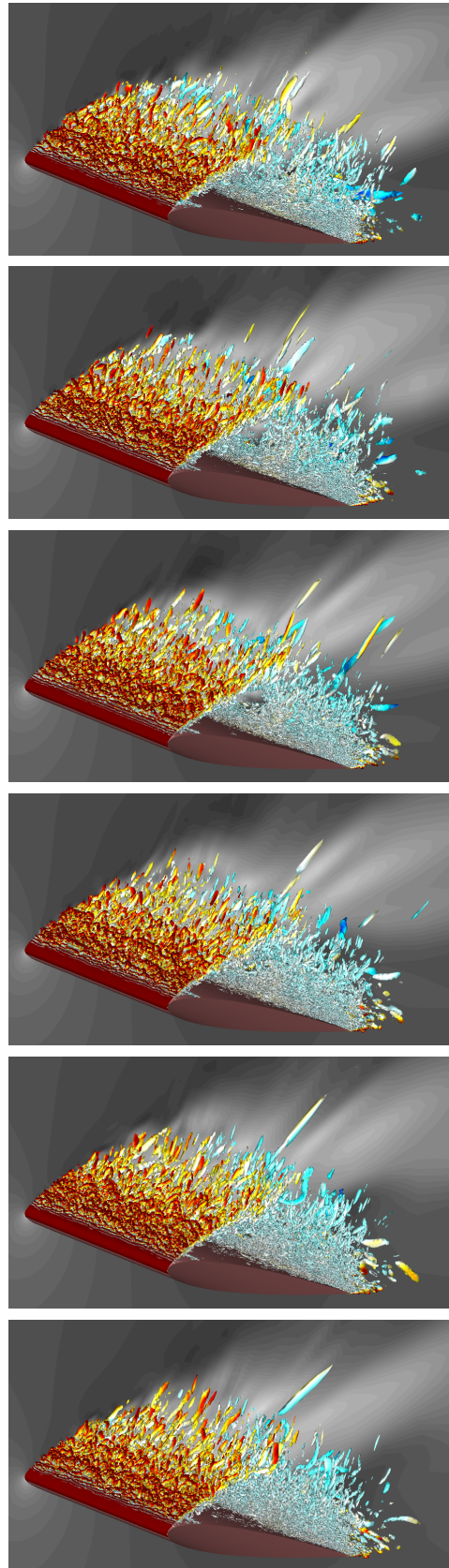


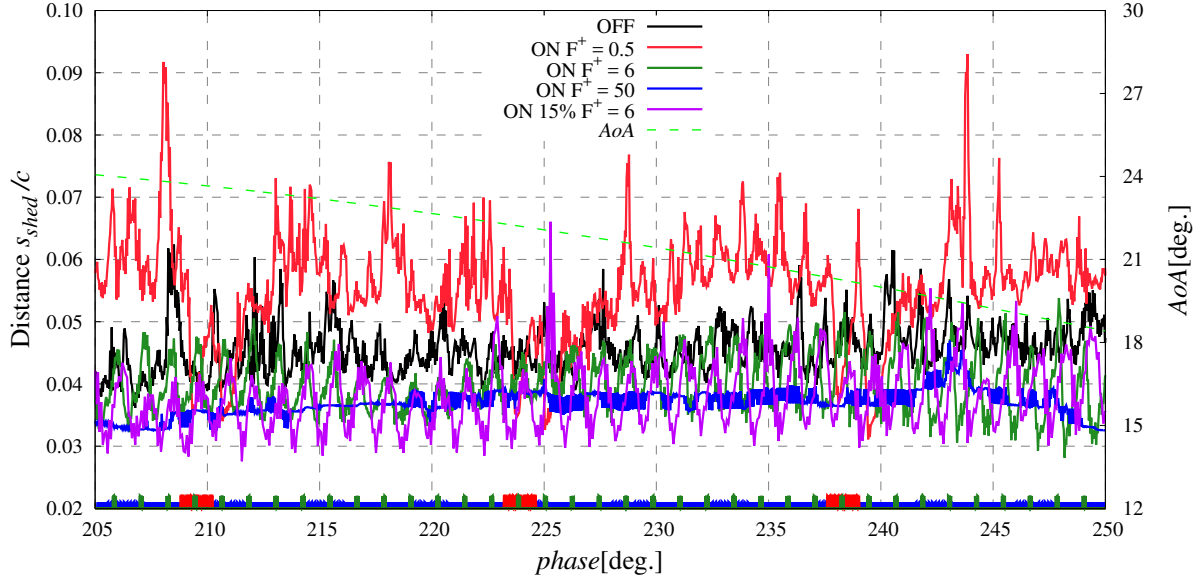


(c) ON  $F^+ = 6$

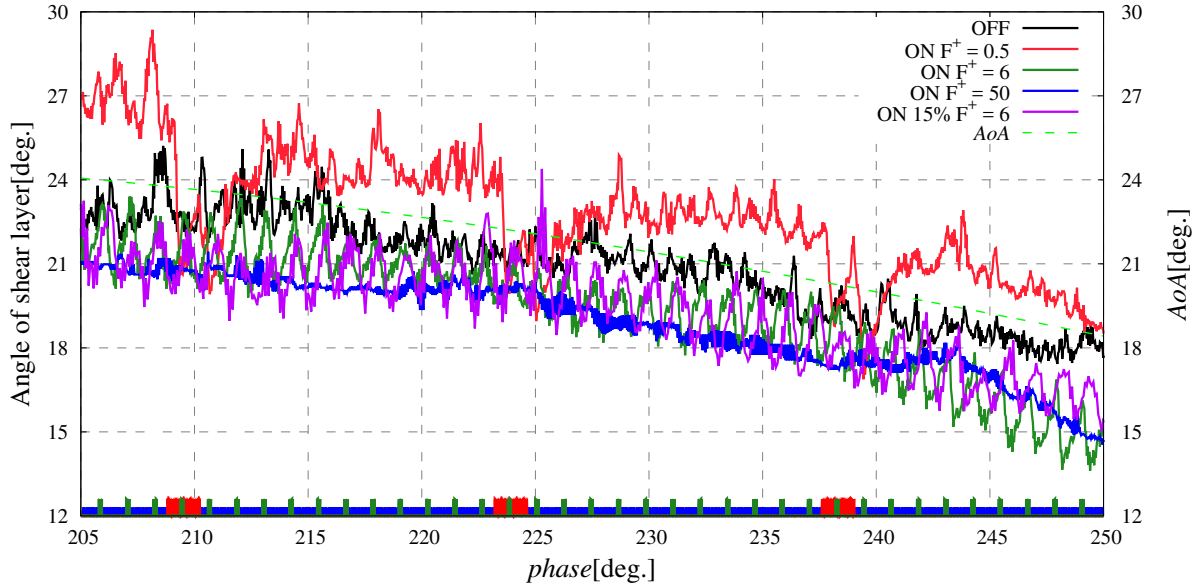
(d) ON  $F^+ = 50$

Figure 5.23: *Continued.*

Figure 5.23: *Continued.*



(a) Distance between separation point and vortex shedding point



(b) Angle of shear layer

Figure 5.24: Behaviour of the shear layer during the *phase* of 205 ~ 250°, *AoA* corresponds to 24 ~ 18.5°.

The actuation timing is presented at the bottom.

To see the control mechanism on the behaviour of the shear layer by the DBD plasma actuator in this stage, Figure 5.25 presents the PSD of the chordwise velocity around the *phase* of  $225^\circ$ , which is the phase right before the breakdown of LSB, at several position on the leading edge shear layer. The natural frequency of the vortex shedding is around  $St$  of  $30 \sim 70$  and the corresponding  $St$  become prominent after  $x/c = 2.0\%$  in the case of OFF. In the case of ON  $F^+ = 50$ , prominent peak is observed only at  $St = 50$  and this indicates the unsteady behaviour of the shear layer is completely controlled by the DBD plasma actuator. In the other controlled cases, the each case's  $F^+$  or  $f_{base}$ , and/or their harmonics within the natural frequency range are enhanced. The case of ON  $15\%F^+ = 6$  also promotes the natural frequency of the vortex shedding, exhibiting the peaks at  $St$  of 36, 42, and 48, which are the harmonics of  $F^+$ . The results from the case of ON  $15\%F^+ = 6$  support the mechanism that the controlled behaviours of the shear layer are brought by the unsteady stimulation of the instability of the shear layer, not necessarily by the direct momentum injection. It also suggests that the DBD plasma actuator have capability of controlling the flow located its upstream with significant effect. These would provide us with an idea of installing the DBD plasma actuator other than in the leading edge. As observed in the case of OFF, the natural frequency of the vortex shedding has some extent of  $St$  range, not showing a sharp peak, due to the fluctuation of the shear layer; It would imply that it is better to employ relatively low frequency actuation such as the case with  $F^+$  of 6, so as to utilize the harmonics of the actuation frequency in order to accommodate the fluctuation of the unsteady frequency of the vortex shedding. Here, in dynamic flowfields, the unstable frequency is affected by the changes of the flow condition and so the utilizing the harmonics of the actuation frequency must be more effective compared with in the stationary flowfield.

As indicated in Figure 5.24(a), the vortex shedding point is significantly and rapidly advanced in association with the actuation in the controlled cases. Note that this is not apparent in the case of ON  $F^+ = 50$  because the actuation with  $F^+$  of 50 is so fast that the behaviour of the shear layer is steadily advanced. Assuming that the vortex shedding interval is not changed, the distance between the vortex which is formed right before the advancement of the vortex shedding point and the vortex which is formed right after the advancement of the vortex shedding point would become large. Then, if the distance between the vortices become large, the interaction between these vortices are weakened and the vortices can grow into more larger vortex. Under this assumption, actuation with low frequency than the natural instability frequency can induce the intermittent shedding of the vortices, and this intermittency might be a key of the formation of the kernel vortex.

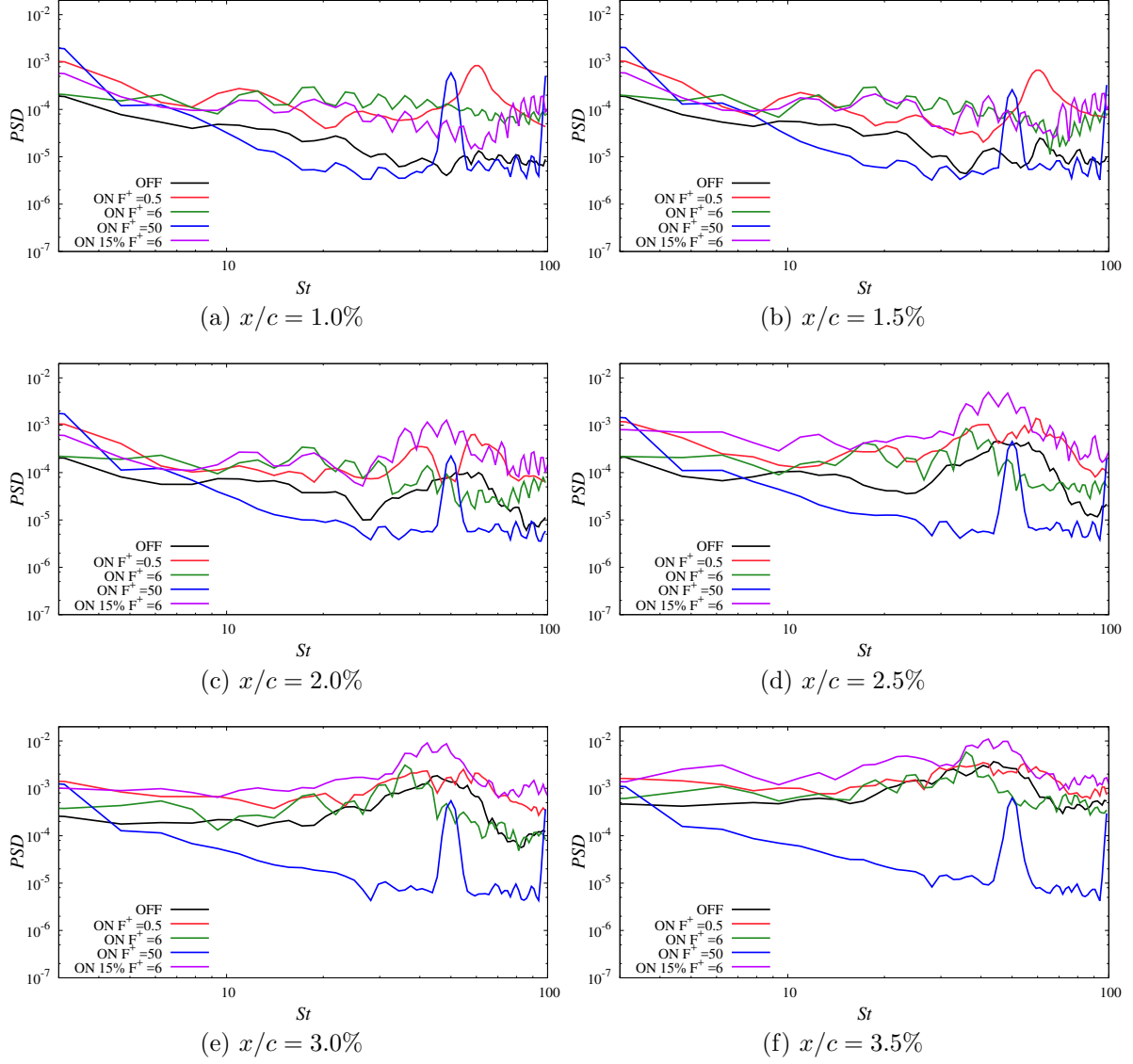


Figure 5.25: PSD of chordwise velocity on shear layer for pitching NACA0012 airfoil around the *phase* of  $225^\circ$  ( $AoA$ :  $22.3 \sim 21.9^\circ$  during pitching down).



Evaluation of the kernel vortices size is presented in Figure 5.26. In this Figure, the phase history of a size index of the vortex shed from the shear layer  $d$  is presented. Here, the second invariant of the velocity gradient tensor (Q criterion) is used as the indicator as the vortex size; the vortex size is estimated by the average of the wall-normal and wall-tangential distance between the point where Q criterion becomes zero around each vortex. The size of the first five vortices shed from the shear layer at each moment are estimated and the size index is defined by the maximum size of these five vortices. Note that the number of evaluated vortices is limited to five and the evaluation of the fifth vortex size is cut off whenever new vortex is shed. Thus, the peak value of  $d$  does not mean that is the maximum attained vortex size, but is just an indicator of the vortex size. As same with the other analyses on the instantaneous shear layer,  $d$  is calculated on the span-averaged instantaneous flowfield and then are phase-averaged. Thanks to the span-averaging in the first step of analysis, coherent vortices which will grow large, i.e., grow into a kernel vortex can be selectively extracted and tracked. In the case of ON  $F^+ = 0.5$  and ON  $F^+ = 6$ , relatively large size index  $d$  is observed. This result is consistent with the visualization of the flowfield (Figure 5.23); only the cases of ON  $F^+ = 0.5$  and ON  $F^+ = 6$  exhibit apparent kernel vortices which can be observed by the visualization. Here, with regard to the kernel vortex in the other cases, the actuation with  $F^+ = 50$  induces only small-sized vortices which easily decay into less-spanwise-coherent fine-scaled vortices and these vortices cannot grow into large vortices. Considering that the case of ON 15% $F^+ = 6$  shows no large kernel vortices in Figure 5.23 and Figure 5.26 whereas the shear layer shows similar behaviour with the case of ON  $F^+ = 6$  (Figure 5.24), the formation of the kernel vortex may owe the direct momentum addition by the DBD plasma actuator.

These results indicate that the relatively large kernel vortices are formed in the case of ON  $F^+ = 6$ , but these do not grow into further large vortex structure unlike the case of ON  $F^+ = 0.5$ . To see this difference, the flowfields at characteristic instance for each case are presented in Figure 5.27. In the case of ON  $F^+ = 0.5$ , the preceding kernel vortex induced by the previous burst actuation have already convects to behind the mid-chord. On the other hand, in the case of ON  $F^+ = 6$ , actuation with  $F^+ = 6$  induces continual kernel vortices and every kernel vortices interfere with their forward and backward vortices as seen by the rib structures. This interaction with two kernel vortices results in higher attenuation, and as a result the kernel vortex cannot grow into further large vortex. To conclude, the unsteady actuation with  $F^+$  lower than the natural vortex shedding frequency is essential to the formation of the kernel vortex. In addition to these, use of sufficiently low burst frequency help the kernel vortex to grow

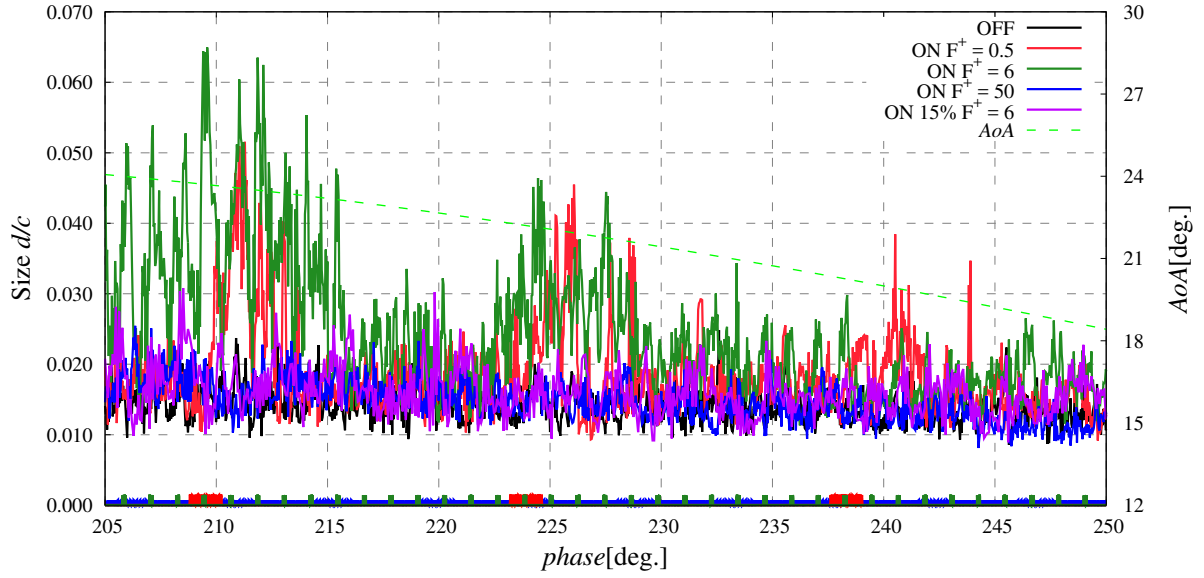


Figure 5.26: Size index for maximum vortex size near the leading edge during the *phase* of  $205 \sim 250^\circ$ , *AoA* corresponds to  $24 \sim 18.5^\circ$ . The actuation timing is presented at the bottom.

into further large vortex.

### 5.4.3 Mechanisms on promoting reattachment

The control mechanisms on promoting reattach observed in the final stage of the dynamic stall process is investigated here.

As seen in Figure 5.12 in section 5.3.5, the reattachment point moves toward the downstream after the reattachment, however, a clear LSB is observed right after the reattachment (around the *phase* of  $280^\circ$ ). The argument on delaying the dynamic stall onset in the previous section was about how to promote the reattachment. Now, on the control effect of promoting the reattachment in this stage, this “promotion of the reattachment” means promoting the recovery from the leading edge stalled state to the reattached state. In the previous section, it is suggested that the local strength of TKE and Reynolds stress in upstream region and near the airfoil surface are important for the behaviour of the LSB in the stage 2. Here, considering that both of the reattachment in these different stages are associated with an LSB, the flow characteristics represented by TKE and Reynolds stress would be considered to play important roles also on the promotion of the reattachment in this stage.

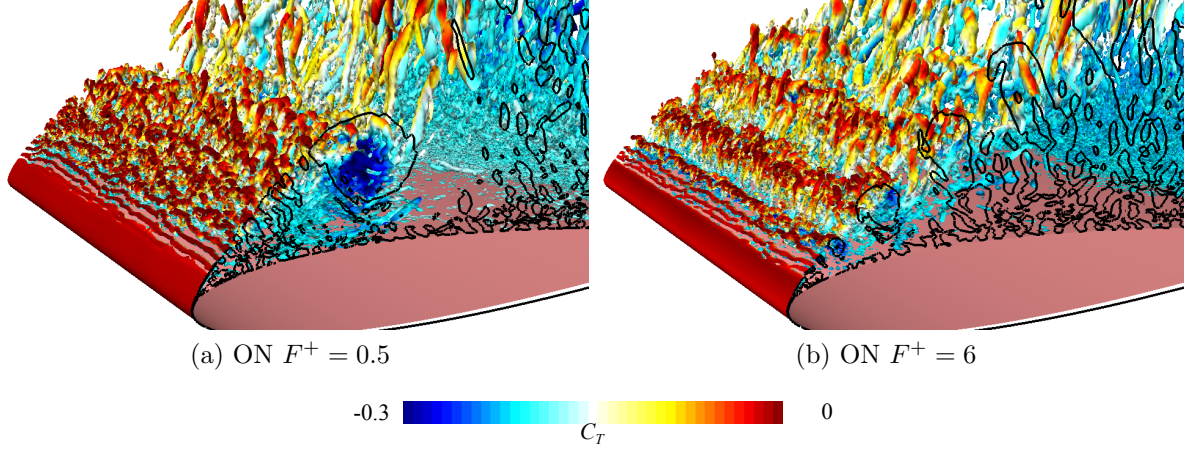


Figure 5.27: Interactions around the large vortices in the case of ON  $F^+ = 0.5$  and ON  $F^+ = 6$ . Instantaneous iso-surfaces for the second invariant of the velocity gradient tensor colored by total-pressure coefficient are depicted with the black contour line for the spanwise-averaged second invariant of the velocity gradient tensor.

### Investigation on phase-averaged flowfield

In Figure 5.10(a), the case of ON  $F^+ = 6$  shows that the flow is already reattached and an LSB is formed whereas the other cases show still massively separated flowfield. The most effective case in promoting reattachment, which is the case of ON  $F^+ = 6$ , promotes the reattachment by  $5.6^\circ$ , as shown in Table 5.5. Figure 5.28 presents the phase- and span-averaged chordwise velocity field with  $C_p$  and  $C_f$  distributions at the phases before the reattachment in the case of ON  $F^+ = 6$  and ON  $F^+ = 0.5$ . Figure 5.29 presents TKE and Reynolds stress fields at the same phase with Figure 5.28. In Figure 5.29(a), the TKE and Reynolds stress fields of the case of ON  $F^+ = 6$  shows their maximum/minimum region near the airfoil surface. Similarly, at the phase of the reattachment of the case of ON  $F^+ = 0.5$  as depicted in Figure 5.29(b), the high TKE/high negative Reynolds stress region come close to the airfoil surface. On the other hand, the cases of OFF and ON  $15\%F^+ = 6$  whose control effects on promoting the reattachment are not good have negative Reynolds stress region far from the airfoil surface.

The distributions of TKE and Reynolds stress along the wall-normal direction are presented in Figure 5.30. In this figure, the phases from the phase at which the flow reattaches in the case of ON  $F^+ = 6$  and to the phase at which the flow reattaches in the case of ON  $F^+ = 0.5$  are depicted. Observing the series of the subfigures with the triangle symbol, which denotes the reattachment point, it is found that the distributions of both TKE and Reynolds stress have characteristic wall-normal distributions right before the

each case's reattachment. First, with regard to TKE, the wall-normal distribution of TKE has long slope which ranges from the point where TKE takes maximum along the wall-normal direction to the airfoil surface. For example, the TKE of the case of ON  $F^+ = 6$  at  $x/c = 0.07 \sim 0.08$  in the Figure 5.30(b), which is right before the reattachment at the *phase* of  $270^\circ$  at  $x/c = 0.09$ , has a long-sloped distribution with some inflection points whereas the maximum TKE is not very close to the airfoil surface. Here, otherwise, the cross-flow distribution of TKE across a general shear layer has Gaussian-like distribution as seen in all the TKE subfigures in Figure 5.30 near the leading edge. The next characteristic shape observed right before the reattachment is the negative peak of Reynolds stress near the airfoil surface. This characteristic shape is related to the first characteristic and indicates the momentum exchange take places near the airfoil surface. These mean that some vortical structures, which are considered as the source of turbulent fluctuation, are significantly interacting with the boundary layer or the airfoil surface and as a result the effect of the momentum exchange by the turbulence penetrates into the boundary layer.

### Investigation on instantaneous flowfield

The flowfield shows the same characteristics with that introduced in the previous subsection (which is about the control mechanism on the enhancement of the aerodynamic force during the full-stall). First, PSD of the chordwise velocity in the phase of  $256^\circ$  on the shear layer is presented in Figure 5.31. In this phase, the instability frequency of the shear layer in the case of OFF is around  $St = 40$ . Similar to Figure 5.25, the prominent peak is observed at  $St = 50$  in the case of ON  $F^+ = 50$  and otherwise is observed around  $St = 40$ .

Figure 5.32 shows the distance between the separation point and the tip of the shear layer ( $s_{shed}$ ), the angle of the shear layer, and the size index of the vortex size shed from the shear layer  $d$  at the phase of reattachment. The case of ON  $F^+ = 50$  has steadily short  $s_{shed}$ , low angle of the shear layer, and small  $d$  among all the cases. The other controlled cases show shorter  $s_{shed}$ , lower angle of the shear layer, and larger size in  $d$  after each burst actuation timing, compared with the case of ON  $F^+ = 50$ . As shown in Figure 5.30, it is suggested that the momentum exchange brought by the turbulent fluctuation is a key of the reattachment in this stage and should take place near the airfoil surface. Therefore, the focus of investigation should be on the vortical structures near the airfoil surface. Observing Figure 5.32 with this focus, the relation between the angle of the shear layer and  $s_{shed}$  can be regarded as an index of the closeness of the

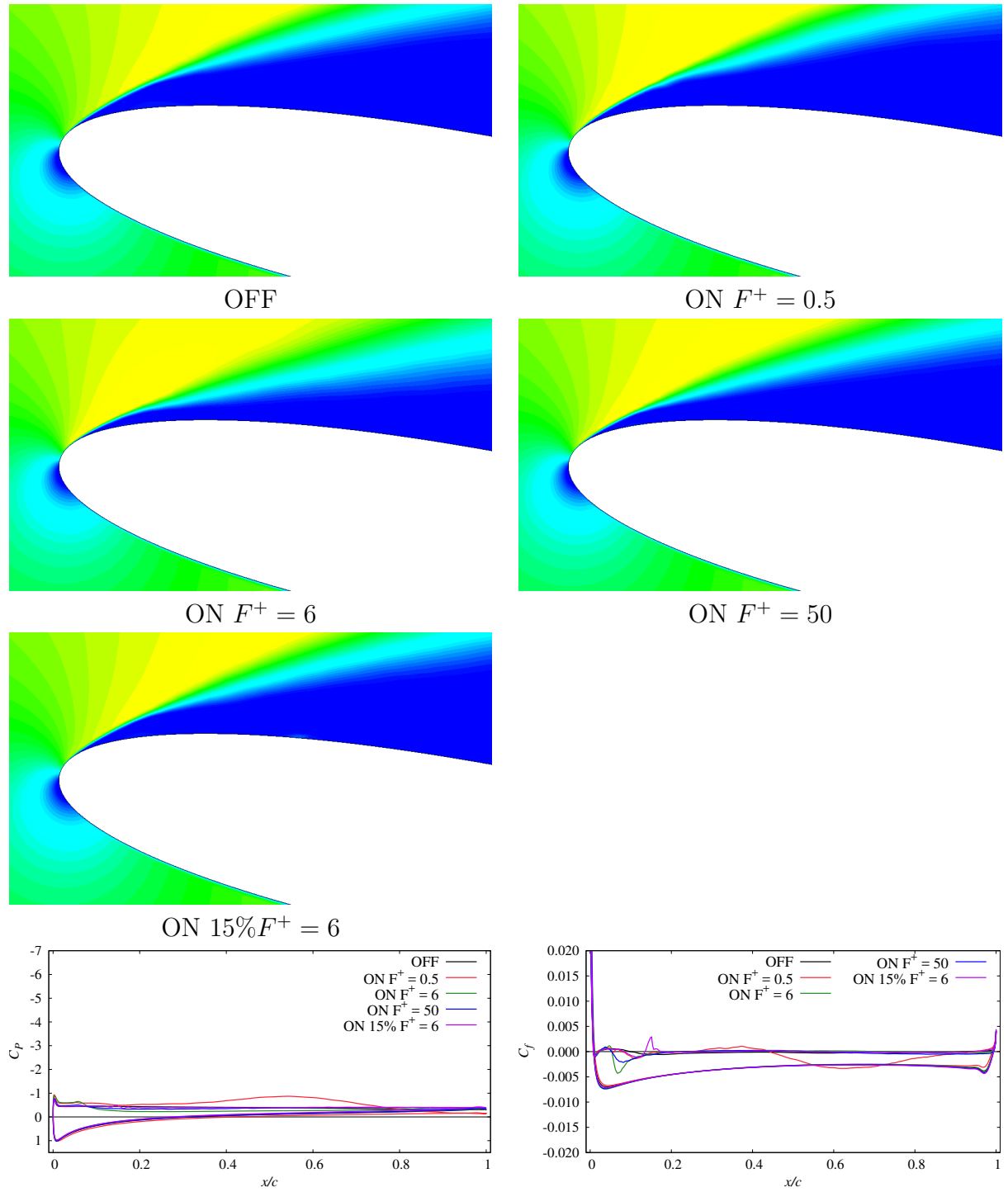
(a)  $phase = 270^\circ$  ( $AoA = 15.1^\circ$  in pitching down)

Figure 5.28: Top three rows: Phase- and span-averaged chordwise velocity field for pitching NACA0012 airfoil.

Bottom row : Phase-averaged  $C_p$  and  $C_f$  distributions.

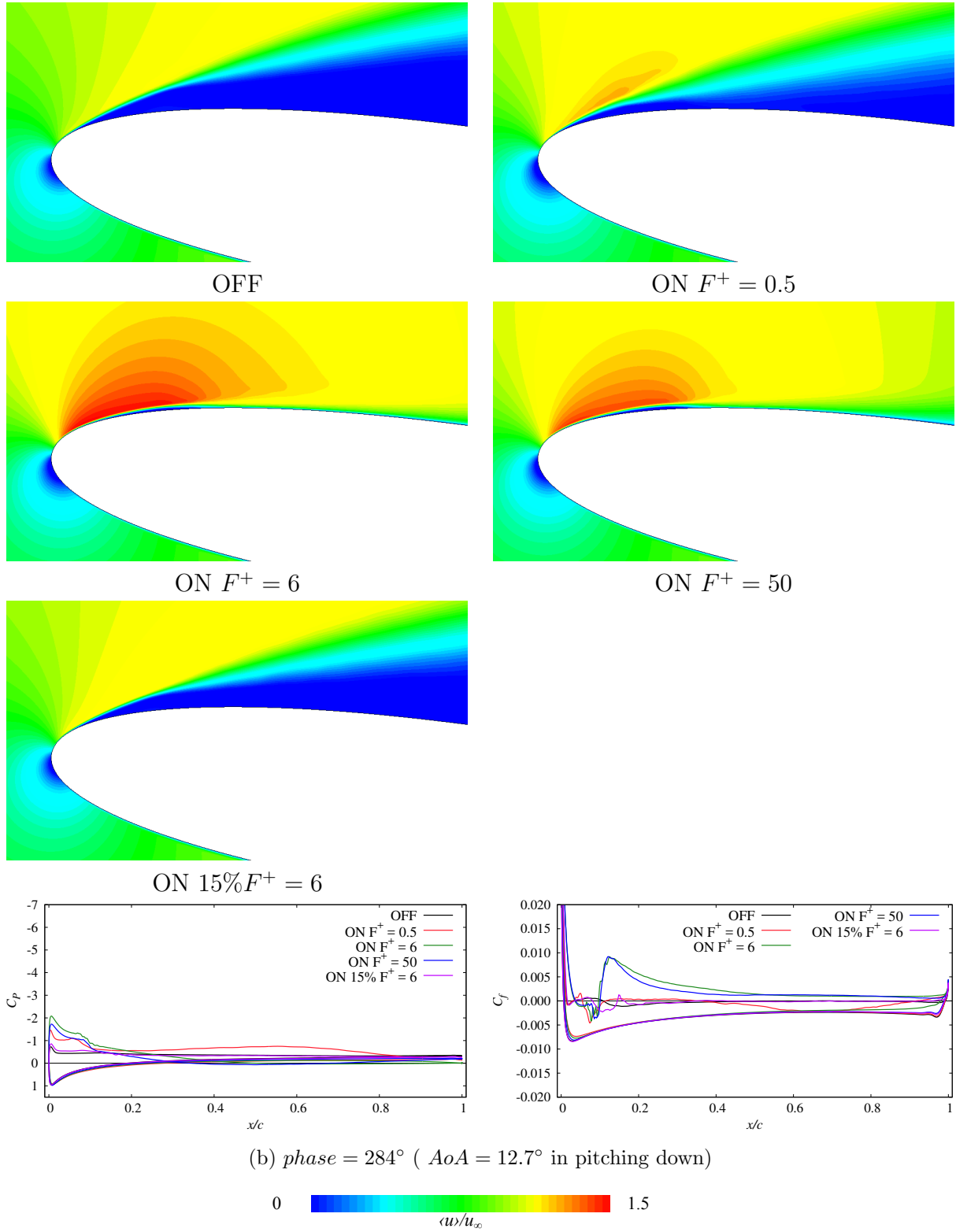
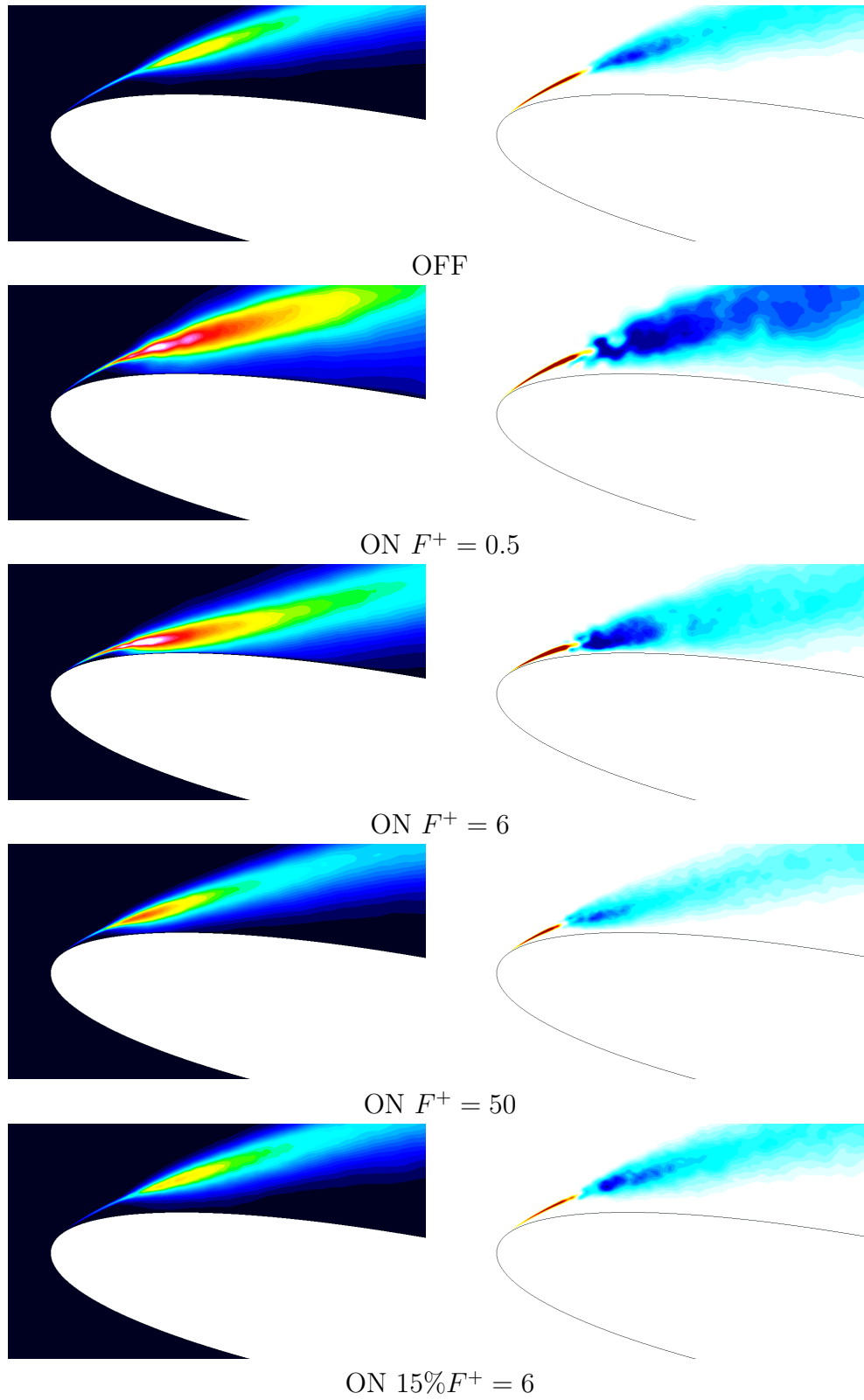


Figure 5.28: *Continued.*



(a)  $phase = 270^\circ$  (  $AoA = 15.1^\circ$  in pitching down)

Figure 5.29: Left column: Phase- and span-averaged TKE field.  
Left column: Phase- and span-averaged Reynolds stress field.

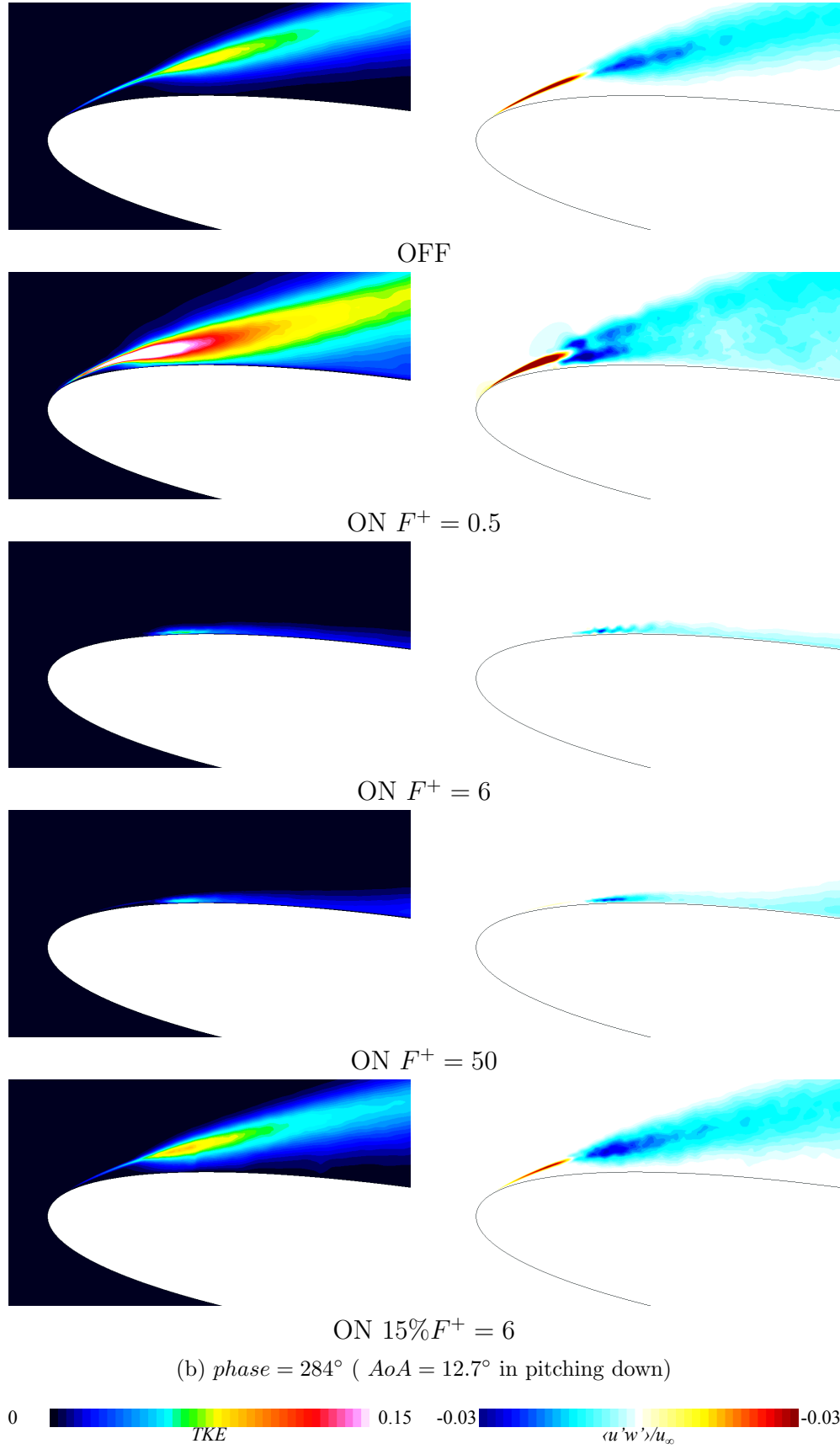


Figure 5.29: *Continued.*



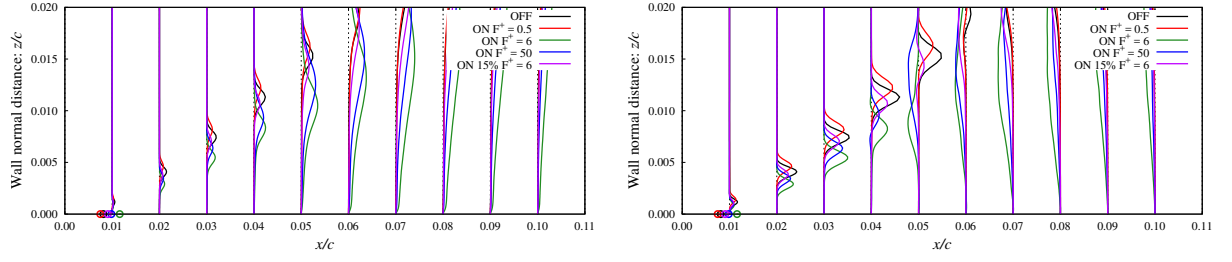
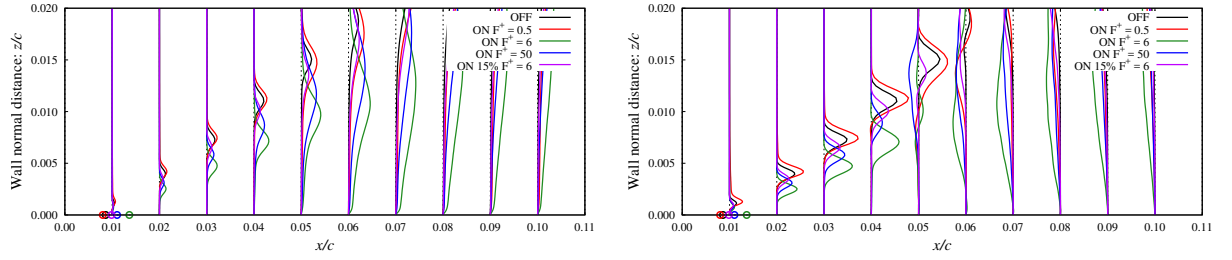
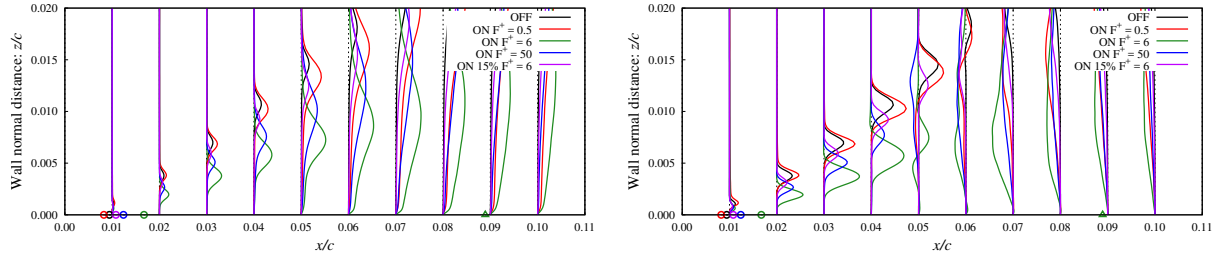
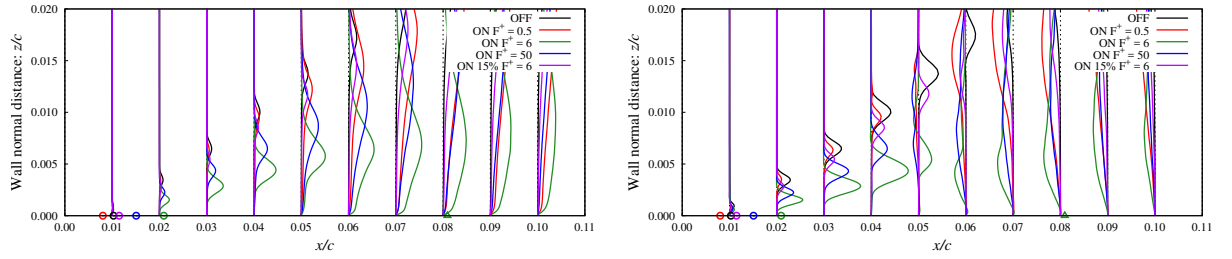
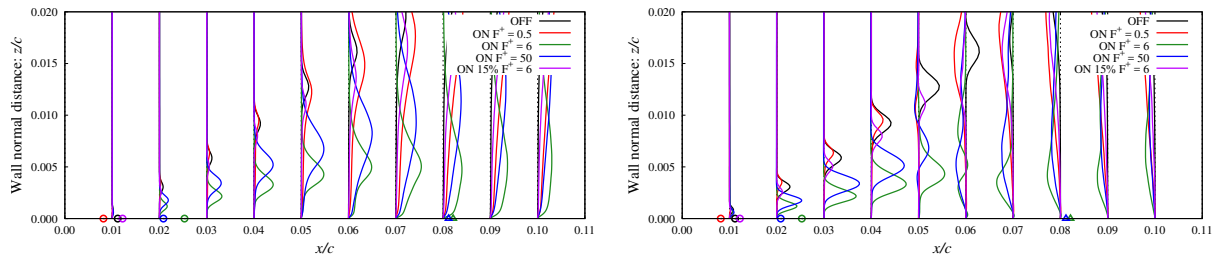
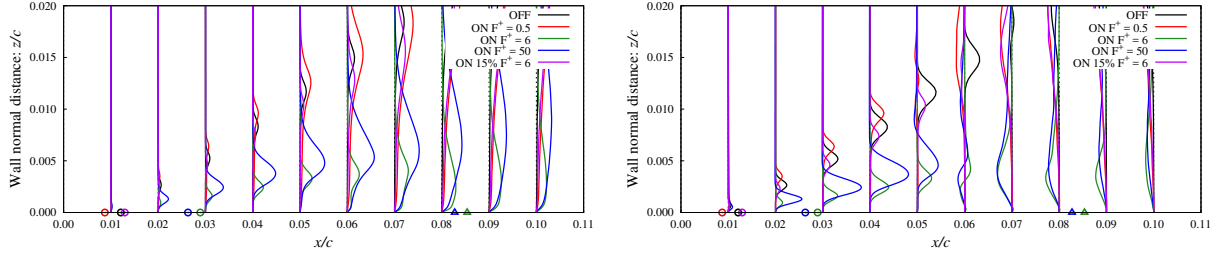
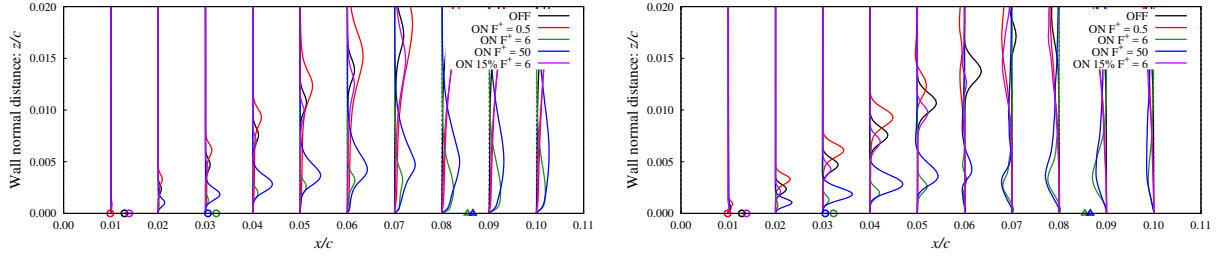
(a)  $phase = 266^\circ$  (  $AoA = 15.7^\circ$  )(b)  $phase = 268^\circ$  (  $AoA = 15.4^\circ$  )(c)  $phase = 270^\circ$  (  $AoA = 15.1^\circ$  )(d)  $phase = 272^\circ$  (  $AoA = 14.8^\circ$  )(e)  $phase = 274^\circ$  (  $AoA = 14.5^\circ$  )

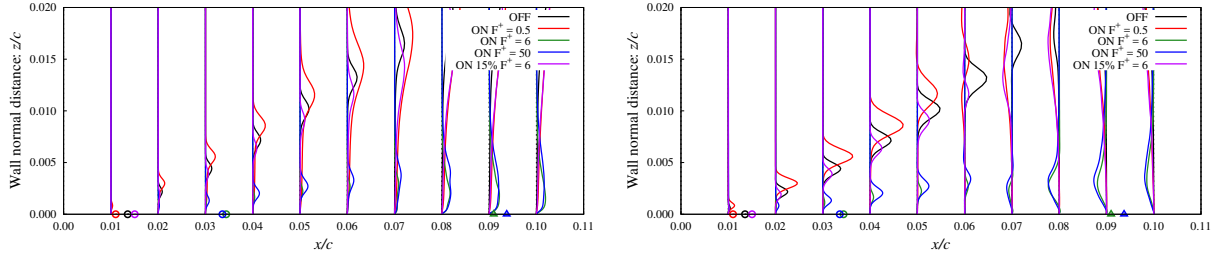
Figure 5.30: Wall-normal distributions of phase- and span-averaged chordwise TKE (left) and Reynolds stress (right) near the leading edge. Separation and reattachment points are presented respectively with circles and triangles.  $AoA$  are of in pitching down.



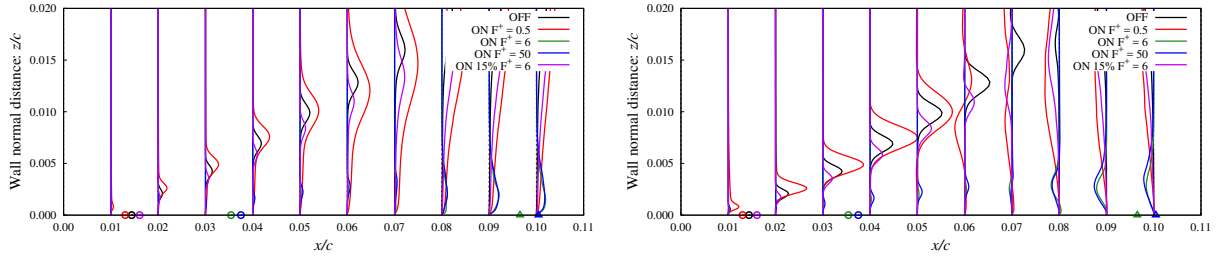
(f)  $phase = 276^\circ$  (  $AoA = 14.1^\circ$  )



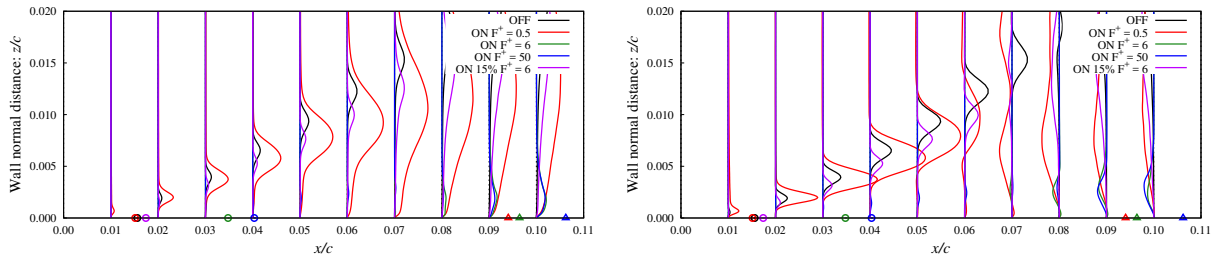
(g)  $phase = 278^\circ$  (  $AoA = 13.8^\circ$  )



(h)  $phase = 280^\circ$  (  $AoA = 13.4^\circ$  )



(i)  $phase = 282^\circ$  (  $AoA = 13.1^\circ$  )



(j)  $phase = 284^\circ$  (  $AoA = 12.7^\circ$  )

Figure 5.30: *Continued.*

vortex to the airfoil surface; either of advancing  $s_{shed}$  or displacing the angle of the shear layer toward the airfoil surface can decrease the wall-normal distance of the formation point of the shed vortices. The size index  $d$  can represent the area under the influence of the turbulent fluctuation by the shed vortices. Note that the characteristics of the flowfield or the shear layer described in the previous subsection can be applied also on the flowfield or the shear layer right before the reattachment. In Figure 5.32, it can be observed that the case of ON  $F^+ = 6$  can create relatively large kernel vortices, and can advance  $s_{shed}$  compared with the case of OFF. This means the influence area of the momentum exchange between the freestream and the boundary layer come closer to the airfoil surface. As for the angle of the shear layer, the shear layer is displaced toward the airfoil surface at every actuation timing and is also displaced by the effect of this momentum exchange. With the combination of these effects, the momentum exchange takes place more close to the airfoil surface as the burst actuation is repeated. This increasing effect can be observed as the rapid displacement of the shear layer in Figure 5.32(b), as apparent in the case of ON  $F^+ = 6$ . In the case of ON  $F^+ = 50$ , the size of the vortices shed from the leading edge is relatively small as aforementioned, and the area under the influence of the turbulent fluctuation is relatively small. Considering that the control effect of promoting the reattachment of the case of ON  $F^+ = 50$  is the second best and that the case of ON  $F^+ = 50$  has steadily short  $s_{shed}$ , one of the important factors of the control mechanism of promoting the reattachment can be said to be the vortex size. Here, the case of ON  $F^+ = 0.5$  shows largest kernel vortex size  $d$ . However, the large vortex rises the shear layer upward, as observed around the phase right after every actuation timing in Figure 5.32(b). These result can be summarized that the effective  $F^+$  for promoting the reattachment should be low so as to form moderate-sized kernel vortices and should not be too low to allow the kernel vortices to grow into further large vortices.

## 5.5 Summary

In this chapter, the control effects of the DBD plasma actuator on the dynamic flowfield around a pitching NACA0012 airfoil are investigated and then the control effects and these mechanisms are arranged. The flowfield around a pitching NACA0012 airfoil at Reynolds number of  $2.56 \times 10^5$  is investigated. The airfoil pitches between  $AoA$  of  $5^\circ$  to  $25^\circ$  with the reduced frequency of  $0.02\pi$ .

First, in order to understand the baseline flowfield and then to determine the DBD plasma actuator parameters to be examined, the flowfields around a stationary and

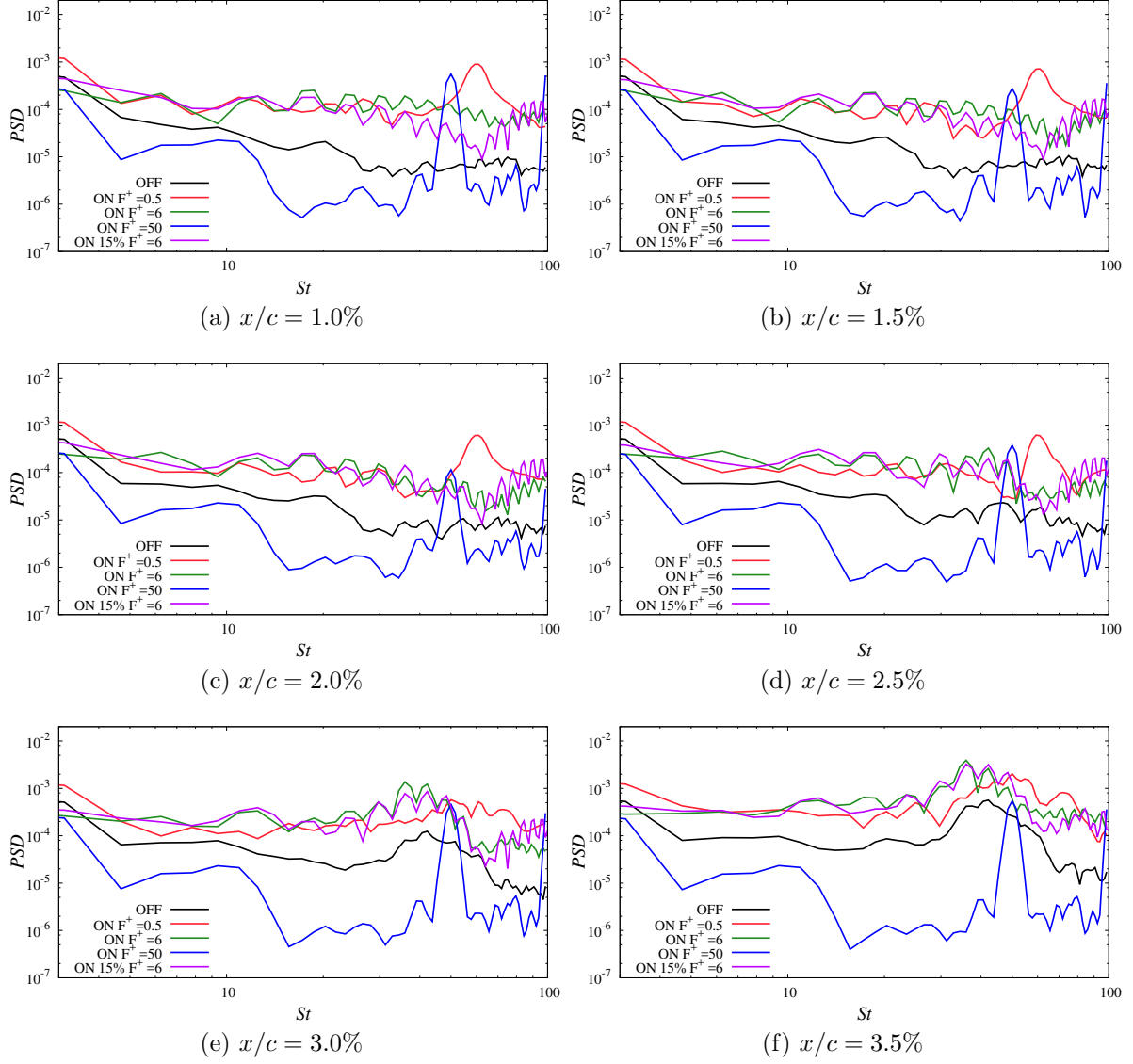
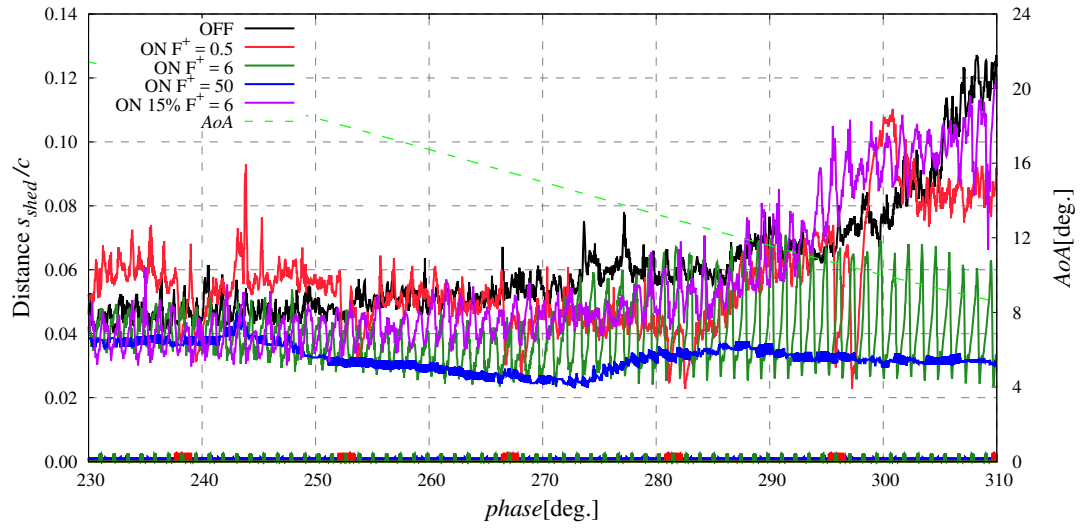
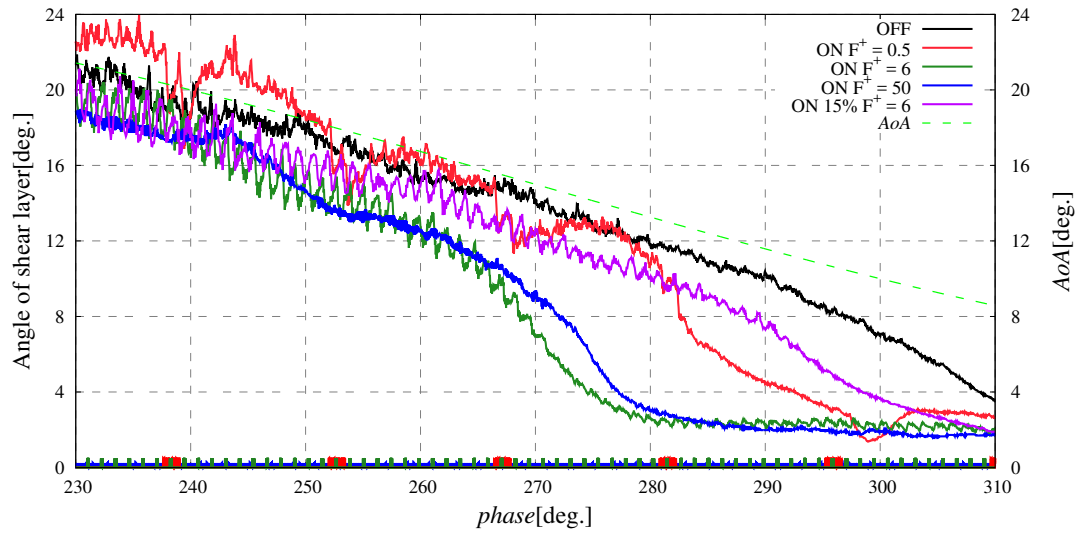


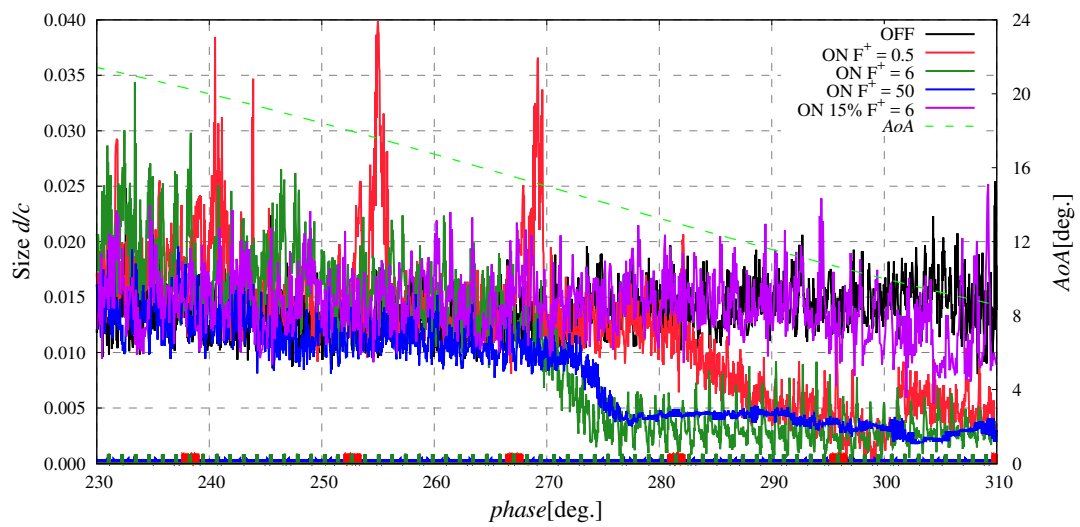
Figure 5.31: PSD of chordwise velocity on shear layer for pitching NACA0012 airfoil around the *phase* of 256° (*AoA*: 18.1 ~ 17.5° during pitching down).



(a) Distance between separation point and vortex shedding point



(b) Angle of leading edge shear layer



(c) Size index for maximum vortex size near the leading edge

Figure 5.32: Closed-up of the properties of the shear layer and the shed vortices around the reattachment phase.

The actuation timing is presented at the bottom.

pitching airfoil without control are investigated. The flowfield around the stationary airfoil at this Reynolds number has a combined type of trailing edge stall and leading edge stall. At low  $AoA$ , the flow separates around the mid-chord and soon reattaches near the trailing edge. The separation and reattachment points move together toward the leading edge and a clear LSB is formed near the leading edge as  $AoA$  increases. The stall angle, which is defined by the  $AoA$  where first drop in  $C_L$  against  $AoA$  is observed, is found between  $AoA$  of  $12 \sim 13^\circ$ . The stall in the stationary flowfield is due to the trailing edge stall, however, the extent of this trailing edge stall is relatively small and the subsequent leading edge stall is observed between  $AoA$  of  $13 \sim 14^\circ$ .

The flowfield around a pitching airfoil also shows the combined type of trailing edge stall and leading edge stall. The extent of the trailing edge stall is so small that its effect does not apparently appear in the aerodynamic performances. The LSB formed near the leading edge plays an important role on the overall characteristics of the flowfield. The general flowfield in dynamic stall is characterized by the formation of LSB, the breakdown of LSB (corresponds to the formation of DSV), the convection of DSV, the full-stall from the leading edge, and recovery to the attached state. The aerodynamic performances before the formation of DSV and after the convection of DSV show relatively gentle slope against  $AoA$ . However, the aerodynamic performances experience sudden and drastic change due to the formation and the convection of DSV. After the convections of DSV and subsequent other large vortices induced by the DSV, full-stalled state is observed. At the final stage of the pitching cycle, rapid recoveries of the aerodynamic performances are observed due to the recovery from the full-stalled state to the attached state.

Based on the investigation of the aerodynamic performances and the behaviour of the reattachment point, five characteristic  $AoA$  are proposed. First four are for the stall;  $AoA$  at which first drop in  $C_L$  is observed,  $AoA$  at which the LSB breaks down,  $AoA$  at which maximum leading edge suction peak in  $C_p$  is observed, and  $AoA$  at which drop in  $C_L$  associated to the dynamic stall is observed. The last one is  $AoA$  at which the flow starts to reattach around the final stage of the pitching motion. Especially, the definition of  $AoA$  at which the LSB breaks down is important on investigating the dynamic stall onset. In the dynamically stalled flowfield, the classical definition of the stall angle, which is defined by the  $AoA$  at which first drop in  $C_L$  is observed, has large lag compared with the  $AoA$  at which the LSB breaks down and thus is not proper as an index of dynamic stall onset.

The DBD plasma actuator parameters for the control cases are determined by integrating the general knowledge of the flow control around airfoils obtained in the previous researches and the investigation results of the flowfield without control obtained in the

current research. After some considerations, four cases are prepared to be examined. The DBD plasma actuator is installed at  $x/c = 0\%$  or  $15\%$ , and actuated with burst frequency  $F^+$  of 0.5, 6, or 50. The burst frequency of  $F^+$  of 0.5 is chosen based on the investigation on the behaviour of the large vortices and the intention is to make use of the momentum exchange by the induced large vortices. The burst frequency of  $F^+$  of 50 corresponds to the sub-harmonics of the instability frequency of the LSB right before the breakdown, and is chosen with the aim to energize the LSB. The other parameters such as  $D_c$  and BR are set as constant. The base frequencies  $f_{base}$  are set as a dependent variable of  $F^+$ . The controlled cases are named as ON  $F^+ = 0.5$ , ON  $F^+ = 6$ , ON  $F^+ = 50$ , and ON  $15\%F^+ = 6$ . Except for the case of ON  $15\%F^+ = 6$ , the DBD plasma actuator is installed at  $x/c = 0\%$ .

The control effects on the aerodynamic performances and the flowfield are investigated prior to the investigation on the control mechanisms. With regard to enhancement of the cycle-averaged lift coefficient  $C_L$  and torque coefficient  $C_Q$ , the case of ON  $F^+ = 0.5$  is the best. When focus is on the cycle-averaged lift-to-drag ratio  $L/D$ , the best cases in enhancing  $L/D$  are the case of ON  $F^+ = 6$  and ON  $F^+ = 50$ . Investigation on the flowfield and the separation and reattachment points revealed that the control effects on aerodynamic performances can be arranged as the following three major ones;

1. Delaying dynamic stall onset
2. Enhancing aerodynamic forces during full-stall
3. Promoting reattachment

The first control effect is delaying the dynamic stall onset. All the controlled cases successfully delay the breakdown of LSB, i.e., delay the dynamic stall onset. The best case in this control effect is the case of ON  $F^+ = 50$ , delaying the breakdown of LSB by  $AoA$  of  $1.1^\circ$ . Considering that the instability frequency of LSB is as high as  $St$  of 100 under the current Reynolds number regime, the cases with high actuation frequency whose low order harmonics can stimulate the instability frequency would have better control effect on delaying the dynamic stall onset. Stimulating the instability frequency of the shear layer can effectively advance the reattachment point and/or displace the shear layer toward the airfoil surface, and as a result the size of LSB (respectively in length and height) can be reduced. In addition to the control mechanism of energizing the LSB, an existence of the control mechanism of changing the history of the flowfield is suggested.

The second control effect is enhancing the aerodynamic forces during the full-stall. This effect is apparent only in the case of ON  $F^+ = 0.5$ . During the full-stall stage, the flowfield in the case of ON  $F^+ = 0.5$  shows large vortex structures while the flowfield in the other cases show no significant flow structures. These large vortices produce significant aerodynamic forces, and as the result the enhancement and oscillation of the aerodynamic performances are brought. The observations of the flowfield near the shear layer revealed that the large vortices are grown from kernel vortices. For the kernel vortices to be formed, it is found that the burst frequency which is lower than the natural instability frequency can help the vortices to grow into relatively large kernel vortices. In order to make the kernel vortex more larger, the use of sufficiently low burst frequency can help the kernel vortices grow into larger structure with mitigating the interaction between the kernel vortices. To make use of the aerodynamic forces of the large vortices, the  $F^+$  which can keep large vortices as much as possible over the airfoil would be better. As a result, it is considered that the most effective  $F^+$  would depend on the characteristic size and velocity.

The third control effect is promoting the reattachment at the final stage of the dynamic stall. With regard to this control effect, the case of ON  $F^+ = 6$  is the best case and the reattachment  $AoA$  is promoted by  $5.6^\circ$ . The role of the kernel vortices is also important for this control effect and the better cases show relatively large kernel vortices. With the combination effect of DBD plasma actuator of inducing the kernel vortices, displacing the shear layer toward the airfoil surface, and advancing the vortex shedding point, the momentum exchange between the freestream and the shear layer come to take place near the airfoil surface. It is also found that the excessive large vortices displaces the shear layer upward and can disrupt the reattachment. These investigations suggest that  $F^+$  should not to be too low to avoid the formation of the large vortices.

In some stages of dynamic stall process, the existence of a significant effect of changing the history of the flowfield, and also a significant upstream-propagating effect of the DBD plasma actuator are indicated. These indirect control effect on dynamic flowfields would be helpful for further advanced control strategies.

The control effects can be divided into some discrete effects. Discussions on the control effects and thus on the effective DBD plasma actuator parameters can be conducted isolated to each other control effect. It is shown that each control effect has each control mechanism, and each mechanism has effective set of the DBD plasma actuator parameters. However, a set of DBD plasma actuator parameter which is effective on utilizing an mechanism can be not effective on utilizing the other mechanisms. This result suggests us the use of adaptive control; if the DBD plasma actuator parameters are changed in



---

association with the change of the flowfield, the DBD plasma actuator can make more use of the effects of each mechanism.



# Chapter 6

## Study on effective control of dynamic flowfield around laminar airfoil

### 6.1 Outline

In this chapter, the studies on effective control of the dynamic flowfield around a laminar airfoil by a DBD plasma actuator are conducted. The objective airfoil is NACA63<sub>3</sub>-618 airfoil. First, the flowfield without control is investigated and then the DBD plasma actuator parameters are determined by integrating the investigation results of the flowfield without control and the arranged control mechanisms on controlling the dynamic flowfield obtained in Chapter 5.

### 6.2 Investigation on flowfield without control

The flow conditions for the NACA63<sub>3</sub>-618 airfoil cases are identical to the NACA0012 airfoil cases, and so the same steps of investigation on the flowfield without control are taken.

#### 6.2.1 Stationary flowfield

The cases for stationary flowfield are summarized in Table 6.1;  $AoA$  are set as 5, 10, 15, 20, and 25° and Reynolds number is set as constant of  $2.56 \times 10^5$ .

Figure 6.1, Figure 6.2, and Figure 6.3 shows the surface pressure coefficient  $C_p$  and friction coefficient  $C_f$  distributions for time- and span-averaged flowfield, the time- and

Table 6.1: Cases for stationary NACA63<sub>3</sub>-618 airfoil without control.

Reynolds number	Angle of attack	Reduced frequency
$2.56 \times 10^5$	5, 10, 15, 20, 25°	N/A

span-averaged streamwise velocity field, and  $C_L$ ,  $C_D$ , and  $C_M$  against  $AoA$ , respectively.

This airfoil exhibits some large differences from NACA0012 airfoil. From Figure 6.1 and Figure 6.2, it is observed that the flow separates around the mid-chord and soon reattaches at low  $AoA$ . Existence of an LSB is clearly observed even at  $AoA$  of 5°. As  $AoA$  increases, the area between the separation and reattachment points, i.e., an LSB, moves toward the leading edge while decreasing its size. From  $AoA$  of 15°, the flow separates around the trailing edge, while an LSB is formed near the leading edge. This secondary separation point moves toward upstream; at  $AoA$  of 20°, a large portion of the flow is separated from the secondary separation point. An LSB is observed at  $AoA$  of as high as 20° and it induces considerably low negative  $C_p$  at the leading edge. The breakdown of LSB and the full-stall from the leading edge is then observed at 25°. These behaviours of the separation points indicate that this airfoil has a combined type of stall characteristic of trailing edge stall and leading edge stall, while the stall type of this airfoil is biased toward the trailing edge stall.

The  $C_L$  curve against  $AoA$  shows gentle stall characteristics with no drastic drop after the stall, whose  $AoA$  is between 15 ~ 20°. Observing Figure 6.1, it is found that the decrease in  $C_L$  is due to the trailing edge separation whereas the negative  $C_p$  at the leading edge is greatly enhanced by the LSB. Here, thanks to the LSB,  $C_D$  at  $AoA$  of 15° is slightly decreased whereas the extent of trailing edge is increased compared with  $AoA$  of 10°. This suggests that the LSB is beneficial for producing lift and thrust under the current configuration. Therefore, it can be said that the stall angle, i.e., the drop in  $C_L$  is determined just by the balance of the thrust by the LSB and the drag by the trailing edge separation and so large changes in flowfield are not necessary observed on the occasion of the stall.

## 6.2.2 Dynamic flowfield

The flow condition for dynamic flowfield without control is listed in Table 6.2; all the parameters are completely the same with the NACA0012 airfoil case.

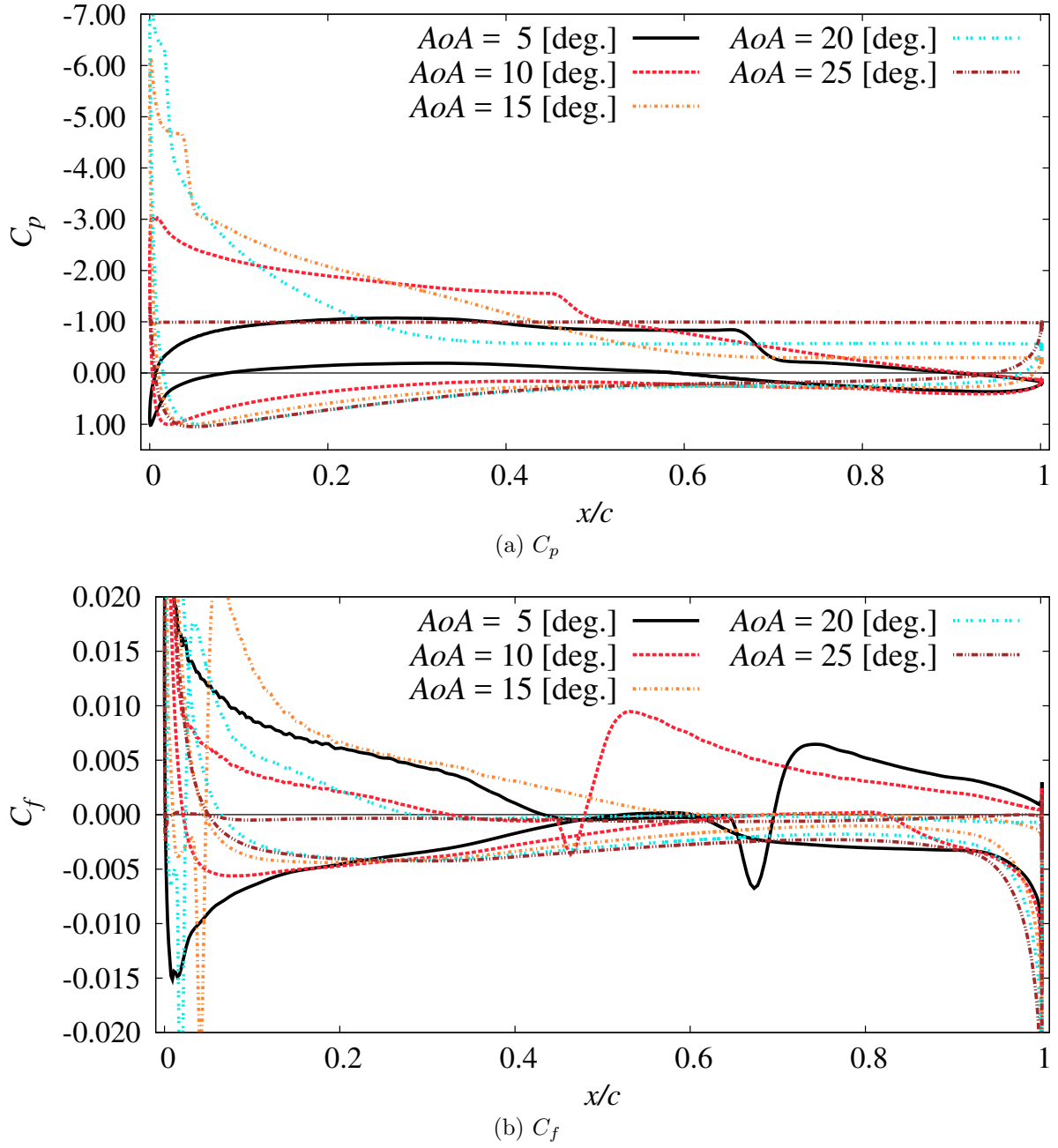
Figure 6.1: Chordwise  $C_p$  and  $C_f$  distributions for stationary NACA633-618airfoil.

Table 6.2: Case for pitching NACA633-618 airfoil without control.

Reynolds number	Angle of attack	Reduced frequency
$2.56 \times 10^5$	$5 \sim 25^\circ$	$0.02\pi$

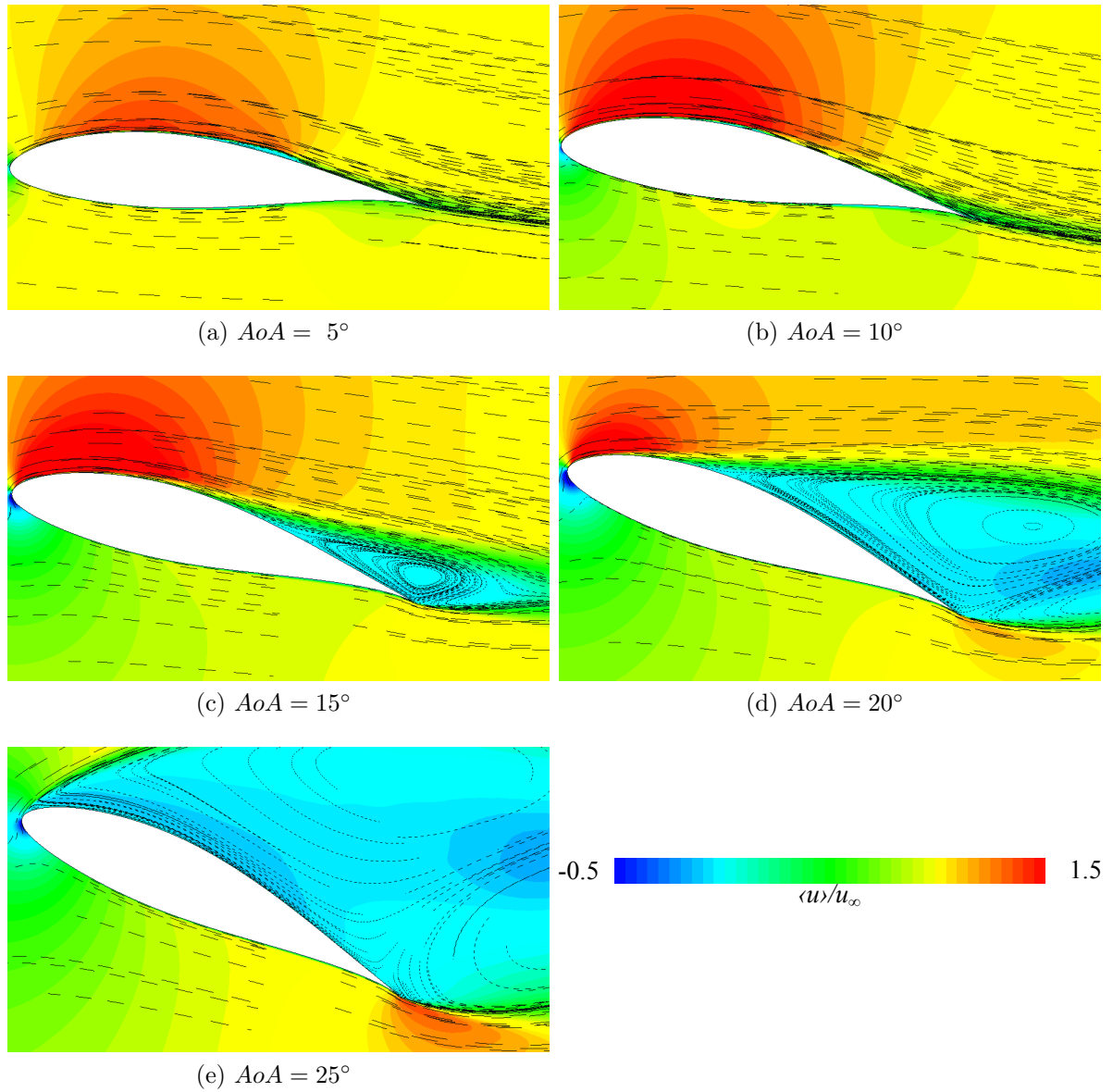


Figure 6.2: Time- and span-averaged streamwise velocity flowfield with streamline for stationary NACA63<sub>3</sub>-618 airfoil.

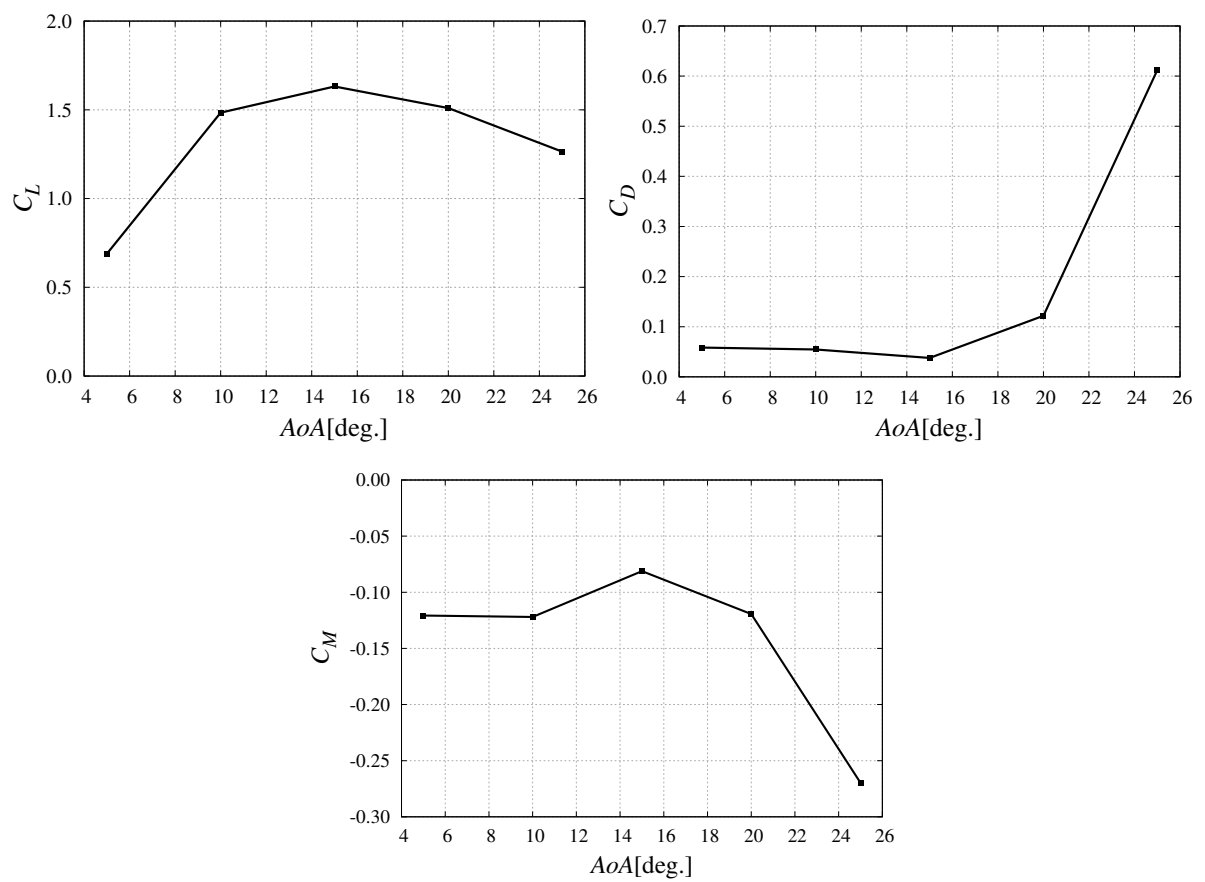


Figure 6.3: Aerodynamic performances for stationary NACA63<sub>3</sub>-618 airfoil.

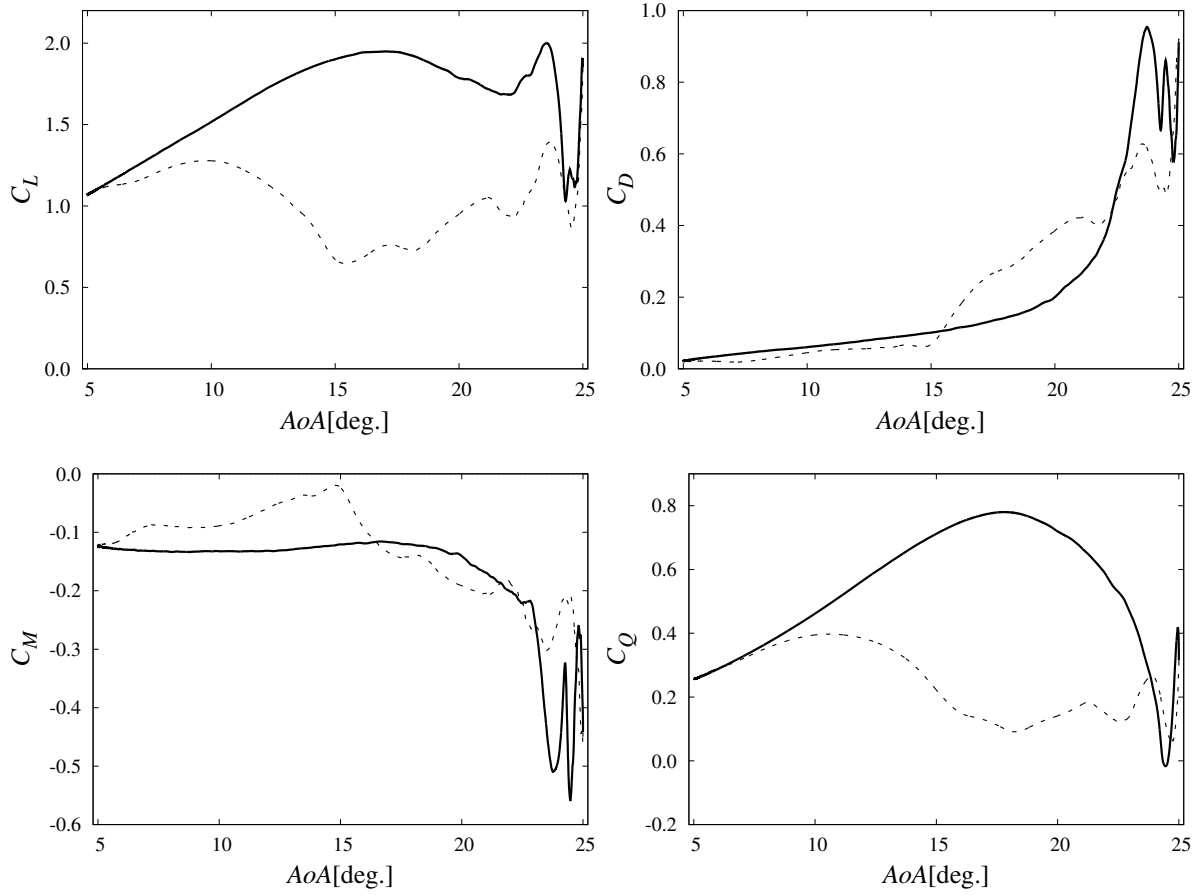


Figure 6.4: Aerodynamic performances against  $AoA$  for pitching NACA633-618 airfoil without control.

Solid lines denote increasing  $AoA$ , dashed lines decreasing  $AoA$ .

### Cycle-wise and phase-wise characteristics

The phase-averaged aerodynamic performances, the phase- and span-averaged flowfields, the instantaneous flowfields, and the separation points are presented in Figure 6.4, 6.5, 6.6, and 6.7, respectively.

At first glance, the gross shape of the curves depicted in Figure 6.4 look greatly different with these of NACA0012 airfoil, however, it is found that the most of the transient of the flowfield can be classified by the same way in NACA0012 airfoil. The dynamic flowfield around this airfoil is also characterized by the formation of LSB, the breakdown of LSB, the convection of DSV, the full-stall from the leading edge, and recovery to the attached state. However, this airfoil still shows some unique characteristics of the flowfield compared with NACA0012 airfoil. The first unique characteristic is the behaviour of the LSB at low  $AoA$ . As seen in Figure 6.7, the separation and reattachment



points are located around the mid-chord at low  $AoA$  (Figure 6.5 and 6.6(a)). This area corresponds to an LSB and its size is decreased as the increase of  $AoA$ . This decrease in size of LSB is brought by the advancement of the reattachment point; the separation point stays around  $x/c = 37\%$  against the change in  $AoA$ , until  $AoA$  reaches to  $10^\circ$ . Then  $AoA$  reaches to approximately  $12^\circ$ , the separation point start to rapidly move toward the leading edge. This move of the separation point is so fast and the separation point disappears in the phase-averaged flowfield, as observed in Figure 6.7 around the *phase* of  $36^\circ$ . The second, notable unique characteristic is the trailing edge separation, which is observed from  $AoA$   $15^\circ$  until the dynamic stall. At  $AoA$  of  $15^\circ$ , the flow begins to separate near the trailing edge aside from the first separation near the leading edge (Figure 6.5 and 6.6(b)). As the result of the balance of the increase in  $C_L$  by the LSB and the decrease by trailing edge separation,  $C_L$  begin to decrease from  $AoA_{LD}$  of  $17.1^\circ$  (soon after Figure 6.5 and 6.6(b)) whereas the breakdown of LSB is observed at  $AoA_{BD}$  of  $19.1^\circ$  (Figure 6.5 and 6.6(c) is at the moment of the breakdown). Then the dynamic stall is triggered by the breakdown of LSB, and sudden and drastic changes in aerodynamic performances are observed.

Figure 6.5 and 6.6(d), (e), (f), and (g) depicts the phase at which  $C_L$  begins to suddenly increase,  $C_L$  takes maximum associated to the convection of DSV,  $C_L$  takes minimum after the shed of DSV, and  $C_L$  takes next maximum associated to the convection of the secondary large vortex from the leading edge, respectively. Here  $AoA_{LDDS}$  is observed at  $23.5^\circ$ . As shown in Figure 6.5 and 6.6(g) and Figure 6.4 around  $AoA$  of  $25^\circ$ , the effect of the secondary large vortex from the leading edge on the aerodynamic performances are considerably large, compared with NACA0012 airfoil. This is because of the characteristic geometry of this airfoil; this airfoil has concaved camber around the trailing edge on the lower side, and it is considered that this characteristic enhance the formation of the trailing edge vortex. With this characteristic, the flowfield around a NACA63<sub>3</sub>-618 airfoil exhibits significantly more large vortices from the leading edge and trailing edge compared with the flowfield around a NACA0012 airfoil.

After all the large vortices have shed, full-stall from the leading edge is observed (Figure 6.5 and 6.6(h)). However, the duration in the full-stall is short compared with NACA0012 airfoil case due to the long duration in which the large vortices from the leading edge dominates the flowfield and dur to the fast recovery to the attached state; the recovery to the attached state begins at  $AoA_{RA}$  of  $16.4^\circ$ . As seen in the flowfield after the reattachment (Figure 6.5 and 6.6(i)), the flow reattaches to the airfoil surface very smoothly; the reattachment starts around  $x/c = 0.1$ , and then the separation and reattachment points moves together toward the trailing edge. During the *phase* between

$274 \sim 296^\circ$  ( $AoA$  of  $14.5 \sim 10.5^\circ$ ), the flow is completely attached to the airfoil in the phase-averaged flowfield. And then, the flow begins to separates around the mid-chord (Figure 6.5 and 6.6(j)) and turn back to the pitching up.

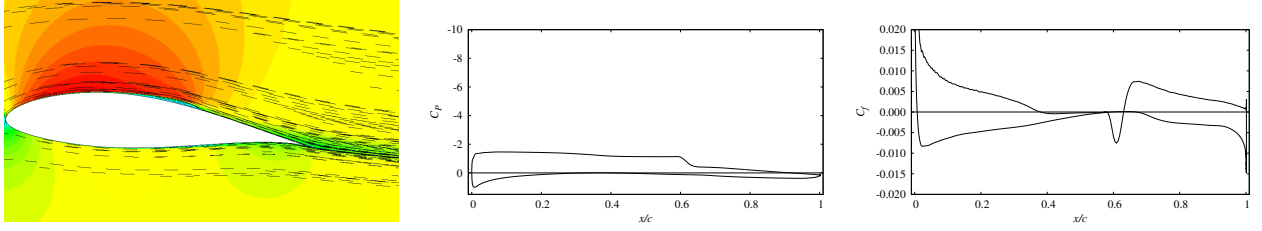
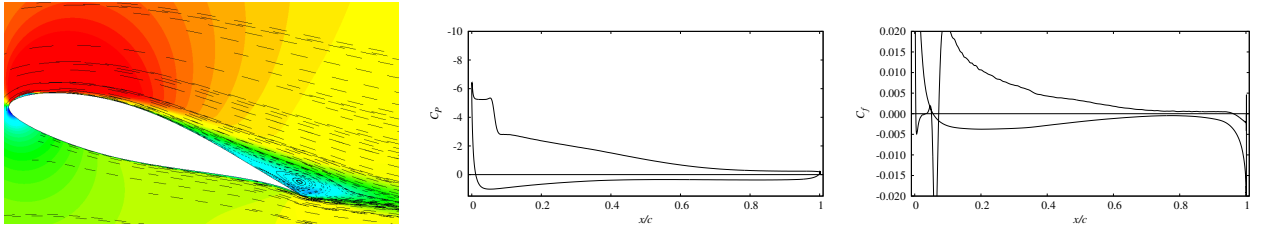
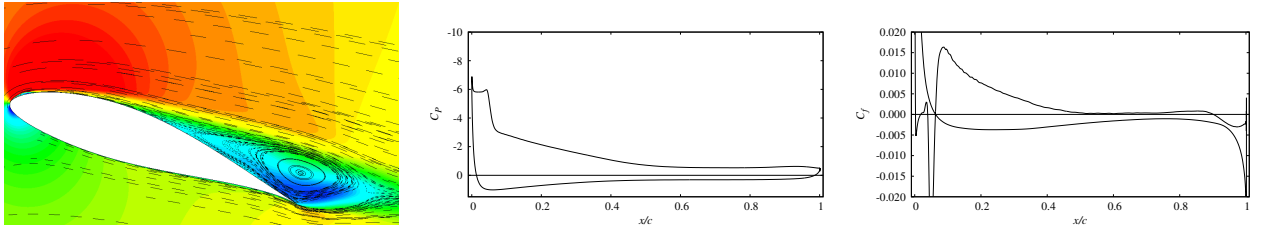
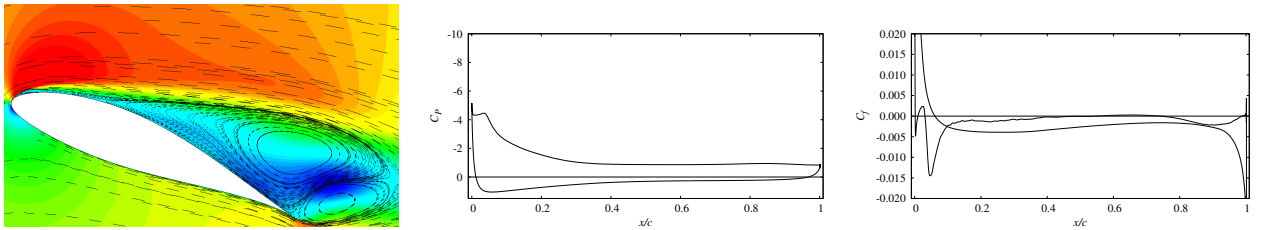
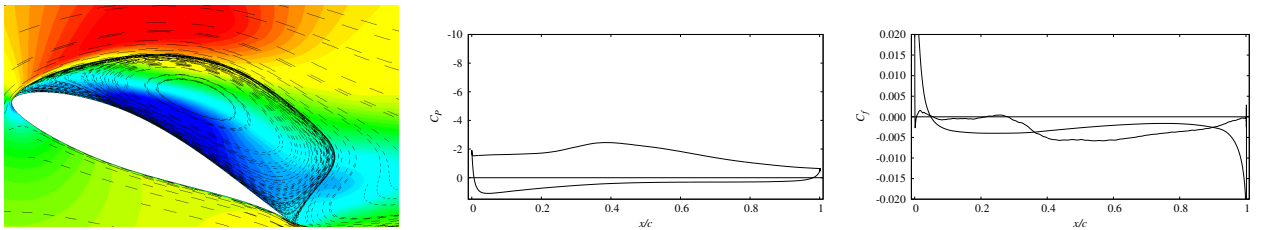
As for the characteristic  $AoA$ , the breakdown of LSB is observed after the first lift drop, and the lift drop associated to the dynamic stall take places at the different  $AoA$ . This characteristic is also the result of the trailing edge stall.

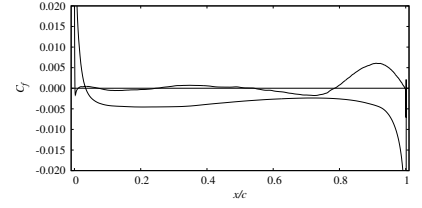
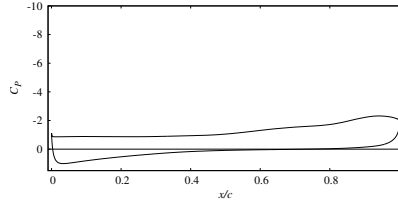
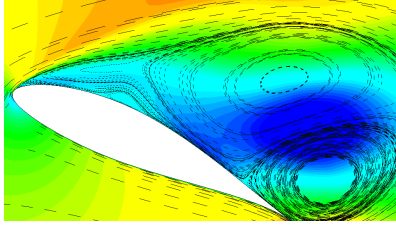
### 6.2.3 Considerations on DBD plasma actuator parameters

As introduces above, the flowfield around NACA63<sub>3</sub>-618 airfoil is characterized by combinations of each flow feature. The curves of the aerodynamic performances show complex aspects compared with NACA0012 airfoil due to such the complex characteristic. Thus, there are seemingly many possible set of the DBD plasma actuator parameters for controlling such a complex flowfield. The findings in the previous chapter is that the dynamic stall process can be classified into stages and the discussions on the effective DBD plasma actuator parameters can be conducted isolated to each other control effect. When focusing on each stage of the dynamic stall process, the dynamic stall process around NACA63<sub>3</sub>-618 airfoil is generally comparable with the flowfield around NACA0012. Therefore, it can be considered that the arranged control mechanisms are applicable on this flowfield. To find effective control strategy on such a complex flowfield with limited trials, the sets of the DBD plasma actuator parameters to be examined are chosen using the arranged findings in the previous chapter.

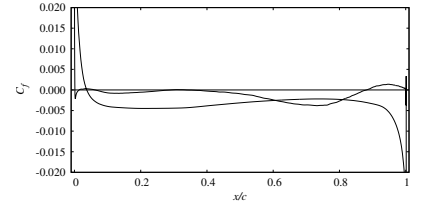
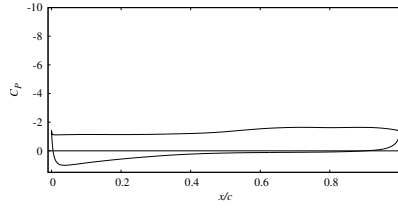
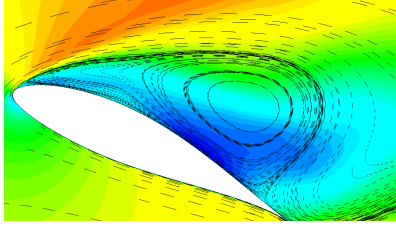
#### DBD plasma actuator parameters for delaying dynamic stall onset

Figure 6.8 shows PSD of the chordwise velocity on the shear layer in the phases before the breakdown of LSB. In this study, the maximum resolved  $St$  is extended to 200 in the NACA63<sub>3</sub>-618 airfoil cases. The LSB rapidly moves toward the leading edge, and this move of LSB steadies down near the leading edge around the *phase* of  $80^\circ$ . After the LSB steadies down, the prominent peak is now observed around  $St = 90$  in Figure 6.8. The study in the previous chapter suggested that the effective DBD plasma actuator parameter, especially  $F^+$ , is the frequency whose low order of harmonics corresponds to the instability frequency. Therefore,  $F^+$  for this case is set to 50, which is the lowest order of the subharmonics of 90. With regard to the installation position, the installation position is chosen to be the leading edge, considering the separation point right before the dynamic stall is close to the leading edge.

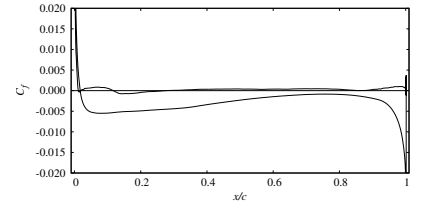
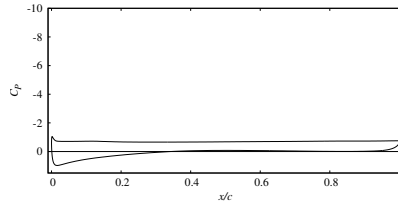
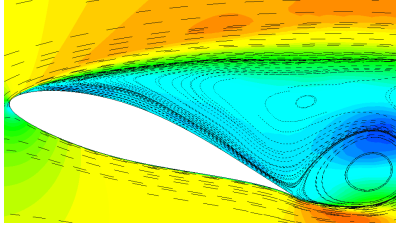
(a)  $phase = 0^\circ$  ( $AoA = 5.0^\circ$  in pitching up)(b)  $phase = 102^\circ$  ( $AoA = 16.9^\circ$  in pitching up)(c)  $phase = 116^\circ$  ( $AoA = 19.2^\circ$  in pitching up)(d)  $phase = 136^\circ$  ( $AoA = 22.1^\circ$  in pitching up)(e)  $phase = 148^\circ$  ( $AoA = 23.4^\circ$  in pitching up)Figure 6.5: Phase- and span-averaged flowfield for pitching NACA63<sub>3</sub>-618 airfoil without control.



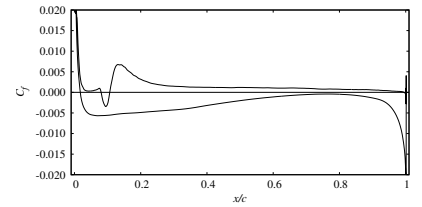
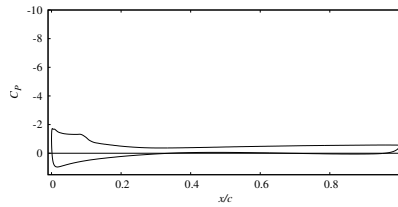
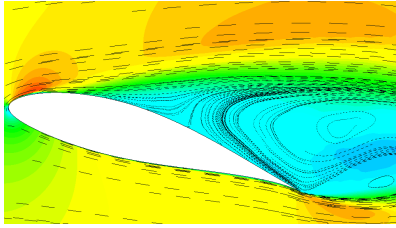
(f)  $phase = 162^\circ$  (  $AoA = 24.4^\circ$  in pitching up)



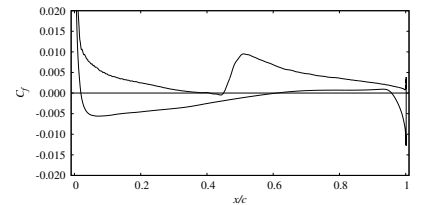
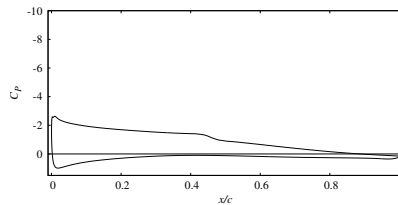
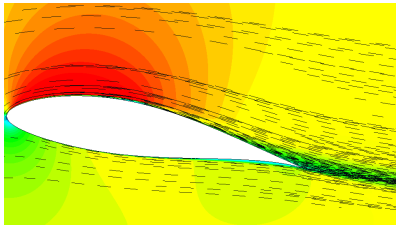
(g)  $phase = 176^\circ$  (  $AoA = 24.9^\circ$  in pitching up)



(h)  $phase = 254^\circ$  (  $AoA = 17.8^\circ$  in pitching down)



(i)  $phase = 266^\circ$  (  $AoA = 15.7^\circ$  in pitching down)



(j)  $phase = 302^\circ$  (  $AoA = 9.8^\circ$  in pitching down)

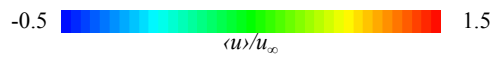


Figure 6.5: *Continued.*

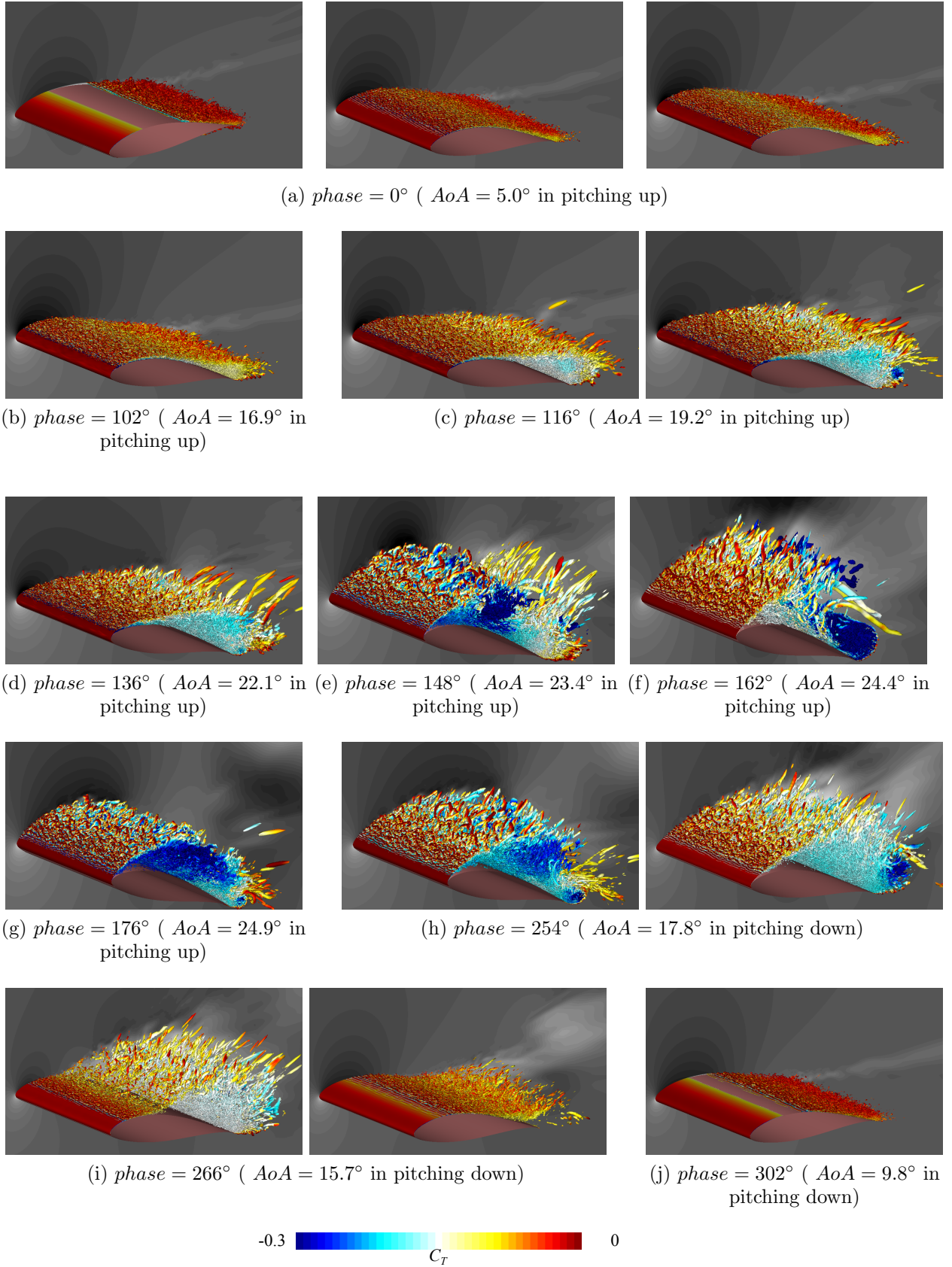


Figure 6.6: Snapshots of instantaneous flowfield for pitching NACA63<sub>3</sub>-618 airfoil without control. The iso-surfaces indicate the second invariant of the velocity gradient tensor colored by total pressure coefficient.

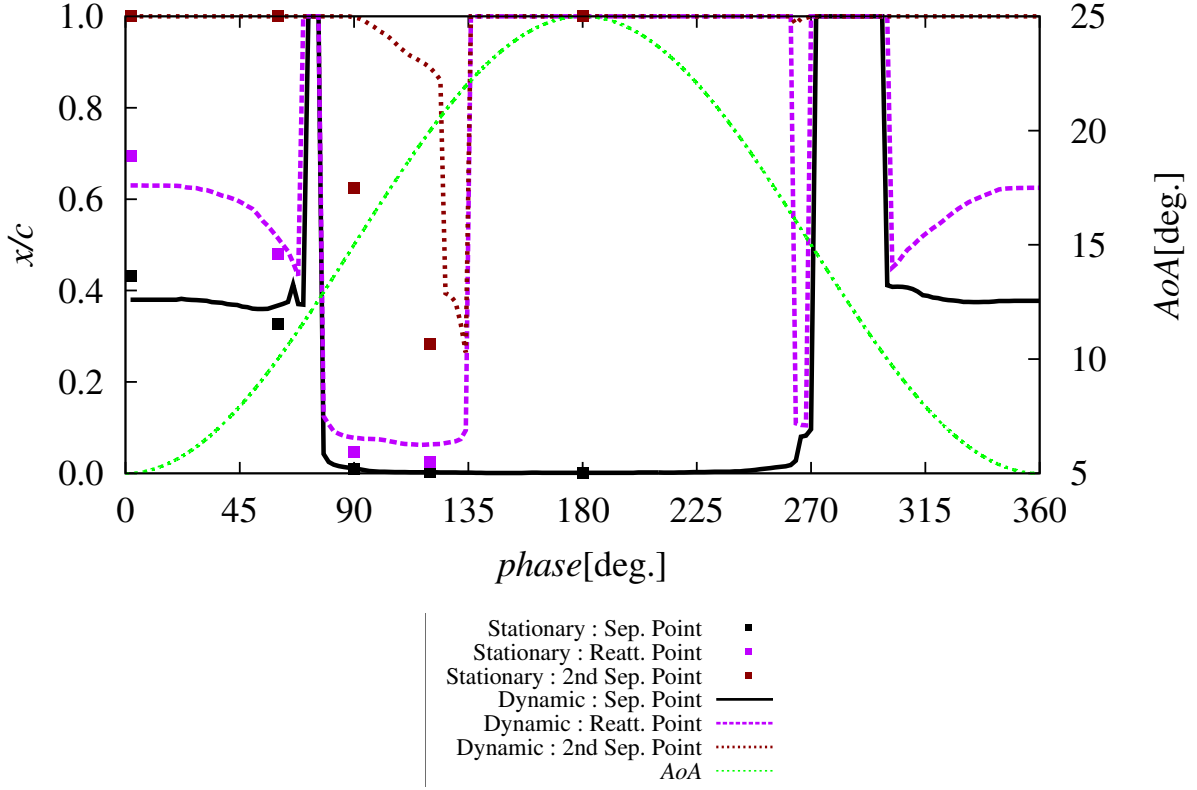
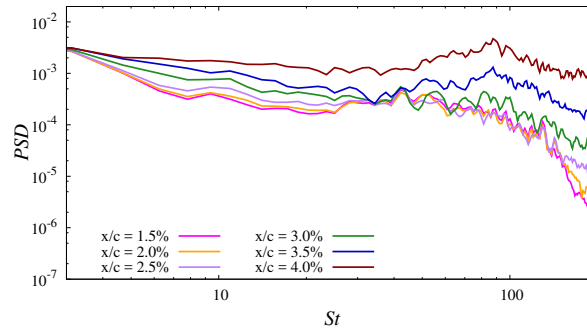


Figure 6.7: Separation, reattachment, and secondary separation points against pitching phase for stationary and pitching NACA63-618 airfoil without control. Corresponding  $AoA$  is plotted with right axis.



(a) Around  $phase = 102^\circ$  ( $AoA = 16.9 \sim 17.5^\circ$ )

Figure 6.8: PSD of chordwise velocity on shear layer for pitching NACA63-618 airfoil before the breakdown of LSB.



### DBD plasma actuator parameters for enhancing aerodynamic force during full-stall

In the previous chapter, it is found that the burst frequency which is lower than the natural instability frequency can effectively grow the vortices into larger vortices. It is also suggested that the effective  $F^+$  depends on the characteristic size and velocity so as to keep many large vortices over the airfoil surface. Figure 6.9 shows the phase-history of the surface pressure coefficient  $C_p$ . In the subfigure, the phase during the full-stalled stage is enlarged. With this figure, especially from the *phase* around  $210 \sim 240$ , where corresponds to the middle of the full-stalled stage, it can be calculated as the convective velocity of the large vortices during the full-stalled stage corresponds to approximately  $0.5u_\infty$ , as the same with the NACA0012 airfoil case. As for the characteristic length of the large vortex, the large vortex emanates from the leading edge and continues to grow until reaches to the trailing edge. This is also the same as the NACA0012 airfoil. Considering that the emanation point of the vortex, pitching  $AoA$  range, reduced frequency and all the flow condition are the same, the coincidence of these parameters are not surprising. Thus, the effective  $F^+$  is identical to the case for NACA0012 airfoil and set as  $F^+ = 0.5$ . With regard to the installation position, the DBD plasma actuator is required to inject momentum into the shear layer and the installation position is set as the leading edge.

### DBD plasma actuator parameters for promoting reattachment

The key for the effective control on promoting the reattachment is the use of the kernel vortex. To induce moderately sized kernel vortices,  $F^+$  is better to be lower than the natural vortex shedding frequency, but should not be too low. Figure 6.10 shows PSD of the chordwise velocity on the shear layer in the corresponding stage. In both of figures, the amplified frequency is observed around  $St$  of 30 and have some large slope. Both of the shape of the PSD and the peak  $St$  observed in Figure 6.10 are comparable with these of the NACA0012 airfoil case. In the current study, therefore,  $F^+$  of 6 is employed in the track of the NACA0012 airfoil case. With regard to the installation position, the DBD plasma actuator is also installed at the leading edge in order to induce the kernel vortices.

### DBD plasma actuator parameters for further effective control

Aside from the three cases, an additional special case is also prepared and investigated. In this case,  $F^+$  is modulated with the change in the flowfield. This idea is derived from the one of the conclusion of the previous chapter; an effective set of DBD plasma

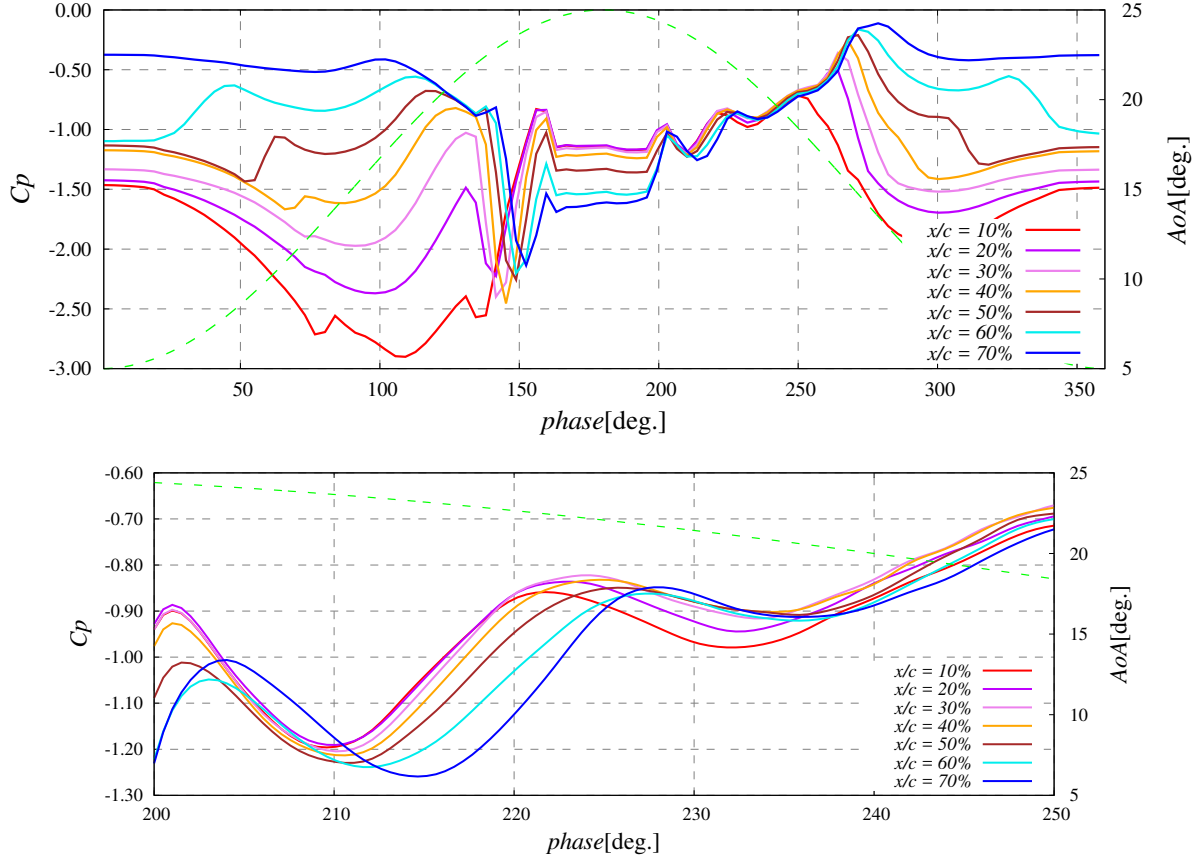
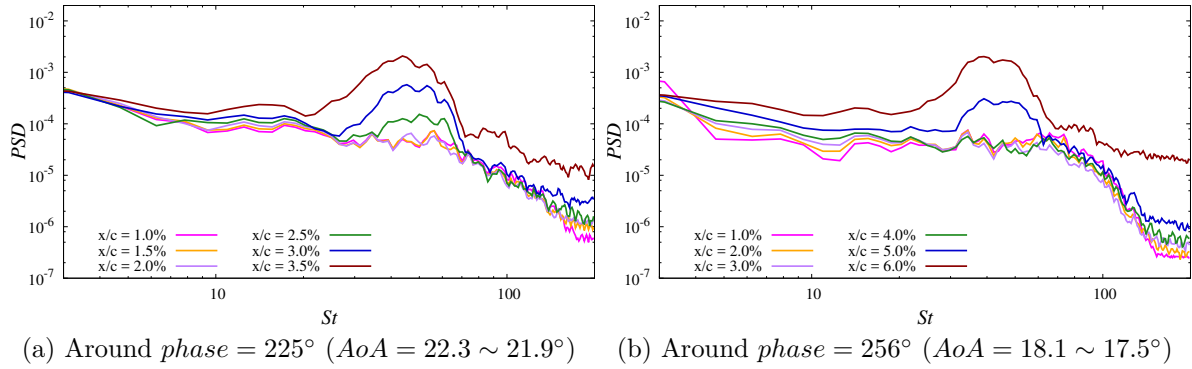


Figure 6.9: Phase history of phase- and span-averaged surface  $C_p$  at various chordwise location.



(a) Around  $phase = 225^\circ$  ( $AoA = 22.3 \sim 21.9^\circ$ ) (b) Around  $phase = 256^\circ$  ( $AoA = 18.1 \sim 17.5^\circ$ )

Figure 6.10: PSD of chordwise velocity on shear layer for pitching NACA63<sub>3</sub>-618 airfoil during the full-stall.



Table 6.3: Cases for pitching NACA63<sub>3</sub>-618 airfoil.

Case name	Installation position	$F^+$	$D_c$	$f_{base}$	$BR$
OFF	N/A	N/A	N/A	N/A	N/A
ON $F^+ = 0.5$	$x/c = 0\%$	0.5	0.25	70	0.1
ON $F^+ = 6$	$x/c = 0\%$	6	0.25	240	0.1
ON $F^+ = 50$	$x/c = 0\%$	50	0.25	200	0.1
ON Predet	$x/c = 0\%$	0.5, 6, or 50 (switched by $AoA$ )	0.25	70, 240, or 200 (switched by $AoA$ )	0.1

actuator on an mechanism can be not effective on the other mechanisms. As concluded in the previous chapter, the effects of controlling the dynamic flowfield can be divided into discrete effects. To gain the best performance of the DBD plasma actuator, then, the effect of an adaptive control that makes use of each discrete control effect at the phase by phase is investigated here.

For a simplicity,  $F^+$  is switched between the predeterminant values according to the  $AoA$  of that time. The predeterminant  $F^+$  are, 0.5, 6, and 50;  $F^+$  of 50 is for stage 2,  $F^+$  of 0.5 is for stage 4, and  $F^+$  of 6 is for stage 5. First, the stage between 2 and 4 is divided by the stage 3, where the control effect is not clear or cannot be prominent, the switching can be taken place anytime in stage 3. In this case,  $F^+$  is switched from 50 to 0.5 at the possible maximum  $AoA_{LDDS}$ , and a result the switching  $AoA$  is set as  $AoA$  of  $24^\circ$ . With regard to the switching from  $F^+$  of 0.5 to 6, the switching is taken places a little before the possible minimum  $AoA_{RA}$  considering that the large vortex displace the shear layer upward and can disrupt the reattachment. In this case, switching  $AoA$  is set as  $20^\circ$  during the pitching down. And then,  $F^+$  is switched from 6 to 50 at the minimum  $AoA$  of  $5^\circ$ . This case is hereafter called as “ON Predet”.

## 6.3 Control of dynamic flowfield

### 6.3.1 Case description

The cases with control for the flowfield around a pitching NACA63<sub>3</sub>-618 airfoil is summarized in Table 6.3.

Table 6.4: Cycle-averaged aerodynamic performances.

Case name	$C_L$	$C_D$	$L/D$	$C_Q$	$\zeta_d$
OFF	1.29	0.239	5.39	0.345	0.0447
ON $F^+ = 0.5$	1.37	0.270	5.09	0.362	0.00624
ON $F^+ = 6$	1.33	0.237	5.62	0.366	0.0353
ON $F^+ = 50$	1.31	0.230	5.69	0.362	0.0399
ON Predet	1.34	0.234	5.72	0.370	0.0244

### 6.3.2 Control effects on cycle-averaged aerodynamic performances

Table 6.4 shows the cycle-averaged aerodynamic performances. Overall, the characteristic changes in the aerodynamic performance are consistent with these observed in the NACA0012 airfoil case; the case of ON  $F^+ = 0.5$  shows large increase in  $C_L$  and  $C_D$  at the same time and as a result enhancement in  $L/D$  is cancelled out to be negative, and the cases of ON  $F^+ = 6$  and ON  $F^+ = 50$  shows  $C_L$  increase without  $C_D$  increase. The best enhancement in  $L/D$  and  $C_Q$  is attained in the case of ON Predet, exhibiting  $L/D$  enhancement by 6.1% and  $C_Q$  enhancement by 7.3%. The second best enhancement in  $L/D$  is attained in the cases of ON  $F^+ = 50$  by 4.1%. With regard to the  $C_Q$ , the second best case is the case of ON  $F^+ = 6$ , which enhances  $C_Q$  by 6.1%. As for  $\zeta_d$ ,  $\zeta_d$  is considerably worsened in the case of ON  $F^+ = 0.5$ , although it is still above zero.

### 6.3.3 Control effects on phase-averaged aerodynamic performances and characteristic $AoA$

Figure 6.11 presents the phase-averaged aerodynamic performances against  $AoA$ . From Figure 6.11(a), the control effects on the aerodynamic performances cannot be clearly distinguished, whereas the control effect is observed in the cycle-integrated aerodynamic performances. This may be caused by the trailing edge vortex; the trailing edge vortices around this airfoil are stronger and observed more often than these around NACA0012 airfoil. And thus the undulation of the aerodynamic performances after the dynamic stall tends to be large and to vary enormously.

The control effects can be observed more clearly by Table 6.5; the characteristic  $AoA$  show that the anticipated control effects are obtained. Here, some values are of rough estimation, due to the large oscillation by the DBD plasma actuator. The best control effect of delaying the dynamic stall onset in the case of ON  $F^+ = 50$ , the clear effect in

Table 6.5: Control effects on  $AoA_{BD}$ ,  $AoA_{DS}$ ,  $AoA_{LD}$ , and  $AoA_{RA}$  for pitching NACA63<sub>3</sub>-618 airfoil.

Values in brackets are of rough estimation.

$AoA_{BD}$ ,  $AoA_{DS}$ , and  $AoA_{LD}$  are in the pitching up and  $AoA_{RA}$  is in the pitching down.

Case name	$AoA_{BD}$	$AoA_{DS}$	$AoA_{LD}$	$AoA_{LDDs}$	$AoA_{RA}$
OFF	19.1°	18.9°	17.1°	23.5°	16.4°
ON $F^+ = 0.5$	(19.1°)	(18.9°)	17.3°	23.6°	(16.1°)
ON $F^+ = 6$	19.2°	(19.0°)	17.0°	23.9°	17.4°
ON $F^+ = 50$	19.7°	19.1°	17.1°	23.8°	16.7°
ON Predet	19.7°	19.1°	17.5°	23.7°	17.1°

enhancing the aerodynamic forces during the full-stall in the case of ON  $F^+ = 0.5$ , and the best control effect of promoting the recovery to the attached state in the case of ON  $F^+ = 6$  are clearly observed. As for the case of ON Predet, this case successfully delay the dynamic stall and promote the recovery to the attached state by the best level. In the best cases,  $AoA_{BD}$  is delayed by 0.6° in the case of ON  $F^+ = 50$ ,  $AoA_{RA}$  is promoted by 1.0°.

Figure 6.12 presents the phase-averaged flowfields against  $AoA$  with  $C_p$  and  $C_f$  distribution for the cases with DBD plasma actuator at the leading edge. Through the entire pitching phase, the control effect is not clear in an overview, however, the control effect can be observed in a closed-up view or detailed analysis, although not presented here to avoid repetition.

## 6.4 Discussions

In this chapter, the control effects of the DBD plasma actuator on the dynamic flowfield around a pitching NACA63<sub>3</sub>-618 airfoil are investigated. The flowfield without control has the combined stall type of the leading edge stall and trailing edge stall, while is biased toward the trailing edge stall. With this characteristic, the aerodynamic performance curves show more complex aspects. On such a flowfield, however, the flow control attempts based on the findings from the flowfield around a NACA0012 airfoil, which has the leading-edge-stall-biased type of stall characteristic, showed good enhancements in the aerodynamic performances. This would be because the beginning and the end of dynamic stall process is characterized by the flow features only around the leading edge and so the flowfield around the trailing edge is of less important on the dynamic

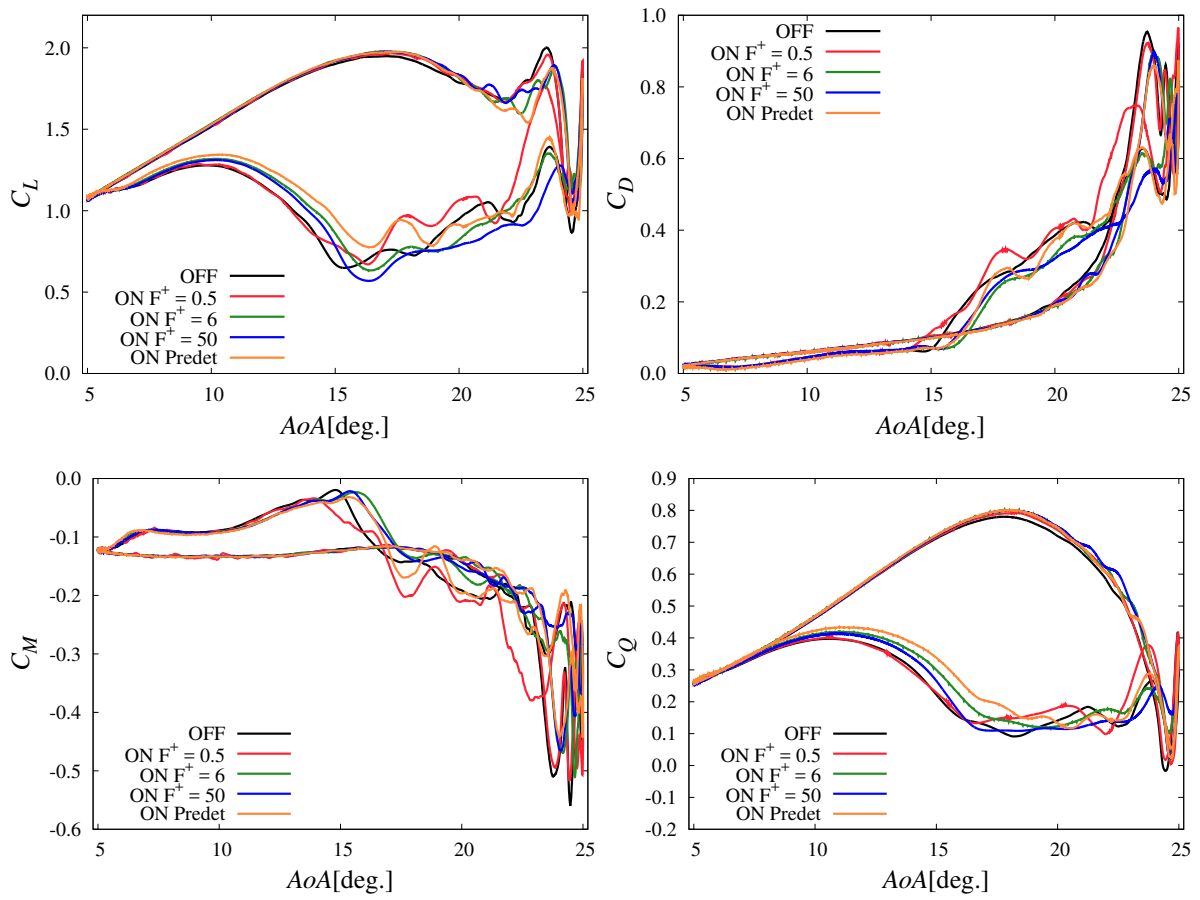


Figure 6.11: Aerodynamic performances against  $AoA$  for pitching NACA633-618 airfoil.

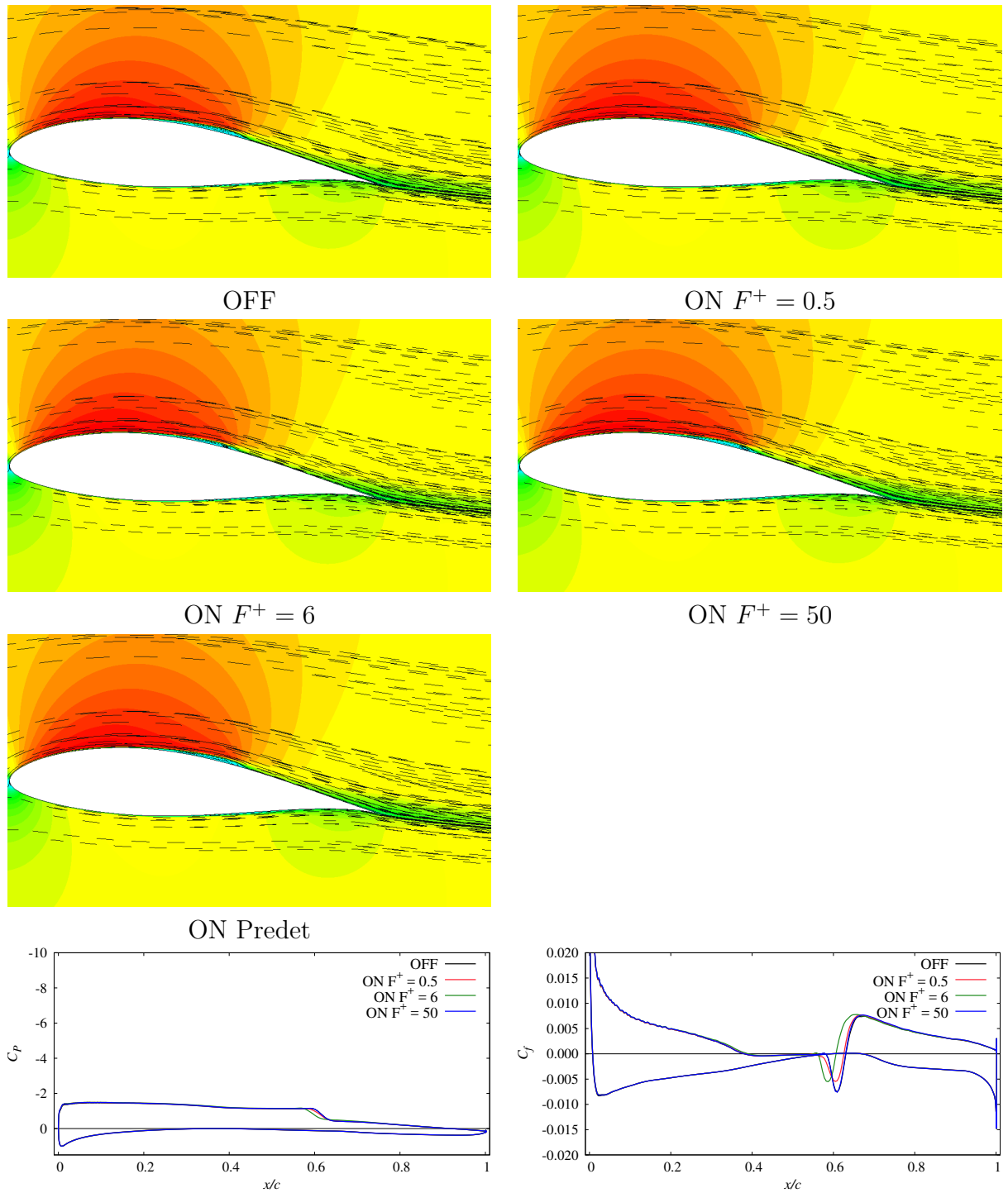
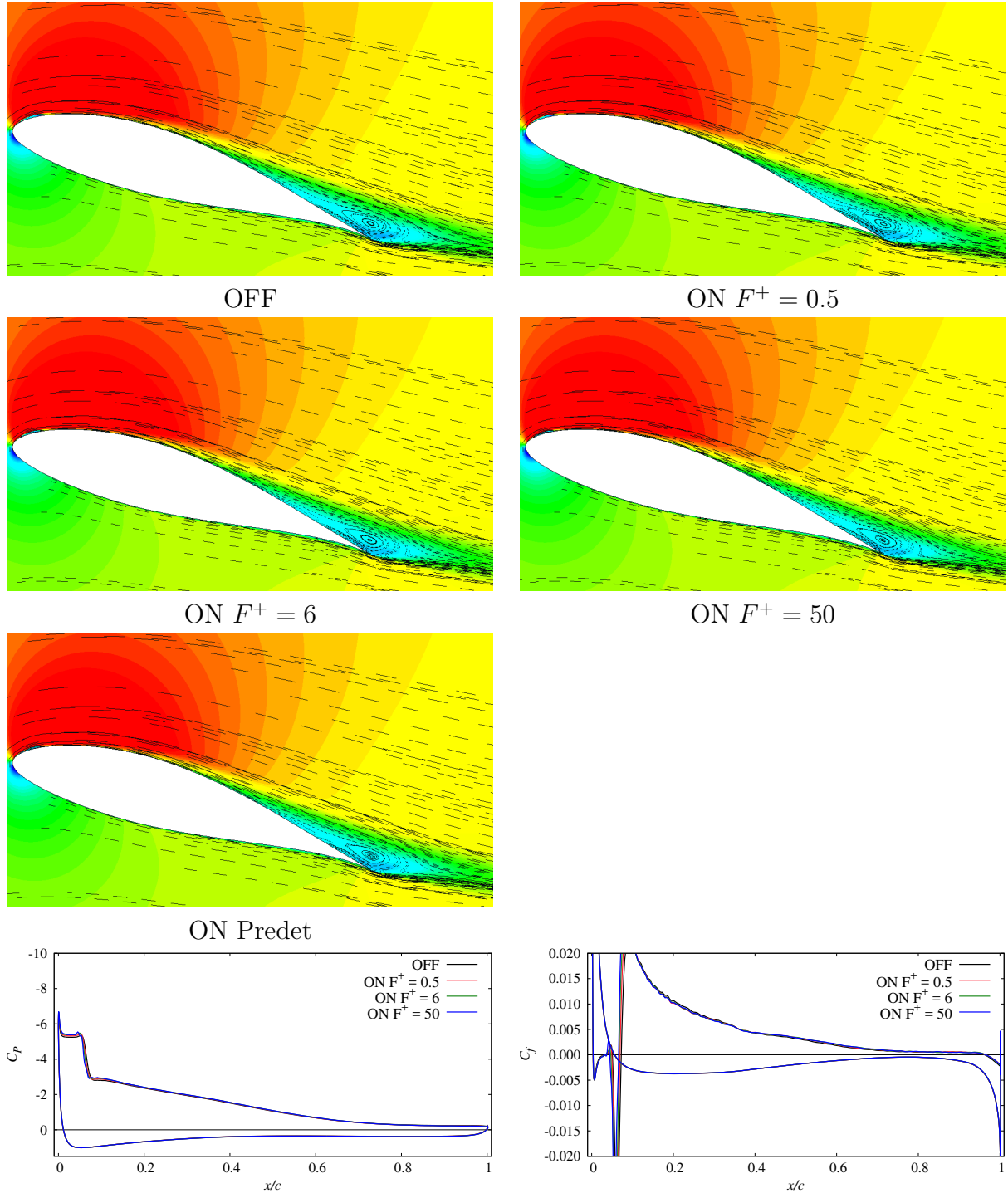


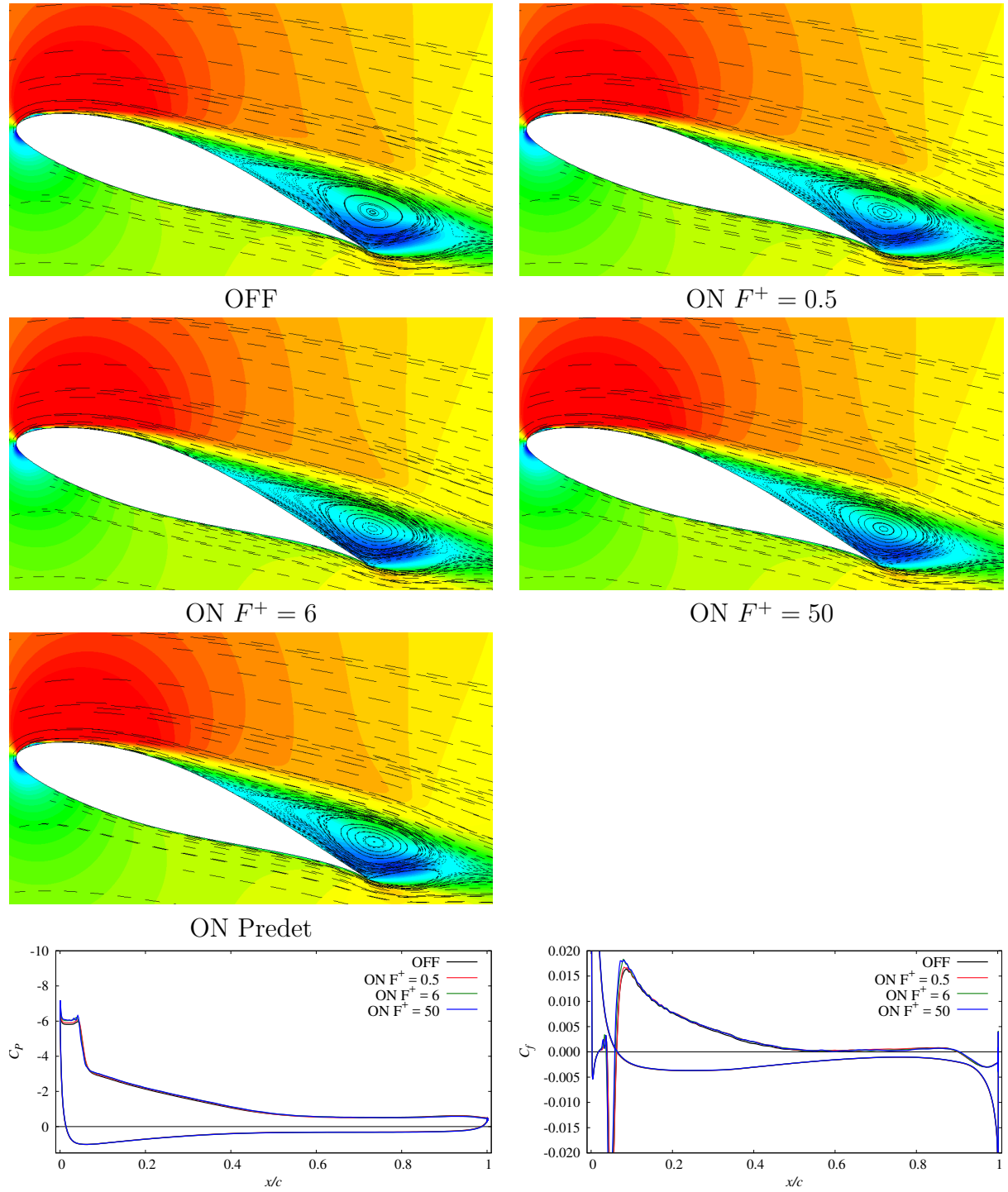
Figure 6.12: Top left to right : Phase- and span-averaged flowfield for basic cases of pitching NACA633-618 airfoil. Left to right: OFF, ON  $F^+ = 0.5$ , ON  $F^+ = 6$ , and  $F^+ = 50$ .

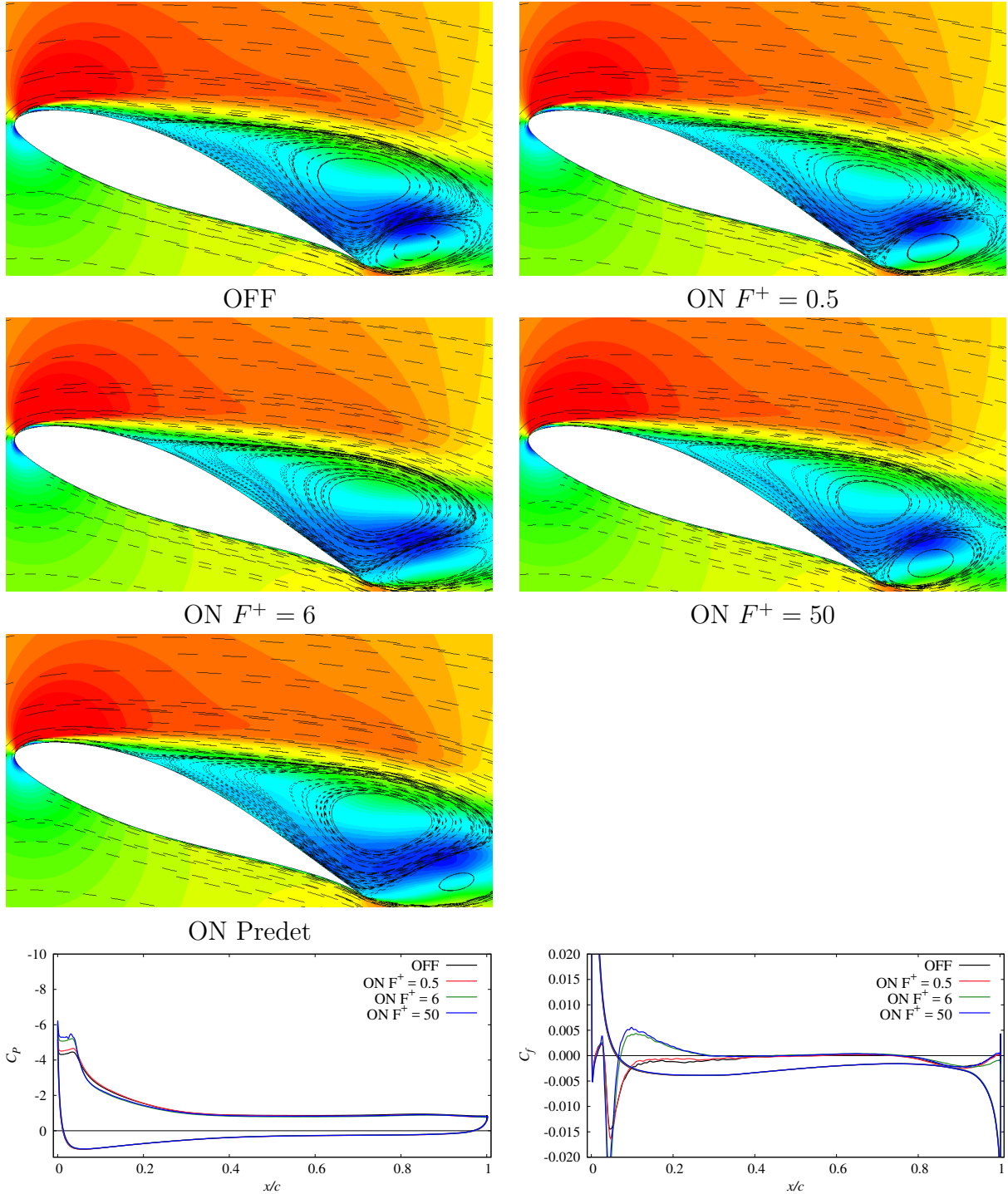
Bottom: Phase-averaged  $C_p$  and  $C_f$  distribution.



(b)  $\text{phase} = 102^\circ$  ( $\text{AoA} = 16.9^\circ$  in pitching up)

Figure 6.12: *Continued.*

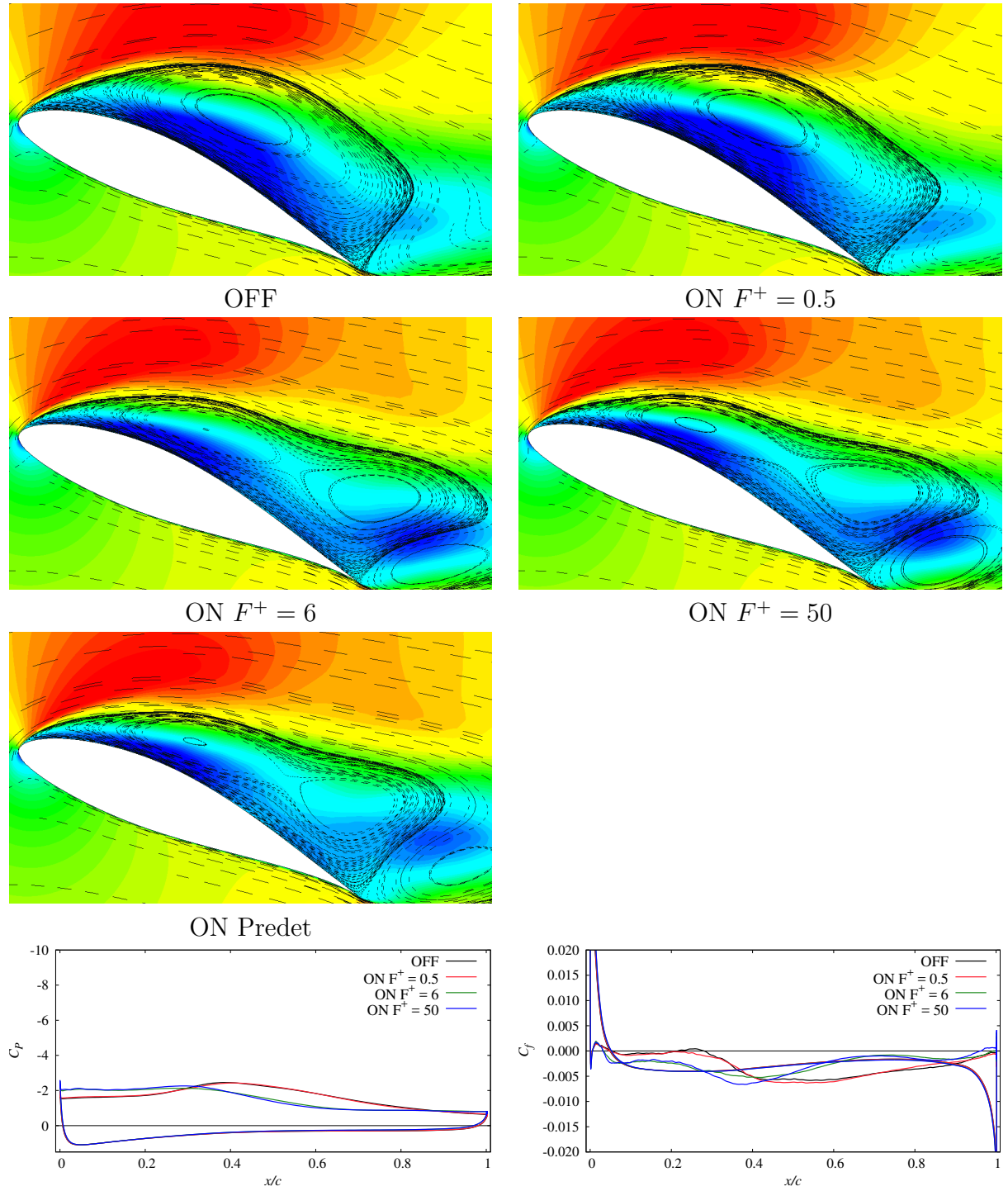
(c)  $phase = 116^\circ$  (  $AoA = 19.2^\circ$  in pitching up)Figure 6.12: *Continued.*

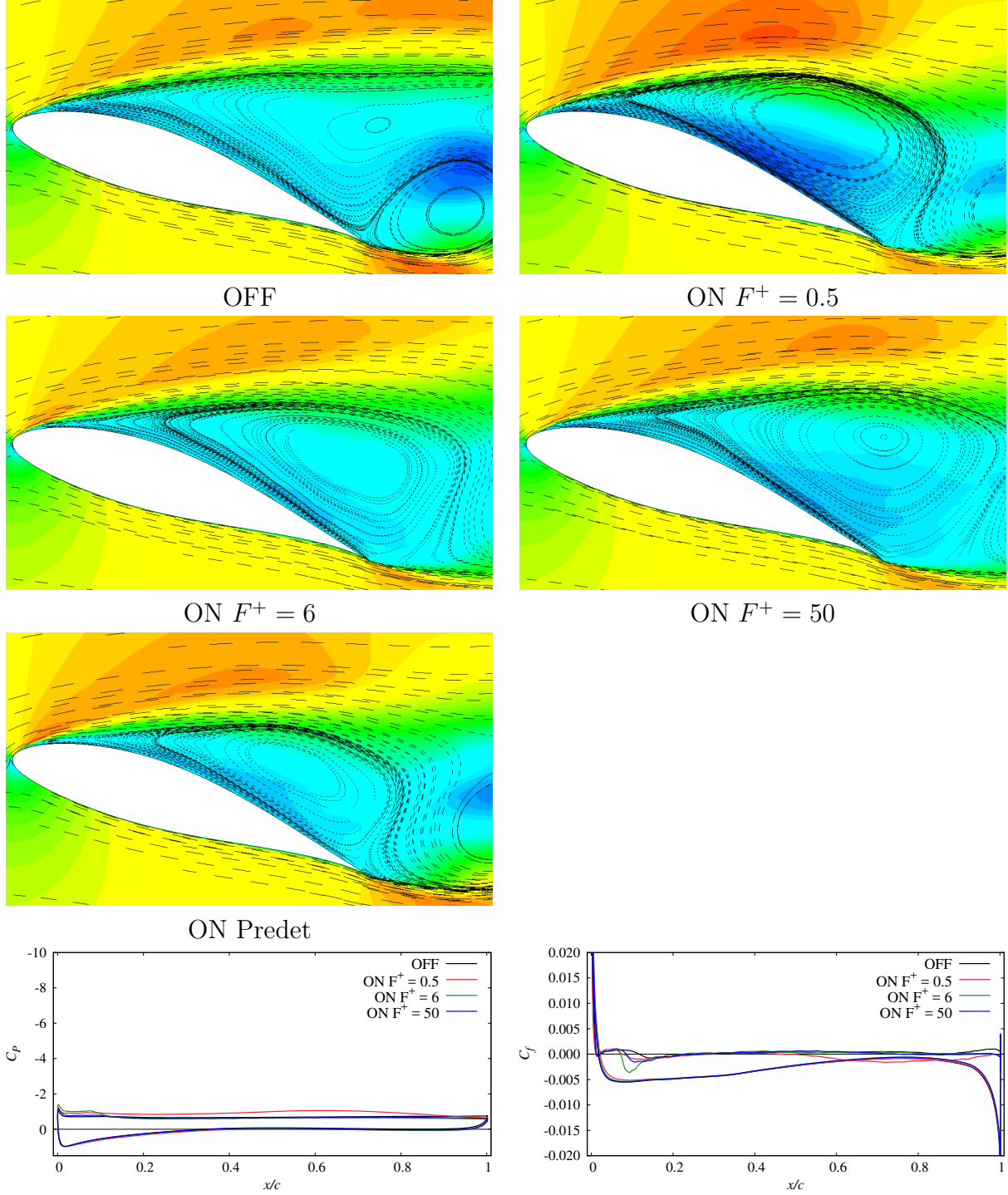


(d)  $phase = 136^\circ$  (  $AoA = 22.1^\circ$  in pitching up)

Figure 6.12: *Continued.*

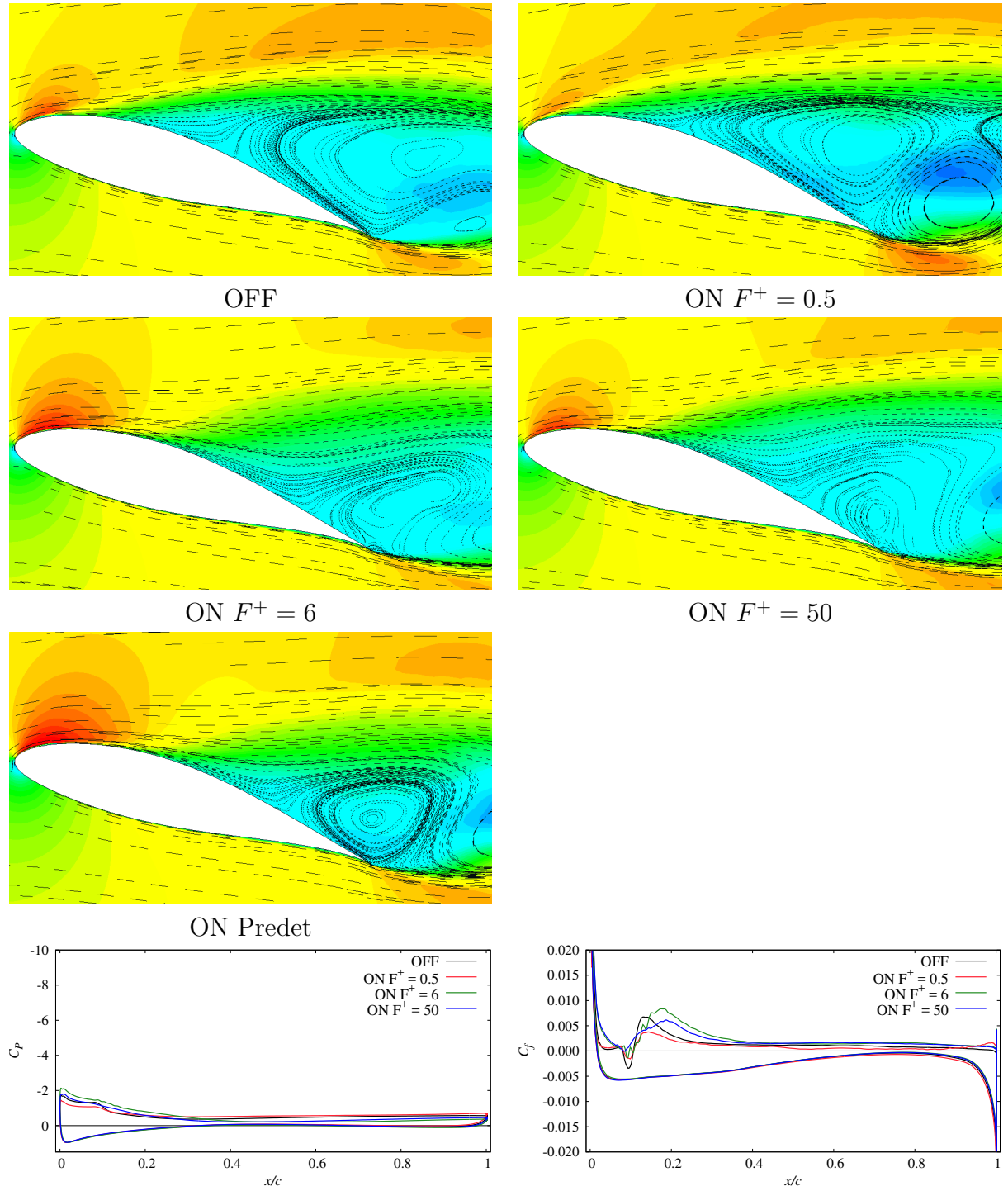


(e)  $\text{phase} = 148^\circ$  ( $\text{AoA} = 23.4^\circ$  in pitching up)Figure 6.12: *Continued.*



(f)  $phase = 254^\circ$  ( $AoA = 17.8^\circ$  in pitching down)

Figure 6.12: *Continued.*

(g)  $phase = 266^\circ$  ( $AoA = 15.7^\circ$  in pitching down)Figure 6.12: *Continued.*

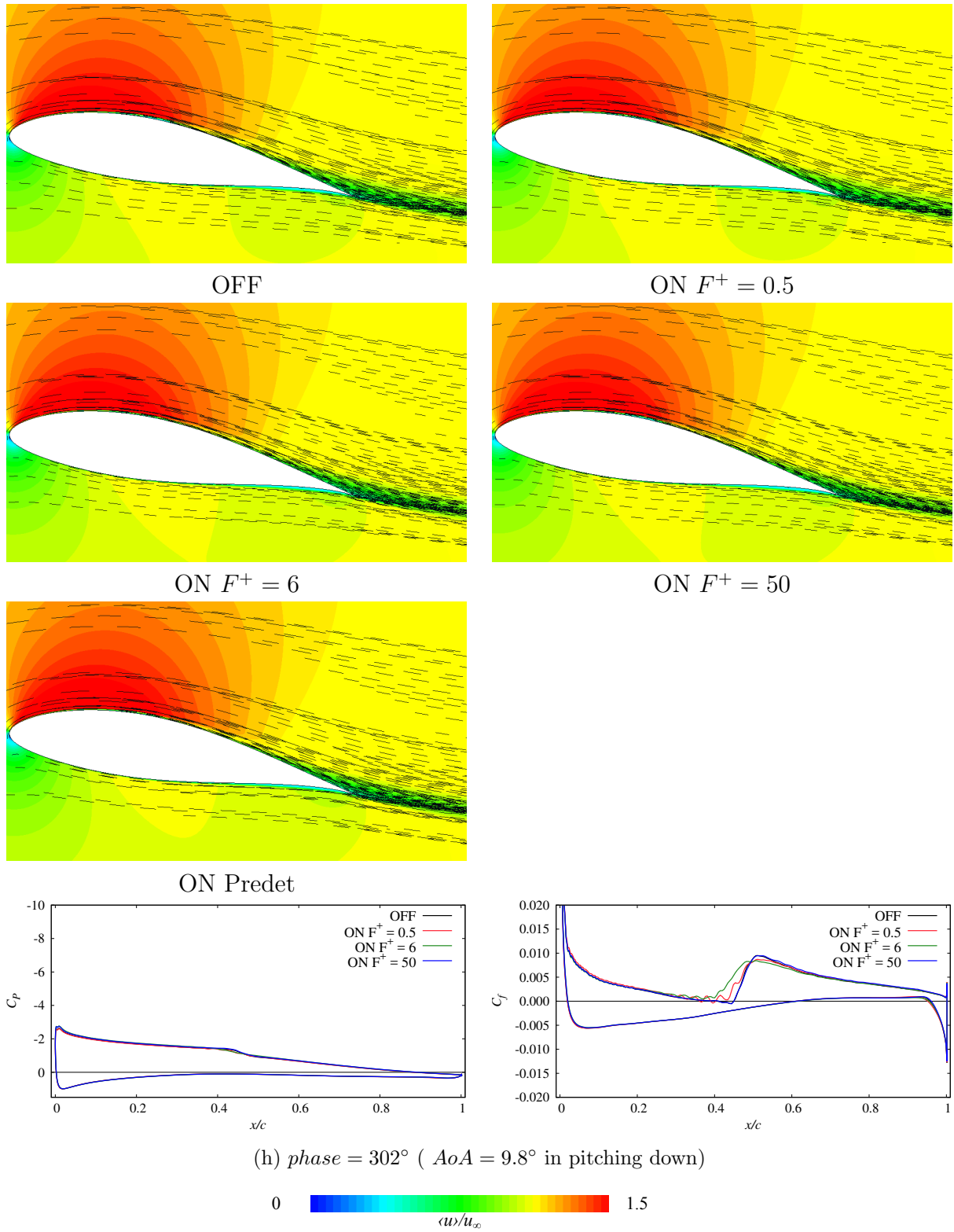


Figure 6.12: *Continued.*

Table 6.6: List of auxiliary cases.

Reynolds number	Angle of attack	Reduced frequency
$2.56 \times 10^5$	$5 \sim 25^\circ$	$0.02\pi$
$2.56 \times 10^5$	$5 \sim 25^\circ$	$0.03\pi$
$2.56 \times 10^5$	$5 \sim 25^\circ$	$0.05\pi$
$6.30 \times 10^4$	$5 \sim 25^\circ$	$0.02\pi$

stall. This result suggests that the control mechanism found in this research is applicable irrespective to the extent of the trailing edge separation, or maybe irrespective to airfoil shapes.

The DBD plasma actuator parameters are determined by the investigation only on the flowfield in the corresponding stage. The result that the control cases successfully enhanced the aerodynamic performances at the expected stage supports the validity of the procedure to determine the DBD plasma actuator parameters. This procedure to determine the DBD plasma actuator parameters is, to summarize, classify the phases into a stage of dynamic stall process and then investigate the each stage's flowfield to determine the DBD plasma actuator parameters to control the each stage's flowfield. The result that the case of ON Predet worked as proper as expected supports the validity of this procedure for determining the parameters.

These results say that both of the control mechanisms and the procedure to determine the DBD plasma actuator parameters are applicable to the flowfield even with large extent of trailing edge separation. To discuss the applicability of the findings, some considerations are made and introduced here. Here, to support the argument, some auxiliary cases are calculated. The cases are listed in Table 6.6. Note that these case are for NACA0012 airfoil and DBD plasma actuator is not installed. Here, the "findings" means these two; the first is the revealed and related understandings of the control effects, mechanisms and the corresponding effective DBD plasma actuator (afore mentioned procedure to determine the DBD plasma actuator parameters) and the second is that the dynamic stall process and the control effects can be divided respectively into some discrete stages/effects and discussions on the control effects and thus on the effective DBD plasma actuator parameters can be conducted isolated to each other control effect.

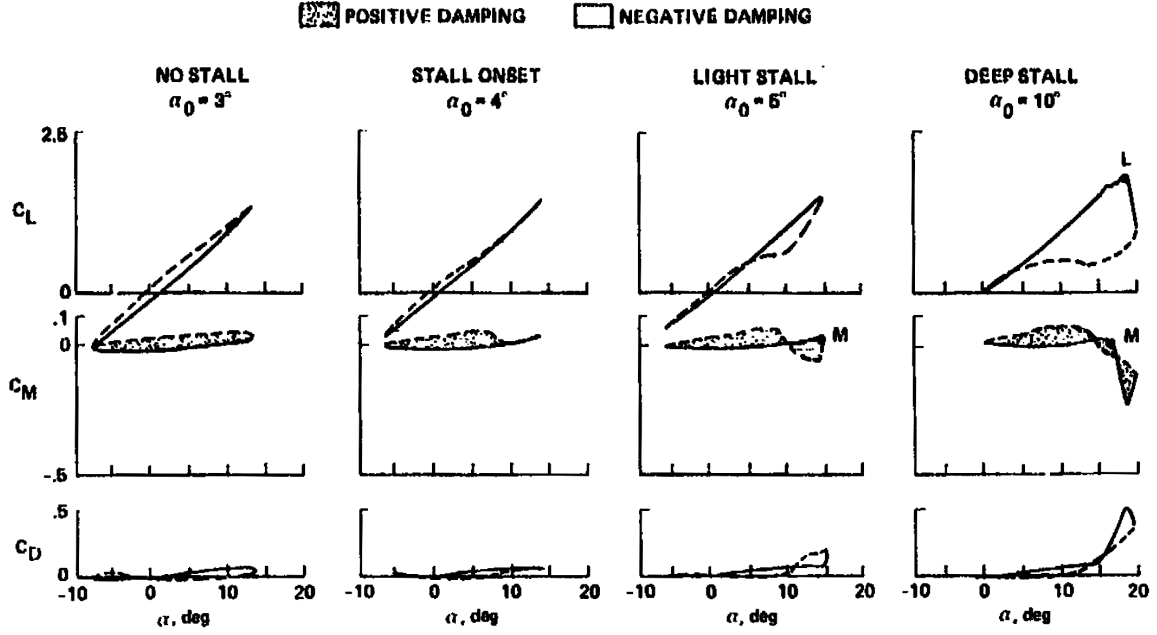


Figure 6.13: Dynamic stall regimes.<sup>3</sup>

$C_L$ ,  $C_M$ , and  $C_D$  curves against  $AoA$  are depicted for the flowfield around a pitching NACA0012 airfoil at Reynolds number of  $\mathcal{O}(10^6)$  with  $k = 0.1$ .

$\alpha = \alpha_0 + 10^\circ \sin \omega t$ , solid lines denote increasing  $\alpha$ , dashed lines decreasing  $\alpha$ .

### 6.4.1 Dynamic stall regimes

McCroskey divided dynamic stall into four categories based on the extent of flow separation.<sup>3</sup> The four categories are illustrated in Figure 6.13. The first two categories the no-stall and stall onset regime. In these two categories, the aerodynamic performances can be predicted well by quasi-steady aerodynamic theory<sup>178</sup> and does not exhibit large hystereses between the pitching up and down. The light stall and deep stall regime exhibits significant aerodynamic hysteresis. The difference in the definitions between the light stall and deep stall regime is the vertical extent of the separated region. In the light dynamic stall regime, the vertical extent of the separated region is the order of the airfoil thickness whereas this can be the order of the airfoil chord in the deep stall regime. The primary parameter that determines the dynamic stall regime is the maximum  $AoA$ .<sup>3</sup> Note that the dynamic stall observed in the current researches are all in the deep stall regime.

### 6.4.2 Applicability to light stall regime

In the light stall regime, the flow experiences the sudden change in the aerodynamic forces on the occasion of stall as seen in Figure 6.13 “LIGHT STALL”.<sup>3</sup> This regime is

known to be sensitive to the changes in airfoil geometry, Reynolds number, and reduced frequency. With regard to the three control effects, first, the dynamic stall onset is forced to occur at the maximum  $AoA$ .<sup>167</sup> This means that the control effect of delaying dynamic stall onset cannot exist in the light stall regime. Next, with regard to the other control effects of enhancing aerodynamic forces during full-stall and promoting reattachment, the flowfield does not always exhibit the leading edge separation depending on airfoil geometries and is not dominated by large vortices.<sup>3,179</sup> This suggests that the control effects of enhancing aerodynamic forces during full-stall and promoting reattachment cannot exist in the light stall regime depending on airfoil geometry or flow conditions. Therefore, it is indicated that the findings are not always valid in the dynamic flowfield in the light stall regime. As aforementioned, the primary parameter that determines the dynamic stall regime is the maximum  $AoA$  rather Reynolds number or the reduced frequency<sup>3</sup> and so the assessment of the  $AoA$  range of the objective dynamic flowfield is of primary importance when considering to control the dynamic flowfields.

### 6.4.3 Applicability to deep stall regime

The deep stall regime is characterized and dominated by a dynamic stall vortex. The flowfield in this regime is less sensitive to the changes in airfoil geometry, Reynolds number, or the reduced frequency than that in the light stall regime.<sup>3</sup>

First, the dependencies of the flowfield or the classification of dynamic stall process on airfoil geometry is very small as seen in Figure 6.14.<sup>3</sup> The consistent result is obtained in the current study that the classification of dynamic stall process is applicable to the flowfield around a laminar airfoil which has the trailing-edge-stall-biased type of stall characteristic.

Then, the dependencies of the flowfield or the classification of dynamic stall process on the reduced frequency is investigated next. Figure 6.15, 6.16, and 6.17 presents the dependency of the aerodynamic performances on the reduced frequency. Observing the flowfield with the aerodynamic performances for various reduced frequencies, it can be said that the classification of dynamic stall process is applicable to the flowfield with various reduced frequency, although the stage 4 where full-stall from the leading edge is observed become relatively shorter with the increase of  $k$ . As seen in the instantaneous flowfields, the aspects of the flowfield such as the formation of LSB right before the dynamic stall, the convection of the large vortex (DSV), and the vortex shedding during the leading edge stall do not significantly change even when the reduced frequency  $k$  changes. These results indicates that the findings can be applied to the dynamic flowfield



in the deep stall regime with various reduced frequencies. Note that the dynamic flowfield with low  $k$  (below  $0.004$ , for example) can be regarded as quasi-steady flowfield<sup>168</sup> whereas that with high  $k$  above  $0.05\pi$  is not well-investigated.

Reynolds number has less importance on the dynamic flowfield or the classification of dynamic stall process.<sup>3</sup> Figure 6.18 presents the classification of dynamic stall process by Carr.<sup>4</sup> The curves are for the dynamic flowfield around a NACA0012 airfoil at Reynolds number of  $2.5 \times 10^6$  with  $k = 0.15$ . The aspects of the curves and the explanation of the flowfield in Figure 6.18 agree well with these of the flowfield around a NACA0012 airfoil at Reynolds number of  $2.56 \times 10^5$  with  $k = 0.05\pi$  (approximately  $0.157$ ), which is presented in Figure 6.17. This result suggests that the dependency of the classification of dynamic stall process on Reynolds number is small. However, it does not mean that the dependency of the dynamic flowfield on Reynolds number is negligible nor that the findings are applicable irrespective to Reynolds number. The previous researches that investigate the details of dynamic flowfield in high Reynolds number regime ( $\mathcal{O}(10^6)$ ) revealed that the dynamic stall in high Reynolds number regime is still characterized by LSB.<sup>180,181</sup> Considering that the two control mechanisms of delaying dynamic stall onset and promoting reattachment are related to LSB, it is considered that the findings are valid to the flowfield at high Reynolds number regime, as long as the dynamic stall is characterized by LSB.

With regard to lower Reynolds number regime, another auxiliary case is calculated to discuss this issue. Figure 6.19 presents the aerodynamic performances and the flowfields for the low Reynolds number case. Comparing Figure 6.19 and 6.15, these two cases with different Reynolds number also agree with each other. With regard to the details of the flowfields, the flow features related to the control mechanisms, i.e., LSB, DSV, shed vortices from the leading edge shear layer are very similar to these at Reynolds number of  $2.56 \times 10^5$ . These suggest the applicability of the findings to low Reynolds number regime.

To conclude, it is suggested that the findings are applicable to the dynamic flowfield around various airfoil shape in the deep stall regime at various Reynolds numbers as long as the dynamic stall is characterized by LSB with the reduced frequency of  $0.02\pi \sim 0.05\pi$  at minimum. Further investigations are required to assess the applicability boundary of the findings.



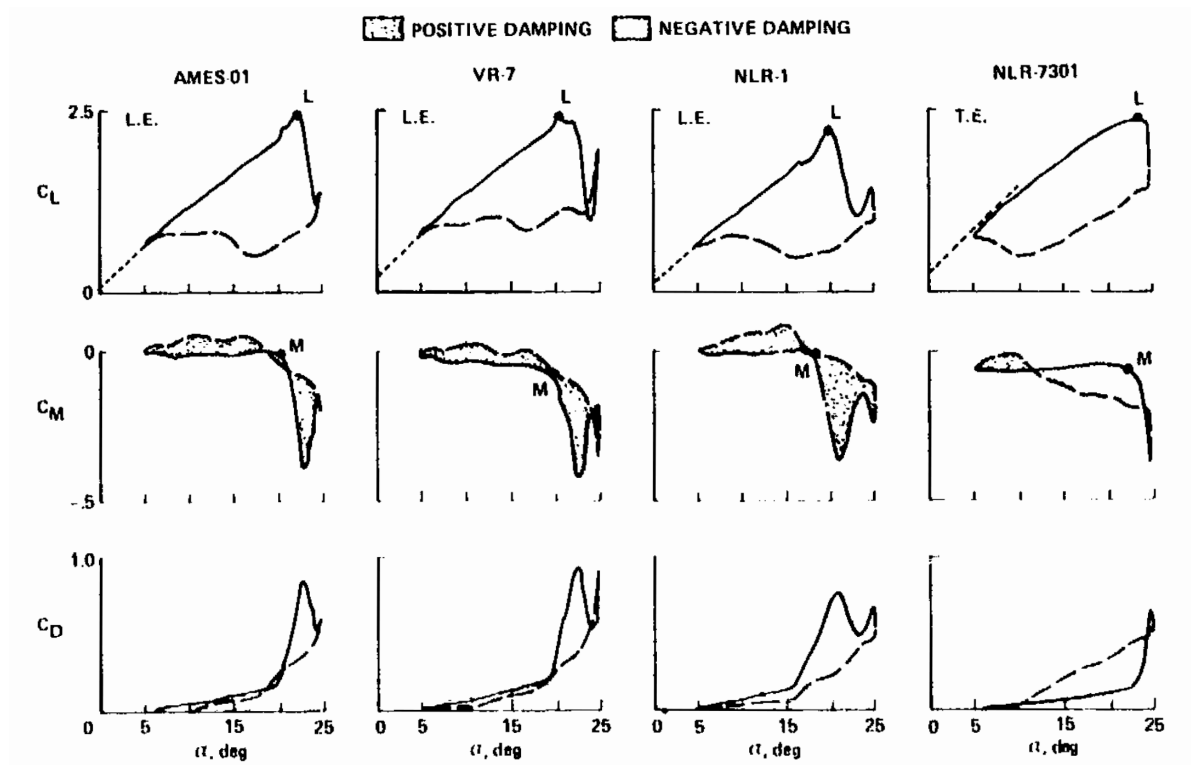


Figure 6.14: Dependencies on airfoil geometry of flowfield in deep stall regime<sup>3</sup>  
 $C_L$ ,  $C_M$ , and  $C_D$  curves against  $AoA$  are depicted for the flowfield around pitching various airfoils at Reynolds number of  $\mathcal{O}(10^6)$  with  $k = 0.1$ .  
 $AoA = 15^\circ + 10^\circ \sin \omega t$ , solid lines denote increasing  $\alpha$ , dashed lines decreasing  $\alpha$ .

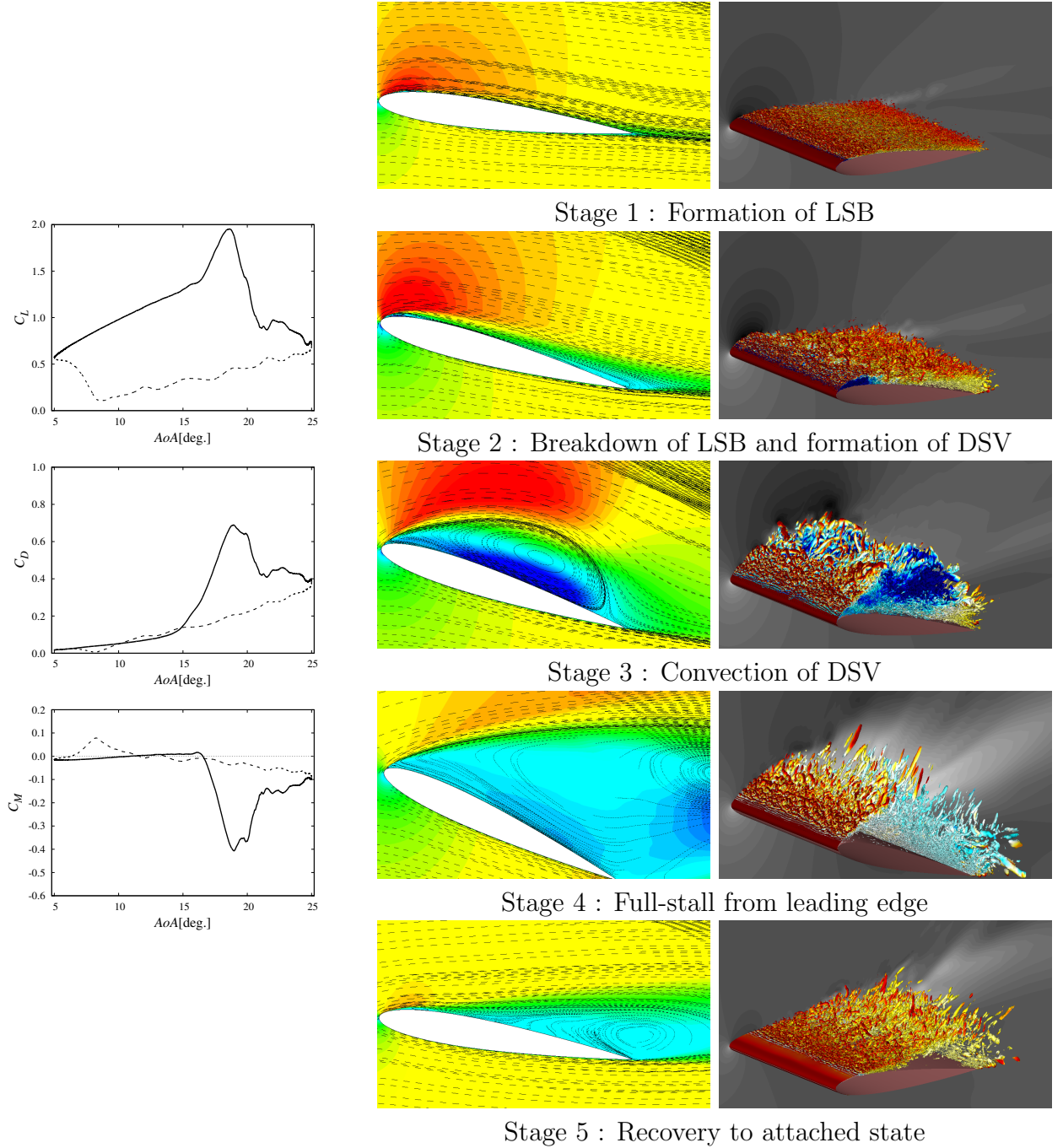


Figure 6.15: Classification of dynamic stall process at Reynolds number  $= 2.56 \times 10^5$  with  $k = 0.02\pi$ .

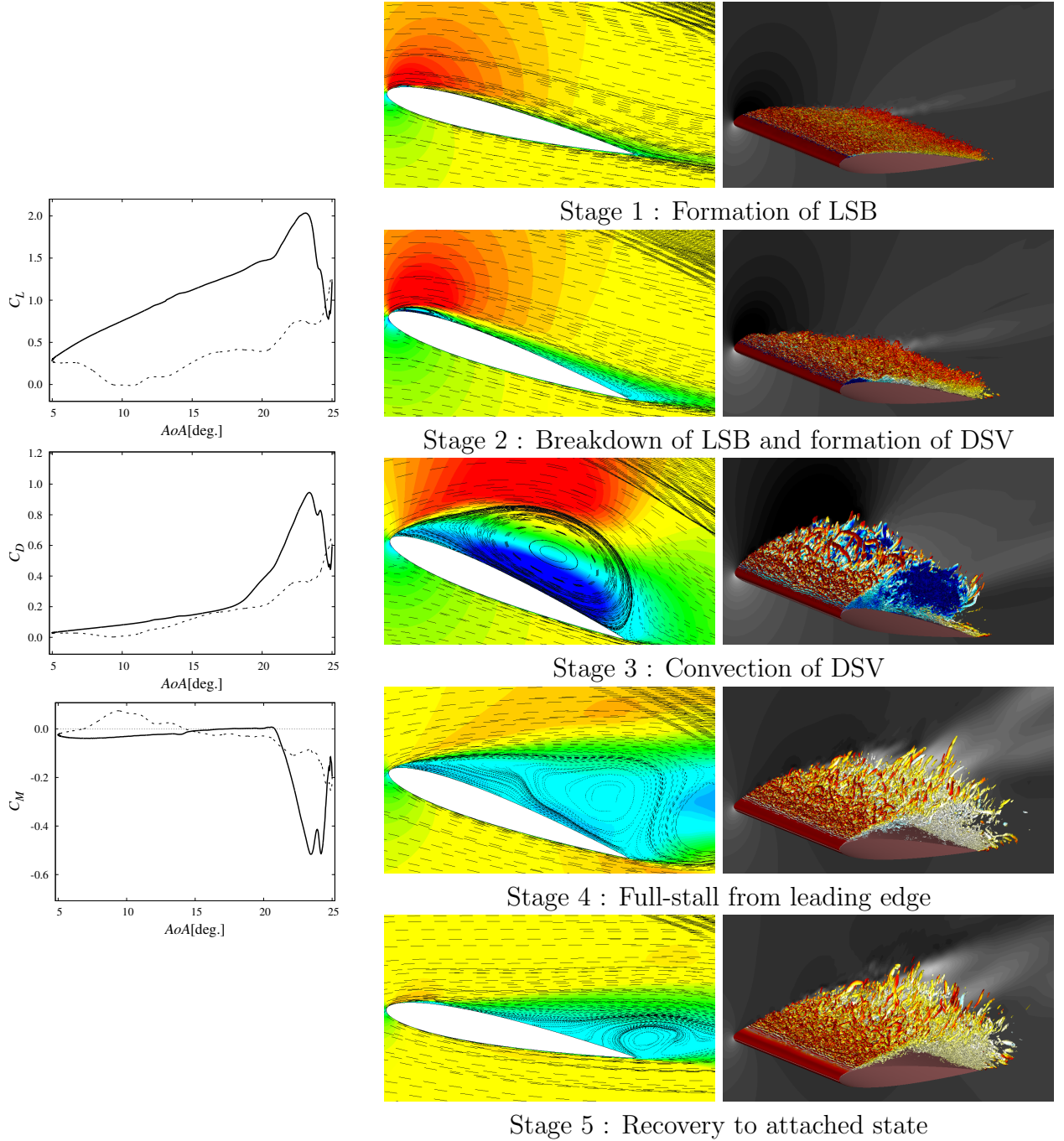


Figure 6.16: Classification of dynamic stall process at Reynolds number  $= 2.56 \times 10^5$  with  $k = 0.03\pi$ .

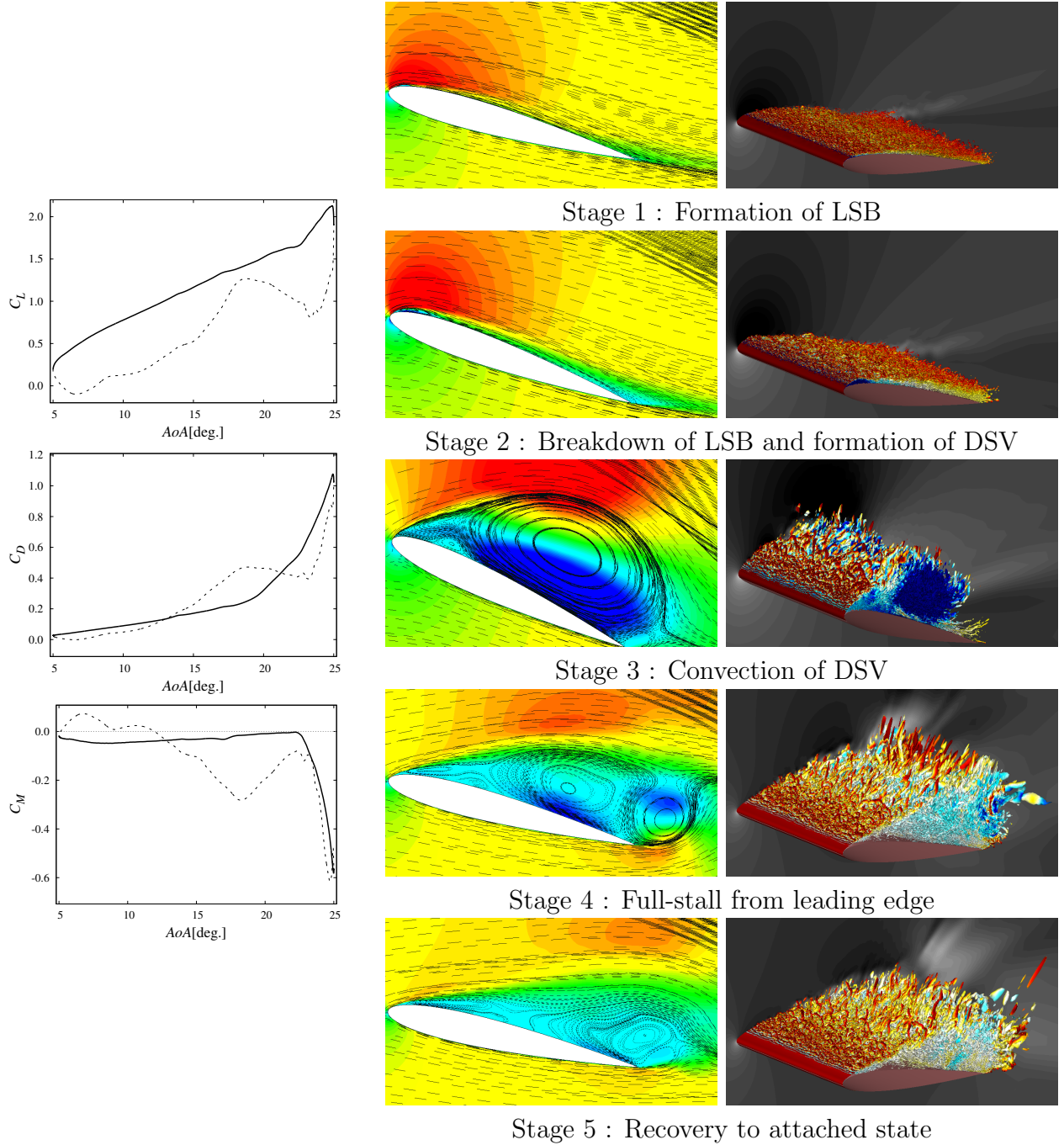


Figure 6.17: Classification of dynamic stall process at Reynolds number  $= 2.56 \times 10^5$  with  $k = 0.05\pi$ .

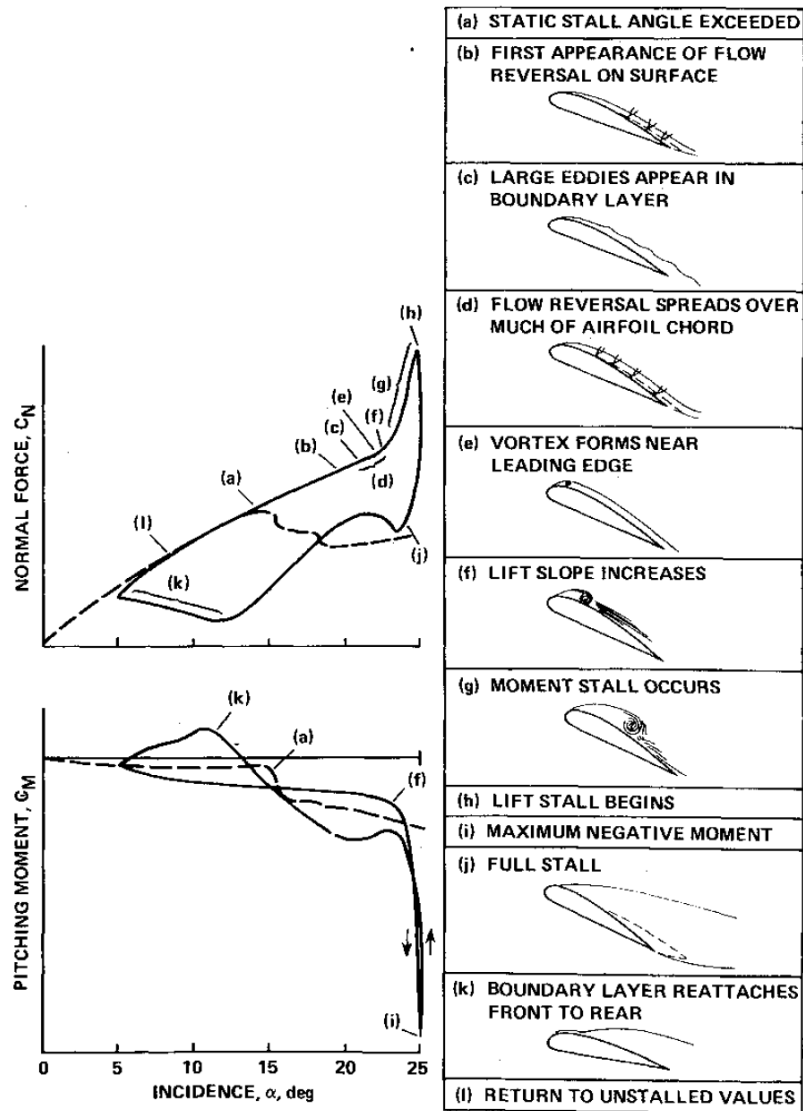


Figure 6.18: Classification of dynamic stall process by Carr.<sup>4</sup> Reynolds number is  $2.6 \times 10^6$  and the reduced frequency  $k$  is 0.15.



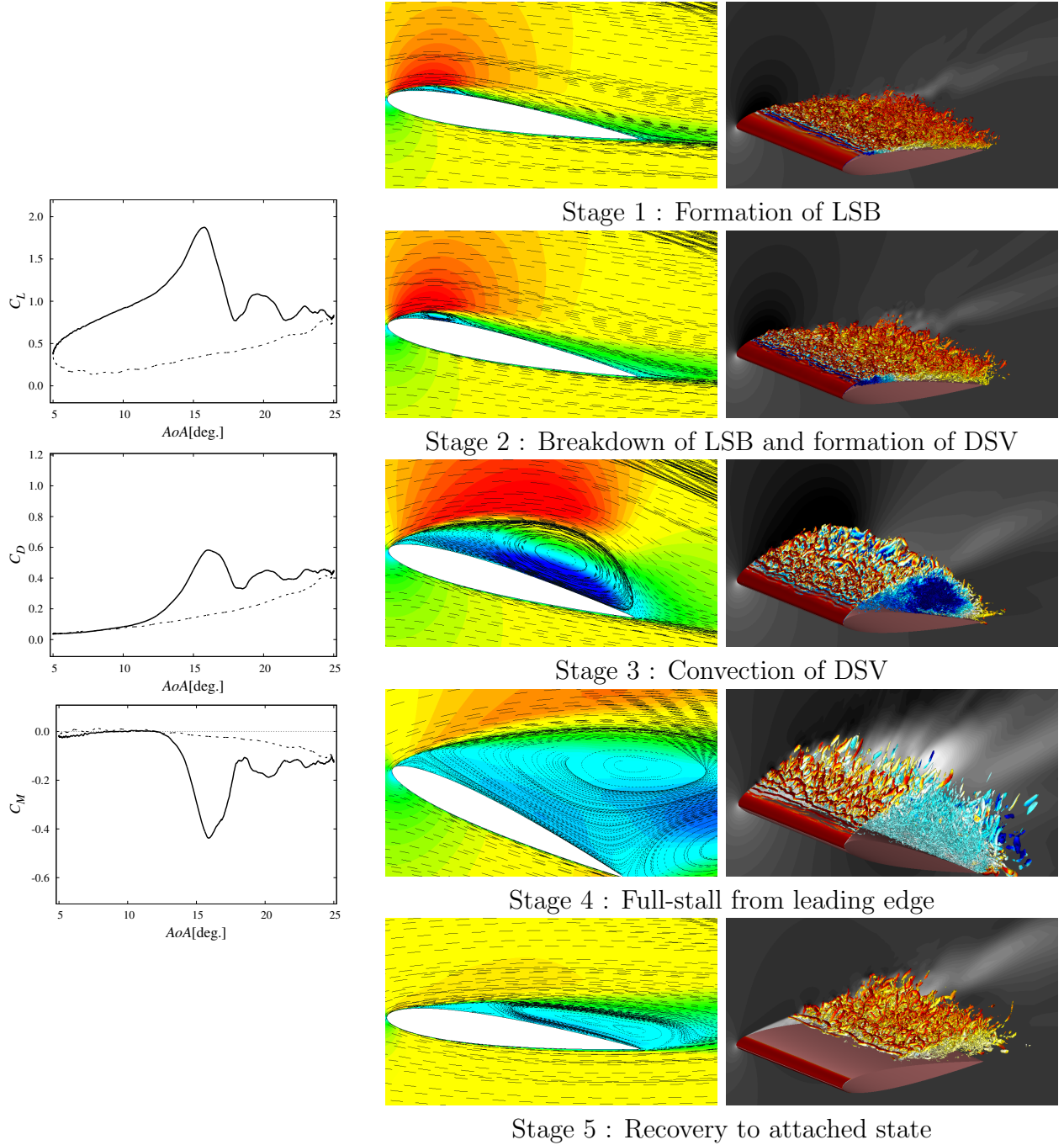


Figure 6.19: Classification of dynamic stall process at Reynolds number  $= 6.30 \times 10^4$  with  $k = 0.02\pi$ .

# Chapter 7

## Concluding Remarks

In this thesis, the dynamic flowfield around a pitching NACA0012 airfoil and a pitching NACA63<sub>3</sub>-618 airfoil are simulated with implicit large eddy simulations (LES) using difference scheme. The goal of this thesis is set to find the effective control mechanisms and effective DBD plasma actuator parameters for controlling the dynamic flowfield around a pitching practical airfoil. Toward this goal, the focus of this research is put on clarifying the relation between the control effects, the control mechanisms, and the corresponding effective DBD plasma actuator parameters. Reynolds number is set to  $2.56 \times 10^5$ , the pitching angle of attack ( $AoA$ ) range is set to  $5^\circ \sim 25^\circ$ , and the reduced frequency is set to  $0.02\pi$ . These flow condition are completely identical to these of the wind tunnel experiment by Mitsuo et al.<sup>2</sup>

First of all, in order to validate the LES results, validation and verification study is conducted. The stationary and dynamic flowfields around a NACA0012 airfoil with various spanwise length is calculated to verify the spanwise length of the computational domain. The result showed there is significant effect of the spanwise length on the LES results. The spanwise length effects appear as the time for the large vortices to attenuate and this spanwise length effect on the attenuation of the vortices become more important in dynamic flowfields, considering that the time scales of the flow structures plays significant role on dynamic flowfields. The investigation results suggest that the sufficient spanwise length to correctly estimate the behaviour of the flowfield is  $1.0c$ . With this sufficient spanwise length, it come to be able to discuss on the flowfield on the entire flowfield. All the results of following chapter are calculated with this sufficient spanwise length.

In Chapter 5, the control effects of the DBD plasma actuator on the dynamic flowfield around a pitching NACA0012 airfoil are investigated and then the control effects and these mechanisms are arranged. The flowfield is that around a pitching NACA0012

airfoil at Reynolds number of  $2.56 \times 10^5$ . The airfoil pitches between  $AoA$  of  $5^\circ$  to  $25^\circ$  with the reduced frequency of  $0.02\pi$ .

First, in order to understand the baseline flowfield and then to determine the DBD plasma actuator parameters to be examined, the flowfields around a stationary and pitching airfoil without control are investigated. The flowfield around the stationary airfoil at this Reynolds number has a combined type of trailing edge stall and leading edge stall. At low  $AoA$ , the flow separates around the mid-chord and soon reattaches near the trailing edge. The separation and reattachment points moves together toward the leading edge and a clear laminar separation bubble (LSB) is formed near the leading edge as  $AoA$  increases. The stall angle, which is defined by the  $AoA$  where first drop in  $C_L$  against  $AoA$  is observed, is found between  $AoA$  of  $12 \sim 13^\circ$ . The stall in the stationary flowfield is due to the trailing edge stall, however, the extent of this trailing edge stall is relatively small and the subsequent leading edge stall is observed between  $AoA$  of  $13 \sim 14^\circ$ .

The flowfield around a pitching airfoil also shows the combined type of trailing edge stall and leading edge stall. The extent of the trailing edge stall is so small that its effect does not apparently appears in the aerodynamic performances. The LSB formed near the leading edge plays important role on the overall characteristics of the flowfield. The general flowfield in dynamic stall is characterized by the formation of LSB, the breakdown of LSB, the convection of dynamic stall vortex (DSV), the full-stall from the leading edge, and recovery to the attached state. The aerodynamic performances before the formation of DSV and after the convection of DSV show relatively gentle slope against  $AoA$ . However, the aerodynamic performances experience sudden and drastic change due to the formation and the convection of DSV. After the convections of DSV and subsequent other large vortices induced by the DSV, full-stalled state is observed. At the final stage of the pitching cycle, rapid recoveries of the aerodynamic performances are observed due to the recovery from the full-stalled state to the attached state.

Based on the investigation of the aerodynamic performances and the behaviour of the reattachment point, five characteristic  $AoA$  are proposed. First four are for the stall;  $AoA$  at which first drop in  $C_L$  is observed,  $AoA$  at which the LSB breaks down,  $AoA$  at which maximum leading edge suction peak in  $C_p$  is observed, and  $AoA$  at which drop in  $C_L$  associated to the dynamic stall is observed. The last one is  $AoA$  at which the flow starts to reattach around the final stage of the pitching motion. Especially, the definition of  $AoA$  at which the LSB breaks down is important on investigating the dynamic stall onset. In the dynamically stalled flowfield, the classical definition of the stall angle, which is defined by the  $AoA$  at which first drop in  $C_L$  is observed, has large



lag compared with the  $AoA$  at which the LSB breaks down and thus is not proper as an index of dynamic stall onset.

The DBD plasma actuator parameters for the control cases are determined by integrating the general knowledge of the flow control around airfoils obtained in the previous researches and the investigation results of the flowfield without control obtained in the current research. After some considerations, four cases are prepared to be examined. The DBD plasma actuator is installed at  $x/c = 0\%$  or  $15\%$ , and actuated with burst frequency  $F^+$  of 0.5, 6, or 50. The burst frequency of  $F^+$  of 0.5 is chosen based on the investigation on the behaviour of the large vortices and the intention is to make use of the momentum exchange by the induced large vortices. The burst frequency of  $F^+$  of 50 corresponds to the sub-harmonics of the instability frequency of the LSB right before the breakdown, and is chosen with the aim to energize the LSB. The other parameters such as  $D_c$  and BR are set as constant. The base frequencies  $f_{base}$  are set as a dependent variable of  $F^+$ . The controlled cases are named as ON  $F^+ = 0.5$ , ON  $F^+ = 6$ , ON  $F^+ = 50$ , and ON  $15\%F^+ = 6$ . Except for the case of ON  $15\%F^+ = 6$ , the DBD plasma actuator is installed at  $x/c = 0\%$ .

The control effects on the aerodynamic performances and the flowfield are investigated prior to the investigation on the control mechanisms. With regard to enhancement of the cycle-averaged lift coefficient  $C_L$  and torque coefficient  $C_Q$ , the case of ON  $F^+ = 0.5$  is the best. When focus is on the cycle-averaged lift-to-drag ratio  $L/D$ , the best cases in enhancing  $L/D$  are the case of ON  $F^+ = 6$  and ON  $F^+ = 50$ . Investigation on the flowfield and the separation and reattachment points revealed that the control effects on aerodynamic performances can be arranged as the following three major ones;

1. Delaying dynamic stall onset
2. Enhancing aerodynamic forces during full-stall
3. Promoting reattachment

The first control effect is delaying the dynamic stall onset. All the controlled cases successfully delay the breakdown of LSB, i.e., delay the dynamic stall onset. The best case in this control effect is the case of ON  $F^+ = 50$ , delaying the breakdown of LSB by  $AoA$  of  $1.1^\circ$ . Considering that the instability frequency of LSB is as high as  $St$  of 100 under the current Reynolds number regime, the cases with high actuation frequency whose low order harmonics can stimulate the instability frequency would have better control effect on delaying the dynamic stall onset. Stimulating the instability frequency of the shear layer can effectively advance the reattachment point and/or displace the

shear layer toward the airfoil surface, and as a result the size of LSB (respectively in length and height) can be reduced. In addition to the control mechanism of energizing the LSB, an existence of the control mechanism of changing the history of the flowfield is suggested.

The second control effect is enhancing the aerodynamic forces during the full-stall. This effect is apparent only in the case of ON  $F^+ = 0.5$ . During the full-stall stage, the flowfield in the case of ON  $F^+ = 0.5$  shows large vortex structures while the flowfield in the other cases show no significant flow structures. These large vortices produce significant aerodynamic forces, and as the result the enhancement and oscillation of the aerodynamic performances are brought. The observations of the flowfield near the shear layer revealed that the large vortices are grown from kernel vortices. For the kernel vortices to be formed, it is found that the burst frequency which is lower than the natural instability frequency can help the vortices to grow into relatively large kernel vortices. In order to make the kernel vortex more larger, the use of sufficiently low burst frequency can help the kernel vortices grow into larger structure with mitigating the interaction between the kernel vortices. To make use of the aerodynamic forces of the large vortices, the  $F^+$  which can keep large vortices as much as possible over the airfoil would be better. As a result, it is considered that the most effective  $F^+$  would depend on the characteristic size and velocity.

The third control effect is promoting the reattachment at the final stage of the dynamic stall. With regard to this control effect, the case of ON  $F^+ = 6$  is the best case and the reattachment  $AoA$  is promoted by  $5.6^\circ$ . The role of the kernel vortices is also important for this control effect and the better cases show relatively large kernel vortices. With the combination effect of DBD plasma actuator of inducing the kernel vortices, displacing the shear layer toward the airfoil surface, and advancing the vortex shedding point, the momentum exchange between the freestream and the shear layer come to take place near the airfoil surface. It is also found that the excessive large vortices displaces the shear layer upward and can disrupt the reattachment. These investigations suggest that  $F^+$  should not to be too low to avoid the formation of the large vortices.

The conclusion in Chapter 5 is that the effects of controlling the dynamic flowfield can be divided into some discrete effects and discussions on the control effect can be conducted isolated to each other control effect. It is shown that each control effect has each control mechanism, and each mechanism has effective set of the DBD plasma actuator parameters. However, a set of DBD plasma actuator parameter which is effective on utilizing an mechanism can be not effective on utilizing the other mechanisms. This result suggests us the use of adaptive control; if the DBD plasma actuator parameters

are changed in association with the change of the flowfield, the DBD plasma actuator can make use of the effects of each mechanism.

To support the conclusions of Chapter 5 and to discuss about the effective control mechanisms and effective DBD plasma actuator parameters for controlling the dynamic flowfield around a pitching laminar airfoil, the conclusions in Chapter 5 are utilized to the dynamic flowfield around a pitching NACA63<sub>3</sub>-618 airfoil.

The flowfield around a NACA63<sub>3</sub>-618 airfoil without control has the combined stall type of the leading edge stall and trailing edge stall, while is biased toward the trailing edge stall. With this characteristic, the aerodynamic performance curves show more complex aspects. The result is that, however, the flow control attempts based on the findings from NACA0012 airfoil showed good enhancements in the aerodynamic performances. This result suggests that the control mechanism found in this research is applicable irrespective to the extent of the trailing edge separation, or maybe irrespective to airfoil shapes.

In addition to the basic cases, a case with adaptive switching of  $F^+$  is also investigated. The result that this adaptive case worked as proper as expected supports the validity of the procedure for determining the parameters; the DBD plasma actuator parameters are determined by the investigation only on the flowfield in the corresponding stage. The result that the control cases successfully enhanced the aerodynamic performances at the expected stage supports the validity of the procedure to determine the DBD plasma actuator parameters.

These results say that both of the control mechanisms and the procedure to determine the DBD plasma actuator parameters are applicable to the flowfield even with large extent of trailing edge separation. The control results and additional considerations on the applicability of the findings suggests that the findings is applicable to dynamic flowfields around various airfoils at various Reynolds number regime as long as the dynamic stall is characterized by LSB, and with various reduced frequencies. To access the applicability boundary of the findings, further investigations are required.

To conclude this thesis, the effective control mechanisms for dynamic flowfield around a pitching airfoil using a DBD plasma actuator is arranged. The control effects are arranged into three; delaying dynamic stall onset, enhancing aerodynamic forces during full-stall, and promoting reattachment. The control mechanisms for each control effect are clarified with the knowledge of the effective DBD plasma actuator. This arranged mechanisms and corresponding effective DBD plasma actuator parameters are applicable to the dynamic flowfield around a pitching laminar airfoil, and the goal of this thesis to find the effective control mechanisms and effective DBD plasma actuator parameters for

controlling the dynamic flowfield around a pitching practical airfoil is attained. Furthermore, the arranged knowledge is valid to the dynamic flowfields around various airfoils at various Reynolds number regime as long as the dynamic stall is characterized by LSB, and with various reduced frequencies.

# References

- [1] Brehm, S. M. C., Heine, B., Kurz, A., and Fasel, H., “Experimental Investigation of Separation and Separation Control on a Laminar Airfoil,” *AIAA-2008-3766*, 2008.
- [2] Mitsuo, K., Watanabe, S., Atobe, T., and Kato, H., “Lift Enhancement of a Pitching Airfoil in Dynamic Stall by DBD Plasma Actuator,” *AIAA 2013-1119*, 2013.
- [3] McCroskey, W. J., “The Phenomenon of Dynamic Stall,” *NASA Technical Memorandum 81264*, 1981.
- [4] Carr, L. W., “Progress in Analysis and Prediction of Dynamic Stall,” *Journal of Aircraft*, Vol. 25, No. 1, 1988, pp. 6–17.
- [5] Lorber, P., McCormick, D., Anderson, T., Wake, B., MacMartin, D., Pollack, M., Corke, T., and Breuer, K., “Rotorcraft Retreating Blade Stall Control,” *AIAA-2000-2475*, 2000.
- [6] Visbal, M., “Control of Dynamic Stall on a Pitching Airfoil Using High-Frequency Actuation,” *AIAA 2015-1267*, 2015.
- [7] Visbal, M. R., “Analysis of the Onset of Dynamic Stall Using High-Fidelity Large-Eddy Simulations,” *AIAA 2014-0591*, 2014.
- [8] Carr, L. W. and McAlister, K. W., “The Effect of a Leading-Edge Slat on the Dynamic Stall of an Oscillating Airfoil,” *AIAA 83-2533*, 1983.
- [9] Greenblatt, D. and Wygnanski, I., “Dynamic Stall Control by Periodic Excitation, Part 1: NACA 0015 Parametric Study,” *Journal of Aircraft*, Vol. 38, No. 3, 2001.
- [10] Muller-Vahl, H. F., “Control of Thick Airfoil, Deep Dynamic Stall Using Steady Blowing,” *AIAA Journal*, Vol. 53, No. 2, 2015.

- [11] Weaver, D., McAlister, K. W., and Tso, J., “Suppression of Dynamic Stall by Steady and Pulsed Upper-Surface Blowing,” *NASA Technical Paper 95-A-005*, 1996.
- [12] Woo, G. and Glezer, A., “Transient Control of Separating Flow over a Dynamically-Pitching Airfoil,” *AIAA-2010-861*, 2010.
- [13] Corke, T. C., Enloe, C. L., and P. Wilkinson, S., “Dielectric Barrier Discharge Plasma Actuators for Flow Control,” *Annual Review of Fluid Mechanics*, Vol. 42, 2010, pp. 505–529.
- [14] Roth, J. R., Sherman, D. M., and Wilkinson, S. P., “Electrohydrodynamic Flow Control with a Glow-Discharge Surface Plasma,” *AIAA Journal*, Vol. 38, No. 7, 2000, pp. 1166–1172.
- [15] Matsuda, H., Tanaka, M., Goshima, S., Amemori, K., Nomura, M., and Osako, T., “Experimental Study on Plasma Aerodynamic Control for Improving Wind Turbine Performance,” *ACGT2012-1058*, 2012.
- [16] Tanaka, M., Amemori, K., Matsuda, H., Shimura, N., Yasui, H., Osako, T., Kamada, Y., and Maeda, T., “Field Test of Plasma Aerodynamic Controlled Wind Turbine,” *EWEA2013-585*, 2013.
- [17] Aono, H., Okada, K., Taku Nonomura and, S. K., Sato, M., Yakeno, A., and Fujii, K., “Effects of Burst Frequency and Momentum Coefficient of DBD Actuator on Control of Deep-stall Flow around NACA0015 at  $Re_c = 2.6 \times 10^5$ ,” *AIAA 2014-0766*, 2014.
- [18] Cooney, J. A., Szlatenyi, C. S., and Fine, N. E., “The Development and Demonstration of a Plasma Flow Control System on a 20 kW Wind Turbine,” *AIAA-2016-1302*, 2016.
- [19] Post, M. L. and Corke, T. C., “Separation Control on High Angle of Attack Airfoil Using Plasma Actuators,” *AIAA Journal*, Vol. 42, No. 11, November 2004, pp. 2177–2184.
- [20] Post, M. L. and Corke, T. C., “Separation Control Using Plasma Actuators: Dynamic Stall Vortex Control on Oscillating Airfoil,” *AIAA Journal*, Vol. 44, December 2006, pp. 3125–3135.

- 
- [21] Bénard, N., Jolibois, J., and Moreau, E., “Lift and drag performances of an axisymmetric airfoil controlled by plasma actuator,” *Journal of Electrostatics*, Vol. 67, No. 2-3, 2009, pp. 133–139.
- [22] Mabe, J. H., Calkins, F. T., Wesley, B., Woszidlo, R., Taubert, L., and I., W., “Single Dielectric Barrier Discharge Plasma Actuators for Improved Airfoil Performance,” *Journal of Aircraft*, Vol. 46, 2009, pp. 847–855.
- [23] Vorobiev, A. N., Rennie, R. M., and Jumper, E. J., “Experimental Investigation of Lift Enhancement and Roll Control Using Plasma Actuators,” *Journal of Aircraft*, Vol. 45, No. 4, 2008, pp. 1315–1321.
- [24] Vorobiev, A., Rennie, R. M., and Jumper, E. J., “Lift enhancement by plasma actuators at low Reynolds numbers,” *Journal of Aircraft*, Vol. 50, 2013, pp. 12–19.
- [25] Rizzetta, D. P. and Visbal, M. R., “Numerical Investigation of Plasma-Based Control for Low-Reynolds-Number Airfoil Flows,” *AIAA Journal*, Vol. 49, No. 2, February 2011, pp. 411–425.
- [26] Huang, J., Corke, T. C., and Thomas, F. O., “Unsteady Plasma Actuators for Separation Control of Low-Pressure Turbin Blades,” *AIAA Journal*, Vol. 44, No. 7, 2006.
- [27] Huang, J., Corke, T. C., and Thomas, F. O., “Plasma Actuators for Separation Control of Low-Pressure Turbine Blades,” *AIAA Journal*, Vol. 44, 2006, pp. 51–57.
- [28] Rizzetta, D. P. and Visbal, M. R., “Simulation of Plasma-Based Flow-Control Strategies for Transitional Highly Loaded Low-Pressure Turbines,” *AIAA-2007-4216*, 2007.
- [29] Li, W., Nonomura, T., Oyama, A., and Fujii, K., “LES Study of Feedback-loop Mechanism of Supersonic Open Cavity Flows,” *AIAA 2010-5112*, 2010.
- [30] Rizzetta, D. P. and Visbal, M. R., “Large Eddy Simulation of Plasma-Based Control Strategies for Bluff Body Flow,” *AIAA Journal*, Vol. Vol. 47, No. 3, 2009, pp. 717–729.
- [31] Gross, A. and Fasel, H. F., “Flow Control for NREL S822 Wind Turbin Airfoil,” *AIAA Journal*, Vol. 50, 2012, pp. 2779–2790.

- [32] Jukes, T. N., Segawa, T., and Furutani, H., “Flow Control on a NACA 4418 Using Dielectric-Barrier-Discharge Vortex Generators,” *AIAA Journal*, Vol. 51, 2013, pp. 452–465.
- [33] Jukes, T. N. and Choi, K.-S., “Control of unsteady flow separation over a circular cylinder using dielectricbarrier-discharge surface plasma,” *Physics of Fluids*, Vol. 21, 2009, pp. 094106.
- [34] Greenblatt, D., Schneider, T., and Schuele, C. Y., “Mechanism of flow separation control using plasma actuation,” *Physics of Fluids*, Vol. 24, 2012, pp. 077102.
- [35] Bénard, N. and Moreau, E., “Response of a Circular Cylinder Wake to a Symmetric Actuation by Non-thermal Plasma Discharges,” *Experiments in Fluids*, 2013.
- [36] Asada, K., Nonomura, T., Aono, H., Sato, M., Okada, K., and Fujii, K., “LES of transient flows controlled by DBD plasma actuator over a stalled airfoil,” *International Journal of Computational Fluid Dynamics*, 2015.
- [37] Sato, M., Nonomura, T., Okada, K., Asada, K., Aono, H., Yakeno, A., Abe, Y., and Fujii, K., “Mechanisms for laminar separated-flow control using dielectric-barrier-discharge plasma actuator at low Reynolds number,” *Physics of Fluids*, Vol. 27, 2015, pp. 1–29.
- [38] Greenblatt, D. and Wygnanski, I. J., “The control of flow separation by periodic excitation,” *Progress in Aerospace Sciences*, Vol. 36, 2000, pp. 487–545.
- [39] Collis, S. S., Joslin, R. D., Seifert, A., and Theofilis, V., “Issues in active flow control: theory, control, simulation, and experiments,” *Progress in Aerospace Sciences*, Vol. 40, 2004, pp. 237–289.
- [40] Sidorenko, A. A., Zanin, B. Y., Postnikov, B. V., Budovsky, A. D., Starikovskii, A. Y., Roupasov, D. V., Zavialov, I. N., Malmuth, N. D., Smereczniak, P., and Silkey, J. S., “Pulsed Discharge Actuators for Rectangular Wings Separation Control,” *AIAA-2007-941*, 2007.
- [41] Patel, M. P., Ng, T. T., Vasudevan, S., Corke, T. C., Post, M. L., McLaughlin, T. E., and Suchomel, C. F., “Scaling Effects of an Aerodynamic Plasma Actuator,” *Journal of Aircraft*, Vol. 45, 2008, pp. 223–236.
- [42] Nonomura, T., Aono, H., Sato, M., Yakeno, A., Okada, K., Abe, Y., and Fujii, K., “Control Mechanism of Plasma Actuator for Separated Flow around NACA0015 at



- Reynolds Number 63,000 -Separation Bubble Related Mechanisms-," *AIAA 2013-0853*, 2013.
- [43] Sato, M., Okada, K., Aono, H., Asada, K., Yakeno, A., and nd Kozo Fujii, T. N., "LES of Separated-flow Controlled by DBD Plasma Actuator around NACA 0015 over Reynolds Range of  $10^4 - 10^6$ ," *AIAA 2015-0308*, 2015.
- [44] Frankhouser, M., Hird, K., Naigle, S., Gregory, J. W., and Bons, J. P., "Nanosecond Dielectric Barrier Discharge Plasma Actuator Flow Control of Compressible Dynamic Stall," *AIAA-2015-2341*, 2015.
- [45] Visbal, M., "Numerical Exploration of Flow Control for Delay of Dynamic Stall on a Pitching Airfoil," *AIAA Paper*, Vol. 2044, 2014, pp. 2014.
- [46] Benton, S. I. and Visbal, M. R., "Investigation of High-Frequency Separation Control Mechanisms for Delay of Unsteady Separation," *AIAA 2016-4241*, 2016.
- [47] Timmer, W. A. and Rooij, R., "Summary of the Delft University Wind Turbine Dedicated Airfoils," *AIAA-2003-352*, 2003.
- [48] Timmer, W. A., "An Overview of NACA 6-Digit Airfoil Series Characteristics with Reference to Airfoils for Large Wind Turbine Blades," *AIAA-2009-268*, 2009.
- [49] Grasso, F., "Usage of Numerical Optimization in Wind Turbine Airfoil Design," *Journal of Aircraft*, Vol. 48, No. 1, 2011, pp. 248–255.
- [50] Hipp, K. D., Benton, S. I., Walker, M. M., and Bons, J. P., "Parametric Optimization of Control for a Post-Stall Airfoil Using Pulsed Jets," *AIAA 2015-1268*, 2015.
- [51] Fukumoto, H., Aono, H., Watanabe, T., Tanaka, M., Matsuda, H., Osako, T., Nonomura, T., Oyama, A., and Fujii, K., "Control of dynamic flowfield around a pitching NACA633-618 airfoil by a DBD plasma actuator," *International Journal of Heat and Fluid Flow*, Vol. 62, 2016, pp. 10–23.
- [52] Aono, H., Abe, Y., Sato, M., Yakeno, A., Nonomura, T., and Fujii, K., "Flow Control using a DBD Plasma Actuator for Horizontal-axis Wind Turbine Blades of Simple Experimental Model," *11th World Congress on Computational Mechanics, 5th Eurppian Conference on Computational Mechanics, 6th European Conference on Computational Fluid Dynamics*, 2014.

- [53] Mulleners, K., Kindler, K., and Raffael, M., “Dynamic Stall on a Fully Equipped Helicopter Model,” *Aerospace Science and Technology*, Vol. 19, No. 1, 2012, pp. 72–76.
- [54] Wolf, C. M. C., Richter, K., Kaufmann, K., Mielke, A., and Raffel, M., “Spanwise Differences in Static and Dynamic Stall on a Pitching Rotor Blade Tip Model,” *Journal of the American Helicopter Society*, Vol. 62, No. 1, 2017.
- [55] Mitsuo, K., and Takeshi Atobe, S. W., Ito, T., and ans Motofumi Tanaka, T. S., “Aerodynamic Characteristics Improvement of a Wind Turbine by Plasma Actuators,” *JSME annual meeting 2013 S052023*, 2013.
- [56] Horstmann, K. and Boermans, L., “EVOLUTION OF AIRFOILS FOR SAILPLANES,” *Technical Soaring*, Vol. 27, No. 3-4, 2003, pp. 87–95.
- [57] Brøndsted, P. and Nijssen, R. P. L., editors, *Advances in wind turbine blade design and materials*, Woodhead Publishing, 2013.
- [58] Fujii, K. and Tamura, Y., “Capability of current supercomputers for the computational fluid dynamics,” *Supercomputing '89: Proceedings of the 1989 ACM/IEEE conference on Supercomputing*, ACM, New York, NY, USA, 1989, pp. 71–80.
- [59] Fujii, K., “Developing an Accurate and Efficient Method for Compressible Flow Simulations -Example of CFD in Aeronautics-,” *The Proceedings: Fifth International Conference on Numerical Ship Hydrodynamics*, 1990.
- [60] Fujii, K. and Satofuka, N., “Flashback: 30 Years Numerical Fluid Mechanics and Aerodynamics in Japan, other Asian Countries and the Western Pacific Rim,” *100 Volumes of 'Notes on Numerical Fluid Mechanics'*, edited by E. Hirschel and E. Krause, Vol. 100 of *Notes on Numerical Fluid Mechanics and Multidisciplinary Design*, Springer Berlin / Heidelberg, 2009, pp. 109–115.
- [61] Fujii, K. and Obayashi, S., “Practical Applications of New LU-ADI Scheme for the Three-Dimensional Navier-Stokes Computation of Transonic Viscous Flows,” *AIAA-1986-513*, January 1986.
- [62] Obayashi, S., Matsushima, K., Fujii, K., and Kuwahara, K., “Improvements in Efficiency and Reliability for Navier-Stokes Computations Using the LU-ADI Factorization Algorithm,” *AIAA-1986-513*, 1986.

- [63] Fujii, K. and Obayashi, S., “Navier-Stokes Simulations of Transonic Flows over a Wing-Fuselage Combination,” *AIAA Journal*, Vol. 25, December 1987, pp. 1587–1596.
- [64] Obayashi, S., Fujii, K., and Gavali, S., “Navier-Stokes Simulation of Wind-Tunnel Flow Using LU-ADI Factorization Algorithm,” TM 100042, NASA, 1988.
- [65] Aono, H., Nonomura, T., Iizuka, N., Ohsako, T., Inari, T., Hashimoto, Y., Takaki, R., and Fujii, K., “Scalar Tuning of a Fluid Solver using Compact Scheme for a Supercomputer with a Distributed Memory Architecture,” *CFD letters*, Vol. 5, No. 4, 2013, pp. 143–152.
- [66] Fujii, K., “Progress and Future Prospects of CFD in Aerospace-Wind Tunnel and Beyond,” *Progress in Aerospace Sciences*, Vol. 41, 2005, pp. 455–470.
- [67] Fujii, K., “CFD contributions to high-speed shock-related problems,” *Shock Waves*, Vol. 18, 2008, pp. 145–154.
- [68] Hirsh, R. S., “Higher Order Accurate Difference Solutions of Fluid Mechanics Problems by a Compact Differencing Technique,” *Journal of Computational Physics*, Vol. 19, 1975, pp. 90–109.
- [69] Fujii, K., *Numerical Methods for Computational Fluid Dynamics*, University of Tokyo Press, Tokyo, 1994, in Japanese.
- [70] Tannehill, J. C., Anderson, D. A., and Pletcher, R. H., *Computational Fluid Mechanics and Heat Transfer*, Taylor & Francis, Washington, D.C., 2nd ed., 1997.
- [71] Liepmann, H. W. and Roshko, A., *Elements of Gasdynamics*, Dover Publications, Inc., Mineola, New York, 2001.
- [72] Masatsuka, K., *I do like CFD Volume 1, second edition*, Lulu Press, 2013.
- [73] White, F. M., *Viscous fluid flows*, 1991.
- [74] Abe, Y., Nonomura, T., Iizuka, N., and Fujii, K., “Geometric interpretations and spatial symmetry property of metrics in the conservative form for high-order finite-difference schemes on moving and deforming grids,” *Journal of Computational Physics*, Vol. 260, No. 0, 2014, pp. 163 – 203.
- [75] Vinokur, “Conservation Equations of Gasdynamics in Curvilinear Coordinate Systems,” *Journal of Computational Physics*, Vol. 14, 1974, pp. 105–125.

- [76] Deng, X., Min, Y., Mao, M., Liu, H., Tu, G., and Zhang, H., "Further studies on Geometric Conservation Law and applications to high-order finite difference schemes with stationary grids," *Journal of Computational Physics*, Vol. 239, 2013, pp. 90–111.
- [77] Abe, Y., Iizuka, N., Nonomura, T., and Fujii, K., "Conservative metric evaluation for high-order finite difference schemes with the GCL identities on moving and deforming grids," *Journal of Computational Physics*, Vol. 232, 2013, pp. 14–21.
- [78] Beam, R. M. and Warming, R. F., "An Implicit Factored Scheme for the Compressible Navier-Stokes Equations," *AIAA Journal*, Vol. 16, No. 4, April 1978, pp. 393–402.
- [79] Chakravarthy, S. R., "Relaxation Methods for Unfactored Implicit Upwind Schemes," *AIAA-1984-165*, January 1984.
- [80] Matsuno, K., "A Time-accurate Iterative Scheme for Solving the Unsteady Compressible Flow Equations," *AIAA-1989-1992*, 1989.
- [81] Lele, S. K., "Compact Finite Difference Schemes with Spectral-like Resolution," *Journal of Computational Physics*, Vol. 103, No. 1, 1992, pp. 16–42.
- [82] Visbal, M. R. and Gaitonde, D. V., "High-Order Accurate Methods for Unsteady Vortical Flows on Curvilinear Meshes," *AIAA-1998-131*, 1998.
- [83] Gaitonde, D. V. and Visbal, M. R., "Further development of a Navier-Stokes solution procedure based on higher-order formulas," *AIAA-1999-557*, 1999.
- [84] Arasawa, T., Fujii, K., and Miyaji, K., "Application of High-Order Compact Difference Scheme to Vortical Flow Computation over a Delta and Double-Delta Wings," *AIAA-2003-3537*, June 2003.
- [85] Arasawa, T., Fujii, K., and Miyaji, K., "High-Order Compact Difference Scheme Applied to Double-Delta Wing Vortical Flows," *Journal of Aircraft*, Vol. 41, No. 4, 2004, pp. 953–957.
- [86] Gordnier, R. E. and Visbal, M. R., "Compact Difference Scheme Applied to Simulation of Low-Sweep DeltaWing Flow," *AIAA Journal*, Vol. 43, No. 8, August 2005, pp. 1744–1752.
- [87] Gordnier, R. E., Visbal, M. R., Gursul, I., and Wang, Z., "Computational and Experimental Investigation of a Nonslender Delta Wing," *AIAA-2007-894*, 2007.

- 
- [88] Sherer, S. E., Visbal, M. R., and Gordnier, R. E., “Computational Study of Reynolds Number and Angle-of-Attack Effects on a 1303 UCAV Configuration with a High-Order Overset-Grid Algorithm,” *AIAA-2009-751*, 2009.
- [89] Morgan, P. E. and Visbal, M. R., “Large-Eddy Simulation Modeling Issues for Flow Around Wing Sections,” *AIAA-2003-4152*, 2003.
- [90] Morgan, P. E. and Visbal, M. R., “Large-Eddy Simulation of Airfoil Flows,” *AIAA-2003-777*, 2003.
- [91] Kawai, S. and Fujii, K., “Prediction of a Thin-Airfoil Stall Phenomenon Using LES/RANS Hybrid Methodology with Compact Difference Scheme,” *AIAA-2004-2714*, 2004.
- [92] Kawai, S. and Fujii, K., “Analysis and Prediction of Thin-Airfoil Stall Phenomena Using Hybrid Turbulent Methodology,” *AIAA Journal*, Vol. 43, No. 5, May 2005, pp. 953–961.
- [93] Kawai, S. and Fujii, K., “Compact Scheme with Filtering for Large-Eddy Simulation of Transitional Boundary Layer,” *AIAA Journal*, Vol. 46, No. 3, March 2008, pp. 690–700.
- [94] Kawai, S. and Fujii, K., “Compact Differencing and Filtering Schemes for Large-Eddy Simulation of Compressible Transitional Boundary Layer,” *AIAA-2007-3842*, 2007.
- [95] Kawai, S. and Fujii, K., “Large-Eddy Simulation of Compressible Transitional Boundary Layer,” *AIAA-2006-7941*, 2006.
- [96] Okamoto, K., Nonomura, T., and Fujii, K., “Computational Analysis of Noise Sources inside the High Speed Flow over a Bump,” *ASME FEDSM-2007-37536*, 2007.
- [97] Okamoto, K., Nonomura, T., and Fujii, K., “Computational Analysis of Noise Sources inside the High Speed Flow over a Generalized Bump,” *AIAA-2008-64*, 2008.
- [98] Shima, E. and Jounouchi, T., “Role of CFD in Aeronautical Engineering (No.14) - AUSM type Upwind Schemes-,” *Proceedings of the 14th NAL Symposium on Aircraft Computational Aerodynamics*, NAL, 1997, pp. 7–12.

- 
- [99] Roe, P. L., "Approximate Riemann Solvers, Parameter Vectors, and Difference Scheme," *Journal of Computational Physics*, Vol. 43, No. 2, 1981, pp. 357–372.
- [100] Liou, M. S., "Progress towards an Improved CFD Method: AUSM+," *AIAA-1995-1701*, 1995.
- [101] van Leer, B., "Towards the Ultimate Conservation Difference Scheme. IV. A New Approach to Numerical Convection," *Journal of Computational Physics*, Vol. 23, No. 3, 1977, pp. 276–299.
- [102] van Leer, B., "Towards the Ultimate Conservation Difference Scheme. V. A Second-Order Sequel to Godunov's Method," *Journal of Computational Physics*, Vol. 32, 1979, pp. 101–136.
- [103] Visbal, M. R. and Gaitonde, D. V., "Computation of aeroacoustic fields on general geometries using compact differencing and filtering schemes," *AIAA-1999-3706*, 1999.
- [104] Koutsavdis, E. K., Blaisdell, G. A., and A. S. Lyrintzis, A. S., "A Numerical Investigation of Two-dimensional Jets Using Spatial Filtering," *AIAA-1999-1875*, 1999.
- [105] Gaitonde, D. V. and Visbal, M. R., "Padé-Type Higher-Order Boundary Filters for the Navier-Stokes Equations," *AIAA Journal*, Vol. 38, No. 11, 2000, pp. 2103–2112.
- [106] Nagarajan, S., Lele, S. K., and Ferziger, J. H., "A Robust High-order Compact Method for Large Eddy Simulation," *Journal of Computational Physics*, Vol. 191, 2003, pp. 392–419.
- [107] Fyfe, D. J., "Economical Evaluation of Runge-Kutta Formulae," *Mathematics of Computation*, Vol. 20, No. 95, 1966, pp. 392–398.
- [108] Courant, R., Friedrichs, K., and Lewyt, H., "On the Partial Difference Equations of Mathematical Physics," *IBM Journal of Research and Development*, Vol. 11, No. 2, 1967, pp. 215–234.
- [109] Iizuka, N., *Study of Mach Number Effect on the Dynamic Stability of a Blunt Re-entry Capsule*, Ph.D. thesis, University of Tokyo, 2006.

- [110] Iizuka, N. and Fujii, K., “Evaluation of Dynamic Base Pitching Moment of a Blunt ReEntry Capsule in Transonic Region,” *Proceedings of 57th International Astronautical Congress IAC06-D2P.1.9*, 2006.
- [111] Nishida, H. and Nonomura, T., “ADI-SGS Scheme on Ideal Magnetohydrodynamics,” *Journal of Computational Physics*, Vol. 228, 2009, pp. 3182–3188.
- [112] Fujii, K., “Efficiency Improvement of Unified Implicit Relaxation/Time Integration Algorithms,” *AIAA Journal*, Vol. 37, No. 1, 1999, pp. 125–128.
- [113] Yoon, S. and Jameson, A., “An LU-SSOR Scheme for the Euler and Navier-Stokes Equations,” *AIAA-1987-600*, January 1987.
- [114] Yoon, S. and Jameson, A., “Lower-Upper Symmetric-Gauss-Seidel Method for the Euler and Navier-Stokes Equations,” *AIAA Journal*, Vol. 26, No. 9, September 1988, pp. 1025–1026.
- [115] Yee, H., “Construction of explicit and implicit symmetric TVD schemes and their applications,” *Journal of Computational Physics*, Vol. 68, No. 1, 1987, pp. 151–179.
- [116] Yee, H. and Shinn, J., “Semi-Implicit and Fully Implicit Shock-Capturing Methods for Hyperbolic Conservation Laws with Stiff Source Terms,” *AIAA-1987-1116*, June 1987.
- [117] Jameson, A. and Turkel, E., “Implicit schemes and LU Decompositions,” *Mathematics of Computation*, Vol. 37, 1981, pp. 385–397.
- [118] Lombard, C. K., Bardina, J., Venkatapathy, E., and Olinger, J., “Multi-Dimensional Formulation of CSCM - An Upwind Flux Difference Eigenvector Split Method for the Compressible Navier-Stokes Equations,” *AIAA-1983-1895*, July 1983.
- [119] Steger, J. L. and Warming, R. F., “Flux Vector Splitting of the Inviscid Gasdynamic Equations with Application to Finite-Difference Methods,” *Journal of Computational Physics*, Vol. 40, 1981, pp. 263–293.
- [120] Hirsch, C., *Numerical Computation of Internal and External Flows, Volume 2*, John Wiley & Sons, 1988.
- [121] Pulliam, T. H. and Chaussee, D. S., “A Diagonal Form of an Implicit Approximate-Factorization Algorithm,” *Journal of Computational Physics*, Vol. 39, 1981, pp. 347–363.

- [122] Pulliam, T. H. and Steger, J. L., "Implicit Finite-Difference Simulations of Three-Dimensional Compressible Flow," *AIAA Journal*, Vol. 18, No. 2, February 1980, pp. 159–167.
- [123] Steger, J. L., "Implicit Finite-Difference Simulation of Flow about Arbitrary Two-Dimensional Geometries," *AIAA Journal*, Vol. 16, No. 7, July 1978, pp. 679–686.
- [124] Obayashi, S. and Kuwahara, K., "An Approximate LU Factorization Method for the Compressible Navier-Stokes Equations," *Journal of Computational Physics*, Vol. 63, No. 1, 1986, pp. 157–167.
- [125] MacCormack, R. W., "A Numerical Method for Solving the Equations of Compressible Viscous Flow," *AIAA Journal*, Vol. 20, No. 9, September 1982, pp. 1275–1281.
- [126] Pope, S. B., *Turbulent Flows*, Cambridge University Press, 2000.
- [127] Smagorinsky, J., "General Circulation Experiments with the Primitive Equations, Part1: The Basic Experiment," *Monthly Weather Review*, Vol. 91, No. 3, March 1963, pp. 99–152.
- [128] Visbal, M. R. and Rizzetta, D. P., "Large-eddy Simulation on General Geometries Using Compact Differencing and Filtering Schemes," *AIAA-2002-288*, 2002.
- [129] Sherer, S. E. and Visbal, M. R., "Implicit Large Eddy Simulations Using a High-Order Overset Grid Solver," *AIAA-2004-2530*, 2004.
- [130] Matsuura, K. and Kato, C., "Large-Eddy Simulation of Compressible Transitional Flows in a Low-Pressure Turbine Cascade," *AIAA Journal*, Vol. 45, No. 2, February 2007, pp. 442–457.
- [131] Gristein, F. F. and Fureby, C., "Recent Progress on MILES for High Reynolds Number Flows," *Journal of Fluids Engineering, Transactions of the ASME*, Vol. 124, 2002, pp. 848–861.
- [132] Kuwahara, K., "Unsteady Flow Simulation and Its Visualization," *AIAA-1999-3405*, 1999.
- [133] Kuwahara, K. and Komurasaki, S., "Direct Simulation of a Flow around an Airfoil," *Proceedings of 14th Computational Fluid Dynamics symposium*, 2000.



- 
- [134] Ooida, J. and Kuwahara, K., “Implicit LES of Turbulence Generated by a Lattice,” *AIAA-2003-4097*, 2003.
- [135] Fujii, K., “Unified Zonal Method Based on the Fortified Solution Algorithm,” *Journal of Computational Physics*, Vol. 118, 1995, pp. 92–108.
- [136] Choi, H. and Moin, P., “Effects of the Computational Time Step on Numerical Solutions of Turbulent Flow,” *Journal of Computational Physics*, Vol. 113, 1994, pp. 1–4.
- [137] Berenger, J.-P., “A Perfectly Matched Layer for the Absorption of Electromagnetic Waves,” *Journal of Computational Physics*, Vol. 114, 1994, pp. 185–200.
- [138] Hu, F., “On Absorbing Boundary Condition for Linear Euler Equations by a Perfectly Matched Layer,” *Journal of Computational Physics*, Vol. 129, 1996, pp. 201–219.
- [139] Freund, J. B., “A Simple Method for Computing Far-field Sound in Aeroacoustic Computations,” *Journal of Computational Physics*, Vol. 157, 2000, pp. 796–800.
- [140] Colonius, T., “Modeling Artificial Boundary Conditions for Compressible Flow,” *Annual Review of Fluid Mechanics*, Vol. 36, 2004, pp. 315–345.
- [141] Hirsch, C., *Numerical Computation of Internal and External Flows*, John Willy and Sons, Inc., 1988.
- [142] Rizzi, A., “Damped Euler-Equation Methods to Compute Transonic Flow Around Wing-Body Combinations,” *AIAA Journal*, Vol. 20, No. 10, October 1982, pp. 1321–1328.
- [143] Shyy, W., Jayaraman, B., and Andersson, A., “Modeling of glow discharge-induced fluid dynamics,” *Journal of Applied Physics*, Vol. 92, No. 11, 2002, pp. 6434–6443.
- [144] Mertz, B. E. and Corke, T. C., “Time-Dependent Dielectric Barrier Discharge Plasma Actuator Modeling,” *AIAA-2009-1083*, 2009.
- [145] Orlov, D. M., Corke, T. C., and Patel, M. P., “Electric Circuit Model for Aerodynamic Plasma Actuator,” *AIAA-2006-1206*, 2006.
- [146] Ibrahim, I. H. and Skote, M., “Simulations of the linear plasma synthetic jet actuator utilizing a modified Suzen-Huang model,” *Physics of Fluids*, Vol. 24, 2012, pp. 113602.

- [147] Suzen, Y. B., Huang, P. G., Jacob, J. D., and Ashpis, D. E., “Numerical Simulations of Plasma Based Flow Control Application,” *AIAA-2005-4633*, 2005.
- [148] Suzen, Y. B. and Huang, P. G., “Simulations of Flow Separation Control using Plasma Actuator,” *AIAA-2006-877*, 2006.
- [149] Suzen, Y. B., Huang, P. G., and Ashpis, D. E., “Numerical Simulations of Flow Separation Control in Low-Pressure Turbines using Plasma Actuators,” *AIAA-2007-937*, January 2007.
- [150] Aono, H., Sekimoto, S., Sato, M., Yakeno, A., Nonomura, T., and Fujii, K., “Computational and experimental analysis of flow structures induced by a plasma actuator with burst modulations in quiescent air,” *Mechanical Engineering Journal*, Vol. 2, No. 4, 2015, pp. 1–16.
- [151] Winkelmann, A. E. and Barlow, J. B., “Flowfield Model for a Rectangular Planform Wing beyond Stall,” *AIAA Journal*, Vol. 18, No. 8, 1980, pp. 1006–1008.
- [152] Yon, S. A. and Katz, J., “Study of the Unsteady Flow Features on a Stalled Wing,” *AIAA Journal*, Vol. 36, No. 3, 1998, pp. 305–312.
- [153] Almutairi, J. H., Jones, L. E., and Sandham, N. D., “Intermittent Bursting of a Laminar Separation Bubble on an Airfoil,” *AIAA Journal*, Vol. 48, No. 2, 2010, pp. 414–426.
- [154] Eisenbach, S. and Friedrich, R., “Large-eddy simulation of flow separation on an airfoil at a high angle of attack and  $Re = 10^5$  using Cartesian grids,” *Theoretical and Computational Fluid Dynamics*, Vol. 22, No. 3-4, 2008, pp. 213–225.
- [155] Frère, A., Hillewaert, K., Sarlak, H., Mikkelsen, R. F., and Chatelain, P., “Cross-Validation of Numerical and Experimental Studies of Transitional Airfoil Performance,” *AIAA 2015-0499*, 2015.
- [156] Mukherjee, S. and Roy, S., “Enhancement of Lift and Drag Characteristics of an Oscillating Airfoil in Deep Dynamic Stall Using Plasma Actuation,” *AIAA 2012-0702*, 2012.
- [157] Davidson, P., Strkie, J. A., and Hind, M. D., “Characterization of Dynamic Stall on 9-12% Thick Airfoils Through Computational and Experimental Methods,” *AIAA 2014-3248*, 2014.

- 
- [158] Zhang, W. and Samtaney, R., “Assessment of spanwise domain size effect on the transitional flow past an airfoil,” *Computers and Fluids*, Vol. 124, 1 2015, pp. 39–53.
- [159] Mellen, C. P., Fröhlich, J., and Rodi, W., “Lessons from LESFOIL Project on Large-Eddy Simulation of Flow Around an Airfoil,” *AIAA Journal*, Vol. 41, No. 4, April 2003, pp. 573–581.
- [160] Lorenzo, A. and de Pablo, V., “DES/DDES post-stall study with iced airfoil,” *AIAA 2011-1103*, 2011.
- [161] Widnall, S. E., “THE STRUCTURE AND DYNAMICS OF VORTEX FILAMENTS,” *Annual Review of Fluid Mechanics*, Vol. 7, 1975, pp. 141–165.
- [162] Crow, S. C., “Stability Theory for a Pair of Trailing Vortices,” *AIAA Journal*, Vol. 8, No. 12, 1970, pp. 2172–2179.
- [163] Laporte, F. and Corjon, A., “Direct numerical simulations of the elliptic Instability of a vortex pair,” *Physics of Fluids*, Vol. 12, No. 5, 2000, pp. 1016–1031.
- [164] Benton, S. I. and Bons, J. P., “Three-dimensional Instabilities in Vortex/Wall Interactions: Linear Stability and Flow Control,” *AIAA 2014-1267*, 2014.
- [165] McCullough, G. B. and Gault, D. E., “Examples of Three representative types of airfoil section stall at low speeds,” Technical Note 2502, National Advisory Committee for Aeronautics, 1951.
- [166] GREGORY, N. and O'REILLY, C. L., “Low-Speed Aerodynamic Characteristics of NACA 0012 Aerofoil Section, including the Effects of Upper-Surface Roughness Simulating Hoar Frost,” Tech. rep., MINISTRY OF DEFENCE, 1973.
- [167] Mulleners, K. and Raffel, M., “The onset of dynamic stall revisited,” *Experiments in Fluids*, 2012.
- [168] McAlister, K. W. and Carr, L. W., “Dynamic Stall Experiments on the NACA 0012 Airfoil,” *NASA Technical Paper 1100*, 1978.
- [169] Wilby, P. G., “The Aerodynamic Characteristics of Some New RAE Blade Sections, and Their Potential Influence on Rotor Performance,” *Paper No.11, 5th European Rotorcraft and Powered Lift Aircraft Forum*, 1979.

- [170] Lorber, P. F. and Carta, F. O., “Airfoil Dynamic Stall at Constant Pitch Rate and High Reynolds Number,” *AIAA 87-1329*, 1987.
- [171] Sheng, W., Galbraith, R. A. M., and Coton, F. N., “A New Stall-Onset Criterion for Low Speed Dynamic-Stall,” *Journal of Solar Energy Engineering*, Vol. 128, No. 4, 2005, pp. 461–471.
- [172] Leishman, J. G., *Principles of Helicopter Aerodynamics*, Cambridge University Press, 2002.
- [173] Sato, M., Okada, K., Nonomura, T., Aono, H., Yakeno, A., Asada, K., Abe, Y., and Fujii, K., “Massive Parametric Study by LES on Separated-flow Control around Airfoil using DBD Plasma Actuator at Reynolds Number 63,000,” *AIAA 2013-2750*, 2013.
- [174] Amitay, M., Kibens, V., Parekh, D., and Glezer, A., “The Dynamics of Flow Reattachment over a Thick Airfoil Controlled by Synthetic Jet Actuators,” *AIAA 99-1001*, 1999.
- [175] Abe, Y., “Mechanism of separated-flow control over an airfoil with synthetic jet devices in low-Reynolds number regime,” *Phd thesis, University of Tokyo*, 2016.
- [176] Pauley, L. L., Moin, P., and Reynolds, W. C., “The structure of two-dimensional separation,” *J. Fluid Mech.*, Vol. 220, 1990, pp. 397–411.
- [177] Hunt, J. C. R., Wray, A. A., and Moin, P., “Eddies, stream, and convergence zones in turbulent flows,” Tech. rep., Center for Turbulence Research, 1988.
- [178] Corke, T. C. and Thomas, F. O., “Dynamic Stall in Pitching Airfoils: Aerodynamic Damping and Compressibility Effects,” *Annual Review of Fluid Mechanics*, Vol. 47, 2015, pp. 479–505.
- [179] McCroskey, W. J., “Unsteady Airfoils,” *Annual Review of Fluid Mechanics*, Vol. 47, 1982, pp. 479–505.
- [180] Ahmed, S. and Chandrasekhara, M. S., “Reattachment Studies of an Oscillating Airfoil Dynamic Stall Flow Field,” *AIAA 91-3225*, 1991.
- [181] Pruski, B. J. and Bowersox, R. D. W., “Leading-Edge Flow Structure of a Dynamically Pitching NACA 0012 Airfoil,” *AIAA Journal*, Vol. 51, No. 5, 2013, pp. 1042–1053.